Study of a new anti-CD37 monoclonal antibody radiolabelled with Luthetium-177 in a B-cell Non-Hodgkin Lymphoma : therapeutic efficacy and mechanisms of action

Alexandre Pichard

THÈSE POUR OBTENIR LE GRADE DE DOCTEUR DE L'UNIVERSITÉ DE MONTPELLIER

En Radiobiologie

École doctorale Sciences Chimiques et Biologiques pour la Santé

Unité de recherche IRCM INSERM U1194

Etude d'un nouvel anticorps anti-CD37 radiomarqué au Lutétium-177 dans le traitement du lymphome B non hodgkinien : efficacité thérapeutique et mécanismes d'action

Présentée par Alexandre PICHARD
Le 23 Novembre 2017

Sous la direction de Jean-Pierre POUGET
et Isabelle NAVARRO-TEULON

Devant le jury composé de

Pierre-Olivier KOTZKI, PU-PH, ICM-IRCM INSERM U1194	Président du jury
Charles DUMONTET, PU-PH, CRCL INSERM U1052	Rapporteur
Tony LAHOUTTE, PU-PH, Vrije Universiteit Brussel Labo ICMI	Rapporteur
Manuel BARDIES, DR2, CRCT INSERM U1037	Examinateur
Peter COOPMAN, CR1, IRCM INSERM U1194	Examinateur
Helen HEYERDAHL, PhD, Director Preclinical Research, Nordic Nanovector ASA	Examinateur
Jean-Pierre POUGET, CR1, IRCM INSERM U1194	Directeur de thèse
Isabelle NAVARRO-TEULON, CR1, ICM-IRCM INSERM U1194	Co-directeur de thèse

UNIVERSITÉ DE MONTPELLIER

Acknowledgements

En premier lieu, je tiens à remercier les membres du jury pour avoir accepté de juger ce travail de thèse et en particulier les Pr Lahoutte et Dumontet pour avoir accepté d'apporter un regard critique sur ce travail en tant que rapporteur. Je tiens également à remercier les examinateurs pour avoir pris le temps de lire ce travail, le Dr Bardiès, le Dr Coopman et le Dr Heyerdahl.

Furthermore, I would like to express my gratitude and thanks to Nordic Nanovector ASA which has funded my thesis. I would like to particularly thank Dr Dahle, Dr Repetto-Llamazares and Dr Heyerdahl. Numerous T-conf performed all along my thesis have always been fruitfull and helped me analysing the results and getting to interesting conclusions.

Je souhaite particulièrement remercier mes deux directeurs de thèse les docteurs Jean-Pierre Pouget et Isabelle Navarro-Teulon. Jean-Pierre et Isa, après une demande de stage tardive, vous m'avez malgré tout accepté alors que vous aviez déjà recruté Riado. Après 4 ans, 7 mois et 12 jours à l'écriture de ces remerciements, j'espère que vous ne regrettez pas (vu ce décompte, j'ose imaginer que non ☺).

Jean-Pierre, je tiens particulièrement à vous remercier pour tout ce que vous m'avez appris ; non pas en tant qu'enseignant car je le confesse aujourd'hui il ne me semble pas avoir eu plus de 11 à votre partiel de radioprotection ; mais énormément en tant que chef d'équipe et directeur de thèse. J'ai adoré nos après-midi philosophiques où nous cherchions par tous les moyens à trouver un côté positif aux résultats moins glorieux. Il y a eu également des moments plus compliqués, où la pression des expérimentations Alpha étaient plus pesantes mais avec du recul tout fini toujours par s'arranger… même l'écriture de cette thèse.

Isa, comment te remercier pour tout ce que tu as fait : pour l'équipe, en sous-marin pour régler les problèmes sans que le chef ne s'en aperçoive ; pour les étudiants avec ta gentillesse et ta disponibilité ; pour les doctorants en les soutenant et en étant certainement l'une des 10 meilleures chefs du monde ; et finalement pour moi, en étant ma meilleure chef du monde et en m'ayant bien plus apporté que juste des informations scientifiques. Pour tout ce que tu fais pour nous et pour ce que tu es pour les gens, Isa je te remercie et te remercierai encore longtemps.

Je tiens également à remercier tous les membres de cette petite équipe qui était en cours d'éclosion lors de notre arrivée et qui grandira, je l'espère, encore longtemps. Vincent pour ces moments de stress pendant les grosses manips Areva ou ITU, pour ces moments de rigolades et

pour ton tact et ta douceur légendaire merci. Cath évidemment, toujours là pour nous, toujours prête à nous aider en toutes circonstances, et merci également pour ces goûters toujours présents dans mon tiroir préféré de Montpellier. Emmanuel bien sûr, le meilleur médecin nucléaire, autant humainement que scientifiquement. Tu as toujours été là pour répondre à nos questions, pour nous aider, pour nous soutenir et pour nous conseiller. Un grand merci pour tout et également pour ce bureau parfait pour ma rédaction. Je remercie également Salomé, première Post-doc à nous surveiller ou à lutter dans des combats de sudoku et de massivemusicquizz acharnés. Je n'oublie évidemment pas l'une des belles rencontres intellectuelles et amicales du labo, Marion, avec nos heures passées dans notre petite pièce de SPECT et nos conversations sur à peu près tous les sujets du monde ;-).

Passons aux gens de passage qui font également la vie du labo au quotidien, Malou évidemment stagiaire de M2 m'ayant bien aidé dans les expérimentations du cycle cellulaire et de l'apoptose. Quelles parties de rigolades dans le labo !! Alan, évidemment pour ces longs, très long moments à l'animalerie et ces fous rires indénombrables. Pauline bien-sûr, cherchant l'AMHR2 sans répit mais disparue sans laisser de trace. Pierre et Eva, derniers stagiaires en date qui auront allié humour et intelligence pour s'intégrer au groupe fermé des ambianceurs du couloir N1F2.

Passons aux sociétaires de ce couloir tant convoité, souvent imité mais jamais égalé ; cette petite bande formée d'anciens et de nouveaux, de jeunes et de moins jeunes, de rigolos et de rieurs. l'anCienne du groupe (Haha), mAdame depuis peu, co-fondatRice de L'Ircm team, je te remercie pour cette ouverture d'esprit qui a fait qu'à NotrE arrivée nous avons pu former cette bande. monsieuR Oeuf, Moins AncIeN puisqu'arrivé 1 an après, mais parmi les plus humoristiquement actifs. toujours à la recherche du bon mot, du jeu de mot et du calambour… pas toujours inspiré mais à chaque fois rigolé, merci. la rugbywoMAn En chef, VoulAnt prier la terre de toute sa voix, mais pas le ciel, il l'entend pas… c'est ta prière païenne (n'y mienne ahah) ; merci pour ce champignon coiffé mi-hallucinogène, mi-gêne tout court. les JeUNes beaux-(skI)eur n'Ont qu'à bien se teniR, celui dont on parle leur mettra tous le nek (en) feu ; siffleur des couloirs et calvaire des rampes d'escaliers, toujours de bons conseils et souriant merci pour ces discussions sérieuses et moins sérieuses mais toujours dans l'extrême … « respect » des convenances (ou pas). je n'oublie paS non plus notre technicienne préférée, pArtie depuis peu (BRavo) pour un avenIr cdi-sé… mainteNAnt vivement la crémaillère ;-) meRci égAlemeNt A notre libanaise ne parlant pas un mot de français en arrivant mais qui repart avec une nouvelle langue en poche.

j'associe évidement vos moitiés devenues entières dans cette team, MI-CAdeau, mi-joueur de foot, MAis ayant toujours les bons mots dans les tuyauX. Et bien-sur vos enfants devenus nos neveux et nièces.

Les nouveaux de la team, Adrien, Ariane, Marie-Lise et Emilia, bonne chance pour vos futurs prix nobels ;-)

Passons à mon compère Riado, nous avons tout partagé (enfin presque), du master au stage, du stage à la thèse, de la thèse à la soutenance et de la soutenance au post-doc. Nous n'étions pas vraiment proches en master mais nous nous sommes approchevoisés au fur et à mesure que les manips, les congrès et les massivemusicquizz avançaient. Je pense que nos deux thèses ont toujours été très liées, j'espère faire aussi bien que toi lors du passage devant le jury. Je te remercie pour tout et aussi pour tout ce que tu m'as appris sur le Bénin ;-) Je suis sûr que nos chemins se croiseront souvent docteur !!!!!!

Concluons pour l'IRCM team, je vous souhaite le meilleur avec beaucoup d'articles mais surtout avec beaucoup de bonne humeur et de bons moments car sans cela la thèse semblera impossible. N'oubliez pas que « les gens qui ne rient pas ne sont pas sérieux » (Alphonse Allais).

Je remercie également les gens qui sont indispensables au laboratoire. Gene et Sabine bien sûr, je ne vous remercierais sûrement pas à la hauteur de ce que vous m'avez appris car je suis arrivé ignorant de tout et vous m'avez enseigné tout ce que je sais aujourd'hui. Merci pour vos conseils, votre aide, votre gentillesse et vos recadrages parfois. Vous êtes l'âme du laboratoire ! J'ai eu la chance de faire une thèse agréable et je ne pourrais pas remercier toutes les personnes qui en sont les acteurs. Je pense à l'administration et particulièrement Nadia chez qui j'allais toujours en urgence pour lancer une commande, ou Chloë que j'ai embêté bien souvent pour un ordre de mission pas toujours dans les temps ou un remboursement qui se fait attendre ; ou encore Daniela qui m'a fait signer douze contrats mais toujours avec le sourire. Il y a également les services communs qui assurent la bonne marche de l'institut et dont on se rend réellement compte qu'ils sont essentiels lorsqu'il y a un problème. Et finalement, toutes les personnes du laboratoire que l'on croise tous les jours et avec qui on interagit ponctuellement mais qui font aussi qu'une thèse avance.

Evidemment, il y a une vie à côté d'une thèse (si, si, restreinte mais essentielle). Je remercie le Tchoumo pour toutes… nos défaites « incompréhensive car en temps normal on le gagne ce match » … pleines d'objectivité et pour tous ces apéros (trop rares pour moi vers la fin).

A mes amis Flo et Gaby, pas ou plus montpelliérains, même si nous ne nous voyons pas autant que je le voudrais, vous êtes pour moi de vrais amis sur lesquels je peux compter !!!

Il est temps de remercier ma famille, je ne dirais jamais assez merci à mes grands-parents pour avoir fait de moi l'homme que je suis ! Alors je profite de ces quelques phrases pour les remercier

d'avoir toujours été là pour moi surtout pendant les 28 premières années de ma vie (puisque j'ai 28 ans).

A toute ma famille qui a une grande part de responsabilité dans cette thèse.

A mon petit frère et ma maman, qui sont des rouages essentiels de ma vie, je serais toujours là pour vous, même si je suis géographiquement loin. Je vous aime.

Revenons à Isa, qui non seulement m'a surveillé et conseillé pendant ma thèse mais qui m'a aussi apporté un élément important dans ma vie :

Tout commença ce 3 février 2015 lors de la soutenance d'HDR de Vincent. Il neigeait et pourtant, je t'ai remarqué derrière ton écharpe et ton gros manteau noir. Pensant que tu étais la fille de Vincent, je ne t'ai pas parlé… après deux heures de soutenance, nous avons été présentés et finalement tu étais LA stagiaire d'Isa et Marion. Aujourd'hui tu es encore là et grâce à toi j'ai pu faire et rédiger cette thèse ; je ne te remercierai pas uniquement pour ça mais je te remercie pour tout le reste et c'est à mes yeux ce qui est le plus important pour notre NOUS …

Table of contents

List of Figures

List of Tables

List of abbreviations

1

^{18}FDG : 2-desoxy-2-fluoro-D-glucose

A

Ab : *Antibody*
ADC : Antibody-drug conjugate
ADCC : *Antibody-dependent cellular cytotoxicity*
ADCP : *Antibody-dependent cell phagocytosis*
Akt : *Protein kinase B*
ALK : *Anaplastic lymphoma kinase*
AP-1 : *Activator protein 1*
ARC : *Antibody radionuclide conjugate*
ATCC : *American type culture collection*
ATM : *Ataxia–telangiectasia mutated*
ATR : *Ataxia telangiectasia and Rad3-related*

B

Bak : *Bcl-2 homologous killer*
Bax : *Bcl-2-like protein 4*
Bcl-2 : *B cell lymphoma-2*
Bcl-6 : *B cell lymphoma-6*
BCR : *B cell receptor*

C

CCL2 : *Chemokine ligand 2*
CCL3 : *Chemokine ligand 3*
CCL4 : *Chemokine ligand 4*
CDK : *Cyclin-dependent kinase*
CDR : *Complementary determining region*
CLL : *chronic lymphocytic leukaemia*
CT : *Computed tomography*

D

DLBCL : *Diffuse large B cell lymphoma*
DNA : *Deoxyribonucleic acid*
DNA–PK : *DNA-dependent protein kinase*
DOTA : *1, 4, 7, 10-tetraazacyclododecane-1, 4, 7, 10-tetracetic acid*
DTPA : *NR-diethylenetriaminepentacetic acid*

E

EBRT : *External beam radiation therapy*
ECACC : *European collection of authenticated cell cultures*
ECOG : Eastern cooperative oncology group
EGFR *Epidermal growth factor receptor*
ERK : *Extracellular signal–regulated kinase*

F

FDA : *Food and Drug Administration*
FISH : *Fluorescence in situ hybridization*
FL : *Follicular lymphoma*
FoxP3 : *Forkhead box P3*

G

GC : *Germinal centre*
G-CSF : *Granulocyte colony-stimulating factor*
GM-CSF : *Granulocyte macrophage colony-stimulating factor*
Gy : *Gray*

H

HIV : *Human immunodeficiency virus*
HL : *Hodgkin lymphoma*
HSC : *Multipotent hematopoietic stem cells*

I

IFN-γ : *Interferon-γ*
Ig : *Immunoglobulin*
IL-10 : *Interleukin-10*
IL-12 : *Interleukin-12*
IL-13 : *Interleukin-13*
IL-2 : *Interleukin-2*
IL-35 : *Interleukin-35*
IL-4 : *Interleukin-4*
IL-5 : *Interleukin-5*
IL-6 : *Interleukin-6*
IL-6Rα : *Interleukin-6 receptor α chain*
IPI : International prognostic index
ITK : *Interleukin-2-inducible T-cell kinase*

L

LET : Linear energy transfer
LQ *: Linear quadratic model*

M

mAb *: Monoclonal antibody*
MALT *:* Mucosa-associated lymphoid tissue
MAPK *: Mitogen-activated protein kinase*
MIRD *: Medical Internal Radiation Dose*
Monomethyl auristatin E *: Monomethyl auristatin E*
MRI *: Magnetic resonance imaging*
MTA *:* Maximal tolerated activity

N

NF-κB *: Nuclear factor-kappa B*
NHL *: Non Hodgkin lymphoma*
NK *: Natural Killer*

P

PCR *: Polymerase chain reaction*
PDK-1 *: Phosphoinositide-dependent protein kinase-1*
PET *: Positron emission tomography*
PI3K *: Phosphoinositide 3-kinase*

R

RKIP *: Raf kinase inhibitory protein*
ROS *: Reactive oxygen species*

S

SOCS3 *: Suppressor of cytokine signaling 3*
SPECT *: Single-photon emission computed tomography*
STAT3 *: Signal transducer and activator of transcription 3*
SYK *: Spleen tyrosine kinase*

T

TCR : *T cell receptor*
TGFβ *: Transforming growth factor-β*
Treg cell *: Regulatory T cell*

W

WHO *: World Health Organization*

INTRODUCTION

I. Lymphoma

A. Generalities

Lymphoma is a cancer type that affects the immune system, especially lymphocytes. Conventionally, lymphoma is divided in two groups: Hodgkin lymphoma (HL) and Non-Hodgkin lymphoma (NHL). Moreover, NHL is a generic term that encompasses many (more than 50) lymphoproliferative malignant diseases (Table 1) with diverse behaviours and responses to treatments. Conversely, HL includes only six subtypes (Table 1) [1]. HL represents 10% of all lymphomas that show a 5-year survival rate higher than 85%. HL was discovered by Sir Thomas Hodgkin in 1832 and is characterised by the presence of Reed-Sternberg cells. This thesis will focus on NHL.

1. Incidence, mortality and prevalence

NHL is the fifth most common cancer in France (tenth in the world) with 11 512 new cases (199 670 in the world) reported in 2012. In France, it is the tenth cause of cancer-related death (11th worldwide) with 4 280 deaths per year [2]. NHL prognosis is variable according to the different histological forms. NHL belongs to the intermediary cancer group in terms of survival (the 5-year survival is 55% in France). However, this value is not representative of the reality because of the survival rate disparities, depending on the NHL types. For example, in France, the 5-year survival rate of mantle cell lymphoma is 45%, whereas that of marginal zone lymphoma is about 87%. These cancers are more frequent in elderly persons (over 60 years of age), but they can develop at any age.

2. Risk factors

Immunosuppression is the most recognized risk factor for NHL. Human immunodeficiency virus (HIV) infection is associated with a higher risk of developing high-grade NHL [3] due to the profound cell-mediated immunodeficiency that allows the deregulated proliferation of B lymphocytes. Other risk factors are organ transplant [4], obesity [5], inherited immunodeficiency syndromes and autoimmune diseases [6]. Epstein-Barr virus, human herpesvirus 8 [7] and human T lymphotropic virus type I [8] are lymphocyte-transforming viruses that can directly infect lymphocytes, disrupt normal cell functions, and promote cell division. Other pathogens, such as hepatitis C virus [9], *Helicobacter pylori* [10] and *Borrelia afzelii* [11], can play a part in the development of some NHL types by inducing a chronic inflammatory response.

Environmental stress agents, such as ionising radiation [12], sunlight [13], agricultural pesticides [14], and dark hair dyes before 1980 [15] also increase the risk of NHL.

B. Non-Hodgkin lymphoma classification

The World Health Organisation (WHO) classification of hematopoietic and lymphoid tumours and the associated monograph provide guidelines for the diagnosis of malignant lymphomas (Table 1) [1]. NHLs are divided in many subgroups according to cell type of origin (B, T and natural killer - NK - cells), disease localisation, and genetic mutations.

Table 1: 2016 WHO classification of mature lymphoid, histiocytic and dendritic neoplasms

Mature B-cell neoplasms
Chronic lymphocytic leukemia/small lymphocytic lymphoma
Monoclonal B-cell lymphocytosis
B-cell prolymphocytic leukemia
Splenic marginal zone lymphoma
Hairy cell leukemia
Splenic B-cell lymphoma/leukemia, unclassifiable
Splenic diffuse red pulp small B-cell lymphoma
Hairy cell leukemia-variant
Lymphoplasmacytic lymphoma
Waldenström macroglobulinemia
Monoclonal gammopathy of undetermined significance (MGUS), IgM
μ heavy-chain disease
γ heavy-chain disease
α heavy-chain disease
Monoclonal gammopathy of undetermined significance, IgG/A
Plasma cell myeloma
Solitary plasmacytoma of bone
Extraosseous plasmacytoma
Monoclonal immunoglobulin deposition diseases
Extranodal marginal zone lymphoma of mucosa-associated lymphoid tissue (MALT lymphoma)
Nodal marginal zone lymphoma
Pediatric nodal marginal zone lymphoma
Follicular lymphoma
In situ follicular neoplasia
Duodenal-type follicular lymphoma
Pediatric-type follicular lymphoma
Large B-cell lymphoma with IRF4 rearrangement
Primary cutaneous follicle center lymphoma
Mantle cell lymphoma
In situ mantle cell neoplasia
Diffuse large B-cell lymphoma (DLBCL), NOS
Germinal center B-cell type
Activated B-cell type
T-cell/histiocyte-rich large B-cell lymphoma
Primary DLBCL of the central nervous system (CNS)
Primary cutaneous DLBCL, leg type
EBV1 DLBCL, NOS
EBV1 mucocutaneous ulcer
DLBCL associated with chronic inflammation
Lymphomatoid granulomatosis
Primary mediastinal (thymic) large B-cell lymphoma
Intravascular large B-cell lymphoma
ALK1 large B-cell lymphoma
Plasmablastic lymphoma
Primary effusion lymphoma
HHV81 DLBCL, NOS
Burkitt lymphoma
Burkitt-like lymphoma with 11q aberration
High-grade B-cell lymphoma, with MYC and BCL2 and/or BCL6 rearrangements
High-grade B-cell lymphoma, NOS
B-cell lymphoma, unclassifiable, with features intermediate between DLBCL and classical Hodgkin lymphoma

Mature T and NK neoplasms
T-cell prolymphocytic leukemia
T-cell large granular lymphocytic leukemia
Chronic lymphoproliferative disorder of NK cells
Aggressive NK-cell leukemia
Systemic EBV1 T-cell lymphoma of childhood
Hydroa vacciniforme–like lymphoproliferative disorder
Adult T-cell leukemia/lymphoma
Extranodal NK-/T-cell lymphoma, nasal type
Enteropathy-associated T-cell lymphoma
Monomorphic epitheliotropic intestinal T-cell lymphoma
Indolent T-cell lymphoproliferative disorder of the GI tract
Hepatosplenic T-cell lymphoma
Subcutaneous panniculitis-like T-cell lymphoma
Mycosis fungoides
Sézary syndrome
Primary cutaneous CD301 T-cell lymphoproliferative disorders
Lymphomatoid papulosis
Primary cutaneous anaplastic large cell lymphoma
Primary cutaneous gd T-cell lymphoma
Primary cutaneous CD81 aggressive epidermotropic cytotoxic T-cell lymphoma
Primary cutaneous acral CD81 T-cell lymphoma
Primary cutaneous CD41 small/medium T-cell lymphoproliferative disorder
Peripheral T-cell lymphoma, NOS
Angioimmunoblastic T-cell lymphoma
Follicular T-cell lymphoma
Nodal peripheral T-cell lymphoma with TFH phenotype
Anaplastic large-cell lymphoma, ALK1
Anaplastic large-cell lymphoma, ALK2
Breast implant–associated anaplastic large-cell lymphoma

Posttransplant lymphoproliferative disorders (PTLD)
Plasmacytic hyperplasia PTLD
Infectious mononucleosis PTLD
Florid follicular hyperplasia PTLD
Polymorphic PTLD
Monomorphic PTLD (B- and T-/NK-cell types)
Classical Hodgkin lymphoma PTLD

Hodgkin lymphoma
Nodular lymphocyte predominant Hodgkin lymphoma
Classical Hodgkin lymphoma
Nodular sclerosis classical Hodgkin lymphoma
Lymphocyte-rich classical Hodgkin lymphoma
Mixed cellularity classical Hodgkin lymphoma
Lymphocyte-depleted classical Hodgkin lymphoma

Histiocytic and dendritic cell neoplasms
Histiocytic sarcoma
Langerhans cell histiocytosis
Langerhans cell sarcoma
Indeterminate dendritic cell tumor
Interdigitating dendritic cell sarcoma
Follicular dendritic cell sarcoma
Fibroblastic reticular cell tumor
Disseminated juvenile xanthogranuloma
Erdheim-Chester disease

In 85-90% of cases, NHLs originate from B lymphocytes, while in the remaining 10-15% of tumours T or NK lymphocytes are involved. B lymphoma represents a heterogeneous group of 52 lymphoid diseases among which the most frequent are diffuse large B cell lymphoma (DLBCL) and follicular lymphoma (FL) (about 40% and 20%, respectively [16]).

Peripheral T (about 10% of all NHL) and NK lymphomas include around 30 lymphoid diseases [16].

1. Cells of origin

Historically, the immune response *via* lymphocytes has been classified as cellular and humoral. The cellular response is mediated by T lymphocytes that recognize and attack their targets directly or indirectly by enlisting the help of other immune cells. Humoral responses are characterised by the production of antibodies by plasma cells, which are differentiated B lymphocytes. Nevertheless, the functions of each lymphocyte subtype are not completely elucidated yet.

Immune cells derive from common progenitors called pluripotent haematopoietic stem cells and located in the bone marrow. These progenitors generate all future red and white blood cells:

- lymphoid stem cells, B and T precursors and NK lymphocytes;

- myeloid stem cells, precursors of monocytes/macrophages, granulocytes (neutrophils, basophils and eosinophils) and also erythrocytes and megakaryocytes (platelets).

On the other hand, dendritic cells originate from both lymphoid and myeloid stem cells (Figure 1).

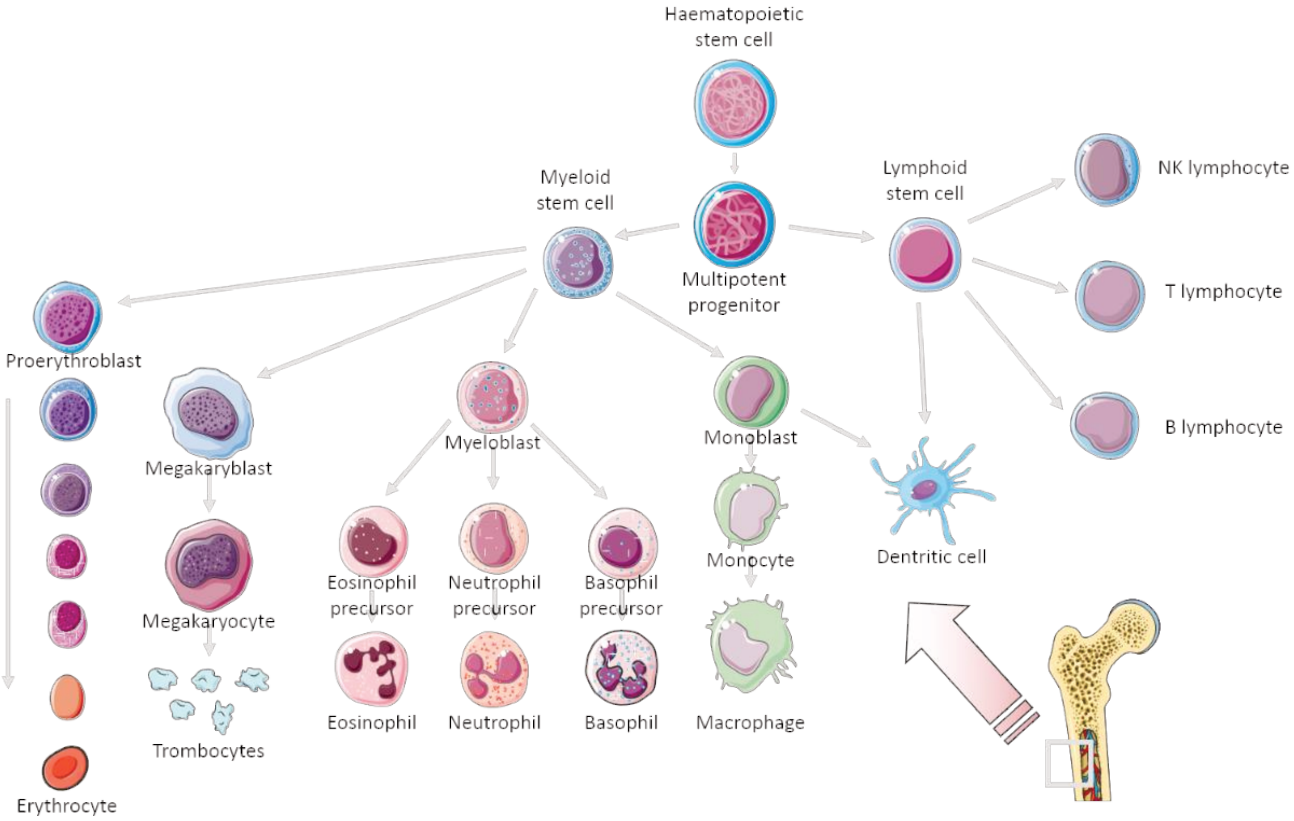

Figure 1: Haematopoietic stem cell differentiation

a. Natural killer (NK) lymphocytes

NK lymphocytes are the biggest lymphocytes and represent 10 to 20% of all circulating lymphocytes. They are generally considered to be components of the innate immune defence because they lack antigen-specific cell-surface receptors and are characterised by the presence of CD56 and CD16 at their surface. NK cell activation is determined by the balance between inhibitory (e.g., major histocompatibility complex class I) and activating (e.g. hemagglutinin or viral ligands) signals. In humans and mice, NK cells are involved in the first line of defence against viral infections [17] and in tumour immunosurveillance [18]. NK cells were originally described as cytolytic effector lymphocytes that can act in the absence of specific immunisation by directly inducing the death of tumour cells and virus-infected cells through small granules in their cytoplasm that contain proteins, such as perforin and proteases, known as granzymes. Subsequently, NK cells have been recognised as major producers of cytokines (such as IFN-γ in many physiological and pathological conditions), growth factors (such as GM-CSF and G-CSF) and chemokines (such as CCL2, CCL3 or CCL4) [19].

b. T lymphocytes

T cell progenitors leave the bone marrow and migrate, *via* the blood circulation, to the thymus where they mature into T lymphocytes. T cells are characterised by the presence on their

surface of CD3 and T cell receptors (TCR). TCR are involved in the activation of T cells by recognition of a specific antigen. Several T cell subgroups can be distinguished:

-CD8-positive T cells (or cytotoxic T cells) are very important for the immune defence against intracellular pathogens, including viruses and bacteria, and for tumour surveillance. By directly interacting with the FAS receptors expressed by infected cells, they induce the death of such cells. They contribute to the killing of infected cells also by producing and releasing cytotoxic granules that contain proteins, such as perforin or granzymes. CD8-positive T cells can also secrete cytokines, such as TNF-α or IFN-γ [20].

-CD4-positive T cells (or helper T cells) play an important role in the immune defence, by releasing cytokines, such as IFN-γ, IL-12, IL-4, IL-5 or IL-13, that activate effector immune cells. CD4-positive T cells are essential for B-cell antibody class switching, for cytotoxic T cell activation and growth, and for enhancing the bactericidal activity of phagocytes, such as macrophages [21].

-Regulatory T cells (Treg cells) are characterized by the presence at their surface of CD4 and CD25 and by the expression of the nuclear transcription factor FOXP3. This cell type acts via different mechanisms: secretion of inhibitory cytokines (IL-10, TGFβ and IL-35), and secretion of molecules that can inhibit the immune response in many settings, such as autoimmune disease, allergy, microbial infection, tumour immunity, organ transplantation, foetal-maternal tolerance and even obesity [22].

c. B lymphocytes

B lymphocytes originate in the bone marrow and their maturation ends in the spleen or in lymph nodes. B cells are characterized by the presence on their surface of CD19 and B cell receptors (BCR) that are involved in antigen identification. Each B cell is activated by a unique and specific antigen. B-cell activation leads to their differentiation into terminally differentiated plasma cells that produce antibodies. However, B cells have also many other functions, such as antigen presentation, production of cytokines (*e.g.*, IL-2, IL-4, TNFα or IL-6) and suppressive activity *via* secretion of IL-10 [23].

The high diversity of TCR and BCR allows T and B cells to deal with the high number of antigens present in an organism. Thus, millions of different molecules can be secreted. This implies that T and B cell maturation is associated with many rearrangements of the DNA (deoxyribonucleic acid) sequences encoding BCR and TCR.

d. DNA rearrangements in B cells

BCR is a transmembrane protein complex, composed of one immunoglobulin (Ig) molecule for antigen recognition, and two CD79 subunits ($CD79_a$ and $CD79_b$) for intracellular transduction signalling (Figure 2).

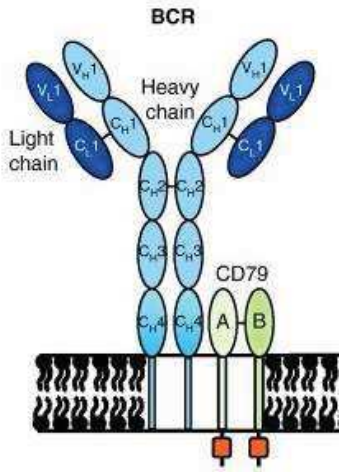

Figure 2: BCR structure [24]

The Ig is made of two variable (V) regions that interact with the antigen, and a constant (C) region that mediates its effector functions. The V regions are constituted of variable segments of heavy (H) and light (L) chains (Figure 2, Figure 12 and §I.D.4.a. p40 for details).

The human body can generate more antibodies (>10^{12} different molecules) than the number of genes in its genome (50 000). B cells produce this huge repertoire of antibodies according to different steps.

In the first phase, the three gene segments V_H (Variable), D_H (Diversity) and J_H (Joining) are joined to encode the H chain V segment (Figure 2). This process is called "V(D)J recombination" (Figure 3a) and is closely regulated. D_H–J_H rearrangements occur first in H-chain genes and are followed by V_H–D_HJ_H rearrangements. About 50 functional V_H gene segments, 27 D_H segments and 6 J_H segments are available at the beginning of the rearrangement, thus allowing the generation of a diverse repertoire of V_H gene rearrangements. This diversity is further increased by the addition or removal of nucleotides at the joining sites of the gene segments. Next, L chain locus rearrangements occur. The V regions of L chains (V_L) are encoded by two gene segments: V_L and J_L. Then, the variable region (V) of the Ig gene is connected to the C region of the Ig gene (Cμ).

In the second phase, when B cells reach germinal centres (GC) in lymph nodes or in spleen (see § I. B. 2.a. iv. a) p25), somatic hypermutation, a process to allow the mutation of antibody-producing genes, is activated, leading to the introduction of point mutations, deletions or duplications in the rearranged V region of Ig genes ('x' in Figure 3b).

In the third phase, class switching will result in the replacement of the originally expressed H chain C region gene (C_H) with that of another Ig gene. The C region of IgM (Cμ) and IgD (Cδ) are exchanged with the C region of IgG (Cγ1) by recombination at the switch regions for these genes (Sμ and Sγ1, respectively) (Figure 3c). This results in an antibody that displays different effector functions, but with the same antigen-binding domain [25].

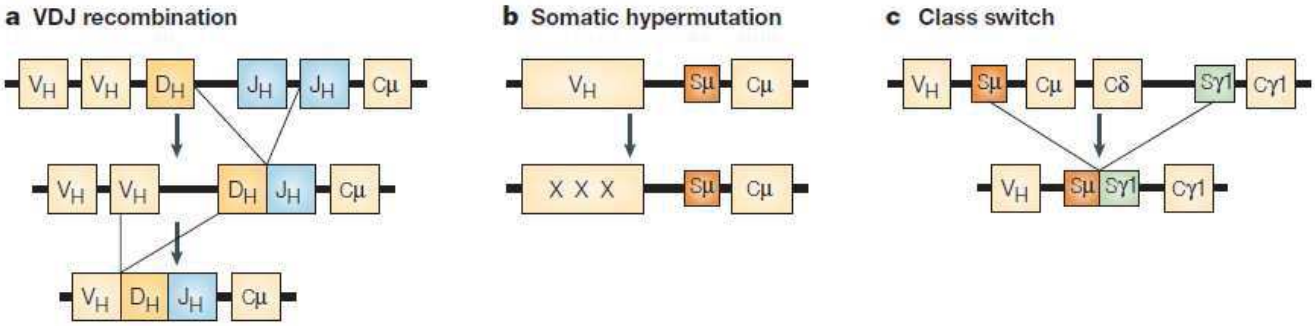

Figure 3: Molecular processes that remodel immunoglobulin genes [25]

e. *DNA rearrangements in T cells*

TCR are structurally similar to Ig and are encoded by homologous genes. TCR genes are assembled by somatic recombination from sets of gene segments in the same way as for Ig genes. However, TCR loci have roughly the same number of V gene segments, but more J gene segments, and there is a greater diversification of junctions between gene segments during gene rearrangement. Moreover, functional TCR do not seem to diversify their V genes after rearrangement through somatic hypermutation. Class switching also is specific to BCR. Indeed, all B-cell effector functions depend on the secretion of antibodies with different H chain C-region isotypes that trigger distinct effector mechanisms. Conversely, T-cell effector functions depend on cell-cell contacts and are not mediated directly by TCR that are only used for antigen recognition [26].

Because of DNA rearrangements during lymphocyte maturation, many DNA mutations are generated that could contribute to lymphomas induction.

Besides the cell of origin, the disease localization is a second criterion for NHL classification, as described below.

2. Non-Hodgkin lymphoma origin

Lymphomas are located in lymphoid organs, but can spread to other organs. The lymphoid organs family is classified in primary organs (thymus and bone marrow) and secondary organs (lymph nodes, spleen, tonsils and mucosa-associated lymphoid tissue). Lymphocytes originate

and grow in primary lymphoid organs, but they mature in secondary lymphoid tissues where they play the role of sentinels.

a. Lymphoid organs

i.Bone marrow

Only bone marrow in short and flat bones (sternum, ribs, vertebrae, iliac bones, cranium, proximal epiphyses of humerus and femur, *etc*.) has haematopoietic activity. Indeed, only these bones contain red bone marrow with multipotent haematopoietic stem cells (HSC), as opposed to yellow bone marrow that is constituted of adipocytes. Bone marrow also includes stromal cells that act as a supporting tissue to allow HSC multiplication and differentiation. The venous sinuses present in the bone marrow are very permissive, allowing the cells to reach the blood vessels through a discontinuous basal lamina.

ii.Thymus

Thymus is a lympho-epithelial organ located in the mediastinum. It plays an essential role in T-cell differentiation. T cells can undergo differentiation also in other tissues (*e.g*., the digestive epithelium), but to a lower extent. Thymus is composed of different cell types: immature T lymphocytes, dendritic cells that play an essential role in T lymphocyte development, epithelial cells that form the thymus structure and secrete indispensable substances for lymphocyte differentiation, and macrophages that eliminate failed T lymphocytes.

iii.Tonsils and mucosa-associated lymphoid tissue

Tonsils are the simplest lymphatic organ. They form a ring of lymphatic tissue around the pharynx entrance. They are named according to their location: palatal, lingual and pharyngeal tonsils. They collect and destroy most pathogens carried by food or air. Specifically, bacteria and particles are captured by the crypts formed at the tonsil surface, pass through the epithelium and reach the lymphatic tissue, where most of them are destroyed. The tonsil lymphatic tissue includes follicles with GCs surrounded by scattered lymphocytes. Tonsils are part of the mucosa-associated lymphoid tissue (MALT) that can be observed along the surface of all mucosal tissues, such as small intestine (gut-associated lymphoid tissue), bronchi (bronchus-associated lymphoid tissue), skin (skin-associated lymphoid tissue), *etc*.

iv.Lymph nodes

Lymph nodes are small bean-shaped organs associated in groups or chains along the lymphatic circulation, well delineated, and with a complex structure. They are present throughout the body, but are more concentrated near and within the trunk. Their size ranges from few millimetres to several centimetres, depending on their state (*e.g*., stimulation, invasion by tumour cells…). Generally, NHLs develop in lymph nodes. For this reason, their structure and functions will be described more in details.

(a) Structure

Lymph nodes are essentially accumulations of diffuse and nodular lymphatic tissue enclosed in the conjunctive capsule that is thicker at the hilus. Afferent lymphatic vessels enter the node at multiple sites, anywhere over its convex surface; efferent lymphatics leave the node at the hilus. Inside, the parenchyma is organized in three areas (Figure 4):

-Cortical area: it is separated from the capsule by the subcapsular sinus (or marginal sinus) that receives the lymph from afferent lymphatic vessels. It is composed of primary lymphoid follicles that are homogeneous formations made of a uniform population of proliferating B lymphocytes. During an immune response, primary lymphoid follicles are modified with the appearance of GCs. Then, follicles are called secondary lymphoid follicles the growth of which is promoted by antigenic stimulation. The GC contains medium- and large-size immune-stimulated lymphocytes in the centre, and is surrounded by the mantle zone composed of naive B lymphocytes. The lymph node cortical area contains almost only B cells, but some T cells and dendritic cells can be found in GCs.

-Paracortical area: it is less dense than the cortical area, without any organized structure and without follicles. It is particularly rich in T lymphocytes and is atrophied after thymectomy, hence the term of T-dependent zone. The paracortical area also contains antigen-presenting cells, such as dendritic cells. In this area, lymphocyte migration between the blood circulation and the lymph node can occur through post-capillary venules.

-Medulla area: the medulla extends to the hilus. It contains a mixed lymphatic population of B and T lymphocytes and also macrophages. These are essentially mature cells in transit.

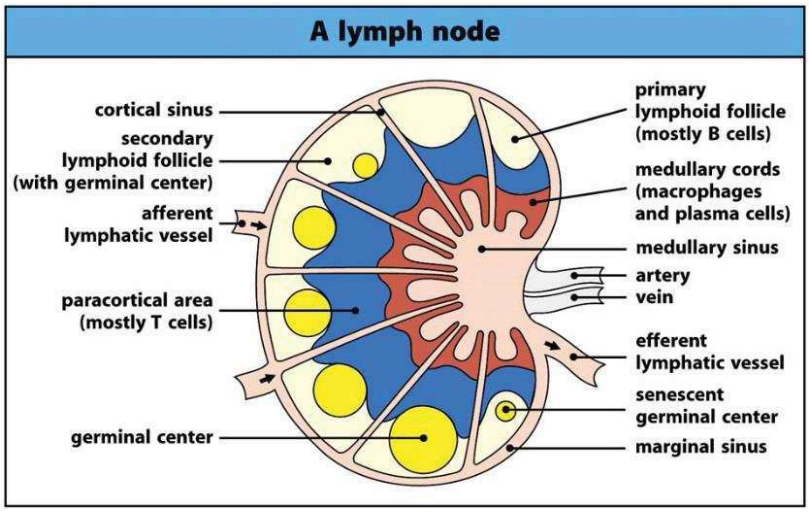

Figure 4: Lymph node structure [27]

(b) Functions

The lymph node main functions are (i) to filter and control lymph; and (ii) to produce and maintain immune cells. These functions are very closely linked. The lymph entering a lymph node comes from the interstitial fluid through afferent lymphatic vessels. Then, within the lymph node, the lymph follows a very complex route with intense mixing, leading to efficient pathogen uptake and elimination by macrophages. As many filtered substances are antigenic, some of them will form antigen-antibody complexes that are held at the surface of dendritic cells, thus triggering lymphocyte stimulation. However, complete filtration requires successive passages through lymph nodes in lymph node chains. Thus, impurity-containing lymph is completely purified before reaching the thoracic duct after filtration through successive lymph nodes.

v.Spleen

Spleen is a highly irrigated organ and the most voluminous lymphoid organ. It is located on the left side of the abdominal cavity, around the anterior part of the stomach. Like lymph nodes, spleen has two major functions: i) lymphocyte proliferation to participate in the immune response; and ii) blood cleaning/purification. The spleen eliminates old erythrocytes and altered platelets. Moreover, splenic macrophages remove debris and foreign bodies from blood. Spleen is surrounded by a fibrous capsule that extends inside through the trabeculae. Trabeculae contain lymphocytes and macrophages as well as a huge amount of erythrocytes and platelets, and are responsible for spleen blood purification function. Spleen domains rich in T and B lymphocytes are called white pulp and forms islets in the spleen red pulp (Figure 5). The white pulp is located around central arteries and contains primary and secondary follicles. The red pulp consists essentially of all the remaining splenic tissue and represents the largest part. It is the site of blood purification by macrophages.

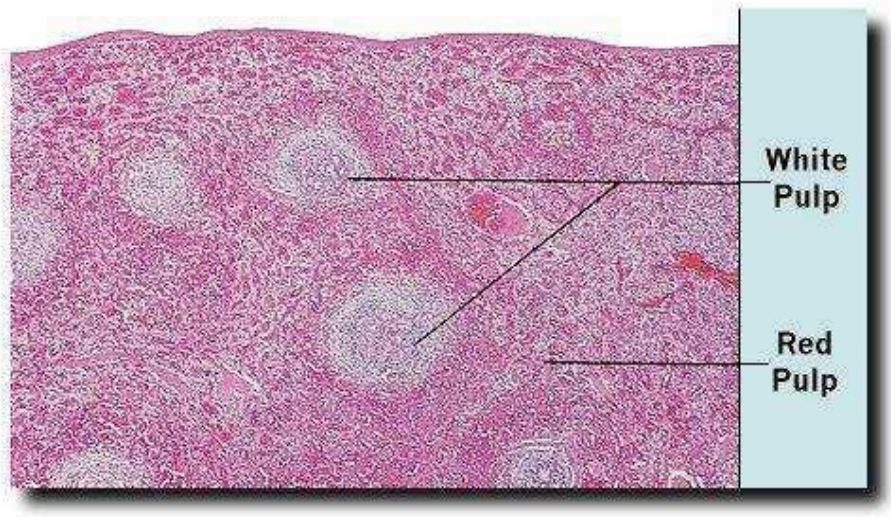

Figure 5: Histological analysis of transversal spleen tissue section [28]

b. Non-Hodgkin lymphoma localization

Besides the classification based on the cell of origin, lymphomas are also categorized according to the tissue they originate from. NHL usually develop within a lymph node, but in 40% of cases, the origin is extranodal. This may include digestive, cutaneous or testis involvement (MALT lymphoma) or other organs, such as spleen.

Furthermore, within a given organ, the precise site of NHL origin and the type and maturation level of the involved cells also affect the classification. For example, FL begins in the follicular area of a lymph node [29]. Consequently, physicians try to determine not only the cell type, but also the site of origin and the genetic characteristics of tumour cells.

3. Genetic mutations

New findings from DNA sequencing studies have provided substantial insights into NHL biology. In B-cell NHL, specific translocations in key genes lead to their deregulation. For instance, in B cells, the H-chain locus on chromosome 14q32 is highly transcribed because these cells require BCR expression for their survival. In B-cell NHL, translocations can put another locus under the control of the H-chain promoter. This leads to overexpression of the protein encoded by this locus (Figure 6). In B-cell NHL, the high-frequency involvement of the H-chain locus in chromosomal translocations is clearly due to genetic recombination and hypermutation at this site during normal B-cell development. By contrast, the exact mechanism by which specific proto-oncogenes, such as Bcl-2 or c-MYC, are involved in these translocations remains relatively unclear. The spatial proximity of proto-oncogenes with the H-chain gene during B-cell activation could be involved. Indeed, Osborne *et al.* have shown that when B lymphocytes are stimulated, the c-MYC and H-chain genes are close to each other, thus increasing the incidence of specific chromosomal translocations [30].

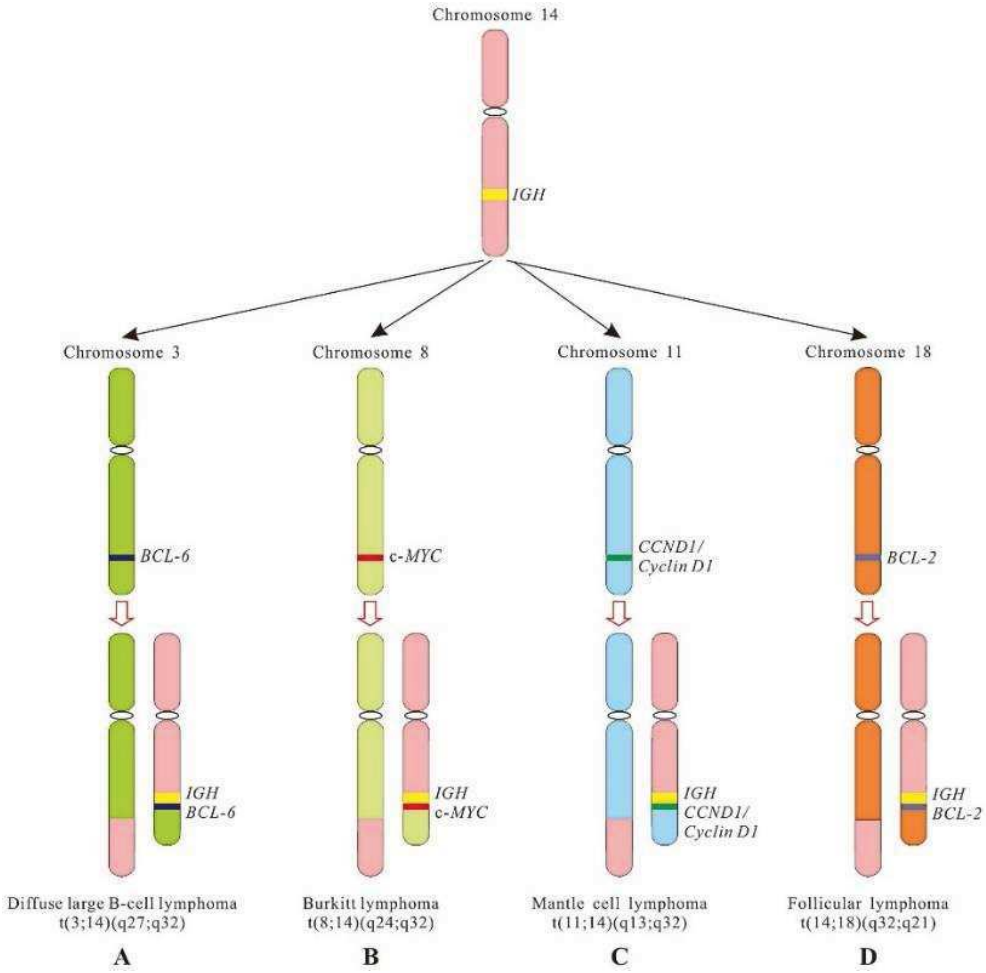

Figure 6: Chromosomal translocations in NHL [31]

FL genetic hallmark is the chromosomal translocation t(14;18)(q32;q21) that is detected in approximately 85% of cases. This translocation puts the B-cell lymphoma-2 (Bcl-2) gene under the control of the H-chain promoter, leading to constitutive expression of the anti-apoptotic protein Bcl-2. However, this translocation is not sufficient for FL diagnosis, because it is absent in 15% of FL and present in about 20%–30% of DLBCL. Moreover, the finding that 46% of 715 healthy people carried this translocation [32] suggests that it is not sufficient to induce NHL and that additional genetic aberrations are necessary. Thus, NHL can present specific translocations, but its development is due to multiple factors.

Genetic mutations have been found also in other NHL types. For instance, mantle cell lymphoma is characterized by the t(11;14)(q13;q32) translocation that leads to the deregulated expression of cyclin D1 and promotion of the G1/S transition in the cell cycle. In Burkitt's lymphoma, c-MYC is overexpressed in 80% of cases as a result of the t(8;14)(q24;q32) translocation. Other translocations, such as the one involving the B-cell lymphoma-6 gene (Bcl-6), have been described and can be markers of good or bad prognosis in NHL [33].

Compared with other lymphoma types, recurrent translocations are less common in T-cell lymphomas. Nevertheless, the t(2;5)(p23;q35) translocation is observed in anaplastic lymphoma kinase (ALK)-positive anaplastic T-cell lymphoma [34]. Less frequently, the t(5;9)(q33;q22) translocation (ITK and SYK fusion) is associated with follicular T-cell lymphoma [35].

To better understand the role of these translocations in tumour initiation/development, the functions of the involved proto-oncogenes are now briefly described.

a. Bcl-2

Bcl-2 is a member of the Bcl family of proteins involved in apoptosis. Specifically, this family plays a role in the permeability of the mitochondrial outer membrane and in calcium homeostasis. Apoptosis is initiated upon loss of the mitochondrial membrane permeability and cytochrome C release from mitochondria. The Bcl family includes about 30 different proteins with pro- (*e.g.*, BAX and BAK) or anti-apoptotic functions (*e.g.*, Bcl-2 and Bcl-xL).

b. c-MYC

c-MYC is a transcription factor that regulates 10-15% of all human genes. Therefore, c-MYC controls a variety of cell functions, such as cell cycle, growth, survival, metabolism and biosynthesis, adhesion, and mitochondrial functions.

c. Cyclin D1

Cyclin D1 plays a key role in cell cycle regulation during the G1/S transition by cooperating with cyclin-dependent kinases (CDK). A major consequence of cyclin D1 overexpression is the deregulation of CDK activity that provides cells with a selective growth advantage. Indeed, when the checkpoint arrest control is compromised, S phase or mitosis will start even in the presence of cell damage, and the ensuing genetic instability may lead to the emergence of a malignant clone.

d. Bcl-6

Bcl-6 is a transcription factor with essential roles in normal B-cell and T-cell antibody responses. This protein acts as a sequence-specific repressor. Bcl-6 also regulates genes involved in cell cycle regulation, such as CDKN1A (encoding p21), and in cell differentiation, such as PRDM1, which is frequently mutated in NHL.

e. ALK

Anaplastic lymphoma kinase (ALK) is a tyrosine kinase receptor that belongs to the insulin growth factor receptor super-family. Most of the time, ALK translocation leads to its constitutive activation and the stimulation of multiple signalling pathways that are involved in cell transformation and the maintenance of a malignant phenotype [36].

4. Indolent *vs* aggressive lymphoma

NHL subtypes are categorized on the basis of the lymphoma cell features, primary localization and genetic features. Moreover, terms to describe the disease growth speed, such as indolent, aggressive and very aggressive lymphoma, are used in the clinic, although they are not included in the WHO classification. For example, the term "indolent lymphoma" describes tumours characterized by slow development, measurable in years. Conversely, "aggressive lymphoma" describes rapidly developing tumours. FL is the most common indolent NHL, whereas DLBCL is the most common aggressive NHL.

C. Non-Hodgkin lymphoma diagnosis

Lymphoma clinical and biological symptoms can widely vary, depending on its location.

1. Early clinical symptoms

The first symptoms can be associated with lymphoid organs, but general, non-disease specific symptoms can also be observed:

- a persistent increase of the size of one or more superficial lymph nodes (adenopathy) that can be noticed under the skin and to the touch; generally, they are not painful.

- unspecific signs, such as prolonged fever with no specific reason, abundant night sweats, fatigue, unexplained weight loss or unexplained itching.

- unexplained increase of liver or spleen volume.

- problems associated with the increased volume of deep lymph nodes that compress other organs. Other symptoms, such as abdominal pain, vomiting and constipation in the case of digestive lymphoma, also have been reported.

2. Diagnosis

First, the physician will determine by clinical examination if lymph nodes and other organs, such as the spleen and liver, have been affected by the disease. For instance, lymph nodes swell in the case of injury, infection, or tumour development near or within the lymph node.

Then, a biopsy of the lymph node or of the tumour mass is carried out to confirm NHL. Immunohistochemistry analyses are used to determine the tumour expression profile. Chromosomal analysis, using fluorescence in situ hybridization (FISH) or polymerase chain reaction (PCR) amplification, is used to detect the presence and nature of gene translocations. Furthermore, blood sample analysis can be performed to highlight the presence of infections (by HIV or hepatitis virus) or to check the bone marrow, liver or kidney physiological functions.

To refine the diagnosis, other exams can be carried out (X-rays, ultrasound or magnetic resonance imaging) to identify other possible causes of the reported symptoms, such as the presence of enlarged lymph nodes in the thorax, or to determine the lymphoma spread. Positron emission tomography (PET) using 2-deoxy-2-(^{18}F)fluoro-D-glucose (^{18}FDG) associated with computed tomography (CT) is also a standard procedure in NHL diagnosis. ^{18}FDG is a glucose analogue labelled with fluorine 18 (^{18}F), a positron emitter. ^{18}FDG accumulates in active metabolic tissues with high glucose consumption, such as brain and also tumours. Thus, PET-CT imaging gives a picture of glucose accumulation in tissues as soon as they are metabolically active. Because of their very low development rate and variable avidity for glucose, the detection of indolent NHL by PET-CT is sometimes difficult.

After the determination of the NHL subtype and localization, disease dissemination is assessed to choose the most appropriate therapy and to make an accurate prognosis. However, due to NHL diversity, no classification system can perfectly predict the prognosis of each subtype.

3. Ann Arbor staging system

The Ann Arbor staging system for lymphomas has roughly the same function as the TNM staging system for solid tumours. It was created for staging HL in 1971 [37], but it is today used for both HL and NHL. This classification was improved by the Cotswold modifications in 1989 [38]. It includes four stages (Figure 7):

Stage I: Involvement of a single lymph node region (called I), or localized involvement of a single extra-lymphatic organ or site in the absence of any lymph node involvement (called IE).

Nota bene: a lymph node region corresponds to the succession of several lymph nodes and not just one ganglion.

Stage II: Involvement of two or more lymph node regions on the same side of the diaphragm (called II), or localized involvement of a single extra-lymphatic organ or site in association with regional lymph node involvement with or without involvement of other lymph node regions on the same side of the diaphragm (IIE). The number of regions involved may be indicated by a subscript, for example, II3 (three lymph node regions involved).

Stage III: Involvement of lymph node regions on both sides of the diaphragm (III). This could be accompanied also by extra-lymphatic extensions in association with the involvement of adjacent lymph nodes (IIIE), spleen (IIIS) or both (IIIE,S).

Stage IV: Diffuse or disseminated involvement of one or more extra-lymphatic organs, with or without associated lymph node involvement; or isolated extra-lymphatic organ involvement in the absence of adjacent regional lymph node involvement, but in conjunction with disease in distant site(s). Any involvement of the liver or bone marrow, or nodular involvement of the lung(s) is always Stage IV. Stage IV disease localization is indicated by specifying the site according to the notations listed for Stage III.

The presence of fever (38°C), drenching sweats, and weight loss (10% of body weight over 6 months) is indicated by the addition of the letter "B", and their absence by the letter "A". Moreover, with tumours bigger than 10 cm, the term "bulky disease" is used.

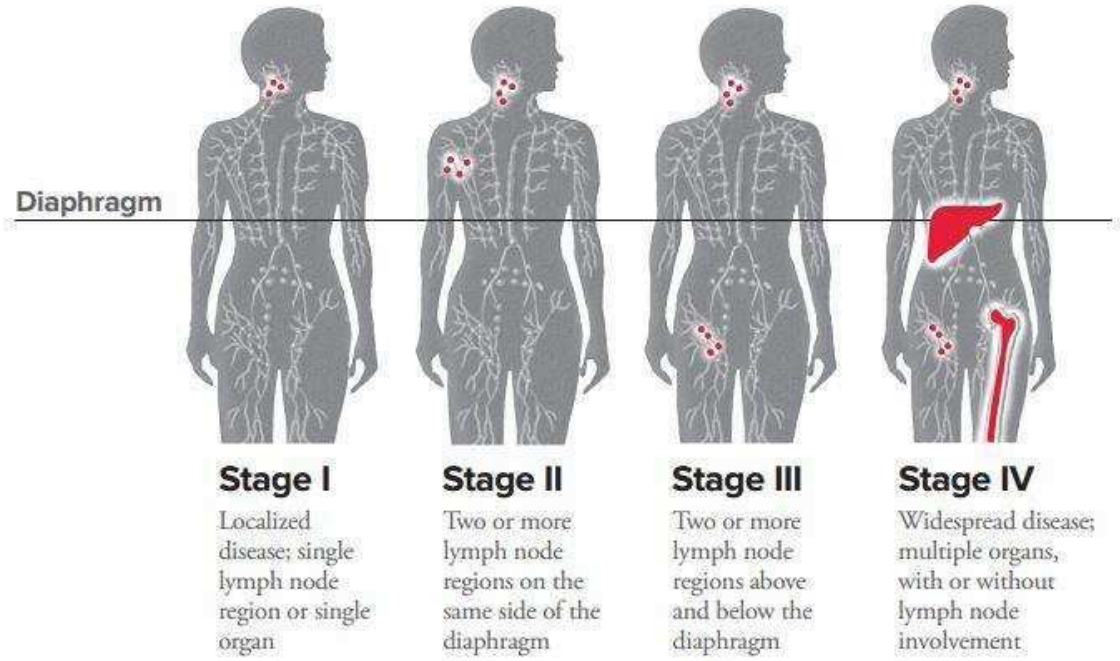

Figure 7: Illustration of the modified Ann Arbor staging system [39]

4. The international prognostic index (IPI)

The IPI is the most used prognostic model for patients with NHL [40]. This index is based on the Ann Arbor staging system and on other additional *criteria* defined on the basis of the results from an international analysis carried out in large lymphoma study groups. The most important elements are:

- Age higher than 60 years
- Stage 3 or 4 in the Ann Arbor staging system

- More than one extra nodal site
- Elevated serum level of lactate dehydrogenase
    - *Lactate dehydrogenase is an enzyme that catalyses the reversible transformation of lactate in pyruvate. Lactate dehydrogenase serum level increase is correlated with advanced cancer and aggressiveness*.
- Physical condition (ECOG 2, 3 or 4)
    - *The Eastern Cooperative Oncology Group (ECOG) scale to assess the performance status by measuring the patient's ability to perform routine tasks and daily activities (Table 2)* [41].

Each of these elements is rated one point. Patients with a score of 0 have a better prognosis than patients with high IPI scores.

Table 2: ECOG performance status

GRADE	ECOG PERFORMANCE STATUS
0	Fully active, able to carry on all pre-disease activities without restriction
1	Restricted in physically strenuous activity, but ambulatory and able to carry out work of a light or sedentary nature (e.g., light house work, office work)
2	Ambulatory and capable of all self-care, but unable to carry out any work activities; up and about for more than 50% of waking hours
3	Capable of only limited self-care; confined to bed or chair for more than 50% of waking hours
4	Completely disabled; cannot perform any self-care; totally confined to bed or chair

For some NHL, such as FL or mantle cell lymphoma, this index is adjusted. For example for FL, haemoglobin level (<12 g/dL) is included in the index (Follicular lymphoma IPI= FLIPI), whereas for mantle NHL, white blood cell count (>6 x 10^9/L) is included in the index (Mantle IPI).

D. Treatments

NHL treatment depends on the tumour histologic type and stage. Several treatments are currently used in the clinic.

1. Surgery

Surgery is rarely used to treat NHL, and it is generally performed only to obtain a biopsy sample for diagnostic and classification purposes. If the tumour is large, surgery can be used to

resect it (*i.e.*, tumour debulking). In the case of splenic marginal zone lymphoma, the spleen may also be removed.

2. External beam radiation therapy

In external beam radiation therapy (EBRT), the emitted ionizing radiations interact with electrons of the encountered molecules. This interaction leads to ionization or excitation of the electron that causes a modification of the affected molecule. External beam radiation inundates tumour cells with high energies (6 to 20 MeV) to induce irreparable DNA breaks or enough repairable DNA breaks to saturate the repair mechanisms, and lead to cell death.

When ionizing radiation penetrates matter, it deposits energy by interaction with the hit molecules. The absorbed dose is the amount of deposited energy per unit mass (Joule/kg) and it is measured in Gray (Gy; 1 Gy is equal to 1 J/Kg). The biological effects, such as tumour regression, are usually proportional to the dose.

The radiation dose usually varies from 25 Gy to 50 Gy and depends on different factors, such as the tumour histologic type, the patient's conditions, the intention of treatment (curative or palliative), the proximity of sensitive organs, and the treatment nature (radiation therapy alone or in combination with other treatments, such as chemotherapy). Most often, radiation treatments consist of five sessions per week during several weeks, with a 2 Gy tumour absorbed dose/irradiation delivered at 1 $Gy.min^{-1}$.

EBRT can be used as the main treatment for some types of NHL, if they are detected at an early stage (stage I or II), because NHL are radiosensitive. For more advanced or aggressive lymphomas, radiation is sometimes combined with chemotherapy. Patients who undergo a stem cell transplant receive whole body irradiation and are treated with high-dose chemotherapy for killing lymphoma cells in the entire body. Radiation therapy can also be used to palliate symptoms caused by a lymphoma that has spread to internal organs, such as brain or spinal cord, or when a tumour causes pain because of nerve compression.

EBRT side effects are loco-regionals due to the irradiation of healthy tissues. Common side effects are tiredness, skin problems (dry, rough, red, painful etc.), nausea and diarrhoea (abdomen irradiation), increased risks of infection, mouth sores and swallowing troubles (head and neck irradiation). These effects are transients and disappear shortly after the treatment end. A possible long-term side effect of radiation therapy is the appearance of a secondary tumour due to irradiation of healthy tissue.

As NHL can be localized but with a possibility of dissemination, EBRT is generally associated with a systemic treatment.

3. Chemotherapy

Differently from loco-regional treatments such as EBRT, chemotherapy is a systemic therapy, and therefore is suitable for already disseminated tumours or at high-risk of dissemination, for instance NHL. Chemotherapy agents are small synthetic molecules that target signalling pathways involved in the regulation of cell proliferation or death, mitotic spindle formation, DNA replication, transcription, or repair. The drug combination, doses, and treatment duration depend on the NHL type and stage. Several chemotherapies are routinely used in the clinic and they are classified according to their mechanisms of action and properties.

a. Alkylating agents and platinum agents

Alkylating agents are highly electrophilic compounds that react with nucleophilic radicals, such as -SH, -OH, -COOH or -NH_2 groups, that are present in nucleic acids and proteins. The link between an alkylating agent and DNA can involve a covalent bond by simple attachment of an alkyl to a purine base, or a connection of the alkylating agent with two adjacent nucleotides to form inter- or intra-strand crosslinks (Figure 8). The binding of these molecules to DNA, and particularly the formation of inter-strand crosslinks, prevents DNA replication and transcription [42], leading to cell death. Alkylating agents mainly bind to purine bases, particularly guanines that have four potential binding sites, whereas adenine residues contain only two binding sites.

Cyclophosphamide, chlorambucil, bendamustine and ifosfamidine are the most common alkylating agents used for NHL treatment.

The mechanisms of action of platinum-based drugs are similar to those of alkylating agents. They create very strong chemical bonds between different DNA strands or inside a DNA strand. Carboplatin, cisplatin and oxaliplatin are the most commonly used platinum agents.

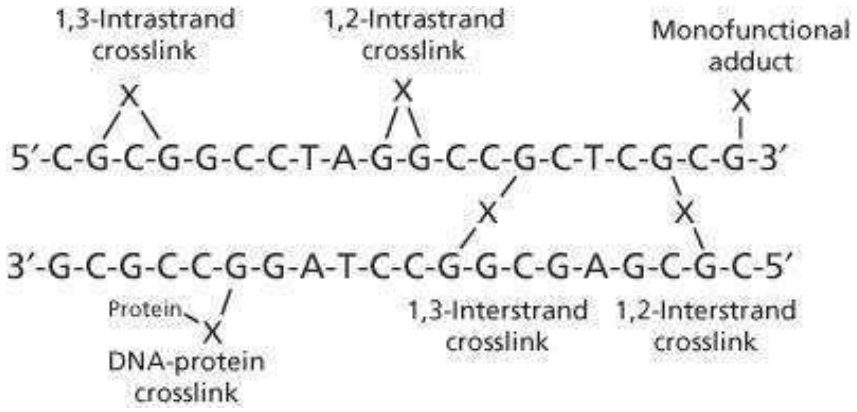

Figure 8: Mono-functional DNA adducts and inter-strand and intra-strand crosslinks induced by DNA damaging agents (X = alkyl or platinum species) [43]

b. *Corticosteroids*

Corticosteroids are synthetic analogues of the natural steroid hormones produced by the adrenal cortex. Like the natural hormones, these synthetic compounds have glucocorticoid and/or mineralocorticoid properties. Mineralocorticoids affect ion transport in the epithelial cells of renal tubules, and are primarily involved in the regulation of electrolyte and water balance. Glucocorticoids are predominantly involved in carbohydrate, fat and protein metabolism, and have anti-inflammatory, immunosuppressive, anti-proliferative, and vasoconstrictive effects. Most of the glucocorticoid anti-inflammatory and immunosuppressive actions can be explained by their interaction with a cytosolic receptor. Glucocorticoid exert their clinical effects predominantly by upregulating the transcription of anti-inflammatory genes, or by downregulating the transcription of inflammation-related genes, thus affecting the downstream production of many pro-inflammatory cytokines and chemokines involved in lymphocyte survival (Figure 9).

Prednisone is probably the most widely used systemic corticosteroid. Due to its high glucocorticoid activity compared with its mineralocorticoid activity, it is generally used as an anti-inflammatory and immunosuppressive agent. Dexamethasone also has minimal mineralocorticoid activity, but has a more potent glucocorticoid activity and longer period of effectiveness than prednisone. However, considering its high potency, long-term treatment with dexamethasone is often associated with severe side effects.

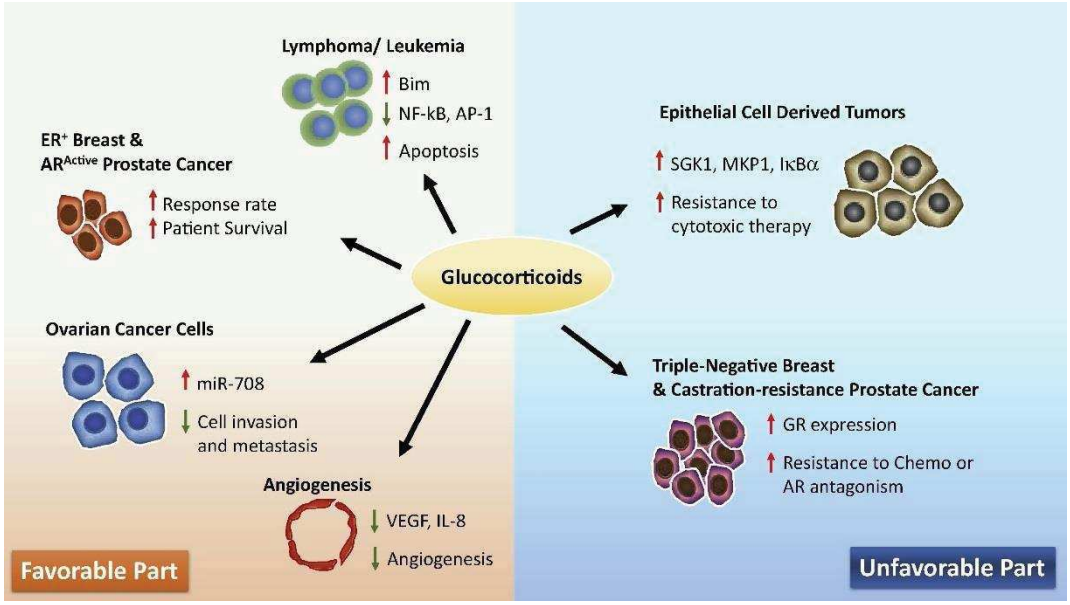

Figure 9: Current understanding of glococortocoids signalling in tumour progression and metastasis [44]

c. *Purine and pyrimidine analogues*

Human cells can salvage purines and pyrimidines for the synthesis of deoxyribonucleotides that are used for DNA synthesis. Analogues of these nucleotide precursors are an important class of anticancer agents. The inhibition of DNA synthesis is the principal action of analogues. Particularly, analogues compete as alternative substrates with the normal deoxynucleotide, thus directly inhibiting the DNA polymerases. Furthermore, purine analogues can inhibit DNA primase, an accessory protein that synthesizes a RNA primer required for initiation of the lagging strand synthesis by DNA polymerase. They also inhibit other enzymes, such as ribonucleotide reductase (resulting in reduction of the cellular deoxynucleotide pools) and DNA ligase I (blocking the AMP binding), and they activate the mitochondrial pathway of the apoptotic cascade.

Fludarabine, pentostatin and cladribine are the most common purine analogues, and cytarabine and gemcitabine the most common pyrimidine analogues used in NHL treatment (Figure 10).

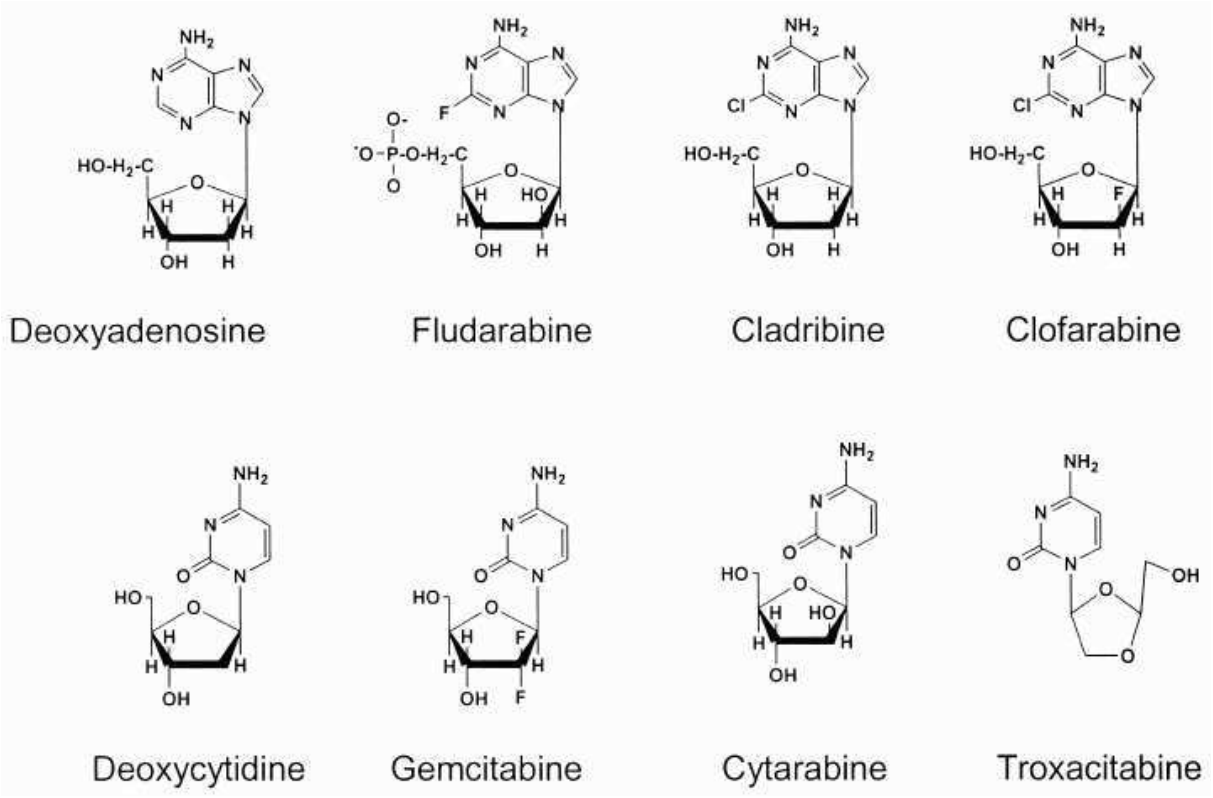

Figure 10: Chemical structures of the purine analogues fludarabine, cladribine, clofarabine, and the pyrimidine analogues gemcitabine, cytarabine, troxacitabine, compared with their natural deoxynucleosides [45]

d. Antifolates

The primary action of antifolates is the inhibition of dihydrofolate reductase, a key enzyme in DNA synthesis for the *de novo* synthesis of purine and thymidine residues. Antifolates disrupt cell proliferation by blocking the folate-dependent one-carbon biosynthesis and methylation reactions. Methotrexate and pralatrexate are two antifolates currently approved for NHL treatment.

e. Topoisomerase II activity inhibitors

Topoisomerase II plays a critical role in DNA replication, transcription and chromosome segregation. Topoisomerase II is an enzyme that participates in DNA over-winding or under-winding. More precisely, topoisomerase II cuts both strands of one DNA double helix, passes another unbroken DNA helix through it, and re-ligates the cut strands. Topoisomerase II inhibitors kill cells by stabilizing a covalent enzyme-cleaved DNA complex that is a transient intermediate in the catalytic cycle of topoisomerase II. The accumulation of cleavage complexes in treated cells leads to the generation of permanent DNA strand breaks that trigger the recombination/repair pathways, mutagenesis, and chromosomal translocations, and can also lead to cell death (Figure 11).

Etoposide, doxorubicin and mitoxantrone are topoisomerase II inhibitors used in NHL treatment.

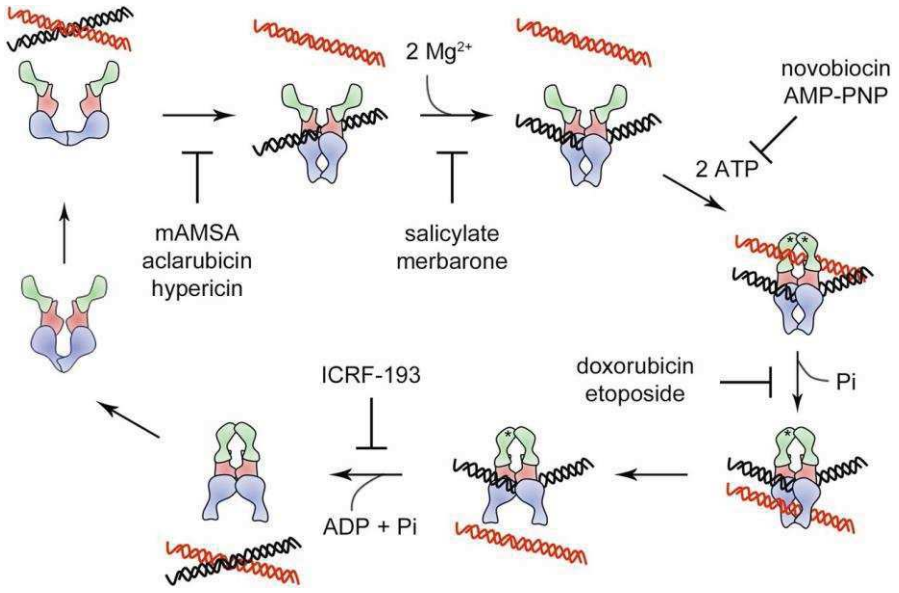

Figure 11: Model of inhibition of topoisomerase II [46]

f. Other mechanisms

Other mechanisms involved in cell division and differentiation can be targeted by chemotherapeutic drugs. For instance, vincristine is an alkaloid agent that prevents microtubule polymerization by binding to free tubulin dimers. This leads to cell cycle arrest and cell death.

Ibrutinib is another molecule used in NHL treatment. This is a selective inhibitor of Bruton's tyrosine kinase. Specifically, it forms a covalent bond with a cysteine residue in Bruton's tyrosine kinase active site, leading to inhibition of its enzymatic activity. This kinase is a signalling molecule of the BCR and cytokine receptor pathways. Its activation through BCR results in activation of pathways that are required for B-cell trafficking, chemotaxis and cell adhesion.

Several molecules can also directly destroy DNA. For example, bleomycin binds to guanosine-cytosine-rich portions of DNA. It can also bind to divalent metals, including iron that can produce Fe(III) and subsequently highly reactive free radicals through Fenton reactions, leading to DNA strand breaks and cell death.

g. Drug combinations

Most of the time, chemotherapy is based on combination of drugs; the most used for NHL treatment are CHOP and CVP:

-CHOP includes Cyclophosphamide, Hydroxydaunorubicin (dauxorubicin), Oncovin (vincristine) and Prednisone;

-CVP contains the same agents as CHOP, but without hydroxydaunorubicin.

Other combinations are DHAOX (high-dose cytarabine, oxaliplatin and dexamethasone), GEMOX (gemcitabine associated with oxaliplatin), FCM (fludarabine, cyclophosphamide, mitoxantrone), DHAP (dexamethasone, high-dose cytarabine and cisplatin), BEAM (carmustine (alkylating agent), cytarabine, etoposide, melphalan (alkylating agent)), *etc*. [47], [48]

h. Side effects

Chemotherapy is a systemic therapy that affects all cells of the organism, but specifically metabolically active and dividing cells, such as cancer cells and proliferating healthy cells (bone marrow haematopoietic cells, skin and hair follicle cells, urogenital system cells, digestive system cells, and mucosal cells). Therefore, chemotherapy may cause side effects, depending on the nature of the used molecule(s). Side effects may also concern heart, kidney and liver cells. Finally, extreme fatigue accompanied by psychological and intellectual weakening can sometimes appear. Despite the severity of these symptoms, chemotherapy side effects are usually temporary and theoretically disappear rapidly after the treatment end. However, some long-term effects can occur, for instance fertility problems or the appearance of secondary cancers.

Chemotherapy is most often given in 3 to 8 cycles of 3 weeks/each. Frequently, it is used in combination with immunotherapy with a significant improvement of the overall survival in many patients.

4. Immunotherapy

Immunotherapy aim is to help and reinforce the immune system.

a. Antibody structure

Antibodies (Ab) are glycoproteins that belong to the immunoglobulin (Ig) superfamily. They include i) a variable part that is different for each Ab and that can recognize the epitope of an antigen, and ii) an effector part that allows the activation of the immune system.

Ig are symmetrical molecules formed by four homologous polypeptide chains linked 2 x 2 by disulphide bonds: two heavy (H) chains and two light (L) chains. The H and L chains consist of domains of about 110 amino acids stabilized by intracatenary disulphide bonds. Traditionally, L chains have two domains (Figure 12):

- one variable VL domain
- one constant CL domain

Conversely, H chains have four (IgD, IgG, IgA) (Figure 12) or five domains (IgM and IgE):

- one variable VH domain
- three or four constant domains, namely CH1, CH2, CH3, CH4

The combination of four peptide chains leads to a particular “Y” shaped three-dimensional structure (Figure 12).

The N-terminal domains of the H and L chains vary considerably from one Ab to another. They are called variable heavy (VH) and variable light (VL) domains, respectively. They contain complementary determining regions (CDR), hyper-variable regions and framework regions. The folding of VH and VL regions leads to a spatial conformation that brings the six CDR together, establishing the binding site for the antigen (paratope). This part of the Ab is responsible for the antigen reconnaissance via the paratope – epitope interaction.

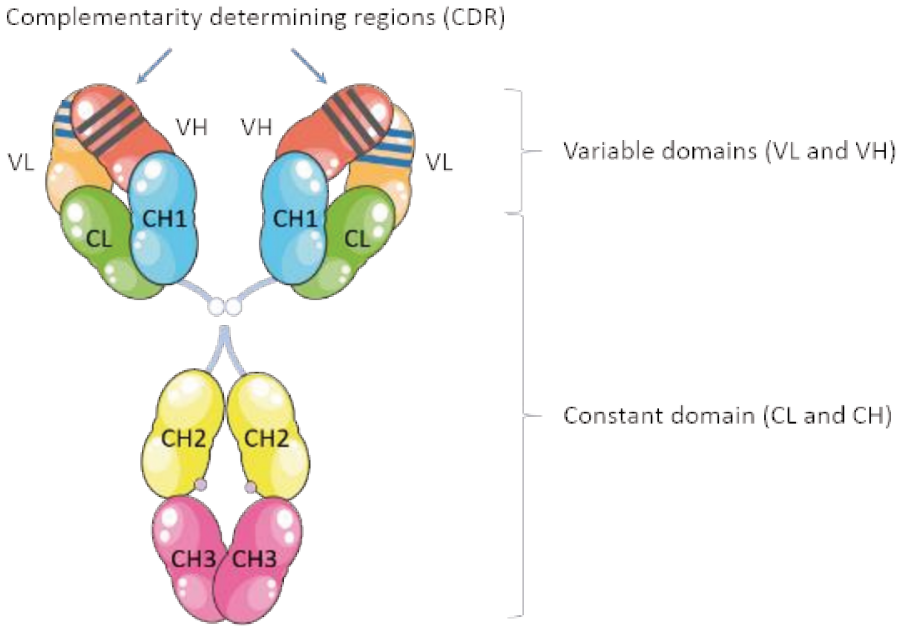

Figure 12: IgG structure

Moreover, five different types of H chain exist, named using the Greek letters γ (gamma), α (alpha), μ (mu), δ (delta) and ε (epsilon) that define the five classes of immunoglobulins (IgG, IgA, IgM, IgD, and IgE, respectively), each with its own biological properties (Table 3). Unlike the variable part, the constant part is not involved in antigen recognition. However, this region is essential for the Ab function via its interaction with the immune system [49].

Table 3: Characteristics of Ab isotypes

Isotype	Heavy chain	Light chain	MW (kDa)	Structure	Function
IgA1 IgA2	α1 α2	λ or κ	150-160	Monomer - tetramer	Most produced Ig. Found in mucosal areas, such as gut, respiratory and urogenital tract, where they prevent colonization by pathogens. Resistant to digestion and secreted in milk.
IgD	δ	λ or κ	150	Monomer	Function unclear. Works with IgM in B cell development; mostly B cell- bound
IgE	ε	λ or κ	190	Monomer	Binds to allergens and triggers histamine release from mast cells and is involved in allergy. Also protects against parasitic worms.
IgG1 IgG2a IgG2b IgG3 IgG4	γ1, γ2, γ3, γ4	λ or κ	150	Monomer	Major Ig in serum. Provides the majority of antibody-based immunity against invading pathogens. Moderate complement fixer. IgG3 can cross placenta.
IgM	μ	λ or κ	900	Pentamer	First-response antibody. Expressed on the surface of B cells and in a secreted form with very high avidity. Eliminates pathogens in the early stages of B cell-mediated immunity before there are sufficient IgG.

Currently, all therapeutic Abs are directed against one epitope on the antigen and are named monoclonal antibodies (mAbs). Conversely, polyclonal antibodies are a mixture of antibodies that recognize different epitopes on one given antigen.

The first mAb used in cancer treatment was developed in mice (OKT3 named Muromonab-CD3, an anti-CD3 mAb). However, when human patients receive murine mAbs, the human immune system identifies these mAbs as non-self molecules and destroys them. This mechanism is particularly true when patients receive several injections of murine mAbs. This led to the humanization of murine mAbs through modification of their H chain. Currently, therapeutic mAbs can be murine (-omab suffix), chimeric (-ximab suffix), humanized (-zumab suffix) or totally human (-umab suffix) (Figure 13).

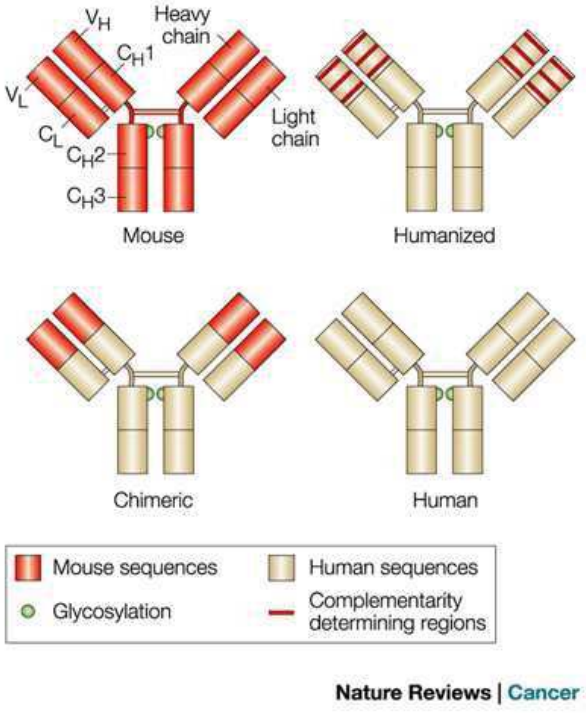

Figure 13: Classification of mAbs in murine, chimeric, humanized and human [50]

b. Mechanism of action of therapeutic monoclonal antibodies

In cancer treatment, mAbs are used to kill tumour cells. The mAb fixation on its epitope can activate four mechanisms, leading to various biological effects.

i.Direct effects

By binding to cell surface receptors, mAbs can directly block intracellular signalling pathways involved in cell survival (for example dacetuzumab, an anti-CD40 mAb). They can also prevent receptor activation by targeting ligands involved in cancer cell survival. This is the case

of the anti-VEGF bevacizumab. On the other hand, mAbs can activate receptor if the intracellular pathway is involved in cell death (for example, the anti-porimin mAb).

ii.Complement-dependent cytotoxicity (CDC)

MAbs can also induce tumour cell death by activation of the complement cascade. The complement cascade is composed of more than 30 proteins present in the plasma and on cell surfaces, and mainly synthesized by the liver. These proteins are organized into a hierarchy of proteolytic cascades that start with the identification of a pathogenic surface and lead to the generation of potent pro-inflammatory mediators that induce the opsonisation of the pathogenic surface through various complement opsonins, and its targeted lysis through the assembly of membrane-penetrating pores, known as the membrane attack complex. The complement system (Figure 14) can be activated when the C1 complex fraction C1q binds to a mAb (most of the time IgG1, IgG3 or IgM) attached to an antigen. This binding results in the activation of the C1r and C1s proteins that cleave C4 and C2 (into C4a, C4b and C2a, C2b respectively). These cleavage products form the C3 convertase C4bC2a that can hydrolyse C3 into C3b and C3a. Then, a C3b molecule can associate with C4bC2a to form C4bC2aC3b, the C5 convertase that cleaves C5 into C5a and C5b. Simultaneously, the major effectors of the complement system are generated as follows [51]:

-anaphylatoxins (C4a/C3a/C5a) that are potent pro-inflammatory molecules derived from the cleavage of C4, C3, and C5.

-membrane attack complex (C5b) that is the terminal assembly of the complement components C5b through C9 and that can directly lyse targeted surfaces.

-opsonins (C3b) that induce phagocytosis of opsonised targets and also serve to amplify complement activation [51].

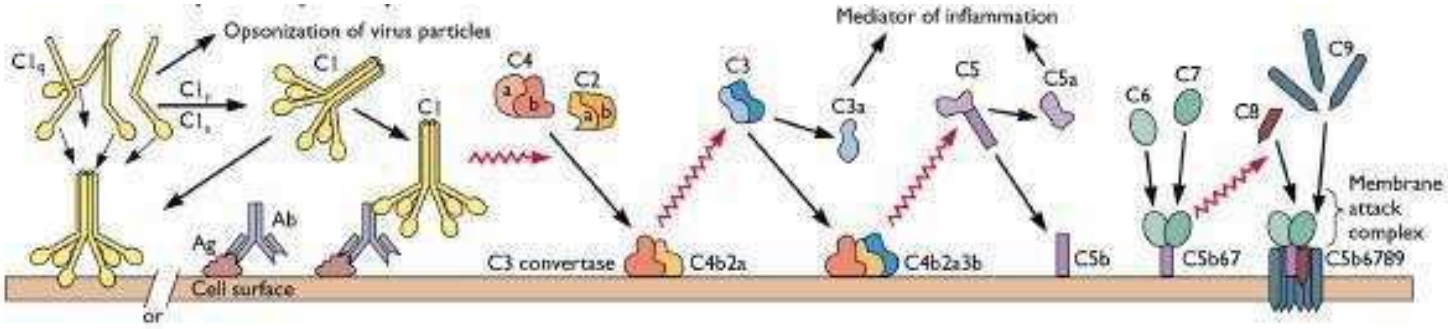

Figure 14: Mechanism of activation of the complement system [52]

iii.Antibody-dependent cell-mediated cytotoxicity (ADCC)

In immunotherapy, mAbs can also directly activate immune cells. NK cell effector functions can be exploited for the treatment of some tumours through their ability to mediate antibody-dependent cellular cytotoxicity (ADCC). NK cells can express both FcγRIIc and FcγRIIIa receptors [53], which bind to the C-terminal domain of mAb H-chains. Upon FcγR binding,

intracellular domains (or associated proteins) are phosphorylated and NK cell degranulation, cytokine secretion, and finally tumour cell lysis occur *via* signal transduction mechanisms that involve binding to ZAP-70 and SYK proteins and activation of the PI3K, NF-κB and ERK pathways [54].

iv.Antibody-dependent cell phagocytosis (ADCP)

ADCC is predominantly attributed to NK cells, although it was proposed that monocytes and macrophages also can induce ADCC. However, recent studies with intravital microscopy showed that Ab-dependent cell phagocytosis (ADCP) is the main mechanism of action of macrophages [55]. It is the mechanism by which Ab-opsonised target cells activate FcγRIIa and FcγRIIIa on the surface of macrophages to induce phagocytosis, resulting in the internalization and degradation of the targeted cell.

c. Monoclonal antibodies in Non-Hodgkin lymphoma treatment

The discovery of the hybridoma technology to produce mAbs by George Köhler and Cesar Milstein in 1975 [56] has had a great impact both on basic biological research and clinical medicine. The specificity of Ab-based therapy is based on the antigen-Ab recognition. Targeted antigens should be easily accessible, highly expressed on tumour cells and possibly restricted to these cells. Because most lymphomas have vascular accessibility, they are a favourable setting for this treatment modality. Many antigens are targeted in NHL treatment, but the marketing authorization of the anti-CD20 mAb [57] was a revolution in term of patient survival.

i.CD20

CD20 is a transmembrane protein with a molecular weight of approximately 35 kDa (Figure 15).

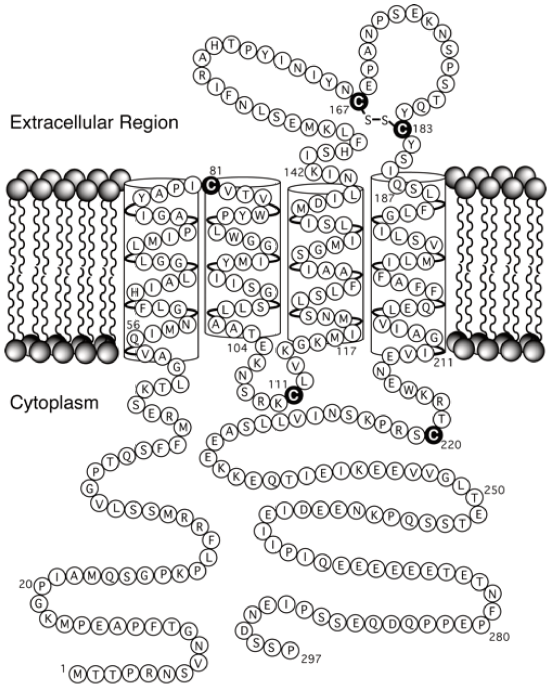

Figure 15: CD20 as presented at cell membrane [58]

It is expressed, from the membrane spanning 4-domains A1 gene, on pre-, naive, and mature B cells, but not on plasma cells and early pro-B cells [59]. CD20 is a potential target for immunotherapy because it is highly expressed in B-cell NHL (about 90%) [60].

CD20 biological function has not been fully elucidated yet. It acts as a calcium ion channel [61], and may also activate intracellular signalling *via* its ability to associate with BCR [62]. Interestingly, CD20 ability to induce cytosolic Ca^{2+} flux appears to be BCR-dependent. Rituximab (also called IDEC-C2B8) (Mabthera®) [57] was the first anti-CD20 mAb approved by the Food and Drug Administration (FDA) (1997) for the treatment of relapsed or refractory CD20-positive follicular lymphoma [63].

(a) Rituximab

Rituximab is the gold standard of NHL treatment. It is a chimeric anti-CD20 IgG1 [64] that recognizes the epitopes $_{(170)}$ANPS$_{(173)}$ and $_{(182)}$YCYSI$_{(186)}$ (in blue in Figure 16), brought together head to head by the disulphide bond C$_{(167)}$-C$_{(183)}$ (in yellow in Figure 16) [65]. The non-internalization of rituximab was a paradigm for a long time; however, some studies reported that it can be internalized more or less rapidly, depending on the NHL subtype and this requires FcγRIIb [66]. Rituximab is a type I mAb. Schematically, type I mAbs stabilize CD20 in lipid rafts, increasing C1q binding and CDC activity [64]. Conversely, type II anti-CD20 Abs do not stabilize CD20 in lipid rafts and thus, do not initiate CDC to the same extent as type I Abs. Type II Abs promote apoptosis, independently of the Bcl-2 and caspase pathways and *via* the lysosome

pathway, in combination with ADCC and ADCP, to kill tumour cells [67]. After mAb binding, the lysosome pathway is activated by actin re-localization that damages the lysosome membranes, thus leading to the release of lysosomal hydrolases into the cytosol that triggers cell death.

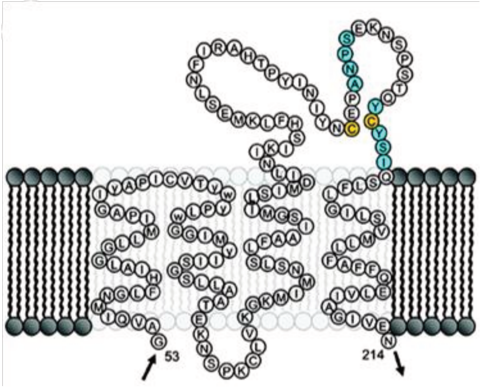

Figure 16: Rituximab binds to a discontinuous epitope within CD20 extracellular domain [65]

Due to B-cell NHL heterogeneity and the many cell types and signalling pathways, the mechanisms involved in rituximab response are complex. Their understanding was the goal of many studies that led to different results [68]. Nevertheless, it is known that rituximab induces cell death *via* CDC [69], ADCC [70] and ADCP [71], but also by directly promoting apoptosis [72], [73] (Figure 17).

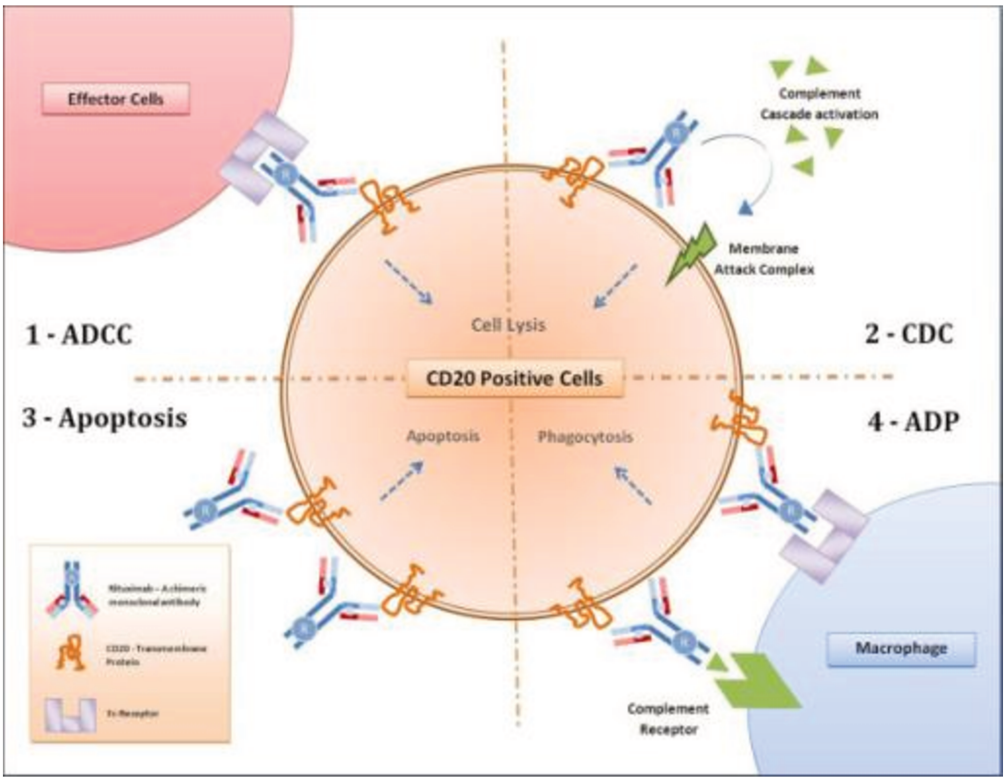

Figure 17: Mechanisms of action for rituximab [74]

(i) Mechanisms of action

Generally, apoptosis is mediated by inhibition of some survival and anti-apoptotic signalling pathways. Rituximab leads to cell death through mitochondria-dependent (intrinsic) apoptosis [75]. Typically, the permeability change of the mitochondrial outer membrane induces the release of cytochrome C from the intermembrane space to the cytosol, where it forms caspase 9 activating complexes. The effector caspases 3, 6 and 7 are then activated by caspase 9-mediated cleavage. This mitochondrial apoptosis pathway is regulated by the members of the Bcl-2 family.

Rituximab induces inhibition of the anti-apoptotic Bcl-2 and Bcl-xL proteins by acting on the following signalling pathways (summarized in Figure 18):

- Rituximab inhibits the p38 MAPK signalling pathway through the Src family kinases. This leads to inhibition of the Sp1 and NF-κB transcription factors, resulting in the downregulation of IL-10 transcription and secretion. Consequently, inhibition of the autocrine loop of IL-10/IL-10 receptor signalling and partial inhibition of IL-10-mediated downregulation of STAT3 result in Bcl-2 downregulation [68][69].

- Rituximab decreases the phosphorylation of components of the ERK1/2 signalling pathway together with upregulation of RKIP expression, leading to a decrease of the ERK1/2 pathway activity. This leads to a decrease in AP-1 DNA binding activity and downregulation of Bcl-xL expression [78]. RKIP can also inhibit the activity of the NF-κB pathway [79] and downregulate Bcl-2 expression.

- Rituximab regulates the expression and activity of Bcl-xL through the AKT pathway. Indeed, rituximab treatment can also inhibit phosphorylation of PI3K, leading to inhibition of PDK-1 and finally AKT. In addition, AKT downregulation inhibits NF-κB activity [80]. Hence, inhibition of the AKT pathway by rituximab results in a significant inhibition of Bcl-xL and Bcl-2.

- Rituximab is responsible for the regulation of the AKT and Bcl-2 pathways by ceramide. When binding to rituximab, CD20 molecules are redistributed to raft micro-domains, thus generating the release of ceramide by the activation of acid sphingomyelinase. Ceramide, a lipid second messenger, may contribute to the propagation of the CD20-mediated growth inhibition signal *via* activation of the PP2A phosphatase that dephosphorylates Bcl-2 [70] and AKT [82].

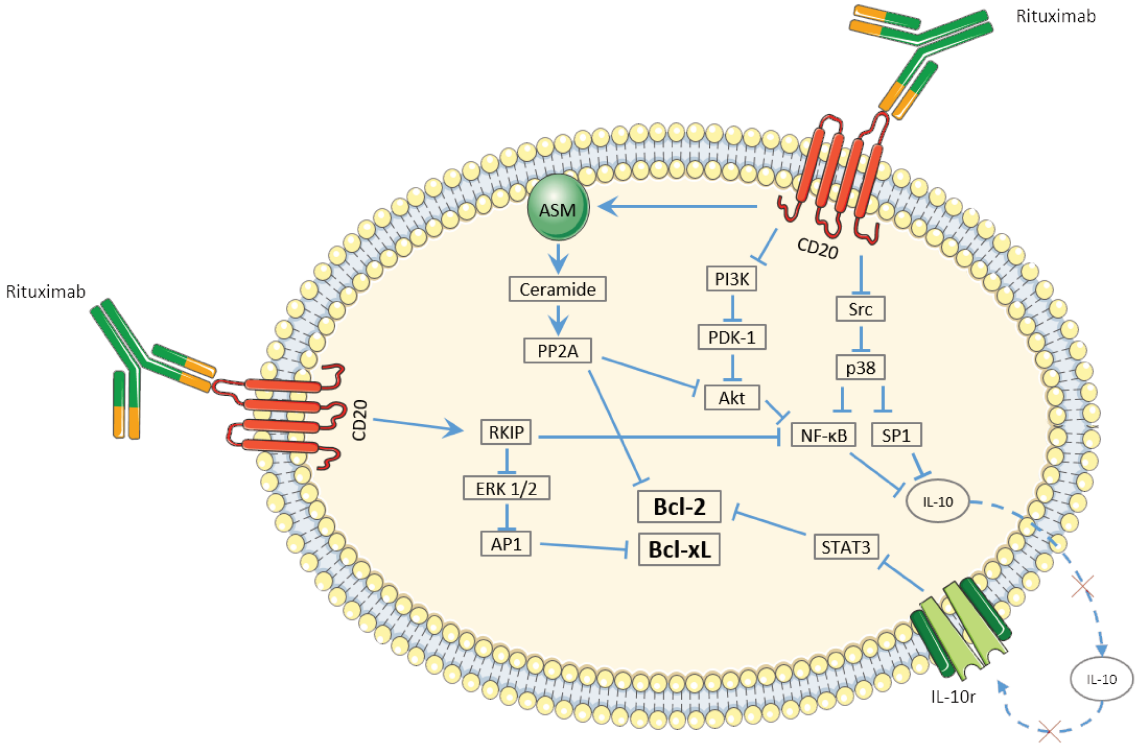

Figure 18: Molecular signalling triggered by rituximab following its interaction with CD20

Moreover, rituximab can bind also to C1q and induce CDC. It is clear that CD20 is an excellent target for CDC because of its high expression and proximity of the mAb-binding-epitope to the membrane [72]. However, CDC role in mediating the clinical antitumor activity of rituximab remains unclear. Various studies have shown that the complement can induce the lysis of mAb-coated target cells [69], [83]–[85]. However, it has been also reported that the complement can inhibit the killing of targeted cells by blocking NK cell–mediated ADCC through C3b molecules [86].

Finally, the importance of ADCC and ADCP in rituximab efficacy was highlighted in a tumour xenograft model where FcγR-deficient and wild type mice bearing tumours were treated with the same mAb. The anti-tumour response was weaker in FcγR-deficient mice than in wild type animals [87]. Moreover, variations in FcγRIII expression in patients correlate with rituximab treatment outcome [71] [88]. The relationship between CDC and ADCC is complex. Complement activation by mAbs can serve to recruit immune effector cells through the release of C3a and C5a. In addition, the complement and its various breakdown products deposited on the tumour cell surface can activate complement receptor signalling, thus increasing phagocytosis and cytotoxicity. However, active complement can disrupt the interaction between mAb and FcγR, thus decreasing mAb-induced NK cell activation via C3b.

(ii) Treatment regimen

Rituximab is administrated by intravenous injection. Patient with CD20-positive indolent NHL usual receive the standard single-agent dose of 375 mg/m^2. Rituximab is injected weekly for 4 weeks (the body surface area is calculated using the formula $\sqrt{\frac{weight \times height}{3600}}$). However, most of the time, rituximab is used in combination with chemotherapy in indolent, but also in aggressive NHL. In this case, it is administered by intravenous injection (375 mg/m^2) on day 1 of each chemotherapy cycle. Lastly, rituximab can also be used in indolent NHL as maintenance treatment after a successful first-line treatment (375 mg/m^2 every 8 weeks for 2 years).

(iii) Side effects and resistance

Rituximab is usually well tolerated, and toxicities are generally mild. Common side effects include pruritus, nausea, vomiting, dizziness, headaches, fevers, and rigors. A major concern is the possibility of infusion-related reactions, such as rigors, chills, and anaphylactic reactions that could lead to myocardial infarction and cardiogenic shock. These reactions occur most commonly during the first rituximab administration. Premedication with acetaminophen and antihistamines is recommended prior to infusion. Reactions usually are reduced by stopping the infusion and then restarting it at a slower rate. Furthermore, muco-cutaneous reactions, such as hypersensitivity, papulopustular eruption, rash, pruritus, fissures and mucositis, have been reported within 1 to 13 weeks following rituximab exposure. Moreover, tumour lysis syndrome has been described in patients with bulky lymphoma, leading to kidney damage. Finally, rituximab induces B-cell depletion, which may compromise the immune system and consequently increase the risk of infection. However, recovery of the normal B-cell population usually occurs 6 to 9 months after therapy discontinuation.

Nevertheless, rituximab major problem in NHL treatment is the development of resistance in about 60% of patients after several injections of rituximab [89]. The generally accepted definition of rituximab resistance is lack of response to a rituximab-containing regimen, or progression within 6 months of treatment with a rituximab-containing regimen. Different mechanisms are at the origin of such resistance.

First, tumour cells can block complement activation through the action of membrane complement regulatory proteins, such as CD46, CD55, and CD59. These inhibitory proteins disrupt the complement cascade or the assembly of the membrane attack complex. Some rituximab-resistant cell lines express high levels of these proteins [90]. Second, modulation of anti-apoptotic regulators (Bcl-2 and Bcl-xL) has been observed in several rituximab-resistant cell lines. Specifically, hyperactivation of the NF-κB and ERK1/2 pathways leads to overexpression of anti-apoptotic proteins of the Bcl-2 family. Resistant cells also can express lower levels of surface

CD20, leading to less rituximab fixation [91]. Finally, repeated exposure of cells to rituximab is followed by a decrease in the expression of BAX and BAK, two pro-apoptotic proteins belonging to the Bcl-2 family [92].

(iv) Efficacy

The downward shift in NHL mortality in the United States coincided with the marketing of rituximab in 1997 (Figure 19), highlighting the efficiency of rituximab treatment in NHL [93].

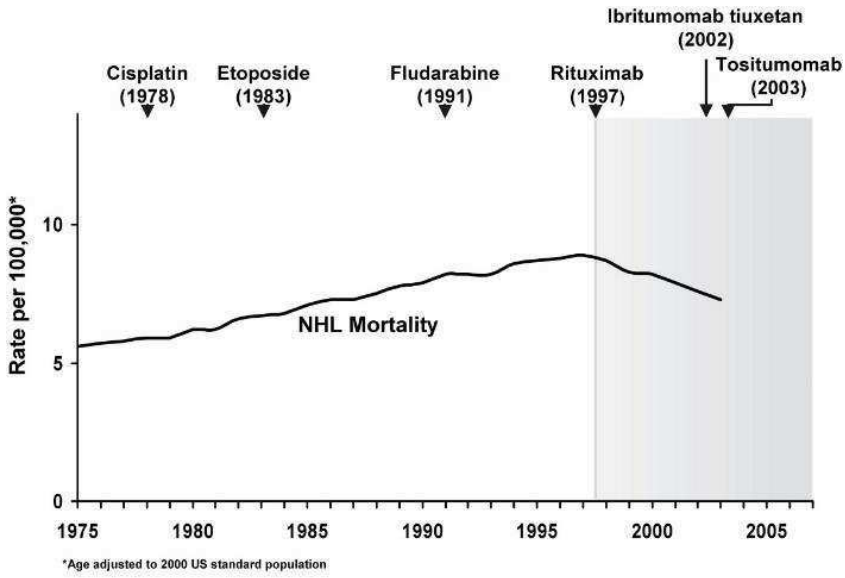

Figure 19: NHL mortality rates and new drugs approved in the United States for the treatment of NHL [93]

The use of single-agent rituximab in patients with relapsed or refractory indolent NHL shows overall response rates (ORR) of 40–50%, with a median time to progression (TTP) of approximately nine months [83][84]. Combined rituximab and CHOP chemotherapy (R-CHOP) produces higher ORR of 95%, with a median TTP of 82 months [96]. In aggressive NHL, rituximab also increases the response to chemotherapy. Patients with DLBCL showed an ORR of about 82% with R-CHOP compared with 69% with CHOP alone [97]. These results highlight the synergy between rituximab and cytotoxic chemotherapy. After treatment with rituximab, the downregulation of Bcl-2 and Bcl-xL expression and of different signalling pathways (p38, AKT, NF-κB and ERK1/2) can increase the apoptosis rate, leading to a better cell response to chemotherapy.

(b) Other anti-CD20 monoclonal antibodies

Because of the high efficacy of rituximab in NHL therapy, other anti-CD20 mAbs were developed. These new mAbs could also bypass (to some extent) the resistance to rituximab therapy.

Currently, there are several new generation anti-CD20 mAbs which have been engineered or modified to increase antitumor activity, Fc binding affinity and provide advantages over rituximab. They may be grouped in two categories: second or third generation anti-CD20 mAb (Table 4).

Table 4: List of anti-CD20 mAbs [98]

CD20 mAbs	MFC/Type	Source	Regimen (dose mg/m2)	Mechanism of action
First generation				
Rituximab (Rituxan, MabThera and Zytux) Approved in US 1997	Biogen, Idec and Genentech Type I mAb	Chimeric	Rituximab (166 patients with Refractory/ relapsed FL, ORR 48%) R-GMCSF (49 Patients with relapsed FL, ORR 74%) R-bendamustine (33 patients with Relapsed FL or MCL, ORR 70%) R-CHOP (63 Untreated patients of DLBCL, ORR 90%)	CDC, ADCC, PCD, ADCP
Y^{90} -Ibritumomab tiuxetan (Zevalin) Approved in US 2002	Biogen IDEC Pharmaceuticals Corp Type I mAb	Murine IgG1κ	Zevalin (54 patients of Rituximab refractory FL, ORR 74%) Zevalin vs Rituximab, randomized multicenter study (143 patients of Relapsed or refractory FL, ORR 80 vs 56%)	High CDC Low ADCC
Tositumomab (B1) and I131-Tositumomab (Bexxar) Approved in US 2003	Corixa, Glaxo Smithkline Type II mAb	Murine IgG2aλ	Bexxar (250 patients of Relapsed/refractory indolent FL and transformed NHL, ORR 47%–68% repectively) Bexxar (76 patients of Stage III or IV FL, ORR 95%) Bexxar +Fludarabine (35 patients of Early stage FL, ORR 98%) Bexxar vs tositumomab (78 patients of Relapsed or refractory NHL, ORR 55% vs 19%)	High PCD Low CDC
Reditux Approved in India2007	Dr. Reddy Laboratories Type I mAb	Murine IgG1	Reditux (72 patients of DLBCL, CR 82%)	Biosimilar
Second generation (Humanized and Fully Human)				
Ocrelizumab (2H7; PRO70769) Phase III	Genentech/Roche/Biogen Type I mAb	Humanized IgG1	Ocrelizumab (47 patients of Relapsed/Refractory FL, ORR 38%)	High ADCC Low CDC
Veltuzumab (IMMU-106; hA20) Phase II	Immunomedics USA Type I mAb	Humanized IgG1κ	Veltuzumab (82 patients of Relapsed/refractory B-cell NHL) 44% ORR in FL 83% ORR in MZL 43% ORR in DLBL	High CDC
Ofatumumab (2F2; HuMax-CD20; Arzerra) Approved in US 2009	Genmab, Glaxosmithkline Type I mAb	Fully Human IgG1κ	OFA, 500–1000 (116 patients of Refractory FL, ORR 13-10%) OFA-CHOP, 500–1000 (59 patients of Untreated FL, 90–100%) OFA-FC, 500–1000 (61 patients of Frontline therapy for CLL, 77–73%)	High CDC
Third generation (Humanized or fully human with modified Fc region)				
Ocaratuzumab (AME-D, AME-133) Phase II	Mentrik Biotech, Applied molecular evolution Type I mAb		Ocaratuzumab, 100–375 (56 patients of Relapsed/Refractory FL, ORR 36%) Ocaratuzumab, 375 (50 patients of Relapsed/Refractory FL with low affinity genotype of FcγRIIIa, ORR 30%)	High ADCC
PRO131921 (RhuMAb; v114) Phase I/II	Genentech Type I mAb	Humanized IgG1 (Engineered Fc portion)	PRO131921, 25–800 (24 patients of Relapsed/refractory B cell NHL, ORR 27%)	High CDC Low ADCC
Obinutuzumab (GA101;Gazyva) Approved in US Nov 2013	Roche Type II mAb	Humanized IgG2κ (Glycoengineered Fc portion)	GA101, 1600/800-400/400 (29 patients of Refractory B-cell NHL, ORR 60-35%) G-CHOP, 1600/800-400/400 (28 patients of Relapsed or refractory FL, ORR 94%) G-FC, 1600/800-400/400 (28 patients of Relapsed or refractory FL, ORR 93%)	High PCD & ADCC, Low CDC
Ublituximab (LFB-R603, EMAB-6) Phase I	GTC Bio therapeutics, LFB Biotechnologies Type I mAb	Chimeric; IgG1 Glycoengineered	Ublituximab, (12 patients of Advanced CLL, ORR 35%)	High ADCC
TRU-015 Phase II	Trubion Pharmaceuticals Inc., Wyeth Single chain protein	SMIL	37 patients of RA patients	High ADCC Low CDC

For example, ofatumumab (Arzera®) was approved in 2009 by the FDA for patients with chronic lymphocytic leukaemia (CLL). It is a human anti-CD20 IgG1. The main difference between

rituximab and ofatumumab is the binding site. It is believed that this difference is in part responsible for the tighter binding of ofatumumab to CD20 compared with rituximab. This leads to higher exposure of the mAb Fc domain and thereby enhanced CDC, ADCC and ADCP [99]. Obinutuzumab (Gazyva®) was approved in 2013 by FDA for patients with chronic lymphocytic leukaemia and follicular lymphoma. It is a humanized and glycoengineered anti-CD20 IgG1 to increase Fc activity. Unlike rituximab and ofatumumab, which are type I anti-CD20 mAbs, obinutuzumab is a type II anti-CD20 mAb. Therefore, it induces higher apoptosis rates *via* the lysosome pathway, in combination with ADCC and ADCP that contribute to tumour cell eradication.

ii.Other therapeutic monoclonal antibodies against NHL in development

Some mAbs are developed in order to treat NHL as it is illustrated in the Table 5 with a high number of targets.

Table 5: List of mAbs for the treatment of NHL [100]

Antibody	Target	Type	Source
Epratuzumab	CD22	IgG1	Humanised
CMC-544	CD22	IgG4	Humanised
Lumiliximab	CD23	IgG1	Chimeric (macaque-human)
SGN-30	CD30		Chimeric
MDX-060	CD30	IgG1κ	Humanised
MDX-1401	CD30		Humanised
XmAbTM2513	CD30		Humanised
SGN-40	CD40	IgGl	Humanised
HCD122	CD40	IgGl	Humanised
Alemtuzumab	CD52		Humanised
Galiximab	CD80	IgG1λ	Chimeric (macaque-human)
Siplizumab	CD2	IgG1κ	Humanised
Apolizumab	HLADR	IgG1	Humanised
Milatuzumab	CD74		Humanised
Mapatumumab	DR		Humanised
Lexatumumab	DR		Humanised
Zanolimumab	CD4	IgG1κ	Humanised

Two mAbs with two strategies of mechanism of action are developed as examples. Alemtuzumab (Lemtrada® approved in 2007 by the FDA and withdraw in 2012 due to high toxicity) is a humanized IgG1 against CD52. CD52 is expressed at high levels by normal and malignant B and T lymphocytes, and at lower expression levels by monocytes, macrophages and eosinophils, mature NK cells, neutrophils and HSC [101]. CD52 is also produced by epithelial cells. CD52 exact biological function remains unclear, but some evidence suggests that it may be involved in T-cell migration and co-stimulation [102]. Alemtuzumab can induce cell death through

CDC, ADCC, ADCP and apoptosis. However, its toxicity is very important, largely due to the profound immunosuppression induced by the treatment.

The programmed death-1 (PD-1) pathway is an immune checkpoint to attenuate T cell–mediated immune responses that could be exploited by tumours to avoid immune surveillance [103]. PD-1 and its ligands PD-L1 and PD-L2 are commonly expressed in tumour or neoplastic microenvironments, and PD-L1 and PD-L2 expression can be upregulated in tumour cells. It is known that PD-L1 interaction with PD-1 on tumour-infiltrating lymphocytes decreases T-cell proliferation and cytotoxic functions, but the role of PD-L2 is less clear. Immune blockade of the PD-1/PD-L1 interaction by mAbs can restore the anti-tumour activity of cytotoxic T cells. Nivolumab (Opdivo®) is a fully human IgG4 that binds to the PD-1 receptor and blocks its interaction with PD-L1 and PD-L2, thereby preventing T-cell inhibition and restoring the anti-tumour immune responses [104]. It is used for HL treatment and probably in the near future for the NHL treatment [104].

iii.CD37

CD37 is a member of the transmembrane 4 superfamily (TM4SF) of tetraspanin proteins (Figure 20), which has four potential membrane-spanning regions. The human CD37 gene maps to chromosome 19q13.3 and encodes a 281 amino acid protein. It is extensively glycosylated with a molecular weight of 40- to 52-kDa.

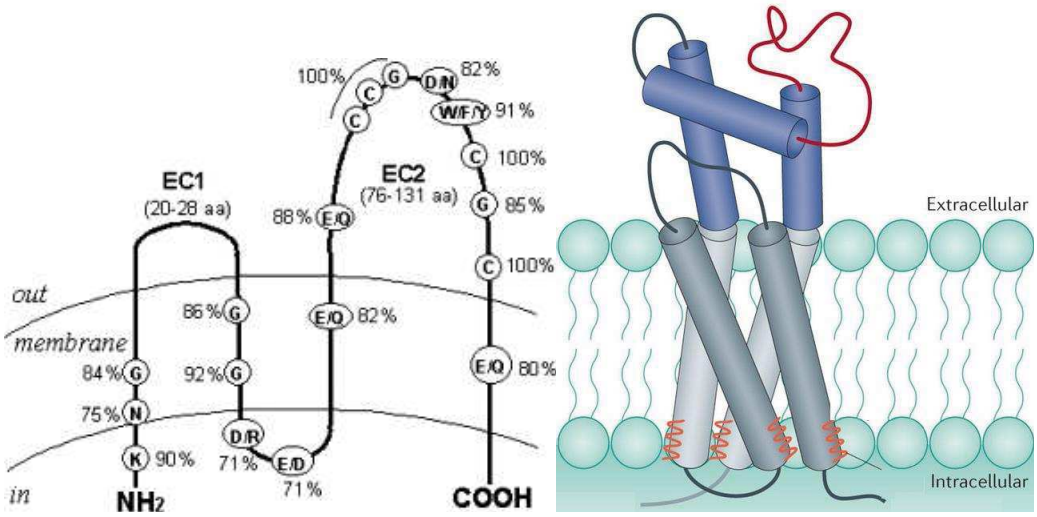

Figure 20: Representation of the consensus structure of the tetraspanin protein family [105]

This protein is highly expressed by mature B-cells, but it is absent in the earliest stages of B-cell development and is lost again following differentiation into plasma cells [106]. CD37 expression is very low in T cells, monocytes and NK cells, and is absent in platelets and erythrocytes [107]. It is highly expressed in mature B-cell malignancies, such as NHL and chronic lymphocytic leukaemia, whereas is low or absent in acute lymphoblastic leukaemia and multiple

myeloma [106]. It is also expressed in T-cell lymphomas in 82% of cases but it is not detected in HL. In Zhao *et al.* 2010 [108], they tested by IHC the CD37 expression on formalin fixed paraffin-embedded samples (n=170). Results indicated 89% (151 of 170 cases) of stained lymphoma tissues were positive for CD37, including follicular lymphoma (80/88), mantle cell lymphoma (39/44), DLBCL (32/38), and marginal zone lymphoma (5/5).

Concerning the healthy tissues, Pereira *et al.* 2015 [109] show that CD37 expression was only detected in lymph node, spleen, bone marrow, colon, small intestine, thymus, and tonsil (198 samples were tested, representing 32 human tissues). These are tissues where lymphocytes are known to reside and they conclude that it is these lymphocytes that were shown to express CD37. It is also important to observed that treatment with rituximab does not influence the CD37 expression [108].

Mice in which CD37 was knocked out show defective IgG1 production in response to T-cell dependent antigens, which is a consequence of the decreased survival of IgG1-secreting B-cells in the days following antigen exposure [110]. Indeed, it was demonstrated that CD37 has an important role in membrane clustering of the α4β1 integrin [111] that is required for optimal T cell–dependent humoral immune response. Typically, in the germinal centre, B cells receive anti-apoptotic signals from dendritic cells through interactions between the α4β1 integrin and its ligand, the vascular cell adhesion molecule–1 (VCAM-1). These signals facilitate B-cell activation. More precisely, activation of α4β1 integrin-CD37 phosphorylates PI3K that activates the AKT pathway (*via* PDK-1) and finally inactivates the pro-apoptotic protein BAD (Bcl-2 family) [111].

Lapalombella *et al*., showed that the cytoplasmic part of CD37 contains two motifs [112]:
- the N-terminal domain that can recruit a complex composed of LYN, SHP1, SYK and PI3Kγ. This complex can dephosphorylate and inactivate AKT, and activate FOXO3a, leading to BIM upregulation (a pro-apoptotic protein belonging to the Bcl-2 family) and subsequently to mitochondrial depolarization and cell death.

- the C-terminal domain that can recruit and activate PI3Kε, an AKT activator. This activation leads to inactivation of GSK3β and promotes cell survival. GSK3β is anti-survival protein involved in the inactivation of β-catenin (survival pathway) by phosphorylation.

Pro-apoptotic and anti-apoptotic signals can be triggered through CD37 activation. Although both pathways are simultaneously induced by CD37 ligation, cell death is favoured.

IL-6 has emerged as a critical tumour-promoting cytokine in NHL [113]. The IL-6 receptor complex is composed of the IL-6 receptor α chain (IL-6Rα) and the common signalling receptor gp130 that together activate the STAT3, PI3K/AKT and MAPK pathways, thus providing

proliferative and anti-apoptotic signals [113]. CD37 is a regulator of suppressor of cytokine signalling 3 (SOCS3) and thereby interferes with the activation of the IL-6 signalling pathway in B cells. Actually, CD37 can bind to SOCS3, which is the major negative regulator of the IL-6 signalling pathway, and can also interact with gp130, which is one of the two proteins involved in the IL-6 receptor complex, thus drawing SOCS3 closer to gp130 and downregulating the IL-6 pathway [114]. Moreover, CD37 is also implicated in the IL-6 pathway through its interaction with Dectin-1 (a β-glucan receptor that plays a prominent role in the immune response against fungi). Dectin-1 activation induces a cellular signalling through interaction with Syk kinases and then the secretion of IL-6. CD37 downregulates Dectin-1 activity and consequently IL-6 secretion [115] (Figure 21).

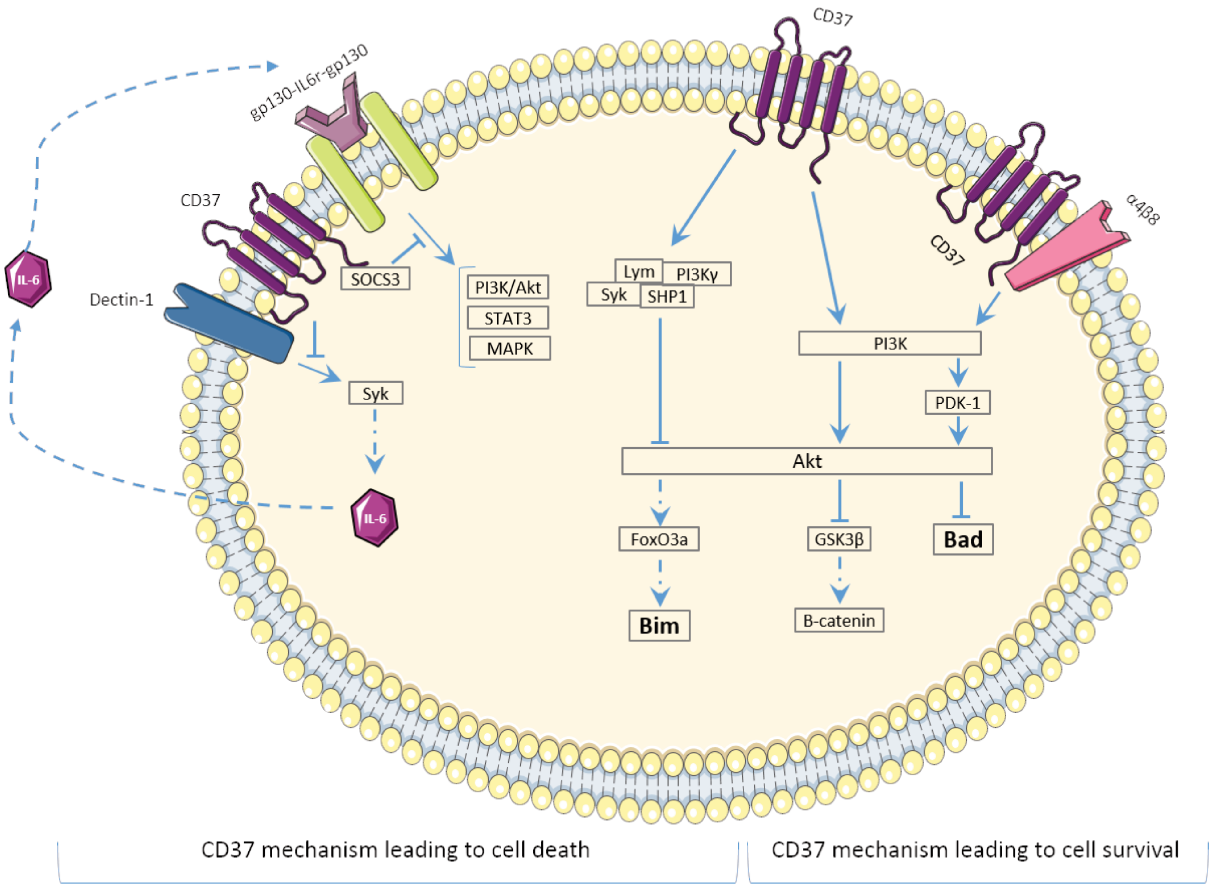

Figure 21: Mechanisms involved in CD37 activation

Given the relative selectivity of B cells, CD37 represents a therapeutic target for malignancies derived from peripheral mature B cells, including chronic lymphocytic leukaemia, hairy-cell leukaemia, B-cell NHL and other B-cell tumours. Its expression pattern makes of CD37 an attractive target for immunotherapy and radioimmunotherapy. Currently, there is no anti-CD37 mAb routinely used in the clinic. However, several mAbs are evaluated in ongoing clinical trials.

(a) Anti-CD37 monoclonal antibodies

Otlertuzumab was the first anti-CD37 mAb tested in clinical trials. It is a modified IgG1 that lacks the L chain constant region (CV) and the first constant region of the H chain (CH1). This modification should increase tissue penetration, while retaining similar pharmacokinetics and activity as a traditional IgG1. A phase I study in patients with Chronic Lymphocytic Leukaemia reported modest activity as single agent (partial responses occurred in only 23% (19/83) of treated patients). Similar results were shown on patient with NHL [116], [117]. However, a randomized phase II trial in patients with Chronic Lymphocytic Leukaemia demonstrated the improved efficacy of otlertuzumab when combined with bendamustine [118]. Indeed, overall response rate was 69% in the otlertuzumab and bendamustine arm and 39% in the bendamustine alone arm and median progression-free survival was 15.9 months in the otlertuzumab and bendamustine arm and 10.2 months in the bendamustine alone arm [119]. BI836826 is an Fc-engineered, to strengthen its ADCC potential, anti-CD37 mAb currently tested in phase I trials.

These clinical studies highlight the therapeutic potential of anti-CD37 molecules, particularly in combination with other agents.

Moreover, anti-CD37 mAbs can be labelled with cytotoxic agents. After fixation of the mAb on its epitope, CD37 is moderately internalized. This allows: (1) maintaining the IgG1 Fc-mediated effector functions, (2) delivering toxins into tumour cells through endocytosis, and (3) mediating potent antibody-induced apoptosis. The CD37-targeted antibody-drug conjugate IMGN529 has each of these functions. IMGN529 is a humanized anti-CD37 IgG1 conjugated to DM1, a drug that inhibits microtubule assembly during mitosis. IMGN529 has shown early signs of clinical activity at tolerable doses in an ongoing phase I trial in adult patients with relapsed/refractory NHL (4 objective responses have been reported on a total of 21 patients) [120].

5. Antibody-drug conjugates (ADC)

ADC are an emerging novel class of anticancer agents that combine the selectivity of targeted treatment with the cytotoxic potency of chemotherapy drugs in order to increase the direct cytotoxic effect. Thus, tumour cells are specifically targeted by a mAb and are then subject to the mAb effect (depending on the mAb: direct effect, CDC, ADCC and ADCP) and also to the drug cytotoxic effect.

a. Composition

ADC are composed of three parts, each of them with a major function.

i.Drugs

To create an effective ADC, it is imperative to have a highly potent cytotoxic drug. Indeed, only a small amount of the administered ADC reaches tumour cells [121]. Therefore, it is crucial

that the conjugated cytotoxic drug is potent at low concentrations. Most cytotoxin classes lead to cell division inhibition and are classified according to their mechanism of action.

Auristatins (monomethyl auristatin E and monomethyl auristatin F) are specific types of mitotic inhibitors that share their mechanism of action with the traditionally used taxane chemotherapeutics. Auristatins interfere with the formation of microtubules by binding to the β-subunit of α-β tubulin dimers in the cytoplasm. Subsequently, they prevent the hydrolysis of GTP molecules on the β-subunit, causing continuous and excessive growth of microtubules, thus blocking the cell in the metaphase stage of mitosis. Similar to auristatins, maytansines (DM1 and DM4 molecules) also interfere with microtubule assembly, but by binding to and capping the 'plus' end of growing microtubules and by blocking the polymerization of tubulin dimers, thus preventing the formation of mature microtubules. Calicheamicins, duocarymycins and pyrrolobenzodiazepine (PBD) dimers are different types of DNA-damaging agents that are functionally similar to alkylating agents [121].

The molecular structure of cytotoxins must be taken into account for their conjugation to the linker.

ii.Linker

The linker chemistry is an important determinant of ADC safety, specificity, potency and activity. Linkers are designed to be stable in the bloodstream and labile at the cancer site to allow rapid release of the cytotoxic drug. Various parameters are taken into consideration when designing the ideal linker. These include the linker cleavability and the position and mechanism of linkage. Another important factor is the number of the drug molecules loaded onto the mAb. It is acknowledged that ADC loaded with 2–4 drug molecules per mAb achieve the best efficacy [122].

Two linker types are used in the clinic: non-cleavable and peptide linkers. Peptide linkers can be efficiently cleaved in tumour cell lysosomes by lysosomal proteases, such as cathepsin-B and plasmin, to release the drug into the cell cytoplasm. Non-cleavable linkers are degraded by a non-specific lysosomal process following ADC-antigen internalization. Protease enzymes within the lysosome can break down the mAb structure, leaving behind a single amino acid still attached to the linker and the cytotoxin. The resulting amino acid–linker–cytotoxin complex is released into the cytoplasm and then becomes the active drug (Figure 22).

The last ADC component is the mAb.

iii.Monoclonal antibodies

The chosen mAb must have the same characteristics as those required for classic immunotherapy (*i.e.*, tumour cell specificity and leading to cell death). Moreover, the ADC-antigen complex needs to be internalized for drug release. Therefore, antigen density on cancer cells and internalization speed are critical decision factors because a too quick internalization inhibits CDC, ADCC and ADCP and a too slow internalization inhibits drug cytotoxicity. Thus, the choice of the mAb-antigen couple is essential for ADC efficacy.

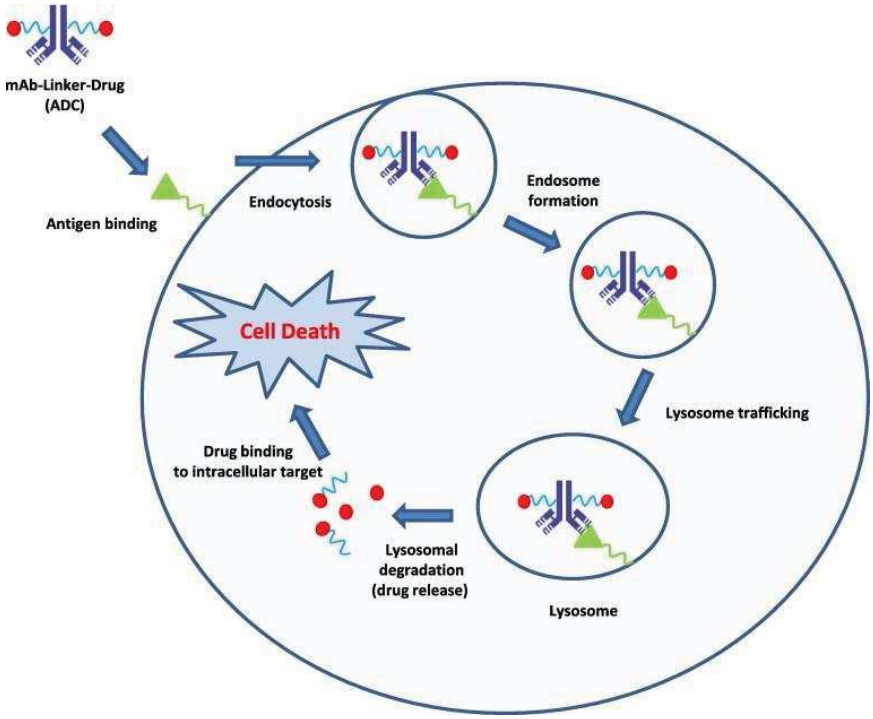

Figure 22: Mechanism of drug release in ADC [123]

b. ADC for Non-Hodgkin Lymphoma treatment

Currently, two ADC are used in clinic: brentuximab vedotin and inotuzumab ozogamicin. Brentuximab vedotin (approved by FDA in 2011) is a chimeric anti-CD30 IgG1 (also named cAC10) associated with monomethyl auristatin A (MMAE) [124], via a protease-sensitive dipeptide linker. Each mAb molecule carries four MMAE groups. Brentuximab vedotin binds to the CD30 receptor and is internalized via endocytosis. Upon exposure to proteolytic lysosomal enzymes, MMAE molecules are released in the cytoplasm. Then, MMAE binding to tubulin disrupts the microtubule network within the cell, leading to the induction of G2/M-phase cell cycle arrest and apoptosis. This therapy showed significant anti-tumour activity in anaplastic large cell lymphoma with a high proportion of patients in durable complete remission and manageable toxicity (the complete remission rate was 32% with a median duration of 20.5 months) [125]. It is also approved in HL treatment.

Inotuzumab ozogamicin is an anti-CD22 mAb associated with calicheamicin which binds to the minor groove of DNA and thus induces double-strand cleavage and subsequent apoptosis. The inotuzumab ozogamicin was approved by FDA for relapsed or refractory B-cell precursor acute lymphoblastic leukemia in August 2017. The approval was based on data from INO-VATE ALL (NCT01564784) which showed 35.8% of 162 patients who received inotuzumab ozogamicin experienced complete remission (vs 17.4% of patients treated with chemotherapy) for a median 8.0 months (4.9 months for chemotherapy treatment) and 89.7% of those patients achieved minimal residual disease (MRD)-negativity (31.6% after treatment with chemotherapy) [126].

Two others ADC are currently in phase II in NHL treatment: pinatuzumab, another anti-CD22 mAb but associated with MMAE and polatuzumab vedotin an anti-CD79b ADC also associated with MMAE.

The two others ADC, are currently in clinical trials. During the phase I, objective responses were noted in 23 of 42 activity-evaluable patients with NHL given single-agent polatuzumab vedotin and seven of nine patients treated with polatuzumab vedotin combined with rituximab. No objective responses were observed in patients with CLL [127]. After treatment with pinatuzumab vedotin, objective responses were observed in 16/39 patients with NHL; 2 of 8 patients treated with pinatuzumab vedotin and rituximab had complete responses. CLL patients showed no objective responses [128].

II. Radioimmunotherapy

In the previous examples, mAbs were armed with cytotoxic drugs to improve their therapeutic efficacy. Another strategy consists in labelling mAbs with radionuclides to combine the cytotoxic effects of ionizing radiations and of antibodies. This approach is called radioimmunotherapy (RIT), and radiolabelled mAbs are also called radiopharmaceuticals or Antibody radionuclide conjugates (ARC). This term is not restricted to antibodies and some radiopharmaceuticals used in the clinic involve radiolabelled peptides against tumour cells or their environment. In NHL treatment, two radiolabelled anti-CD20 mAbs were approved by FDA.

In RIT, antibodies keep all their functions (specific targeting of tumour cell, CDC, ADCC or ADCP), like during immunotherapy or ADC. However, radionuclides provide further advantages over drugs because Ab internalization does not need to be efficient, and the range of emitted particles can contribute to tumour cell killing through cross-fire irradiation. This is particularly interesting when antibody diffusion within the tumour is limited.

RIT includes two major components: the mAb and the radionuclide (Figure 23).

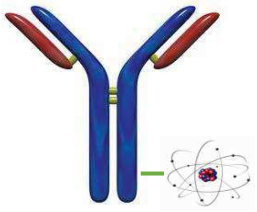

Figure 23: Schematic representation of a radiolabelled mAb

A. Monoclonal antibodies

The mAb choice depends on different parameters that are mostly similar to those described for immunotherapy. Like in immunotherapy, the selected antigen is crucial; it must be strongly expressed on tumour cells and weakly on healthy cells. This allows the protection of the healthy tissues and the limitation of subsequent radiation-induced side effects. It also allows bringing radiolabelled mAbs on tumour cells in sufficient amount for a tumouricidal effect. In RIT, the internalization of the antigen-mAb complex must be considered, although it is not required. Such internalization is mediated by endocytosis. The mechanism of endocytosis leads to acidification of the endosome to form a lysosome. Depending on the chemical bond between mAb and radionuclide (halogen bond) or according to the chelator-radionuclide affinity (see §II.B.3. p64), endosome acidification can lead to radionuclide release. Once free, the radionuclide can leave the cells and be transferred to the blood flow and then be taken up by healthy organs, leading to unspecific irradiation and severe side effects.

B. Radionuclides

A large number of radionuclides are available for RIT. The physical period (half-life), the type of emitted particles and the emission range are important parameters to consider for the radionuclide choice in RIT [129], [130]. However technical constraints, such as availability, possibility of labelling and cost, also should be taken into account.

1. Half-life

A radionuclide is an atom with an unstable nucleus. To reach stability, the nucleus emits particles that carry energy expressed in electronvolts (eV). The number of atoms decaying per second is called activity. It is expressed in Becquerel (Bq), corresponding to one decay per second.

In therapy, the particles emitted by radionuclides include alpha, beta$^-$ particles and Auger electrons. The probability of emission (λ) is linked to the physical half-life of the radionuclide (T).

The half-life corresponds to the time required for 50% of the initial atoms to decay. This feature is decisive for the radionuclide choice when designing a radiopharmaceutical for RIT. Indeed, if the isotope has a very short half-life, a high number of decays are emitted before the mAb fixation on tumour cells. Conversely, a long half-life leads to weak irradiation of tumour cells with less cytotoxicity. Currently, the radionuclides used in the clinic for NHL treatment have half-lives between 2.67 days and 8.02 days.

2. Radiation types

As mentioned above, the particles emitted by radionuclides for therapy are alpha and beta particles and Auger electrons. Generally, radionuclides also emit other types of radiation, such as gamma and X-rays, and emission is very often not pure (*i.e.*, different particles can be emitted). Moreover, the general term electron encompasses many types of electrons (internal conversion, beta$^-$, Coster-Kronig etc.) depending on their origin.

a. Alpha particles

Alpha (α) particles are emitted by nuclei with high atomic number (A) (*i.e.*, many protons (Z) and neutrons). In this case, the radionuclide emits one alpha particle made of two protons and two neutrons, corresponding to a helium nucleus.

$$^{A}_{Z}X = {}^{A-4}_{Z-2}Y + {}^{4}_{2}He$$

Alpha particles possess high energy, ranging from 5 to 9 MeV and drop it off in a short range (50-100µm, equivalent to more or less 2-10 cells). Their low availability, high production cost, and limited availability of suitable chelators have been for long a limitation to α emitter RIT. Although no radiopharmaceutical is approved for clinical use, many ongoing clinical studies are testing mAbs radiolabelled with α emitters [131]. Indeed, their short range in tissues allows high specificity of irradiation with weak irradiation of healthy tissues. ^{212}Bismuth, ^{213}Bismuth, ^{225}Actinium, ^{211}Astatine, ^{149}Terbium or ^{227}Thorium are the most promising α radionuclides.

b. Beta$^-$ particles

Beta$^-$ (β$^-$) particles are negatively charged electrons that are emitted by unstable nuclei showing an excess of neutrons and converting a neutron into a proton. In order to stay electrically neutral this transformation must emit an electronegative particle (electron), and to balance energy, the nucleus also emits a neutrino. Thus, the formed nucleus has one additional proton (Z+1) and one less neutron.

$$^{A}_{Z}X = {}_{Z+1}{}^{A}Y + {}^{0}_{-1}e + \bar{\nu}$$

The β^- particle energy can range from 10 keV to 2-3 MeV. The distance of β^- particles in tissues is relatively long and is proportional to the energy of the emitted β^- particle: more energetic particles have longer paths (from some hundreds micrometres to more than 11 millimetres [for ^{90}Yttrium], equivalent to 10-10 000 cells). This range has advantages, but also drawbacks. Indeed, a non-targeted tumour cell can be irradiated by radiation originated from the adjacent targeted cells. This phenomenon is called cross-fire irradiation and allows increasing RIT efficacy, because it is possible to kill tumour cells not directly reached by mAbs.Moreover, healthy tissue close to the tumour or exposed to circulating radiolabelled mAbs also can be irradiated. Currently, the two authorized RIT for NHL treatment use β^- emitters (^{90}Yttrium and ^{131}Iodine).

c. Auger electrons

After an electron capture or internal conversion processes, an electron vacancy is created within the atom at the level of the internal electron shell. It is followed by a rearrangement of the electron shell. The atom returns to a stable state through an electron transition. This electron rearrangement is accompanied by an emission of energy that can take two forms:

- radiative: predominant during the K shell vacancy and resulting in the emission of a characteristic photon X.

- non-radiative: more likely on the L shell vacancy and on the upper shells. These are the Auger, Coster-Kronig (CK) and super Coster-Kronig (super CK) transitions, each leading to the ejection of one electron.

Thus, these non-radiative transitions multiply the number of electronic vacancies and lead to a phenomenon of cascade emission of low-energy electrons grouped under the name of Auger electrons. Around 5 to 50 electrons of different energies are created after each electron capture or internal conversion process. Auger electrons have very low energy (<25 keV) and for this reason, these electrons have a nanoscale intracellular path (<50 µm). Several Auger emitters are used in RIT, including ^{125}Iodine, ^{111}Indium, ^{195m}Platinium and ^{67}Gallium. Due to the low path in tissues, Auger radionuclides are suitable for treating isolated cancer cells or micro-metastases.

d. X and gamma rays

X and gamma emissions are not used for therapy, but for diagnosis. Generally, gamma (γ) emission follows α or β emissions. Indeed, α and β disintegrations lead to a rearrangement of the nucleus with the generation of a son nucleus that is more stable, but in excited state. Thus, to reach its fundamental state, the son nucleus releases the surplus of energy as γ radiation. The energy of γ-rays is variable and usually ranges from 10 keV to 3 MeV. This particle is uncharged and without mass. Thus, it interacts weakly with matter, leading to a long path in matter. This feature is both

an advantage and an inconvenient. Indeed, the long path of γ photons allows them to go through the body and to be detected by single-photon emission computed tomography (SPECT) that can be used for diagnosis. Moreover, γ photons can be detected with the aim of following the path of a radionuclide and to determine the quantity of fixed radionuclides in the tumour (dosimetry) during α or β therapy. However, γ photons also irradiate the close area around the patient, with a possible irradiation of neighbouring persons.

$$^{A}_{Z}X^{*} = {}^{A}_{Z}X + \gamma$$

e. Linear energy transfer (LET)

Because α particles are heavy and charged, they cause an enormous amount of ionizations when they collide with atomic electrons in the matter, knocking them out of their atoms. They mostly interact by Coulomb repulsion (repulsive force between two positive or negative charges) with the electrons present in the atoms of the target, leading to excitation or ionization of matter. Each collision results in a small loss of energy from the α particle that steadily slows down. Because the produced ionization is so dense, the α particle soon loses all its energy along a linear track, as a result of many electron collisions, and rapidly comes to a stop. The range depends on the initial particle energy, but for α particles it is always short (<100 μm).

Because β^- particles are lighter and only single charged, they produce sparser ionization than α particles and they are more easily deviated from a straight line as they ionize atoms in the matter. Electrons mainly interact with biological material by electronic repulsion and, according to their energy, they can excite or ionize matter. After a rollercoaster track, β^- particles eventually stop and, like alpha particles, they show a definite range (Figure 24). However, as they produce less dense ionization, they slow down more gradually than alpha particles and have a longer range.

Auger electrons are interesting particles. Due to their very short path, they deposit their energies rapidly in the matter (in the range of nm).

The amount of energy released by the particles along their track is described by the linear energy transfer (LET) expressed in kilo- or Mega-electronvolts released per micrometre (keV/μm or MeV, respectively). The LET is a key parameter to understand the biological effects of ionizing radiation. Radiations are divided in two groups: high-LET and low-LET radiations.

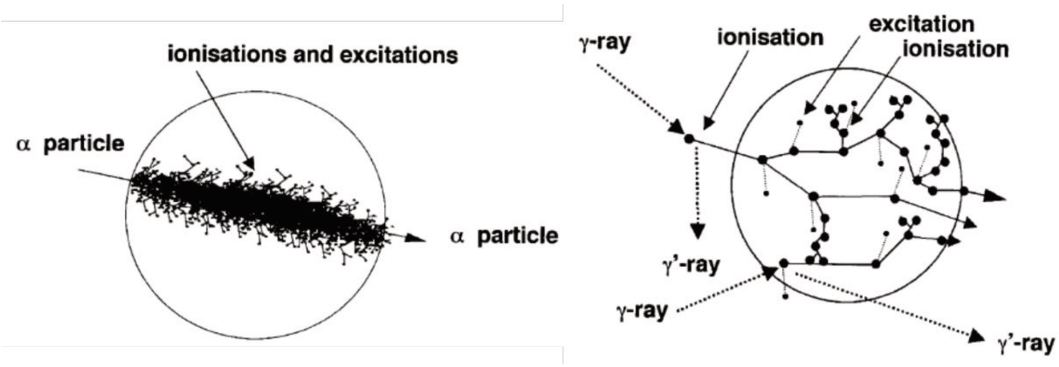

Figure 24: Schematic representations of the track structure of high- and low-LET radiation [132].

β particles have a low-LET, around 0.2 keV/µm, because the interactions between electrons and matter are weak. Conversely, α particles and Auger electrons, which have high level of interaction with matter, have a high-LET (between 50 and 230 keV/µm, and 4 to 26 keV/µm, respectively).

3. Monoclonal antibody radiolabelling

Antibodies can be radiolabelled directly via a covalent bond between mAb and radionuclide, or indirectly using bifunctional chelators that covalently bind to the mAb and also chelate the radionuclide. For both direct and indirect labelling, mAb reactive functions are the major targets. Thus, the primary amine and the lysine residue in the N-terminus of the polypeptidic chain (NH_2) are mostly targeted. Due to their high biolabelling potential, the thiol function (SH) of the cysteine and the phenol function of the tyrosine are also targeted.

The radionuclide physical and chemical properties are also important because they can affect mAb labelling. Indeed, the radiolabelling step must be simple, reproducible and quick, and in agreement with the radionuclide half-life. The specific activity obtained at the end of the radiolabelling, showing the amount of radionuclide per mAb, must be the highest possible for good cytotoxicity without affecting the mAb targeting ability. Finally, radiolabelling must be stable once the radiolabelled mAbs are injected in the patient, because many irreversible side effects can appear in the case of loss of the radionuclide due to the tropism for healthy organs (iodine for thyroid [133], yttrium for bone and liver, and lutetium for bone [134]) of many of them. A modification of the biodistribution due to the lack of stability of the radiolabelled mAb can lead to significant toxicity during treatment.

a. Halogen radionuclides

Halogen chemistry is well understood and it is known that it can form stable covalent bonds with mAbs with minimal alteration of the protein function. Halogens are directly introduced by halogenation (*i.e.*, substitution by one halogen in the presence of enzymatic or

chemical oxidants) of tyrosine and histidine residues of mAbs. ^{125}I and ^{131}I are the main halogens used in the clinic or with high potential.

b. Metallic radionuclides

Unlike halogens, conjugation of metallic radionuclides, such as ^{90}Y, ^{111}In, ^{177}Lu, ^{99m}Tc, to mAb requires a chelating agent. The chelating agent preferentially binds to mAbs on their primary amines and particularly on the lysine residues that are among the most represented amino acids with a primary amine. More precisely, during labelling, the isothiocyanate function (N=C=S function) of the chelator reacts with this N-terminal function, leading to the formation of a thio-urea bond. The choice of chelating agent largely depends on the physical properties and oxidation state of the radio-metal ion to be conjugated. Usually, a bi-functional chelating agent is used that can bind covalently to the mAb and concomitantly chelate radio-metals, without affecting the mAb kinetic and thermodynamic stability. The chelator provides the donor atoms that saturate the coordination sphere of the metal complex, stabilizing it. Currently, the most used chelators are: 1, 4, 7, 10-tetraazacyclododecane-1, 4, 7, 10-tetracetic acid (DOTA) and NR-diethylenetriaminepentacetic acid (DTPA). DTPA and the other acyclic chelators show a high rate of association (chelator/radio-metal), whereas DOTA and other macrocyclic chelators have slower dissociation rates [135].

4. Examples of radionuclides used in NHL: ^{131}I, ^{90}Y and ^{177}Lu

a. ^{131}Iodine

Iodine 131 (^{131}I) was used to radiolabel tositumomab (anti-CD20 mAb) in Bexxar®. ^{131}I is one of the 37 iodine isotopes, with only one stable isotope (^{127}I). ^{131}I belongs to the halogen family and has 78 neutrons and 53 protons. It is formed by fission reaction in a nuclear power reactor (breakdown of uranium or plutonium nuclei) or during a nuclear explosion. It has a half-life of 8.02 days and decays to ^{131}Xenon through β^- disintegration (associated with γ emissions) (Table 6). The maximum depth of penetration of the emitted β particles in tissue is around 3 mm.

Table 6: Decay scheme of ^{131}I [136]

Main Radiations	Percentage	Energy
β-	0.896	0.606 MeV
γ	0.815	367 keV
β-	0.0039	0.807 MeV
γ	0.00021	164 keV
β-	0.0723	0.334 MeV
γ	0.0716	637 keV

The γ emissions are present in 90% of decays and have relatively high energies. This is an advantage as much as an inconvenient. Indeed, due to these emissions, after injection of a vector radiolabelled with ^{131}I, patients can be imaged by SPECT to follow the ^{131}I-vector fixation to its target and to determine the tumour absorbed dose. However, the γ emissions can spread from the treated patient and can irradiate neighbouring people. Thus, patients must be isolated in a shielded room and kept under observation in the hospital.

b. ^{90}Yttrium

^{90}Y is one of the 33 isotopes of yttrium, with only one stable isotope (^{89}Y). It was used to radiolabel the anti-CD20 mAb ibritumomab tiuxetan (Zevalin®) for NHL therapy. ^{90}Y belongs to the transition metal family and has 51 neutrons and 39 protons. It is a decay product of ^{90}Strontium, which makes up about 5% of the nuclear daughter isotopes when uranium is fissioned. It has a half-life of 64.1 hours and decays to ^{90}Zirconium through pure β^- disintegration of 2.28 MeV (no associated with γ emission (<0.002%)). The maximum depth of penetration of the emitted β particles in tissue is around 11 mm and the mean depth of penetration around 2.5 mm.

As ^{90}Y disintegration is not followed by γ emissions, radiation protection management of the patient is not required, differently from ^{131}I. However, due to its high energy, the emitted β^- particle has a long path in matter, leading to more cytotoxic effects than ^{131}I for the tumour, but also for healthy tissues. Thus, ^{90}Y produces more non-specific irradiation and more side effects than ^{131}I.

c. ^{177}Lutetium

^{177}Lu is one of the 35 isotopes of lutetium, with only one stable isotope (^{175}Lu). ^{177}Lu belongs to the lanthanide family and has 106 neutrons and 71 protons. Both “direct” and “indirect” reactor production routes can be followed to obtain ^{177}Lu. The direct route is based on neutron irradiation of ^{176}Lu targets. This production method is attractive in terms of simplicity in target processing and cost effectiveness; however the relatively high quantity of ^{177m}Lu (0.02%) in the final product is the negative point. Indeed, ^{177m}Lu has a half-life of 106.1 days and has a high energetic γ emission that requires a specific radiation protection management of the patient after injection of the vector radiolabelled with ^{177m}Lu. The indirect production route (neutron irradiation of ^{176}Yb) needs a very difficult chemical separation of ^{177}Lu from the target atoms, ^{176}Yb. Moreover, production yields are low due to the poor ^{176}Yb thermal neutron reaction cross-section, compared with the “direct” production from ^{176}Lu. However, the substantial advantage of this method is the absence of long-lived radioactive impurities (^{177m}Lu) (Figure 25).

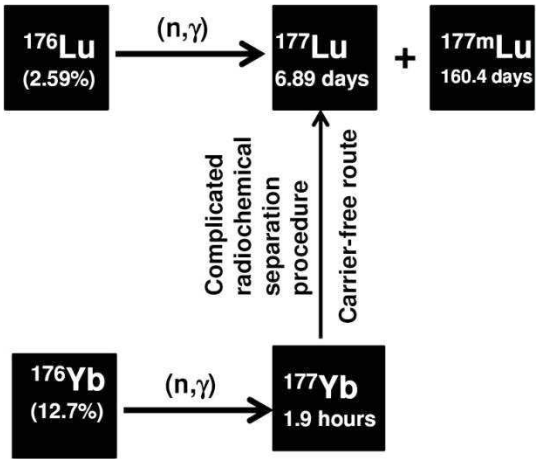

Figure 25: Two different routes for ^{177}Lu reactor production [137]

^{177}Lu half-life is 6.65 days and it decays to ^{177}Hafnium through β^- disintegration (associated with γ emissions) (Figure 26). The maximum depth of penetration of the emitted β particles in tissue is around 2.5 mm and the mean depth of penetration around 0.67 mm.

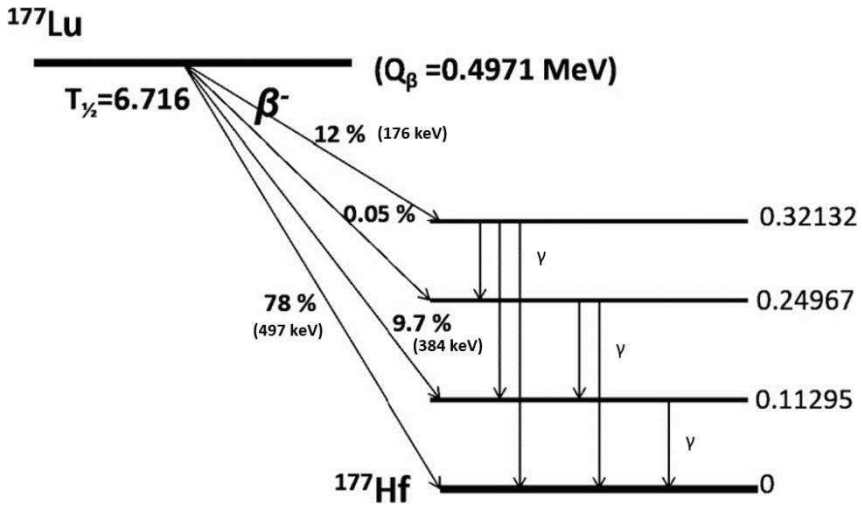

Figure 26: Simplified decay scheme of ^{177}Lu [137]

^{177}Lu has the advantages of both ^{131}I and ^{90}Y radionuclides without their inconveniences. Indeed, like ^{131}I, the moderate energy of the β^- particle allows a better specificity of the irradiated tissues than ^{90}Y. Moreover, radiation protection management of the patient is not needed thanks to the low percentage of γ emissions, differently from ^{131}I, while SPECT imaging is still possible (Table 7).

Table 7: Principal characteristics of ^{90}Y, ^{131}I, ^{177}Lu

	^{90}Y	^{131}I	^{177}Lu
Half-life	2.67 days	8.04 days	6.71 days
Radiation	β^-	β^-, γ (100%)	β^-, γ (17%)
Mean beta energy	933 keV	182 keV	133 keV
range in water	4.3 mm	0.4 mm	0.25 mm
Maximum beta energy	2284 keV	807 keV	497 keV
range in water	11.8 mm	3.6 mm	1.9 mm

C. Radioimmunotherapy in Non-Hodgkin lymphoma treatment

Two RIT have been approved by the FDA for NHL treatment: Zevalin® (Spectrum Pharmaceuticals, Irvine, USA) and Bexxar® (GlaxoSmithKline (GSK), Philadelphia, USA). RIT has been integrated in the clinical practice "for the treatment of relapsed or refractory low grade, follicular, or transformed B-cell non-Hodgkin's lymphomas or for the treatment of previously untreated follicular lymphoma in patients who achieve a partial or complete response to first-line chemotherapy".

1. Bexxar®

Bexxar® is composed of a mAb, tositumomab, radiolabelled with ^{131}I [138]. Tositumomab is a murine anti-CD20 IgG2a that has exclusively been used in a radiolabelled version. Like obinutuzumab, it is a type II mAb that strongly induces lysosome-dependent apoptosis, as well as ADCC and ADCP. As ^{131}I is a halogen, the radiolabelling between tositumomab and ^{131}I is direct without the need of a chelator.

In the clinic, the administration schedule of ^{131}I-tositumomab is based on the activity clearance from the organism as measured by SPECT. The treatment begins on day 1 with a pre-dose of 450 mg of unlabelled tositumomab, intravenously injected over 60 min. This injection improves tumour targeting by ^{131}I-tositumomab by saturating non-specific binding sites on non-malignant B cells, predominantly in the blood circulation and spleen. Then, the pharmacokinetic curve of each individual patient is determined after injection of a small amount of ^{131}I-tositumomab (185 MBq) over 20 min. Immediately, SPECT imaging is performed to obtain whole-body gamma counts before micturition. Two additional scans are done 2 to 4 days after the injection and again 6 to 7 days later to follow the ^{131}I-mAb biodistribution. The residence time of ^{131}I-tositumomab is calculated and used for determining the appropriate activity of ^{131}I for reaching the desired total body dose of 75 cGy, which is recommended to limit haematological

toxicity. This dose decreases to 65 cGy for patients with relative thrombocytopenia. Finally, the real treatment with ^{131}I-tositumomab (preceded again by 450 mg of unlabelled tositumomab) will start between 1 and 2 weeks later (Figure 27). Prior to the treatment, like in the case of immunotherapy, the patient is pre-medicated with paracetamol and an antihistaminic drug to decrease the risk of allergic reactions.

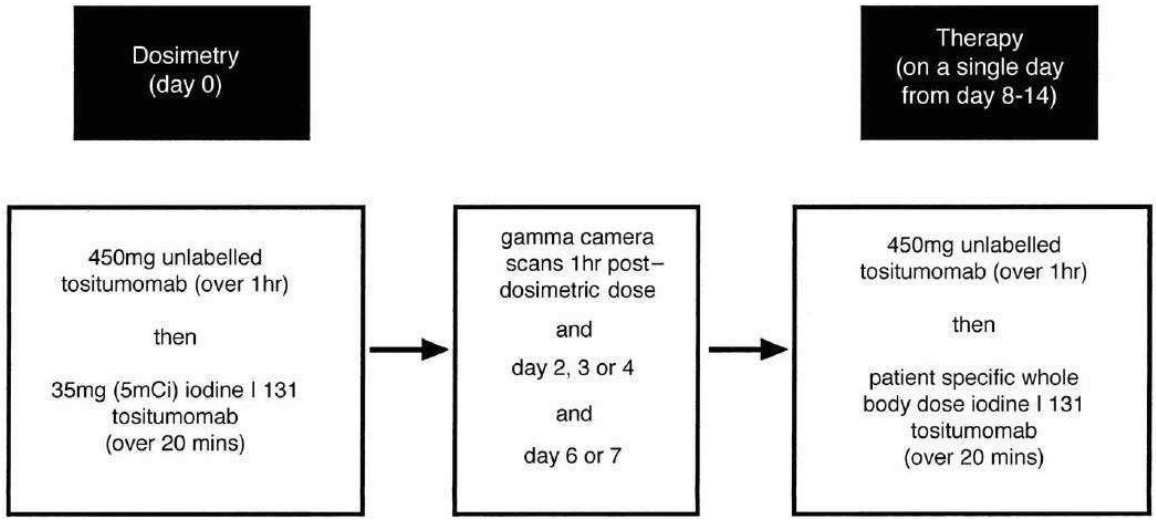

Figure 27: Bexxar® administration [139]

To avoid thyroid uptake due to ^{131}I release, thyroid blockade with potassium iodide or Lugol's solution is initiated at least 24h prior to the first infusion and continued for 14 days after the therapeutic dose, to saturate the uptake of free iodine. The most common adverse reactions include neutropenia, thrombocytopenia, and anaemia that can be prolonged and severe. Less common, but severe adverse reactions include pneumonia, pleural effusion and dehydration. Infusion reactions, delayed onset hypothyroidism and development of human anti-mouse antibodies (due to the repeated injections of murine mAb) have also been reported.

Many clinical studies were performed to examine the therapeutic efficacy of ^{131}I-tositumomab in pre-treated patients with low-grade and transformed NHL [121][125]. Prior to Bexxar®, patients received several cycles of treatment (chemotherapy and rituximab). All these studies showed that patients who had three or four prior therapies could still respond to ^{131}I-tositumomab. ORR ranged from 47 to 68% and complete response rates from 20 to 38%. Furthermore, these trials demonstrated ^{131}I-tositumomab therapeutic efficacy in patients who had progressed after treatment with rituximab, regardless of their previous response to it. Finally, these data suggest that more and lengthier complete remissions could be obtained by administering ^{131}I-tositumomab earlier in the patient's treatment path.

Other trials combining standard chemotherapy (CHOP, fludarabine or CVP) with ^{131}I-tositumomab as up-front therapy in patients with FL suggested that partial tumour reduction by chemotherapy may be converted to a complete and durable response by the subsequent administration of RIT [134] [135].

GSK discontinued the manufacture and sale of the BEXXAR® therapeutic regimens (tositumomab and ^{131}I-tositumomab) on the 20th February 2014. The decision to discontinue Bexxar involved a thoughtful and careful evaluation of patient needs and the clinical use of the therapy. The use of Bexxar has been extremely limited and was projected to continue to decline.

2. Zevalin®

^{90}Y-ibritumomab tiuxetan (Zevalin®) is composed of a mAb (ibritumomab) bound to a chelator (tiuxetan) trapping ^{90}Y [146]. Ibritumomab is a murine anti-CD20 IgG1 and it is the parent of the chimeric antibody rituximab. They share the same therapeutic type I mechanism of action. Ibritumomab is covalently linked to the MX-DTPA linker-chelator tiuxetan that provides a high-affinity chelation site for ^{90}Y.

^{90}Y-ibritumomab treatment regimen can be completed in 1 week. The activity is calculated based on the patient's weight in kilograms. The recommended activity for patients with relapsed or refractory NHL is 14.8 MBq/kg (0.4 mCi/kg) if the platelet count is normal, or (0.3 mCi/kg) if platelet count is low (<150 000/μL). The maximum activity of ^{90}Y-ibritumomab is 1184 MBq (32 mCi). Following pre-medication with paracetamol and an antihistaminic drug, rituximab (250 mg/m^2) is intravenously injected over 3–4 hours on day 1. The, rituximab (250 mg/m^2) is given again on day 7, 8 or 9. This is followed within 4 hours by the administration of the calculated activity of ^{90}Y-ibritumomab over 10 minutes (Figure 28). Before November 2011, a pre-treatment with 185MBq of ^{111}Indium-ibritumomab (γ-emitter) was done after the first injection of rituximab. SPECT images were acquired after 2 or 24 hours and then at 48 or 72 hours to determine the mAb biodistribution. However, this step is not performed any longer because a central review showed that it altered the biodistribution in approximately 1% of patients. Moreover, after treatment with ^{90}Y-ibritumomab, the clinical safety outcomes of these patients were similar to those of patients with a normal biodistribution [147]. Because of the pure beta emission from ^{90}Y, once the ^{90}Y-ibritumomab infusion is completed, patients do not require isolation, and only minimal radiation precautions are needed, such as avoiding contact with bodily fluids for the first week after treatment. Zevalin® administration is associated with the same side effects reported for Bexxar® (mainly haematological toxicities).

Figure 28: Schematic of ^{90}Y-ibritumomab administration [148]

Numerous clinical studies were performed to examine the therapeutic efficacy of ^{90}Y-ibritumomab in different subtypes of NHL (mostly FL and DLBCL) after different numbers and types of treatment [149]–[152]. They all showed that patients could still respond to Zevalin® even after several previous therapies, for example in [152] 75% of patients (n=448) achieved a complete response. Moreover, chemotherapy, administered in patients treated with RIT, was not associated with higher toxicity but with higher efficacy. Finally, earlier injection of Zevalin® led to better outcomes.

3. Betalutin®

Betalutin® consists of the murine anti-CD37 IgG1 lilotomab (also called HH1), radiolabelled with ^{177}Lu *via* a chelator (DOTA). Lilotomab targets the human glycoprotein CD37 that is abundantly expressed on the surface of malignant B cells in NHL [106]. This mAb targets the CD37 epitope $_{206}$HLARSRH$_{212}$ with an equilibrium dissociation constant (Kd) in the nanomolar range [153]. Also, when CD37 is targeted by lilotomab, the complex antigen/mAb is internalized [154].

^{177}Lu-lilotomab is developed for treating patients with relapsed or refractory B-cell NHL because there are currently no curative treatments for this malignancy. Moreover, B cells of patients who had undergone several cycles of rituximab treatment can exhibit reduced levels of CD20 receptors. Therefore there is an advantage for therapies that targets other receptors, such as Betalutin®. Furthermore, another advantage to use Betalutin® is that it is prepared as a ready-to-use formulation that is administered as a single injection in an outpatient setting, with no radiolabelling needed at the treatment centre.

The therapeutic efficacy of this new radiopharmaceutical has been studied in several preclinical studies [153]–[157]. This radiopharmaceutical is not currently approved yet but based on preclinical results, a Phase I clinical trial was performed to determine the therapeutic activity injectable to patients with minimal side effects. Three activities were administered to eight patients: 10, 15 and 20 MBq/kg, with or without pre-injection of unlabelled lilotomab. Moreover, with the help of SPECT images, a dosimetric study was performed to correlate the tumour

absorbed dose with the injected activity, and the bone marrow absorbed dose with toxicity. This study showed that although the variability between tumour uptakes is considerable, there is a correlation between tumour dose and patient dosage level. Moreover, the results indicated that 15 MBq/kg could be the highest injectable activity. Haematological toxicity was more severe in patients who received high bone marrow absorbed doses, but pre-dosing with lilotomab reduced this absorption [158], [159].

4. Radioimmunotherapy limitations and optimization for Non-Hodgkin Lymphoma treatment

RIT has demonstrated its efficacy in NHL treatment. However, RIT use remains limited; in fact only 5%–10% of patients eligible for RIT received this treatment in USA in 2007 [160], and today it is even lower.

Different reasons have been put forward to explain RIT under-use: the hypothetical important side effects, the perception of high cost, the long time to administer RIT (currently reduced for Zevalin®) and the difficulty to refer a patient to a nuclear physician. Particularly, the management of patients with NHL is usually supervised by haematologists/oncologists who are not always used to RIT practices and, consequently, more conventional therapeutic options are chosen.

However, all these explanations are not based on real facts. Indeed:

- Multiple courses of chemotherapy cause significantly higher levels of early and late toxicities than RIT, which is associated with minimal disruption of the patients' routine (independently of their age) [161]. Moreover, published data suggest that the risk of developing a second lymphoma/leukaemia is not higher in patients treated by RIT than in patients treated with cytotoxic chemotherapy, for instance alkylating agents.

- RIT cost is similar (around 40 000$ [162]) to that of chemotherapy plus rituximab (around 33 000$ [163]), the current standard of care for patients with NHL.

- The difficulty for oncologists to refer a patient to a nuclear physician can be due to the low interest of the nuclear physicians for the RIT. Conversely, many nuclear physicians think that RIT is an important treatment that will grow in importance in the future [148][149]. For RIT expansion, it appears crucial not only to demonstrate the treatment safety and efficacy, but also to streamline the referral process, in order to improve collaboration between specialists. Economic incentives should also be considered for the referring physician.

Several techniques are used to protect healthy organs from unspecific irradiation. For example, haematopoietic growth factors or even peripheral blood stem cells can also be injected to limit RIT myelosuppressive effects. Fractionation, a protocol in which a radiolabelled antibody is injected in several times at a reduced injected activity, makes it possible to deliver radiolabelled antibodies more uniformly (the size of the tumour and the number of cancer cells decrease after the first administration), reduce toxicity, increase cumulative activity in the tumour and prolong the response. Nevertheless, fractionation requires the use of a chimeric, humanized or human Ab to avoid any immune response after repeated injections of radiolabelled murine mAbs.

To improve RIT efficacy, high dose protocols are tested. These approaches require autologous or allogeneic stem cell transplantation and consist in injecting radiolabelled mAbs at myeloablative activity (for example [166]), or a combination of radiolabelled mAbs (at standard or escalated activity) with high dose chemotherapy [145], [167], [168]. RIT can also be considered alone as a front-line treatment. Indeed, an injection of Zevalin® earlier in the course of the disease leads to better outcomes: the best results of RIT alone (at non-myeloablative activity) have been obtained as first-line treatment of FL [140].

III. Radiobiology

The study of the biological effects of ionizing radiations is called radiobiology. Most of what we know about radiobiology comes from studies performed using EBRT.

Most of the time, in RIT, the same activity is administered to all patients, at most after correction in function of the patient's weight, without considering individual pharmacokinetic data. This leads to under- or over-treatments and side effects. Therefore, research work on dosimetry and radiobiology (*i.e.*, understanding what radiation does in the context of RIT) is crucially needed for treatment optimization. However, dosimetry is rarely performed due to the difficulty of dose calculation. Nonetheless, dosimetry is an essential prerequisite to understand the mechanisms involved in the tumour or cell responses and is indispensable to learn general information on the radiation effects.

In EBRT, the dose-effect relationship is linear and it is very well characterized. The paradigm of the "general" radiobiology is that the biological effects are proportional to the absorbed dose, because almost all the radiobiological studies have been done in the context of EBRT. However, this is not always the biological reality, because this point of view does not take into account the different key parameters of RIT, such as the non-targeted effect or the biological effect of the vector. Indeed, the absorbed dose represents only the characterization of the energy

deposit ("radio") in the target and it does not take into account the "biology" of RIT, which is a large part of the cell response. Many parameters differ between RIT and EBRT:

- time of irradiation (many days for RIT *vs* 1 minute for EBRT)

- mixed irradiation due to the different emissions of the radionuclide

- dose range (15-30 Gy for RIT *vs* 50-80 Gy for EBRT)

- dose rate (in the range of cGy/h for RIT *vs* 120 Gy/h for EBRT)

- dose distribution heterogeneity (due to the fixation heterogeneity of the radiolabelled vector and also to the particle path length)

- presence of a vector (which can have an effect by itself)

Thus, it is necessary to have a specific radiobiology for RIT that takes into account the specific features of the different RIT parameters.

RIT therapeutic efficacy can be explained by two components: i) targeted effects due to the cell irradiation, and ii) non-targeted effects due to the secretion of molecules by irradiated cells to kill non-irradiated cells.

A. Targeted effects of ionizing radiations

1. Direct effects

They are the consequence of the direct absorption of ionizing radiations by macromolecules (DNA, lipids, proteins…). Ionization or excitation can lead to the rupture of a covalent bond in two radicals. Therefore, they are defined as "direct effects" of ionizing radiations, without the intervention of intermediary molecules. DNA is the radiation major target, leading to cell death. When ionizing radiations hit DNA molecules, pyrimidines (thymine and cytosine) and purines (adenine and guanine) loose electrons, and transfer reactions of electric charges can be generated along the DNA chains with a preferential localization at guanines. This results in the formation of 8-oxo-guanine. Most of the time, the direct effect of ionizing radiation is observed after irradiation with high-LET radiation emitters. Conversely, low-LET radiation emitters usually induce indirect effects.

2. Indirect effects

The organism is composed of 70% water. Thus, the major interaction between ionizing radiations and matter is through water. This interaction is named water radiolysis and plays a main role in the harmful effects of ionizing radiations [169].

a. Water radiolysis

The ionization of a water molecule is generated by energy absorption of about 13 eV; it allows the formation of $H_2O^{+\cdot}$.

$$H_2O \xrightarrow{Irradiation} H_20^{+\cdot} + e^-$$

$$H_20^{+\cdot} + H_2O \rightarrow H_3O^+ + OH^\cdot$$

The free e^- is captured by a water molecule to create an aqueous electron, e^-_{aq} that forms $H^\cdot$ (reducer) and $OH^\cdot$ (oxidant).

$$e^- + H_2O \rightarrow e^-_{aq} \begin{matrix} \overset{+H2O}{\nearrow} \\ \underset{+H_3O^+}{\searrow} \end{matrix} \begin{matrix} H^\cdot + OH^\cdot \\ H^\cdot + H_2O \end{matrix}$$

The formed $HO^\cdot$ is the second most powerful oxidant after fluorine. This radical has a very short lifespan and is considered to be the main agent leading to lesions. In accordance with its lifespan, it reacts with the molecules in its close environment (H_2O, O_2 and also organic molecules).

Excitation is the second interaction between ionizing radiation and water. The excited water molecule can stabilize itself through the following mechanism:

$$H_2O^* \longrightarrow OH^\cdot + H^\cdot$$

$$H_2O^* \longrightarrow H^+ + OH^\cdot + e^-$$

All the created radicals ($H^\cdot$ or $OH^\cdot$) can diffuse in the environment and cause lesions on DNA chains or on other biomolecules, such as lipids or proteins. Furthermore, radicals can also react with each other, resulting in the formation of stabilized molecules according to the radicals' spatial repartition.

$$2\ OH^\cdot \rightarrow H_2O_2$$

$$2\ H^\cdot \rightarrow H_2$$

$$H^\cdot + OH^\cdot \rightarrow H_2O$$

H_2O_2 (hydrogen peroxide) is a very strong oxidant that can generate much damage.

The major reactions between radicals and biomolecules are: hydrogen abstraction, hydroxylation or rearrangement of two radicals.

$$RH + X^\cdot \rightarrow R^\cdot + XH$$

$$R^\cdot + OH^\cdot \rightarrow ROH$$

$$2\ R^{\cdot} \rightarrow R\text{–}R$$

In the case of biomolecules showing unsaturation, such as double bonds, bond opening and formation of addition compounds can be observed.

b. Oxidative stress

Oxygen has been known as a cell radiosensitization source for a long time [170]. Moreover, hypoxic cells present a high resistance to radiation effects, highlighting the crucial role of oxygen in this cell response. Cell radiosensitization is due to several radicals (listed in Table 8). Oxygen radicals are named reactive oxygen species (ROS).

Table 8: Free radicals derived from oxygen

FREE RADICALS DERIVED FROM OXYGEN

$O_2^{\cdot -}$	Superoxide radical
$HO_2^{\cdot}$	Hydroperoxyl radical
OH	Hydroxyl radical
$RO_2^{\cdot}$	Peroxyl radical
$RO^{\cdot}$	Alkoxyl radical

Cells can produce several antioxidant molecules to fight against radicals: superoxide dismutases, glutathione peroxidases, catalases, glutathione S-transferases and others. Each antioxidant enzyme preferentially targets a reaction compound to stop the oxidation cascades. For example, superoxide dismutase takes charge of $O_2^{\cdot}$ *via* 2 H^+ to form O_2 and H_2O_2. It transforms a highly reactive compound (superoxide radical) into a less reactive compound (hydrogen peroxide). However, H_2O_2 also is toxic for cells and will be catabolized by other enzymes (catalase or glutathione peroxidase) for elimination. Cells also produce non-enzymatic molecules to counterbalance the radical attacks: water-soluble (for example, glutathione, ascorbic acid and uric acid) and lipid-soluble molecules that protect the cell membranes and membrane proteins (for example, vitamin E and carotenoids).

Ionizing radiations lead to direct induction of rupture of covalent bonds (and consequently to breaks in macromolecules), or to the rupture of water molecules. This rupture creates unpaired electrons (free radicals) that react between them and with neighbouring macromolecules, leading to waterfall attacks (Figure 29).

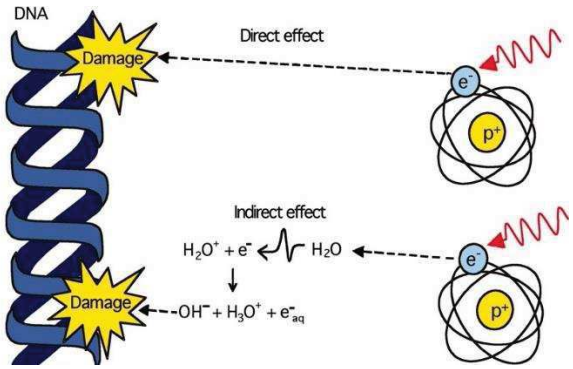

Figure 29: Direct and indirect effects of ionizing radiations on the double helix of DNA [171]

High-LET particles interact with almost all the molecules they meet while crossing the cell, inducing abundant ionization of water molecules and especially of macromolecules. Thus, high-LET particles act mainly via direct effects. For low-LET particles, the probability of ionization of a macromolecule is much weaker. Due to the high water content (70%) of the body, water has the highest probability of being ionized. As a consequence, low-LET particles act mainly through indirect effects.

3. Biological effects

Following irradiation, cells identify the damage and try to repair it. If the damage is not repaired, cells can die or can be modified (e.g., morphologic transformations, genetic mutations and chromosomal aberrations), with long-, middle- and short-term consequences.

Many macromolecules are sensitive to ionizing radiations. However, DNA is the main target.

a. DNA damage

The DNA molecule contains the genetic information. Thus, its integrity is highly controlled because modifications of the nucleotide sequence or structure can introduce errors in the genetic code and modify the genome transcription. Accordingly, ionizing radiation causes more effects by targeting DNA than other compartments [172].

Radiation can cause different types of DNA lesions in function of the reached area (Figure 30)

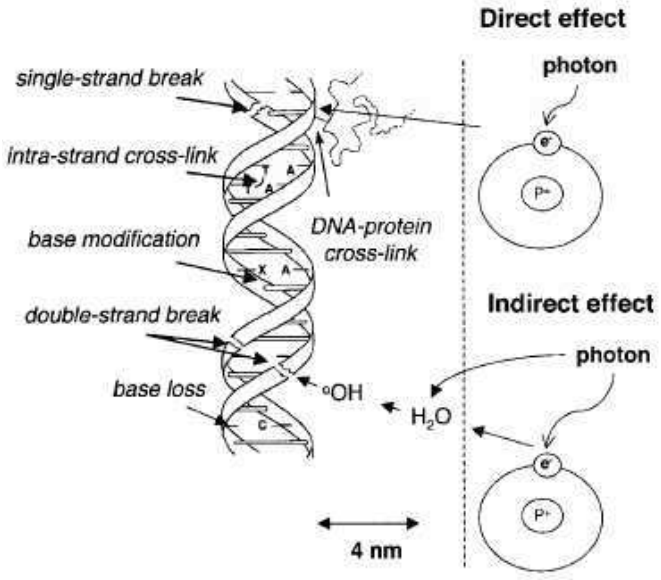

Figure 30: Schematic representation of DNA lesions ([132]

i.Single-strand breaks

DNA single-strand breaks are the main lesions caused by ionizing radiations. They result in the rupture of the bond between phosphate and sugar, due to removal of one hydrogen by the radical OH·. These breaks are linearly formed as a function of the absorbed dose and are the majority of the lesions upon low-LET particle irradiation. Nevertheless, this process is not efficient in term of mortality because these lesions are easily repaired by the cell DNA repair systems.

ii.Double-strand breaks

A DNA double-strand break is a rupture of both strands at very weak sites and is one of the most deleterious lesions. It can be the results of the attack by several OH·; however, it can be caused also by the attack of just one OH· on the deoxyribose with transfer of the radical to the homologous strand. These breaks are less frequent than single-strand lesions (about 40 per Gy for γ irradiation [173]), and their number increase with the LET. Their repair is complex and requires cell cycle arrest to allow the repair or the activation of the cell death pathway.

iii.Base modifications

Ionizing radiation can also modify bases on DNA. All four bases that form DNA can be affected, but thymine is the most reactive. OH· attacks mainly the cycle at position 5 in pyrimidines, and the cycle at position 8 in purines [174]. Base modifications are the most common DNA lesions (about 2 000 per Gy for γ irradiation).

iv.Crosslinks

Three types of DNA crosslinks can be observed in response to irradiation: DNA-DNA intra-strand crosslink, DNA-DNA inter-strand crosslink, and DNA-protein crosslink. The number of DNA-protein crosslinks following irradiation with low-LET particles is around 30 per Gy. They are

created when two radicals are generated on DNA and on one amino acid of a close protein (particularly between tyrosine and thymine) [175].

v.Chromosomal aberrations

Chromosomal aberrations are not a type of DNA damage in the strict sense of the term. Indeed, unrepaired or wrongly repaired double-strand breaks can lead to deletions or chromosomal aberrations. Chromosomal aberrations bring different forms of chromosomal modifications together: fragmentation of one or several chromosomal strands, intra-chromosomal exchanges and inter-chromosomal exchanges.

If these damages occur before the S phase of the cell cycle, they can be replicated and both chromatids can be affected. Conversely, in the case of unrepaired breaks during the G2/M phases of the cell cycle, generally one single chromatid is affected. Chromosomal aberrations are usually lethal (Figure 31).

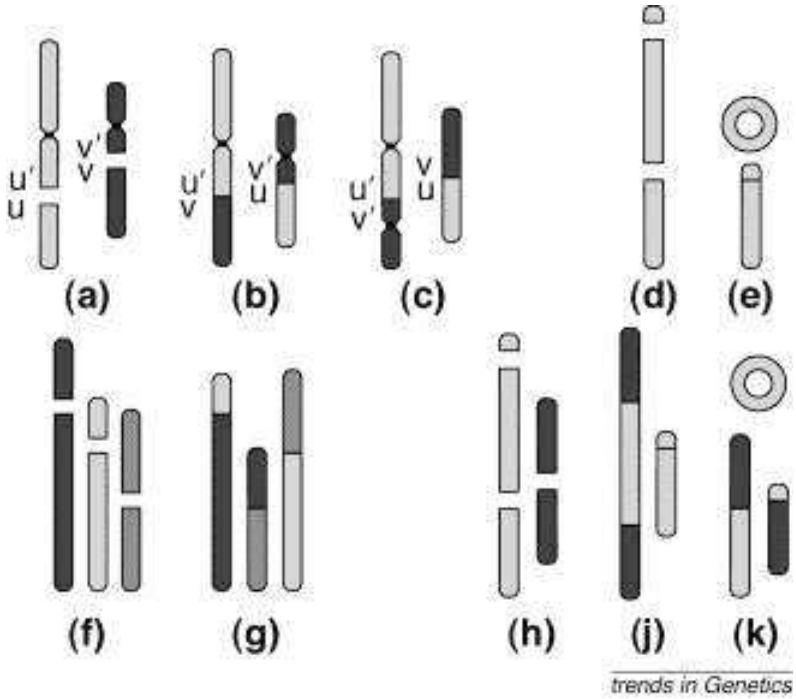

Figure 31: Schematic representation of chromosomal aberrations [176]

Ionizing radiations are not the single cause of chromosomal aberrations. During lymphocyte maturation, DNA modifications may occur and it has been shown that gene translocations can be at the origin of several lymphomas [30], [31], [33]–[35].

b. Protein damage

Like DNA, proteins can be affected by ionizing radiations. They can be cleaved or oxidized through the direct and indirect effects of ionizing radiations, leading to a disorganization of their

structure. Particularly, the thiol groups can be easily oxidized. Once modified, proteins are non-functional and generally become hydrophobic, creating aggregates inside and around the cell.

c. Membrane damage

The cell membrane is composed of, amongst others, polyunsaturated fatty acids that can react with $OH^{\cdot}$ and produce peroxide fatty acid through the chain reaction of lipid peroxidation. This peroxidation leads to membrane disorganization with modifications of its fluidity and permeability.

Furthermore, many biological mechanisms take place at the cell membrane. Especially, acid sphingomyelinase in the membrane can be activated by ionizing radiation [177]. As seen previously (§I.D.4.c.i.a).i) p47), upon activation, it hydrolyses ceramide that plays a role in cell death through apoptosis activation.

4. Biological responses

At the cellular level, damaged DNA can lead to genomic instability and finally cell death or modification of the cell functions (malignant transformation). Therefore, it is essential for cells to detect and repair DNA damages.

a. DNA damage detection

At double strand break sites, the mechanisms of DNA damage detection are dependent on the transient recruitment of the MRE11/RAD50/NBS1 (MRN) complex. It is followed by the recruitment/activation of Ataxia–telangiectasia mutated (ATM; a member of the family of PI3K-related kinases), DNA-dependent protein kinase (DNA–PK) and Ataxia telangiectasia and Rad3-related (ATR). These three effectors phosphorylate various targets that contribute to the overall DNA damage response. Usually, histone H2AX is the first phosphorylated protein and its activation leads to the recruitment of other proteins (MDC1, 53BP1, and BRCA1) that are ATM substrates and mediators in the DNA-damage response [178]. The MRN complex can also mediate the resection of double strand breaks, followed by single-stranded DNA coating with RPA and recruitment of ATR and its binding partner ATRIP, and the subsequent ATR-dependent phosphorylation of clapsin, RAD17, BRCA1, and others. This ATR pathway is predominantly implicated in single strand break repair. [179]

Upon DNA break detection, different mechanisms are put in place. In parallel, cells can act on the cell cycle to allow DNA repair.

b. Cell cycle modifications

The cell cycle is tightly regulated to allow the proper duplication of the genome that will be passed to the two daughter cells. Following irradiation, gene sequences can be altered. Thus,

the cell repair mechanisms stop or slow down cell cycle progression, to repair these errors (summarise in Figure 34).

The cell cycle is divided in five phases. G0 is the first phase, in which cells are quiescent. To begin the cell division, cells move to the G1 phase. During this phase, cells grow and are metabolically active (synthesis of the proteins and enzymes required for DNA duplication), but do not replicate their DNA. This occurs during the S phase where cells synthetize DNA and replication takes place. Once the DNA amount is doubled, cells move to the G2 phase where they grow rapidly and prepare for division. Finally, in the M phase, chromosomes are formed and condensed, and cells divide (Figure 32).

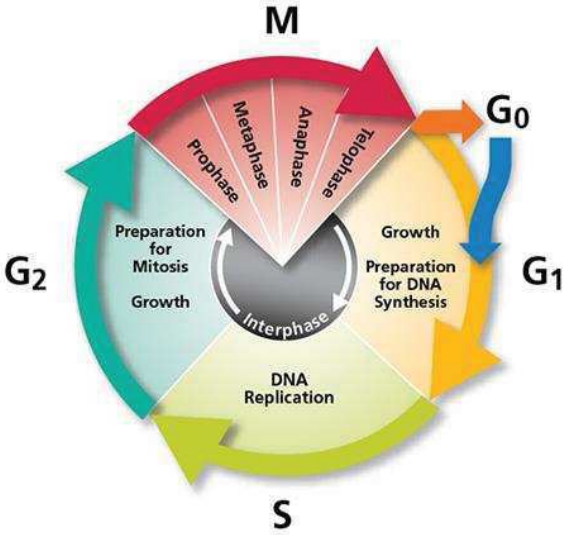

Figure 32: Cell cycle progression [180]

After detection of lesions caused by irradiation, several control mechanisms are activated [179]:

-ATM and ATR are activated and phosphorylate CHK2 and CHK1, respectively [181], [182]. This can induce phosphorylation of CDC25A, leading to its proteosomal degradation. This results in G1/S arrest, due to inefficient CDC45 loading that is required for replication. In addition, activated ATM, ATR, DNA–PK, CHK2 and CHK1 phosphorylate and stimulate p53, a key player in DNA-damage checkpoints. Then, p53 activates p21 that inhibits two G1/S-promoting cyclin-dependent kinases (CDK), CDK2 and CDK4. This leads to sustained G1 arrest to allow the repair of damaged DNA (Figure 33).

-Activation of the G2/M DNA-damage checkpoint inhibits mitotic entry of damaged cells. This checkpoint is regulated by the phosphatase CDC25C and p53. In normal conditions, CDC25C dephosphorylates CDK1 on tyrosine 15 and threonine 14 [183], inducing the formation of the

CDK1–cyclin B kinase complex to allow progression to mitosis. However, phosphorylation of CDC25C by CHK2 or CHK1 stimulates its binding to the conserved regulatory protein 14-3-3. This leads to CDC25C cytoplasmic sequestration and prevents mitotic entry. P53 also contributes to regulation of the G2/M checkpoint, but to a lesser extent, through transactivation of p21 and 14-3-3. Moreover, p21 can inhibit phosphorylation of CDK1. 14-3-3 sequesters CDC25C in the cytoplasm and promotes activation of WEE1, a tyrosine kinase that negatively regulates CDK1, thus blocking mitosis entry. WEE-1 is a nuclear kinase that phosphorylates CDK1 on tyrosine 15 to inhibit its functions. CDK1 inhibition is also mediated by MYT-1, another nuclear kinase that phosphorylates CDK1 on threonine 14 (Figure 31).

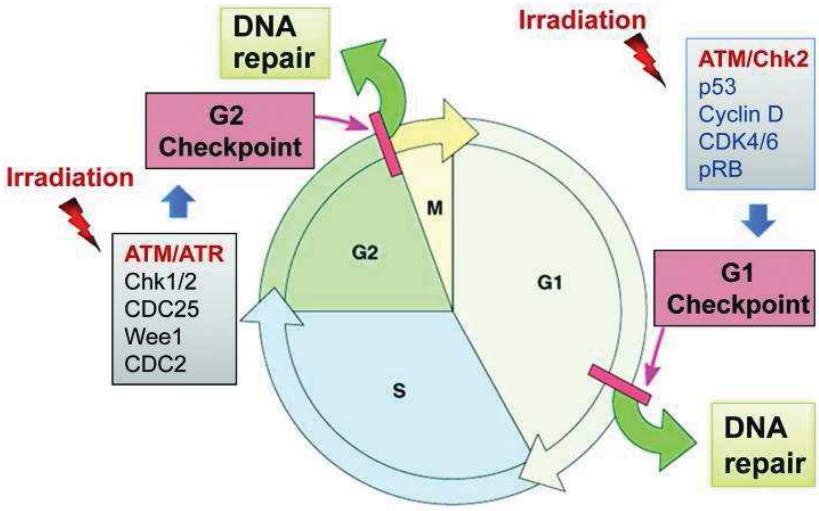

Figure 33: Cell cycle checkpoints [184]

- Activation of the DNA-damage checkpoints stops the cycling of damaged cells and allows the activity of DNA-repair mechanisms. Once repair is completed, cells can exit the checkpoints and start cycling again. If repair is incomplete, cells may start cycling again and transmit the errors to their daughters. Alternatively, cell death mechanisms, such as apoptosis, may be induced.

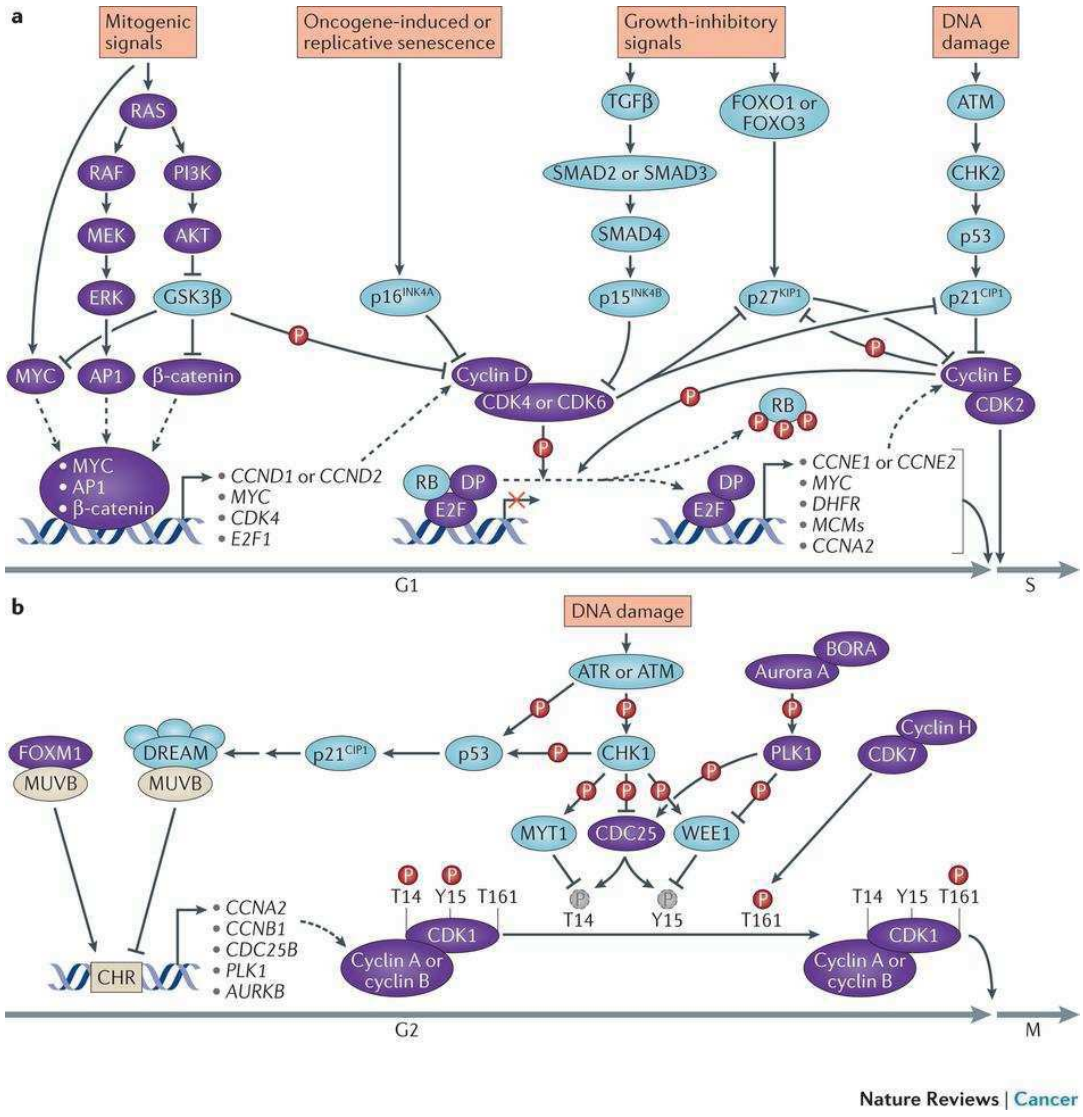

Figure 34: Proteins and pathways implicated in regulation of G1-S (a) and G2-M (b) cell cycle transitions [185]

c. DNA-repair mechanisms

Once the DNA damage is detected, different repair mechanisms can be activated to restore the DNA sequence as faithfully as possible. These pathways include: (1) the direct reversal pathway, (2) the mismatch repair pathway, (3) the nucleotide excision repair pathway, (4) the base excision repair pathway, (5) the homologous recombination pathway, and (6) the non-homologous end joining pathway (Figure 35). The underlying mechanisms will not be discussed in detail.

-Direct reversal pathway: alkylating agents can transfer methyl or ethyl groups to a guanine, thereby modifying the base and interfering with its pairing with cytosine during DNA replication. Unlike other pathways, this mechanism is not multistep. It is mediated by the enzyme

O-6-methylguanine-DNA methyltransferase that transfers the alkyl group from the DNA to its own active site.

- Mismatch repair (MMR) pathway: this mechanism plays an important role in repairing mismatches, which are small insertions and deletions occurring during DNA replication. Interestingly, this pathway is implicated in somatic hypermutation and class switch recombination during lymphocyte development.

- Nucleotide excision repair (NER) pathway: over 30 different proteins are involved in this pathway. It is generally activated to repair lesions on single strand DNA. It removes the lesions that distort the DNA double helix, interfere in base pairing and block DNA duplication and transcription.

- Base excision repair (BER) pathway: this pathway deals with base damage, the most common insult to cell DNA. It removes the injured bases and replaces them or fill in vacant sites.

The repair of double strand breaks can be mediated by two major repair pathways, depending on the context of DNA damage.

- Homologous recombination (HR) pathway: it is the major repair pathway during the S and G2 phases of the cell cycle. It involves replacement of the injured DNA sequences by an identical sequence, synthesized from the homologue chromosome.

-Non-homologous end joining (NHEJ) pathway: it is the major repair system of double strand breaks in human cells. It can be activated during all cell cycle phases. It involves a suture of the two ends of the double strand break and leads to loss of genetic information, differently from the previous mechanism. This pathway is also involved during the three steps of Ig production (V(D)J recombination, somatic hypermutation and class switching).

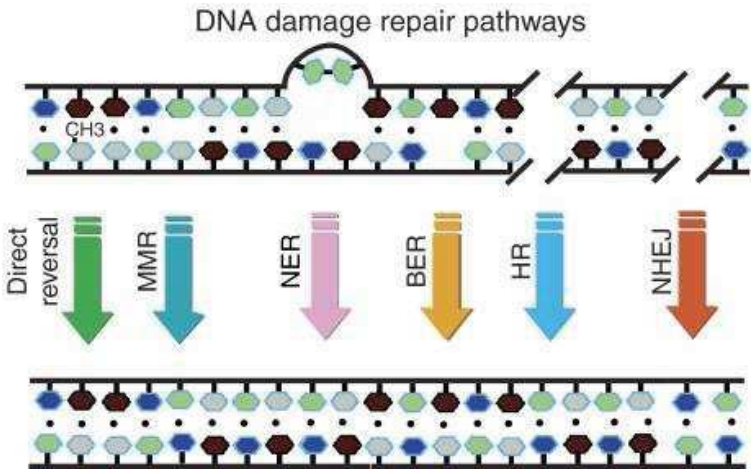

Figure 35: DNA repair pathways [186]

d. Cell death mechanisms

If the damage caused by ionizing radiation cannot be properly repaired, cells can die. Three major death mechanisms have been described:

-Cell death by mitotic catastrophe. This is the abrupt loss of the ability to finish the cell division during mitosis, and occurs after accumulation of chromosomal aberrations. It is characterized by the formation of enormous cells or binucleated cells and by the formation of cells containing micronuclei, leading to the loss of the genetic materials. Sometimes, cells going through an abnormal mitosis also can generate abnormal cells.

-Necrosis. This is a passive cell death mechanism, characterized by loss of membrane permeability, dilation of cytoplasmic vesicles and random DNA fragmentation. Thus, the cell content is poured in the extracellular space and attacks the neighbouring cells, causing inflammation.

-Apoptosis, or programmed cell death. It is characterized by reduction of the cell volume, chromatin condensation, nucleus fragmentation (DNA fragments of 180 to 200 base pairs) and formation of apoptotic bodies. Apoptosis is rigorously controlled by proteins of the Bcl family and involves caspase activation. Apoptosis is the main death mechanism induced by irradiation in cells from the lymphoid and myeloid lineages [187]. Significantly less apoptosis is observed in cells of epithelial origin. The activation of apoptosis through the mitochondrial pathway involves increased permeability of the mitochondrial outer membrane. This process is mainly controlled and mediated by members of the Bcl-2 family. This family is divided into pro-apoptotic and anti-apoptotic members. The pro-apoptotic members constitute two subfamilies, the BAX-like family (BAX, BAK, BOK) and the BH3-only proteins (BID, BAD, BIM, BIK, BMF, NOXA, PUMA, HRK). Conversely, the anti-apoptotic members (Bcl-2, Bcl-XL, Bcl-W, MCL1, Bcl2A1, Bcl-B) prevent apoptosis activation. The regulation of this family is complex and not fully elucidated. Bcl-2 and Bcl-xL are the two major anti-apoptotic proteins that inhibit apoptotic death through different mechanisms: by controlling the activation of caspase proteases, by direct binding to BAX [188], and also by retrotranslocation of BAX from the mitochondrial membrane into the cytosol [189]. PUMA and NOXA also are important proteins involved in the radiation responses (after p53 activation) [190], [191]. In parallel, BAD could play an opposite role (after activation of p53). It is trapped by 14-3-3 in the phosphorylated state, but once dephosphorylated, BAD promotes the release of cytochrome C through its heterodimerization with Bcl-xL or Bcl-2 (thus, inhibiting their functions). However, the precise mechanisms involved in apoptosis regulation are not well understood and continue to be the subject of much research.

The balance between pro- and anti-apoptotic signals triggers or not apoptosis activation. When the pro-apoptotic signals become predominant, BAX–BAK pores are formed in the mitochondrial outer membrane, which is the first step of apoptosis activation. Permeabilization of the mitochondrial outer membrane allows the release of several proteins, including cytochrome C, SMAC/DIABLO, OMI/HTRA2, EndoG, CAD and AIF from the mitochondria to the cytoplasm [192]. The release of cytochrome C leads to the binding and activation of APAF1 that mediates the activation of caspase-9. SMAC/DIABLO and OMI/HTRA2 also interact with and suppress the action of inhibitors of apoptosis proteins. A second group of pro-apoptotic proteins (AIF, endonuclease G and CAD) are then released from the mitochondria, translocate to the nucleus and cause DNA fragmentation (CAD needs to be activated by caspase-3 cleavage).

Once caspase 9 is activated, subsequently it cleaves and activates (Figure 36):

-initiator caspases (caspase 2, 8, 9, 10) to amplify the activation of the apoptotic pathway

-inflammatory caspases (caspase 1, 4, 5) to control the secretion of inflammatory mediators

-effector caspases (caspase 3, 6, 7). They, in turn, cleave cell death substrates that collectively produce the phenotypic cell changes characteristic of apoptotic cell death.

These activations lead to the successive cleavage of cytoplasmic and nuclear proteins (PARP, MAPK and cytoskeleton proteins).

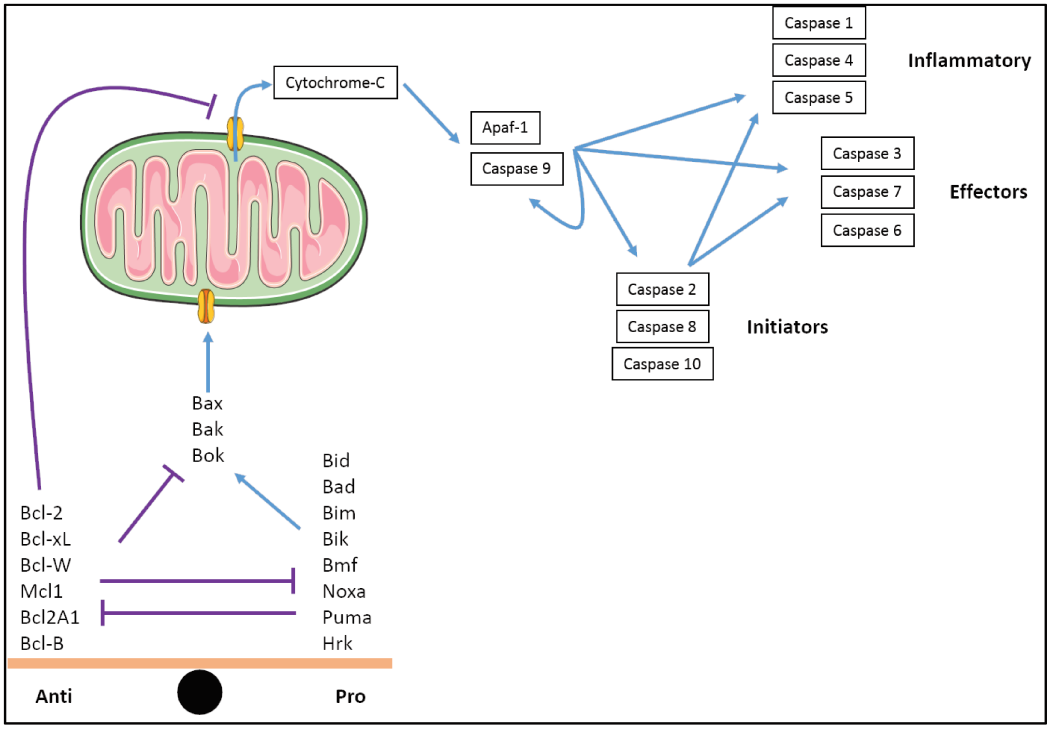

Figure 36: Schematic representation of the apoptosis pathway

In physiological conditions, apoptosis is crucial for the regulation of lymphocyte development. Indeed, deregulation of this pathway can lead to lymphoma development. During treatment (EBRT, chemotherapy or ionizing radiations), pro-apoptotic signals are increased. The balance between pro- and anti-apoptotic proteins is tilted in favour of apoptosis, leading to cell death. Therefore, apoptosis is the major cell death pathway involved in the lymphoma cell response to the different treatments.

B. Non-targeted effects of ionizing radiation: bystander and abscopal effects

The concept of bystander effect is recent and was described first in 1992 [193]. It is defined as the induction of lesions in non-irradiated cells that are close to irradiated cells. It is generally observed after low-dose EBRT (<0.5Gy).

The transmission of mediators between irradiated cells and neighbouring cells might involve cell–cell interactions through intercellular communications or *via* the release of soluble signals in the extracellular medium that may have distant biological effects (abscopal effects) [194], [195]. These mediators can be ROS, cytokines (Interleukin 8, Interleukin 6, TNF or Interleukin 33), Ca^{2+}, and extracellular DNA. However, not all molecules that act as mediators are known and the importance of each mediator is not prioritized. Bystander effects include mutations, clastogenic effects, cell death, apoptosis, and cell transformation [196], [197].

While the direct effects of radiation (due to cell ionization) are generally defined by a linear dose-effect relationship, bystander effects are characterized by a lack of dose-effect relationship. Indeed, effects do not progressively increase with higher absorbed doses, and bystander effects rapidly reach a plateau (Figure 37). For this reason, bystander effects are observed with weak absorbed doses and low dose rates, although they have been detected also after EBRT with high absorbed dose. Moreover, the type of ionizing radiation is an important parameter for bystander effect induction. Specifically, high-LET particles (such as Auger or α particle) induce a more important bystander response than low-LET particles (such as β particle) [198].

In addition, after irradiation, not all cell types can secrete bystander mediators to induce the death of neighbouring cells; and the corollary is that not all cell types can respond to these signals.

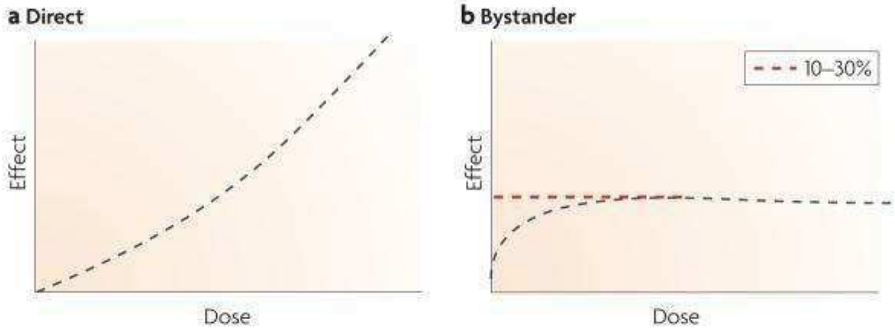

Figure 37: Schematic representation of the dose-effect relationship for direct irradiation (a) and for bystander effects (B) in RIT treatment [199]

The name abscopal comes from the Latin *ab* (position away from) and *scopus* (mark or target). Abscopal effects are believed to arise from the ability of local irradiation to elicit systemic immune effects to control the non-irradiated tumour burden. Irradiation acts as an immune modulator in the tumour microenvironment through several mechanisms. However, the abscopal mechanism of action remains unexplained, although a variety of underlying biologic events can be hypothesized, including a possible role for the immune system [200]. Irradiation can induce cell death and release of immunogenic factors that subsequently trigger the release of a number of endogenous damage-associated molecular patterns. These molecules contribute to the priming of the immune system by triggering dendritic cells, thereby resulting in improved antigen presentation to T lymphocytes. However, abscopal effects are not often observed, possibly because dendritic cell function is impaired in many patients with tumours [201].

C. Dosimetry in radioimmunotherapy: MIRD formalism

The reference method in nuclear medicine for the dose calculation is based on the recommendation by the Medical Internal Radiation Dose (MIRD) committee [202]. Since 1968, this multidisciplinary group proposed [203] a formalism to calculate the mean dose in a target area, starting from irradiation by a source area. In RIT, to evaluate the tumour absorbed dose, the tumours are most of the time considered as the source and as the target. Different target scales are conceivable in clinical and pre-clinical conditions: whole body, organ, tissue, single cell and even subcellular compartment, such as the nucleus.

Dosimetry calculation can be influenced by many different parameters, such as the particle type, the energies of each particle, the radionuclide activity, the emission localization and the effective half-life. The effective half-life is a combination of the radionuclide physical half-life

and the radiolabelled vector pharmacokinetics (also called biological half-life), showing the radiolabelled vector elimination rate in the body.

1. General principles

The MIRD formalism is based on the hypothesis that radiation crossing the target is uniformly distributed and therefore, that the distribution of the absorbed dose is homogenous in the target. The continuous updating of this formalism gives a reliable methodology to evaluate the absorbed dose by organs, tissues or group of cells, for diagnostic or therapeutic applications in the clinic or in research. To understand dosimetry, different physical values are defined.

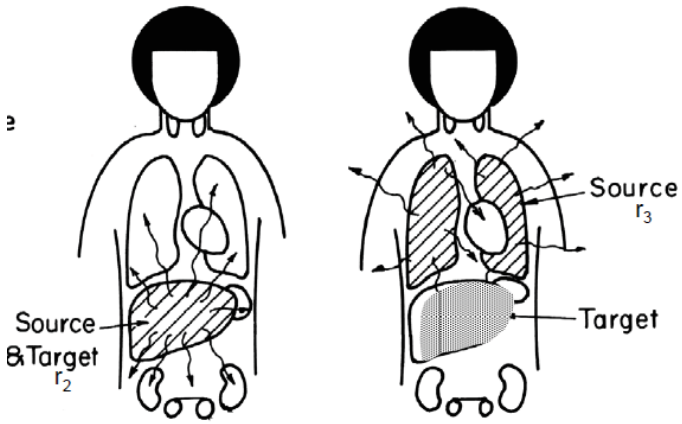

Figure 38: Schematic representation of the MIRD formalism at the whole body scale

a. Absorbed fraction

The absorbed fraction (ϕ) corresponds to the fraction of the energy emitted by the source area (s) that is absorbed by a target area (t) [204]:

$$\phi_{(t \leftarrow s)} = \frac{E}{E_0}$$

where E is the absorbed energy in the target area and E_0 the initial emitted energy; ϕ has no unit and can be divided by the mass of the target organ (m_t) to make the mass absorbed fraction ($\Phi_{t \leftarrow s}$):

$$\Phi_{(t \leftarrow s)} = \frac{\phi_{(t \leftarrow s)}}{m_t}$$

Φ is expressed in kg^{-1}.

b. Mean emitted energy

A radionuclide can emit different types of radiation (i) that can have different energies. The mean emitted energy (Δ) groups together these different parameters and is defined by the equation:

$$\Delta = \sum_i \Delta_i = \sum_i E_i Y_i$$

where E_i is the mean energy (in Joule) of the type of particle i, and Y_i is the number of particles i emitted by nuclear disintegration (in $Bq^{-1}.s^{-1}$). Thus, Δ_i represents the mean emitted energy for one type of particle (i), and the total energy of all radiation types is Δ (in $J.Bq^{-1}.s^{-1}$).

c. *Cumulated activity*

Dosimetry quantifies the energy deposit in a target volume on the basis of the radiations emitted from a source. For this, it is crucial to determine the total number of emitted decays by the source. The cumulated activity ($\tilde{A}_s$) shows this parameter. It is calculated as the integral of the source activity variation ($A_s(t)$), from the injection of the radiolabelled vector to its elimination (∞).

$$\tilde{A}_s = \int_0^{\infty} A_s(t)dt$$

It is expressed in MBq.s.

d. *Absorbed dose*

The absorbed dose is the major parameter in dosimetry. It is defined as the product of the cumulative activity of the source ($\tilde{A}_s$) by the mass absorbed fraction ($\Phi_{t\leftarrow s}$) that represents the total number of decays crossing the target by mass unit. This value is multiplied by the mean emitted energy (Δ) to finally obtain the absorbed dose (D_t):

$$D_{(t)} = \tilde{A}_s \Phi_{(t\leftarrow s)} \Delta = \int_0^{\infty} A_s(t)dt \frac{\phi_{(t\leftarrow s)}}{m_t} \sum_i E_i Y_i$$

D_s is expressed in Gray (Gy) and is equivalent to $J.kg^{-1}$.

The MIRD committee introduced the factor S to simplify the equation of the absorbed dose. The S factor gathers, independently of the time together, $\Phi_{t\leftarrow s}$ and Δ, such as:

$$S_{t\leftarrow s} = \Phi_{(t\leftarrow s)} \Delta = \frac{\phi_{(t\leftarrow s)}}{m_t} \sum_i E_i Y_i$$

The S factor shows the mean absorbed dose by a target organ, at a particular time post-injection, per unit of cumulated activity in the target organ. It is expressed in $Gy.MBq^{-1}.s^{-1}$.

Therefore, the absorbed dose equation is:

$$D_{(t)} = \tilde{A}_s \, S_{t\leftarrow s}$$

If the target area is irradiated by several source areas, the mean absorbed dose is:

$$D_{(t)} = \sum_X \tilde{A}_X \, S_{t \leftarrow X}$$

Thus, the cumulated activity emitted by the source considers the temporal aspects of the dose calculation (biological elimination of the vector and radioactive decay) and the S factor takes into account the physical aspect (geometry of the model, emitted particle by the radionuclide and energy deposit).

The S factor can be calculated with analytic methods and stochastic methods (Monte-Carlo and Point-Kernel) using standard or personalized models. These values are also available in tables for a large number of radionuclides and geometric combinations (from spheres to complex models).

2. Determination of the absorbed dose

Differently from EBRT, in RIT, the dose distribution is not homogenous in the organ, tissue, and even at the cell scale. Thus, studying the absorbed dose at a smaller scale (cell scale rather than whole body scale) allows a better correlation of the calculated absorbed dose with the biological effects.

a. At the whole body scale

The mean absorbed dose at the organ or tumour scale is the major parameter studied in the case of clinical RIT. First, anatomic images are obtained from magnetic resonance imaging (MRI) or CT images by manual or automatic segmentation. Then, anatomic images are combined with γ photon images obtained by SPECT or PET (for example Figure 39) to correlate the anatomical images and radiolabelled vector distribution in the body.

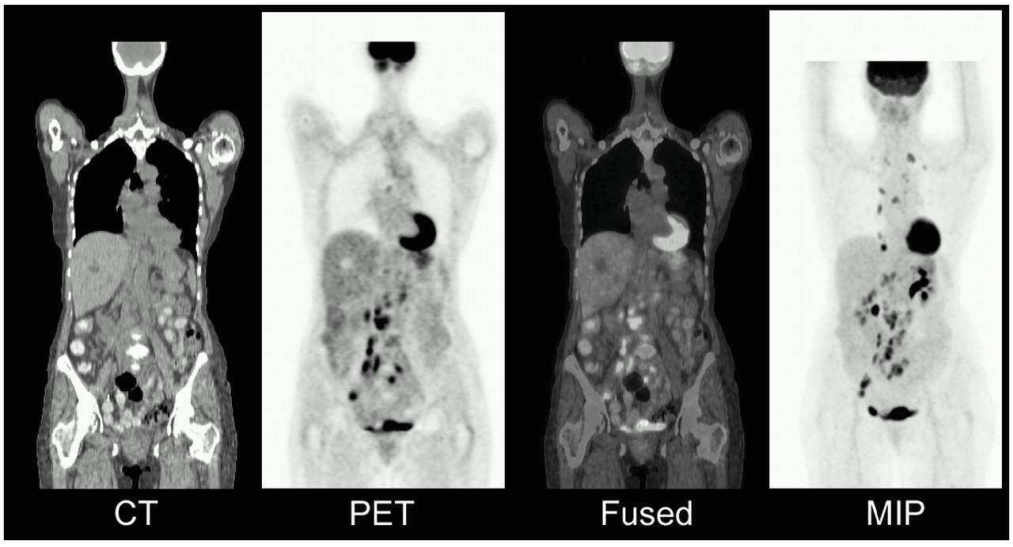

Figure 39: PET/CT images of a patient with DLBCL and invasion of multiple mediastinal and para-aortic lymph nodes [205]

Thus, using PET-CT or SPECT-CT images (or MRI), it is possible to determine the activity of the radiolabelled vector in an organ at the time of the acquisition. By doing several acquisitions at different times, the radiolabelled vector fixation kinetics in the different organs can be determined. Then, the cumulative activity ($\tilde{A}_s$) can be calculated by integral *calculus* of the activity curve as a function of time. The S factor can be determined from pre-existing tables or calculated by using the Monte-Carlo or Point-Kernel methods [206], by keeping in mind that the tumour can be both the source and the target because in α or β^- therapy the particle path is short.

This was the principle used for RIT with Bexxar® and also with Zevalin® before 2011.

b. At the organ scale

To obtain a more accurate and pertinent dosimetry (mainly for research), the activity distribution in the organ can be determined. Indeed, the radiolabelled vector fixation in the organ can be heterogeneous in function of (i) the organ vascularization that influences the radiolabelled vector diffusion in the different compartments of the organ; (ii) the diffusion potential of the radiolabelled vector in the organ, and (iii) the antigen density homogeneity on the cell surface, according to the cell localizations in the organ. This approach allows the determination of the radioactivity distribution and then the dose distribution, not only as an averaged absorbed dose for that organ but also as a precise distribution inside that organ.

To determine the radioactivity distribution into an organ, biopsies can be performed and analysed or the organ can be dissect (in the case of animal models). Autoradiography, with film or imagers, can be performed to quantify the activity inside groups of cells and even inside single cells (with high resolution techniques) (Figure 40).

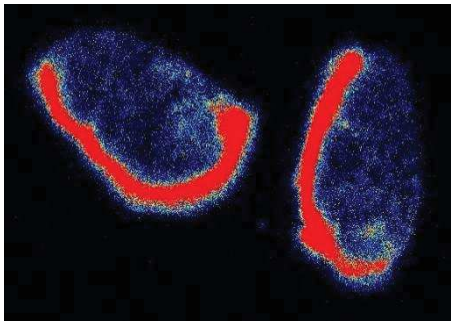

Figure 40: Example of digital autoradiography of tumours in a mouse xenografted with human NHL cells (Ramos) and treated with Betalutin®

c. At the cell scale

In research, studies are focused not only on tumour growth, but also on the individual cell response to understand the mechanisms involved in RIT effects. Here, dosimetry consists in calculating the cell absorbed dose after RIT of cultured cells.

As described previously, the formula to calculate the absorbed dose (D) is:

$$D_{(t)} = \tilde{A}_s \, S_{t \leftarrow s}$$

Indeed, the cell absorbed dose is described as the product of the total number of disintegrations hitting the cell (Ã), and the S factor defines the physical aspect (geometry of the model, emitted particles by the radionuclide and energy deposit).

Three irradiation sources are considered (Figure 41):

-Self-irradiation, due to irradiation by the radiolabelled mAb fixed to the receptor of the crossed cell.

-Cross-fire irradiation, due to irradiation by the radiolabelled mAb fixed to the receptor of a neighbouring cell;

-Volume irradiation, due to the presence of the radiolabelled mAb in the culture medium.

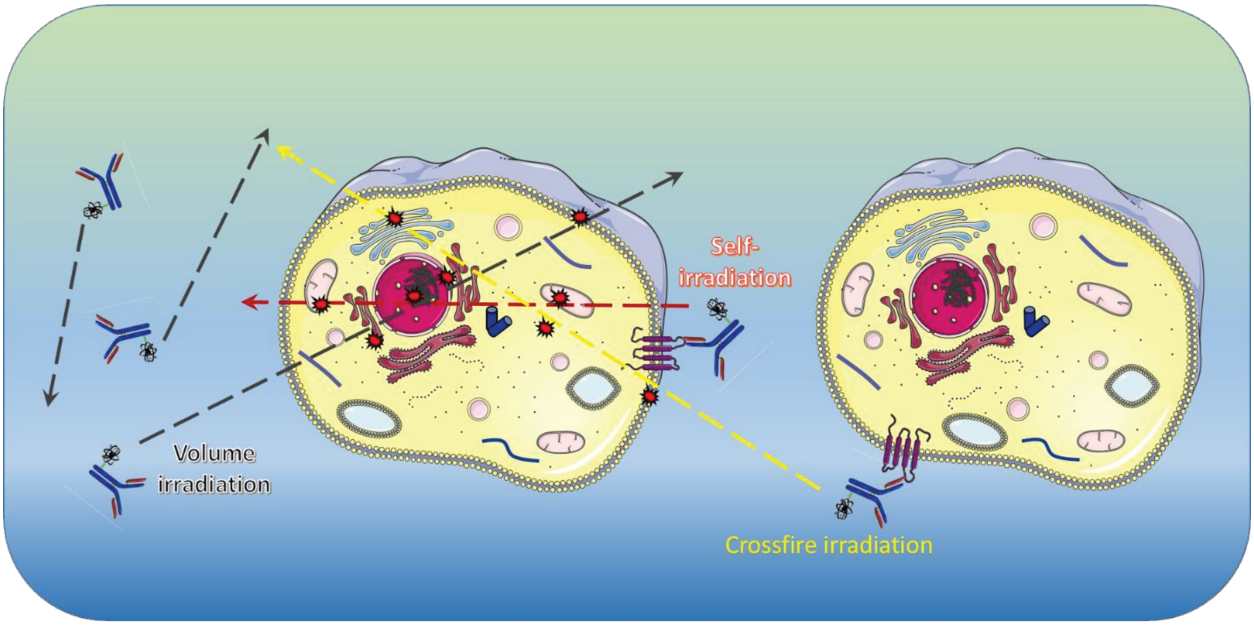

Figure 41: Schematic representation of the three sources of irradiation in RIT

To take into account these three types of irradiation during RIT, the equation for the cell absorbed dose is as follows:

$$D = D_{self} + D_{cross} + D_{volume}$$

$$D_{(c)} = \tilde{A}_c \, S_{c \leftarrow c} + \sum \tilde{A}_s \, S_{c \leftarrow s}(d_s) + \tilde{A}_m \, S_{c \leftarrow m}$$

where $\tilde{A}_c$ is the cumulated activities in the target cell, $\tilde{A}_s$ the cumulated activities in the neighbouring cell, and $\tilde{A}_m$ the cumulated activities in the medium. The three S factors are distinct.

3. Determination of the S factor

The S factor shows the energy depositions of the different radionuclide emissions for a particular geometry, independently of time. The MIRD committee listed the S factors for a high number of radionuclides and geometric combinations [207]. In the clinic, the mean absorbed dose at the organ scale is currently determined based on the S factor tables from the MIRD committee. However, the S factor can also be more precisely calculated using standard dosimetric models or personalized models.

a. Direct Monte-Carlo method

The direct calculation with the Monte-Carlo method allows simulating physical phenomena described by the laws of probability through the use of random numbers. The stochastic characters of the interaction between matter and radiations allow the application of these methods with high precision. The generation of pseudo-random numbers with these approaches allow sampling probability functions to simulate different phenomena (type of emitted particles, type of interaction, energy …). Several codes are used for dosimetric applications, such as MCNP, EGS, GEANT or PENELOPE [208].

Up to now, the major limitation of Monte Carlo calculations to estimate the absorbed doses was the calculation time required for the simulations. However, technological advances allowed reducing the calculation time, thus authorizing the use of the Monte Carlo codes in the clinical routine. However, other methods have been developed to estimate the energy deposits in matter. The Point-Kernel method is the most used approach for internal dosimetry in the clinic.

b. Indirect Point-Kernel method

The Point-Kernel method is based on the distribution of the absorbed dose around an isotropic isolated source in an endless homogenous medium. It defines the mean absorbed dose delivered at a radial distance given by emitted particles from the isotropic point source. For a heterogeneous distribution of the activity, the calculation of the absorbed dose distribution in the matter is based on the principle of superposition. Thus, if the energy transfer function is known from one point to another, any source volume can be considered as a juxtaposition of point sources. Then, the absorbed energy in a volume is the sum of the deposited energies for each of the point sources. The distribution of the absorbed dose is obtained by using the dose Point-Kernel convolution of the three-dimensional activity distribution. As this convolution is extremely time-consuming, Fourier transforms are often used to reduce the calculation time. However, this method is based on the hypothesis that the medium is homogenous; yet the human body is a

complex geometry with different densities (*e.g*., bone, lung and soft tissues) and this is an important limitation to the use of this method.

Both Monte-Carlo and point-Kernel methods can be employed either to calculate directly the distribution of the absorbed dose for a particular geometry and the given distribution of the cumulated activity, or to compute the S factors used in the MIRD formalism. [209], [210]

THESIS OBJECTIVES

The rise of immunotherapy, especially with the development of the anti-CD20 rituximab, significantly improved the efficacy of the NHL treatments. In clinic, rituximab is currently used in combination with chemotherapies to potentiate their effects and to consolidate responses to treatment. However, patients frequently become refractory to this therapy and the CD20 targeting becomes no longer efficient. In this context, a new antibody radiolabeled conjugate (ARC), namely Betalutin®, was developed by Nordic Nanovector to overcome rituximab resistance. Betalutin® is a new ARC composed of the anti-CD37 lilotomab monoclonal antibody (mAb) radiolabelled with ^{177}Lu.

The aim of my research work was to investigate in three human NHL preclinical models the therapeutic efficacy of the Betalutin® and to determine the molecular mechanisms underlying tumour cell response. Final aim of this work was to determine NHL that could most benefit from this treatment and also relevant combination partners. For this purpose, the biological effects of ^{177}Lu-lilotomab on NHL were compared with those of rituximab but also of lilotomab, of ^{177}Lu-rituximab or ^{177}Lu-cetuximab.

In the part I of my work, the therapeutic efficacy of ^{177}Lu-lilotomab was studied *in vitro* in three NHL cell lines (DOHH2 for transformed FL, Ramos for Burkitt lymphoma and Rec-1 cell line for Mantle lymphoma) exposed to both radiolabelled or unlabelled antibodies. Clonogenic survival together with proliferation were measured and a mathematical model was developed for investigating the relationship between the cytotoxic effects of radiation (^{177}Lu) and of antibody constituting radiolabelled mAbs.

Part II of my work relied on *in vivo* model consisting of mice bearing subcutaneous Ramos and DOHH2 tumour xenografts and treated with the latter antibodies. Therapeutic efficacy and haematological toxicity have been investigated and completed by a dosimetric approach based on conventional biodistribution studies or SPECT-CT analyses.

Part III consisted of investigating the molecular mechanisms involved in cell responses to radiation. Main attention was devoted to the mechanisms controlling apoptosis and cell cycle progression.

MATERIALS & METHODS

I. B-Cell lymphoma models, monoclonal antibodies and animal models

A. Cell lines

Ramos, DOHH2 and Rec-1 cell lines were obtained from ATCC (American type culture collection) and ECACC (European collection of authenticated cell cultures). They express CD20 and CD37 antigens and could then be targeted with rituximab and lilotomab, respectively. The cells were grown between 2-10 x10^5 cells/mL at 37°C in a humidified atmosphere of 95% air/5% CO_2 in RPMI supplemented with 10% heat-inactivated foetal bovine serum, 100 µg/ml of L-glutamine, and antibiotics (0.1 U/ml penicillin and 100 µg/ml streptomycin). They were routinely tested for mycoplasma contamination using the Mycotest assay (Life Technologies).

Ramos cell line was collected from a Burkitt's lymphoma of a 3-year-old boy. These cells are characterised by the expression of IgMλ and the presence of the t(8,14) translocation overexpressing c-Myc oncogene [211].

DOHH2 cell line was established from the pleural effusion of a 60-year-old man with refractory immunoblastic B cell lymphoma progressed from follicular centroblastic/centrocytic lymphoma (follicular lymphoma derived of GC). This cell line is characterised by the secretion of IgGλ and by the athypic presence of the t(8;14;18)(q24;q32;q21) translocation leading to a overexpression of c-Myc and also Bcl-2 [212], [213]. This anomaly induces that the DOHH2 cell line is a transformed FL (follicular lymphoma) progressing to transformed DLBCL (diffuse large B cell lymphoma).

Rec-1 cell line was established from the lymph node or peripheral blood from a 61-year-old man with terminal DLBCL progressing to transformed mantle lymphoma. This cell line is characterised by the presence of the t(11;14)(q13;q32) overexpressing the cyclin D1 (Rimokh 1994) [214].

B. Antibodies

Rituximab is a chimeric anti-CD20 IgG1 recognising the epitope $_{(170)}$ANPS$_{(173)}$ and $_{(182)}$YCYSI$_{(186)}$, with a nanomolar equilibrium dissociation constant. This mAb is developed by Roche (Basel, Switzerland) under the trademark name MabThera® in Europe.

The lilotomab is a murine anti-CD37 IgG1 mAb directed against the epitope $_{206}$HLARSRH$_{212}$ of the CD37 receptor, with a nanomolar equilibrium dissociation constant. This mAb is developed by Nordic Nanovector ASA (Oslo, Norway) and commercialised as Lutetium-177 [^{177}Lu]-lilotomab satetraxetan (Betalutin®, previously known as ^{177}Lu-DOTA-HH1).

The cetuximab (Erbitux®, Merck KGaA, Darmstadt, Germany) has been used as non-specific mAb. This mAb is directed again the epidermal growth factor receptor (EGFR) which is highly expressed in many cancers but not in the NHL cells. In this project, it was used radiolabelled with ^{177}Lu to investigate the radiation-induced effects of ^{177}Lu alone since it did not bind any of the three B- cell lymphoma models used.

C. Animal models

Athymic Nude-Foxn1 mice (6 weeks/old female) and C.B-17/IcrHanHsd-Prkdc-scid mice (6 weeks/old female) from Envigo (Gannat, France) were used. Mice acclimated for 1 week before experimental use. They were housed at 22°C and 55% humidity with a light-dark cycle of 12h. They were maintained under pathogen-free conditions and food and water were supplied *ad libitum*.

II. *In vitro* studies

A. Monoclonal antibody radiolabelling

MAbs (rituximab, lilotomab and the non-specific cetuximab) conjugated with p-SCN-benzyl-DOTA were obtained from Nordic Nanovector at a concentration of 10 mg/mL and were maintained at 4°C. $^{177}LuCl_3$ was obtained from Perkin Elmer at a volumic activity of 370 MBq in 8 µL of 0.05 M HCl and at specific activity > 740 GBq/mg. Radiochemical purity was >97% with radionuclidic purity > 99.94%. Arbitrarily, mAbs were labelled with ^{177}Lu at a specific activity of 200 MBq/mg. Typically, 10 µl of 10 mg/mL DOTA-mAb were mixed with 25 µl 0.25 M NH_4OAc (pH 5.5) and pre-heated for 5 min at 37°C. 1 µl of $^{177}LuCl_3$ was added to the reaction mixture (200 MBq/mg) and incubated further at 37°C for 45 min (Figure 42). Reaction was stopped by adding formulation buffer (100 µL) (PBS, 7.5% BSA, 1 mM DTPA, pH 7.5). Reaction mixture was purified with a PD-10 column (GE Healthcare UK Ltd., Buckinghamshire, England) with PBS as the eluate. Radiochemical purity was determined by applying 1 µl of the reaction onto thin layer chromatography (TLC) and separation was done in a migration vial containing 1 ml of PBS. The strip was cut in two and the activity of each part was measured in a gamma detector. The radiolabelling yield was obtained by dividing the value for the lower part by the total value. It was

generally above 99%. Yield was determined as the ratio between activity of ^{177}Lu added and activity of ^{177}Lu-mAbs collected. Immunoreactivity of ^{177}Lu-mAbs was determined using binding assay. Typically, 4 counting tubes containing at least 16 ×10^{6} Ramos cells in 200 µL PBS/BSA (0.5%) were used. Two tubes were treated with 20 µg of unlabelled mAbs. 15 min later, 10 ng of radiolabelled mAb were added into the 4 tubes and incubated 1h at room temperature. Radioactivity was measured with a gamma counter before and after washing (three times with PBS-BSA 0.5%). Immunoreactivity was defined as the ratio between bound/total of radioactivity (%).

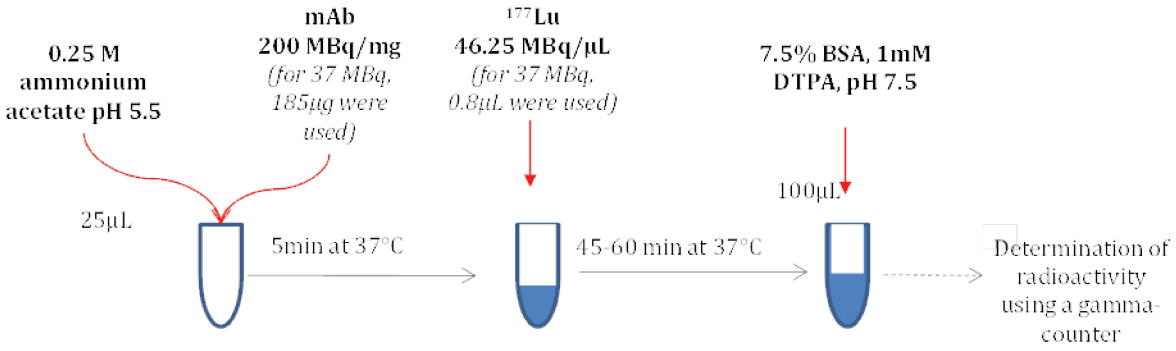

Figure 42: Schematic representation of the protocol used for mAb radiolabelling with ^{177}Lu

B. Determination of the number of CD20 and CD37 receptors at the surface of Ramos, DOHH2 and Rec-1 cells

The number of CD20 and CD37 receptors at the surface of Ramos, DOHH2 and Rec-1 cells was determined using Scatchard binding assay (Figure 43). Typically, 1 ×10^{6} Ramos, DOHH2 and Rec-1 cells grown in tubes containing 100 µL culture medium were incubated with increasing amount (0- 6.25 nM; average specific activity of 200 MBq/mg) of radiolabelled mAbs (lilotomab or rituximab) for 1h at room temperature. Radioactivity was next gamma-counted and the cells were washed twice with PBS in order to remove unbound radioactivity. Cells were next resuspended in 1mL of culture medium and an aliquot fraction was used for cells numbering and bound radioactivity was next determined. The ratio between bound and free radioactivity was determined. It was next expressed as a function of bound radioactivity.

Experimental conditions can be important source of errors and can modify results. As previously described, experimentations were done at room temperature. Indeed, at 37°C, internalisation can increase the final result of receptors per cell even if 1h is a relatively brief time. Experiment could be done at 4°C, however at this temperature, suspension cells showed a modified cell morphology being able to distort results (hunched cell). Thus, we chose room

temperature to this experimentation because the time of incubation is relatively short, the cell morphology is protected and internalisation is reduced compared to 37°C.

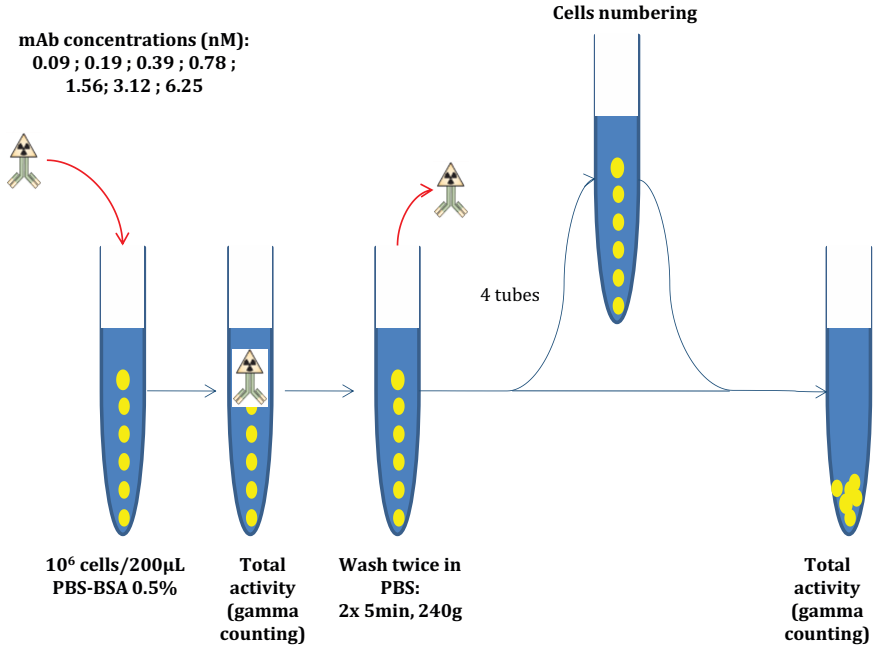

Figure 43: Schematic representation of the protocol used for Scatchard binding assay

The Scatchard method allows the calculation of the dissociation constant (Kd) and the total number of antigen. Indeed, a determined number of cells is placed in presence of increase concentration of radiolabelled mAb. For each concentration, the ratio bound/free activity is calculated. Finally, a Scatchard plot is traced, corresponding to bound activity as a function of the ratio bound/free activity. Knowing the number of cells in each well and the characteristics of the mAb radiolabelling (number of ^{177}Lu per mAb), the number of receptors per cell and the Kd could be calculated (Figure 44).

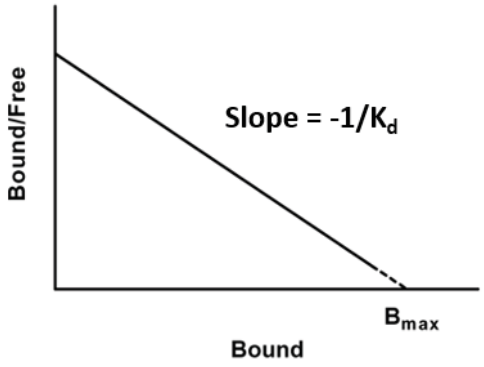

Figure 44: Schematic representation of Scatchard plot

C. Determination of the therapeutic efficacy of ^{177}Lu-mAbs on B-cell lymphomas

Therapeutic efficacy of ^{177}Lu-lilotomab, ^{177}Lu-rituximab and ^{177}Lu-cetuximab was investigated using clonogenic assay (Figure 45). Since cells were in suspension, we developed a protocol using MethoCult® medium (H4435, Stemcell technologies) a methylcellulose medium with recombinant cytokines and EPO for human cells. A concentration of 1 ×10^6 Ramos and DOHH2 cells/mL were grown in 12 micro-well plates containing 1mL of RPMI medium before being incubated with increasing activities (0; 0.5; 1; 2; 4 and 6 MBq/mL) of ^{177}Lu-labelled mAbs (lilotomab, rituximab or irrelevant cetuximab) for 18h at 37°C/ 5% CO_2 (Figure 45). Next, cells were collected and centrifuged and washed twice with medium before being resuspended in 5mL of RPMI medium and counted. From 1500 to 45000 cells were mixed with 4.5 mL of MethoCult® medium and seeded (1.5mL/dish). The number of seeded cells /dish range between 500 and 15 000, depending on the mAb and on the test activity. Petri dishes were next kept for 12 to 16 days for determining the number of colonies. Colonies containing 50 or more cells were scored and the surviving fraction was calculated. All the experiments were repeated at least three times in triplicate. Using this approach, the cytotoxicity of mAbs or radiolabelled mAbs that could kill cells within the first 18h was not taken into account.

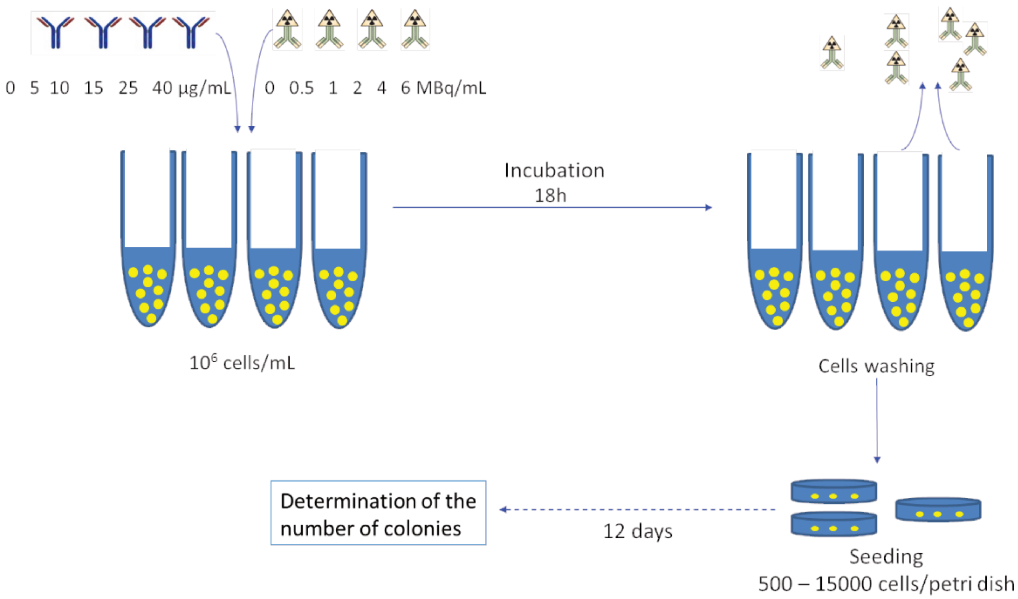

Figure 45: Schematic representation of the protocol used for clonogenic survival measurement

D. Molecular mechanisms involved in cell response after RIT (Figure 46)

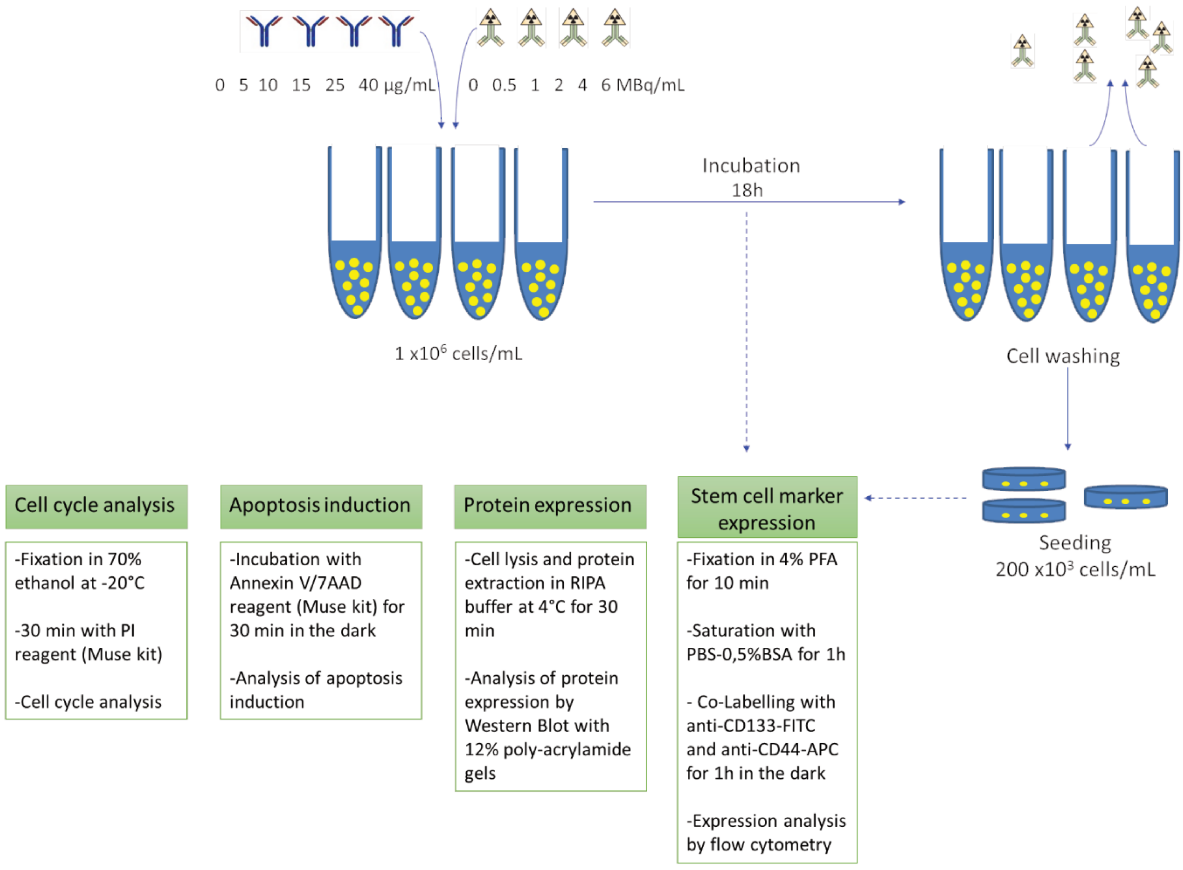

Figure 46: Schematic representation of mechanistic studies

1. Cell cycle analyse

Cell cycle arrest was assessed in 1 ×10⁶ Ramos, DOHH2 or Rec-1 cells/mL grown in 12-well plates and exposed for 18h to 0, 2 (data not shown) and 6 MBq/mL of ^{177}Lu-lilotomab, ^{177}Lu-rituximab and ^{177}Lu-cetuximab or with corresponding amounts of unlabelled mAbs (0, 15 and 40 µg/mL). Cells were harvested at day 0, 2h, 18h, 1d, 2d, 3d, of RIT then fixed in 70% ethanol at −20 °C for 3 hours and stained with Cell Cycle kit (with PI) reagent from Merck Millipore in the dark for 30 min at room temperature before analysis using an Muse® flow cytometer. The percentage of cells in G0/G1, S and G2/M phases was then calculated (mean of three experiments in triplicate).

2. Apoptosis induction

Apoptosis induction was assessed in 1 ×10⁶ Ramos, DOHH2 or Rec1 cells/mL grown in 12-well plates and exposed for 18h to 0, 2 (data not shown) and 6 MBq/mL of ^{177}Lu-lilotomab, ^{177}Lu-rituximab, ^{177}Lu-cetuximab or with corresponding amounts (0, 15 and 40 µg/mL) of unlabelled mAbs. Cells were harvested at 0, 2h, 18h, 1d, 2d, 3d of RIT. At each time point, apoptosis was

detected with cell cycle kit reagent from Merck Millipore (Annexin V Kit with 7-AAD) in the dark for 30 min at room temperature before analysis using Muse® flow cytometer.

3. Analysis of protein expressions by Western Blot

Protein expression was assessed in 1 ×10^6 Ramos, DOHH2 or Rec-1 cells/mL grown in 12-well plates and exposed for 18h to 0 and 6 MBq/mL of ^{177}Lu-lilotomab. Cells were harvested at 0, 2h, 18h, 1d, 2d and 3d of RIT. At each time point, cells were rinsed and incubated in RIPA buffer (Santa Cruz) at 4°C for 30 minutes. Cells were centrifuged and supernatant (containing proteins) were collected. Proteins were electrophoresed through SDS-PAGE using 12% poly-acrylamide gels and electrotransferred onto nitrocellulose membranes. Blots were incubated with anti-CDK1, anti-p-CDK1(Tyr15) (clone 10A11), anti-p-CDK1(Thr14), anti-p-CDK1(Thr161), anti-CDK7, anti-Wee-1 (clone D10D2), anti-Myt-1, anti-p-CHK1 (Ser345) and anti-human GAPDH (1/1000, Cell Signaling Technologies, Leiden, The Netherlands) primary antibodies. Blot were washed and incubated with horseradish peroxidase-conjugated anti-mouse lg (115-036-072, Jackson ImmunoResearch) or with horseradish peroxidase-conjugated anti-rabbit lg (7074, Cell Signaling). Signal detection of immunoblots was carried out using the enhanced chemiluminescence protocol according to the manufacturer's instructions (Clarity™ Western ECL blotting substrates, 1705061, BioRad). PXi analyser (Ozyme) was used to measure levels of protein expression.

4. Wee-1 and Myt-1 inhibitors

Cells were treated for 18h with 1 µM of the selective Wee-1 kinase inhibitor MK-1775 (Selleckchem, Houston, USA) or of the dual Wee-1/Myt-1 inhibitor PD-166285 (EMD Merck Millipore/Calbiochem, Molsheim, France) alone or in combination with 6 MBq/mL, 2 MBq/mL and 0.5 MB/mL of ^{177}Lu-lilotomab for Ramos, Rec-1 and DOHH2 cells respectively. At different times after start of incubation, proteins were extracted to measure the CDK1 phosphorylation levels, in parallel, proliferation was determined and at 18h and 24h after start of incubation, the percentage of cells in G2/M was assessed (experiments were performed three time except the cell cycle analysis).

5. Expression of stem cell markers: CD44 and CD133

Stem cell markers (CD133 and CD44) were assessed in 1 ×10^6 Ramos, DOHH2 or Rec-1 cells/mL grown in 12-well plates and exposed for 18h to 0 and 6 MBq/mL of ^{177}Lu-lilotomab, ^{177}Lu-rituximab or ^{177}Lu-cetuximab. Cells were harvested at 0, 2h, 18h and each day from 1d to 10d of RIT. At each time point, cells were fixed with PFA 4% for 10 minutes, washed twice with PBS and sterilely stored in PBS at 4°C. Stem cell markers were detected with anti-CD133-FITC (clone: AC133, Milteniy) and anti-CD44-APC (clone: IM7, Merck Millipore). 0.5 x10^6 cells were

saturated for 1h in PBS-BSA 0.5%. Next cells were centrifuged and incubated with anti-CD133-FITC (2µL) and anti-CD44-APC (0.125µg) for 1h at room temperature in the dark. Finally, cells were rinsed twice and analysed using Gallios® flow cytometer (Beckman Coulter).

E. Cellular Dosimetry

1. Cellular uptake of radioactivity and cells numbering

As a preliminary step towards cellular dosimetry, the uptake of radioactivity was determined in Ramos, DOHH2 and Rec-1 cells exposed for 18h either to ^{177}Lu-lilotomab, ^{177}Lu-rituximab or ^{177}Lu-cetuximab (Figure 47). Typically, 1 ×10^6 Ramos, DOHH2 and Rec-1 cells/mL of culture medium were incubated for 18h with increasing activities (0; 0.5; 1; 2; 4 and 6 MBq/mL) of ^{177}Lu-labelled mAbs. Then, cells were washed twice with culture medium and seeded in 12 micro-well plates containing 1 mL of culture medium at a concentration of 200 ×10^3 cells/mL. At various times, (2h, 18h, 24h, 48h, 72h and 144h), cells were collected, washed twice with PBS, resuspended in 1 ml of PBS and gamma counted (Hewlett Packard, Palo Alto, CA). An aliquot fraction (8 µL) was used for cells numbering using cell counter (Muse, Merck Millipore). The activity per cell (Bq/cell) was calculated and plotted as a graph expressing the uptake of radioactivity per cell (Bq/cell) as a function of time (hours). For all cell lines and each mAb, experiments were done in triplicates and repeated at least three times.

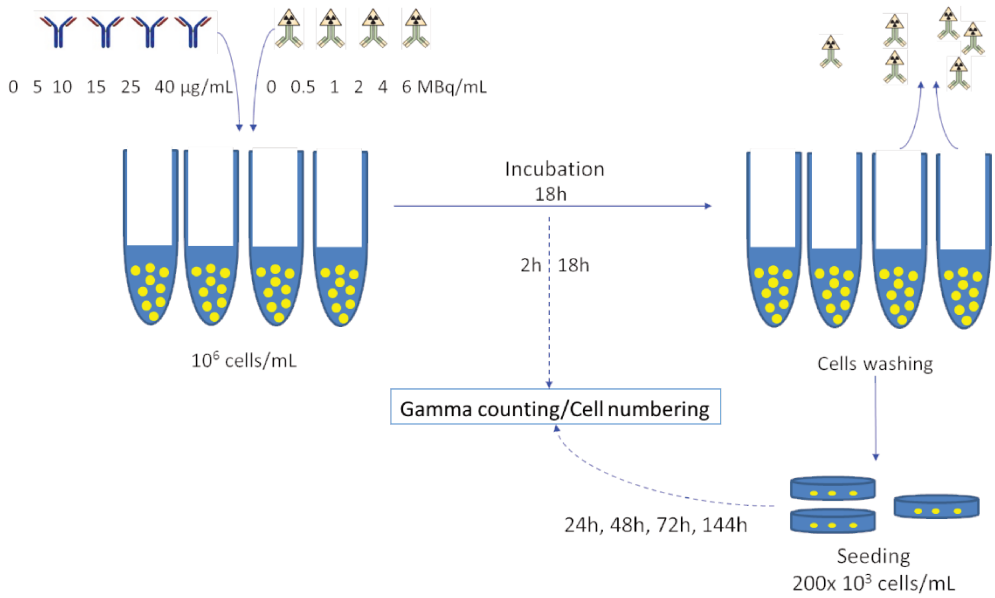

Figure 47: Schematic representation of the protocol used for determining the cellular uptake of radioactivity

2. Cell geometry and behaviour in flask culture

The cell and nucleus dimensions of Ramos cells were determined after propidium iodide staining and fluorescent microscopic analysis of Ramos cells. For both cell and nucleus, the area and the size corresponding to the largest and smallest diameters were determined. For DOHH2 and Rec-1 cells, the cell dimension were determined with Scepter™ 2.0 Cell Counter (Merck) and the nucleus dimensions were determined after Dapi staining and fluorescent microscopic analysis.

During incubation with the radiopharmaceuticals the cells showed the tendency to accumulate at the centre of the culture, and to form clusters of different sizes. Since the density of cells (isolated), and clusters was very heterogeneous within the culture well, a preliminary determination of these parameters was performed on the basis of pictures acquired by optical microscopy. Four sets of pictures were acquired, corresponding to Ramos and DOHH2 cells treated with ^{177}Lu-rituximab and ^{177}Lu-lilotomab. Three regions were identified in the culture well: centre, halfway and edge. For each region, and for each of the four cell/antibody combinations, two pictures were taken at x50 and x200 magnifications, in order to measure the cell density in each area.

III. *In vivo* studies

Figure 48 shows a schematic representation of *in vivo* experiments.

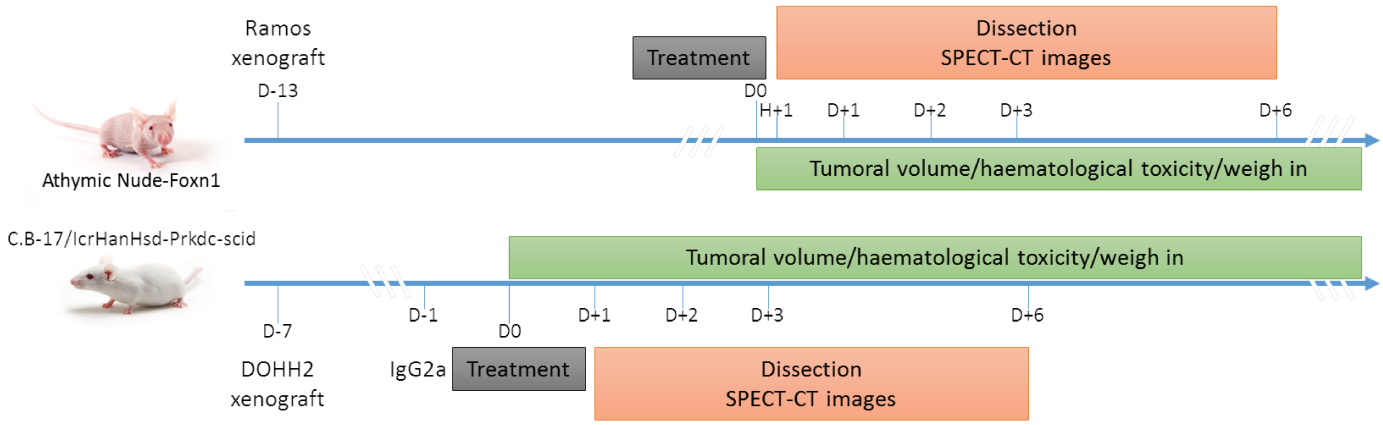

Figure 48: Schematic representation of in vivo experiments

A. Determination of maximal tolerated activity (MTA)

a. In athymic nude mice

Mice were intravenously injected with 100 µL of ^{177}Lu-lilotomab, ^{177}Lu-rituximab or ^{177}Lu-cetuximab in NaCl. Three different activities were assessed: 400, 500 or 600 MBq/kg (n=4 for each

test activity and for each mAb) and additionally 300 and 350 MBq/kg for ^{177}Lu-rituximab. Then mice were weighed every three days to evaluate the potential toxicity of the treatment (end points were weight loss higher than 20% or any signs of sickness or discomfort).

b. In Scid mice

One day before treatment with ^{177}Lu-mAbs, mice were intraperitoneally injected with 10 mg/kg of murine unspecific IgG2a (M7769, Sigma-Aldrich, Saint-Louis USA). Then, mice were intravenously injected with 100 µL of ^{177}Lu-lilotomab, ^{177}Lu-rituximab or ^{177}Lu-cetuximab in NaCl. Three different activities were assessed, 75, 125 or 150 MBq/kg (n=4 for each test activity and for each monoclonal antibody). Finally, mice were weighed every three days to evaluate the potential toxicity of the treatment (end points were weight loss higher than 20% or any signs of sickness or discomfort) (Figure 49).

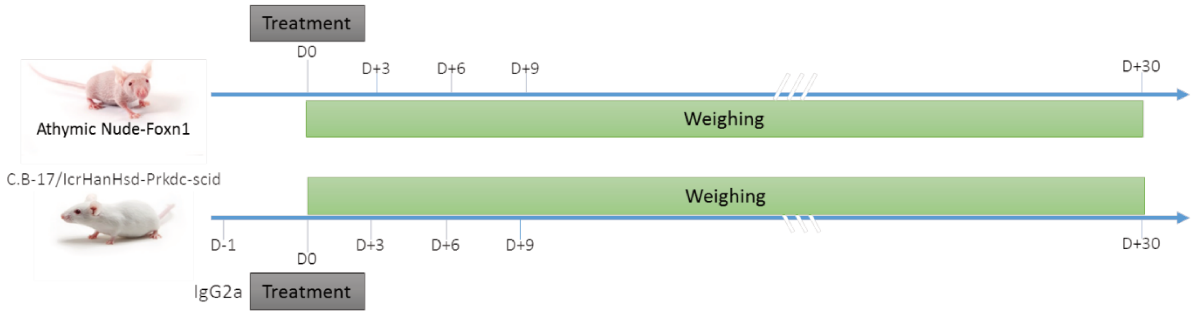

Figure 49: Schematic representation of MTA studies

B. Survival experiments

a. In athymic nude mice

Mice were subcutaneously xenografted with 10 x10^6 Ramos NHL cells resuspended in 100 µL of fresh serum-free medium in the right flank. Mice were treated 13 days post xenograft when tumour volume reaches 100-200 mm^3. In control groups, mice (n=8/treatment group) were intravenously injected with 100 µL of NaCl, lilotomab or rituximab mAb at the same quantity used during the RIT and at high concentration (10 mg/kg). For RIT experiments, mice (n=6-9/treatment group) were intravenously injected (100µL) with MTA of either ^{177}Lu-lilotomab, ^{177}Lu-rituximab or ^{177}Lu-cetuximab mAb. Tumour growth was evaluated by measuring the tumour volume with a calliper (a, b, c were the three diameters) and animal weight was determined two or three times per week.

The tumour volume was calculated using the following equation:

$$Tumour\ volume = \frac{(a \times b \times c)}{2}$$

Mice were sacrificed using CO_2 asphyxiation or cervical dislocation, when the tumour volume reaches 2000 mm^3 or when the weight loss was higher than 20% or signs of sickness or discomfort (Figure 50).

b. *In Scid mice*

Mice were subcutaneously xenografted with 10 x10^6 DOHH2 NHL cells in 100 µL of fresh serum-free medium in the right flank. One day before treatment (D+6 post-xenograft), mice were intraperitoneally injected with 10 mg/kg of unspecific IgG2a (M7769, Sigma-Aldrich, Saint-Louis USA). Mice were treated 7 days post xenograft (n=7/treatment group), in control groups, mice were intravenously injected with 100 µL of NaCl, lilotomab or rituximab mAb at the same quantity used in the RIT experiment and at high concentration (10 mg/kg). For RIT experiments, mice were intravenously injected (100µL) with MTA of ^{177}Lu-lilotomab, ^{177}Lu-rituximab or ^{177}Lu-cetuximab. Tumour growth was assessed by measuring the tumour volume using a calliper (a, b, c were the three diameters) and animal weight was determined two or three times a week. The tumour volume was calculated using the previous equation. Mice were sacrificed using CO_2 asphyxiation, when the tumour volume reached 2000 mm^3 or when the weight loss was higher than 20% or signs of sickness or discomfort (Figure 50).

c. *Haematological toxicity*

Blood samples (about 12 µL) were collected from tail vein twice a week the first month post-treatment. They were analysed using the Scil Vet abc system (SCIL Animal Care Co., Altorf) to determine haematological toxicity (Figure 50).

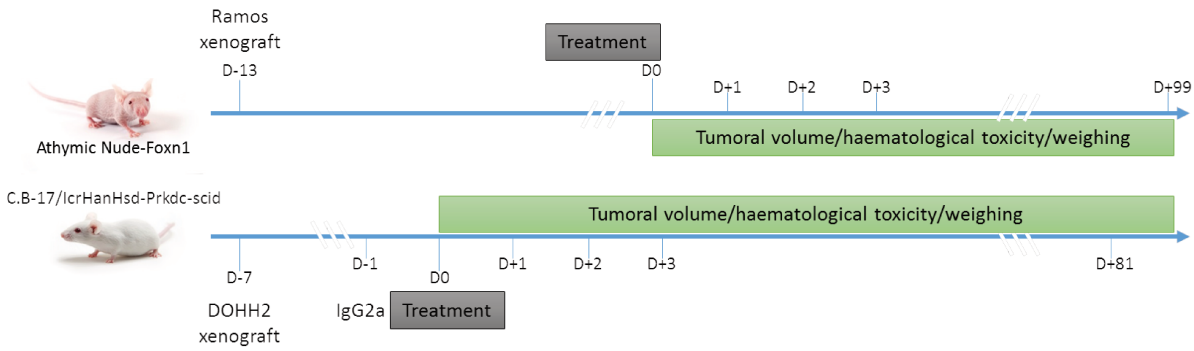

Figure 50: Schematic representation of survival studies

C. *In vivo* dosimetry

1. Biodistribution experiments

a) In athymic nude mice

Mice were subcutaneously xenografted with 10 million of Ramos cells as in therapeutic experiment. 13 days later, mice were intravenously injected with therapeutic experiment used in survival experiment. Two protocols were then performed (Figure 51).

-First protocol: 25 mice were treated with ^{177}Lu-lilotomab. At each time point post-treatment (1h, 1d, 2d, 3d and 6d), SPECT-CT images were performed on five mice and these mice were necropsied. Each organs were collected, weighed and their uptake of radioactivity were measured through γ-counting. This protocol allows the comparison between the *ex vivo* counting and the *in vivo* image-based biodistributions.

-Second protocol: mice were intravenously injected with ^{177}Lu-rituximab or ^{177}Lu-cetuximab (5 mice per treatment). At different times post-treatment (1h, 1d, 2d, 3d and 6d), each mouse were SPECT-CT imaged and at the last time point, mouse were necropsied. This protocol was to perform an *in vivo* Biodistribution (to reduce necropsied mice number).

a. In Scid mice

75 mice were subcutaneously xenografted with 10 million of DOHH2 cells. 6 days later, mice were intraperitoneally injected with 10 mg/kg of IgG2a (M7769, Sigma-Aldrich, Saint-Louis USA). Next day, mice were intravenously injected with the therapeutic activities used in survival experiment of ^{177}Lu-lilotomab, ^{177}Lu-rituximab or ^{177}Lu-cetuximab (25 mice per radiolabelled mAb). Then, at different times post-treatment (1d, 2d, 3d and 6d), mice were sacrificed by lethal injection (2.5 mL/kg) of ketamine (26 mg/mL)/medetomidine (0.30 mg/mL) (n=5 mice/time of dissection). Finally, each organs were collected, weighed and their uptake of radioactivity were measured.

For each organ, percentage of injected activity per gram of tissue as a function of time were plotted (corrected decays).

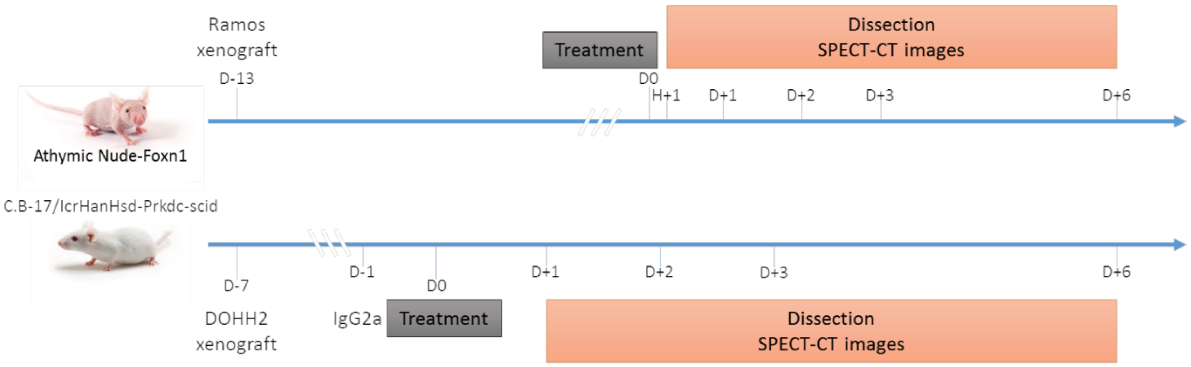

Figure 51: Schematic representation of biodistribution studies

2. S-factor determination

S-factors $S_{(t \leftarrow s)}$ correspond to the average absorbed dose in a target region t per radioactive disintegration in a source region s. S-factor takes into account contributions of all types of emitted particles by the source and composition of the matter. S-values used in this project were obtained by Monte-Carlo simulations in the MOBY voxelised phantom with ^{177}Lu [215].

IV. Statistical analysis

The statistical analysis was performed by the Department of statistics of ICM Val d'Aurelle, Montpellier. Data were described using median, mean and standard deviation. A linear mixed-regression model was used to determine the relationship between tumour growth and number of days after graft in *in vivo* experiments. Survival rates were estimated from the xenograft date to the date of the event of interest (i.e., a tumour volume of 2000 mm^3) using the Kaplan–Meier method. The log-rank test was used to compare survival curves between groups. *In vitro* data (cell cycle and inhibitor effects) were compared with the non-parametric Kruskal-Wallis test. The significance level was set at $p < 0.05$. Statistical analyses were performed using the Stata software v13.0 (Stata Corporation College Station, USA).

RESULTS & DISCUSSION

I. *In vitro* studies of the therapeutic efficacy

The first part of my PhD project consisted of investigating *in vitro* in B-cell lymphoma models the therapeutic efficacy of ^{177}Lu-lilotomab and to compare it with that of rituximab using clonogenic assay and dosimetry approaches (for radiolabelled mAbs). Additional experiments also investigated the cytotoxic effects of ^{177}Lu-rituximab and of the non-specific ^{177}Lu-cetuximab and unlabelled mAbs.

A. Therapeutic efficacy on B-cells lymphoma

The clonogenic survival of B-cells lymphoma exposed to unlabelled or radiolabelled mAbs was determined. In radiobiology, clonogenic test is the reference method for determining cell survival. The test investigates the ability for a cell to form a colony several days (10-12) after radiation exposure. It is related to the target theory that considers that cancer stem cells have to be hit to prevent colony growth, namely tumour growth.

The therapeutic efficacy of the unlabelled or radiolabelled mAbs was determined by clonogenic survival. However, clonogenic assay could not be performed on Rec-1 cell line because they did not form colonies. Thus, for this cell line the therapeutic efficacy was determined by proliferation assay.

1. Clonogenic survival of unlabelled rituximab and lilotomab

a. Ramos cell line

Figure 52 shows the clonogenic survival of Ramos cells exposed for 18h to 0 to 40 µg/mL of lilotomab or rituximab.

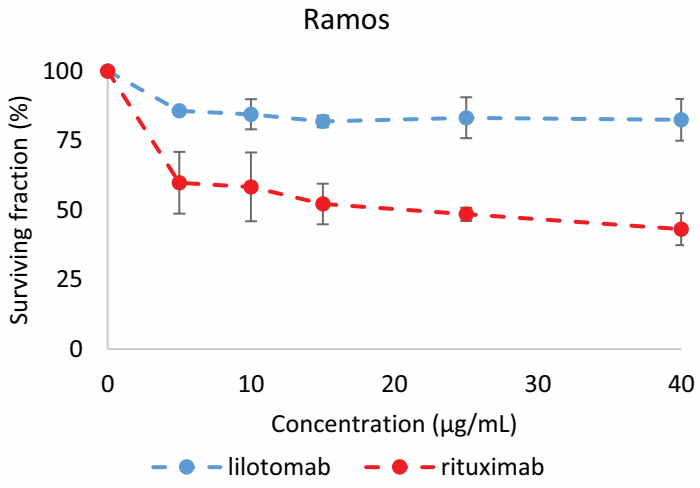

Figure 52: Clonogenic survival of Ramos cells exposed to 0- 40 µg/mL of lilotomab or of rituximab for 18h

A mild cytotoxicity was associated with unlabelled lilotomab. A plateau was observed at 15% cytotoxicity for concentration as low as 5 µg/mL. Compared with control, this decrease was statistically significant for all the test concentrations ($p < 0.001$). Conversely, a strong cytotoxicity was observed after treatment with rituximab. The minimum surviving fraction (43 ± 6%) was shown after treatment with 40 µg/mL rituximab. Compared with control, the decrease was statistically significant for all the test concentrations ($p < 0.001$).

b. DOHH2 cell line

Figure 53 shows the clonogenic survival of DOHH2 cells exposed for 18h to 0 to 40 µg/mL of lilotomab or rituximab.

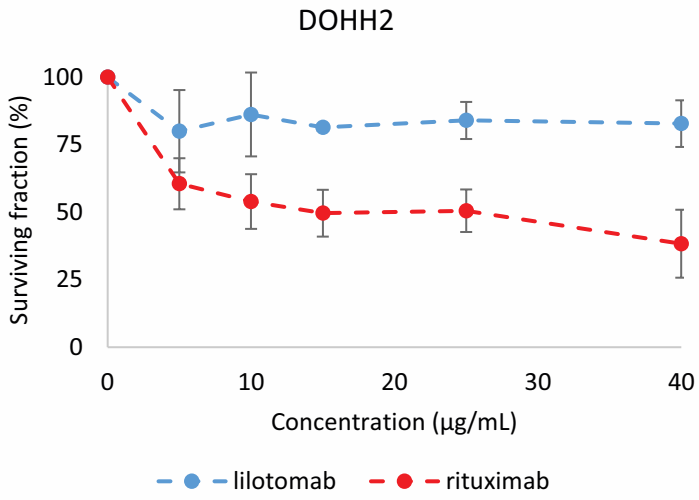

Figure 53: Clonogenic survival of DOHH2 cells exposed to 0- 40 µg/mL of lilotomab or of rituximab for 18h

Again, a mild cytotoxicity of unlabelled lilotomab was observed and a plateau was observed around 15% cytotoxicity. Compared with control, the decrease in survival was statistically significant ($p < 0.05\%$) for all the tested concentrations ($p = 0.0058$). Conversely, a strong cytotoxicity was observed after exposure to rituximab. The minimum surviving fraction (38 ± 12%) was measured at 40 µg/mL. Compared with control, the decrease was statistically significant for all the test concentrations ($p = 0.0058$).

To conclude, both cell lines show similar surviving fractions after treatment with lilotomab or rituximab respectively, and the rituximab was more efficient in cell killing than lilotomab.

2. Clonogenic survival of ^{177}Lu-mAbs as a function of test activities

The cytotoxic effects of rituximab and lilotomab were next assessed after radiolabelling with ^{177}Lu.

a. Ramos cell line

Figure 54 shows the clonogenic survival of Ramos cells after treatment for 18h with 0 to 6 MBq/mL of ^{177}Lu-lilotomab, ^{177}Lu-rituximab or ^{177}Lu-cetuximab.

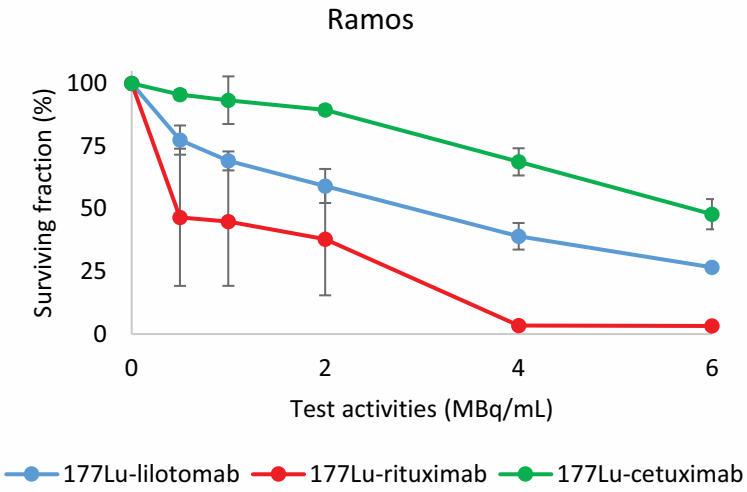

Figure 54: Clonogenic survival of Ramos cells exposed to 0- 6 MBq/mL of ^{177}Lu-lilotomab, ^{177}Lu-rituximab or ^{177}Lu-cetuximab for 18h

When Ramos cells were incubated with 0 to 2 MBq/mL of ^{177}Lu-cetuximab, only a slight decrease in clonogenic survival was observed (>89% of surviving fraction). However, at 4 and 6 MBq/mL, decrease in clonogenic survival was more pronounced with values about 68 ± 5% and 48 ± 6%, respectively. The latter decrease was statistically significant ($p < 0.001$) and could be explained, because ^{177}Lu-cetuximab does not bond Ramos cells but the irradiation produced by radioactivity contained in cell culture medium can irradiate cells (non-specific irradiation, responsible for the so-called volume dose).

Clonogenic survival of Ramos cells incubated with increasing activities of ^{177}Lu-lilotomab was shown to decrease down to 27 ± 1% after exposure for 18h to 6 MBq/mL. This decrease was activity-dependent and was statistically significant for all test activities ($p < 0.001$) when compared with control.

^{177}Lu-rituximab was very efficient in killing Ramos cells since clonogenic survival dropped to 3 ± 0.4% at 6 MBq/mL. Compared with control, decrease in survival of treated cells was statistically significant for activity as low as 0.5 MBq/mL ($p < 0.001$).

In Ramos cells, decreases in survival were always more pronounced after treatment with radiolabelled specific mAbs than with ^{177}Lu-cetuximab, and the ^{177}Lu-rituximab was more efficient in cell killing than ^{177}Lu-lilotomab.

b. DOHH2 cell line

Figure 55 shows clonogenic survival of DOHH2 cells after treatment for 18h with 0 to 6 MBq/mL of ^{177}Lu-lilotomab, ^{177}Lu-rituximab or ^{177}Lu-cetuximab.

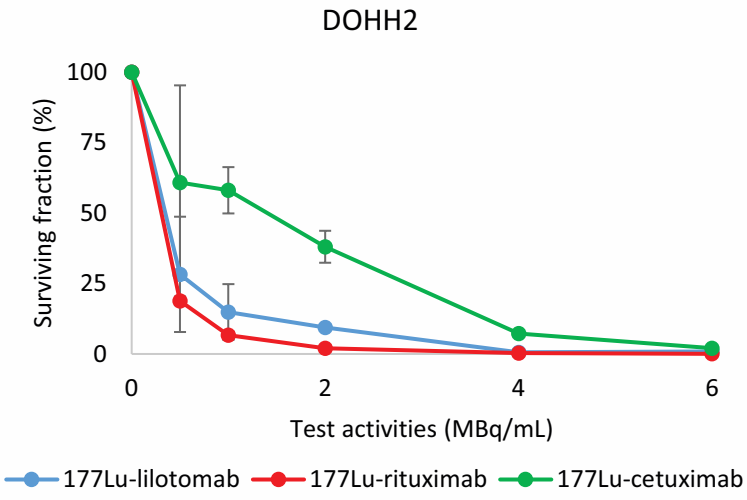

Figure 55: Clonogenic survival of DOHH2 cells exposed to 0- 6 MBq/mL of ^{177}Lu-lilotomab, ^{177}Lu-rituximab or ^{177}Lu-cetuximab for 18h

When DOHH2 cells were incubated for 18h with 0 to 6 MBq/mL of ^{177}Lu-cetuximab, a statistically significant decrease in clonogenic survival was observed ($p= 0.0021$). Survival was then 2 ± 0.3% at 6 MBq/mL. These data highlight the high non-specific cytotoxic effect of ^{177}Lu in this cell line mainly due to volume dose (non-specific irradiation).

Clonogenic survival of DOHH2 cells incubated with increasing activities of ^{177}Lu-lilotomab was shown to decrease down to 0.6 ± 0.3% after exposure to 6 MBq/mL. Compared with control, clonogenic survival was significantly decreased for activity as low as 0.5 MBq/mL ($p< 0.001$).

^{177}Lu-rituximab, was very efficient in DOHH2 cells killing and clonogenic survival was 0.05 ± 0.002% at 6 MBq/mL. Decrease was statistically significant for all the test activities ($p< 0.001$).

In DOHH2 cells, the observed decreases were always more pronounced after treatment with radiolabelled specific mAbs than after treatment with ^{177}Lu-cetuximab. ^{177}Lu-rituximab and ^{177}Lu-lilotomab showed similar cytotoxicity at the highest test activities (<1%).

3. Cells proliferation for Ramos, DOHH2, Rec-1 cells

Typically, therapeutic efficacy is determined through the clonogenic survival assay. However, given that Rec-1 cell line did not form any colony, the proliferation of Rec-1 cell line was thus determined after treatment with ^{177}Lu-mAbs. Nevertheless, the tendency of the Rec-1 response was analysed rather than the exact values by themselves because for the two other cell lines, the clonogenic survival was the reference method.

Figure 56 shows proliferation of Ramos, DOHH2, and Rec-1 cells exposed for 18h to 6 MBq/mL ^{177}Lu-lilotomab, ^{177}Lu-rituximab and ^{177}Lu-cetuximab.

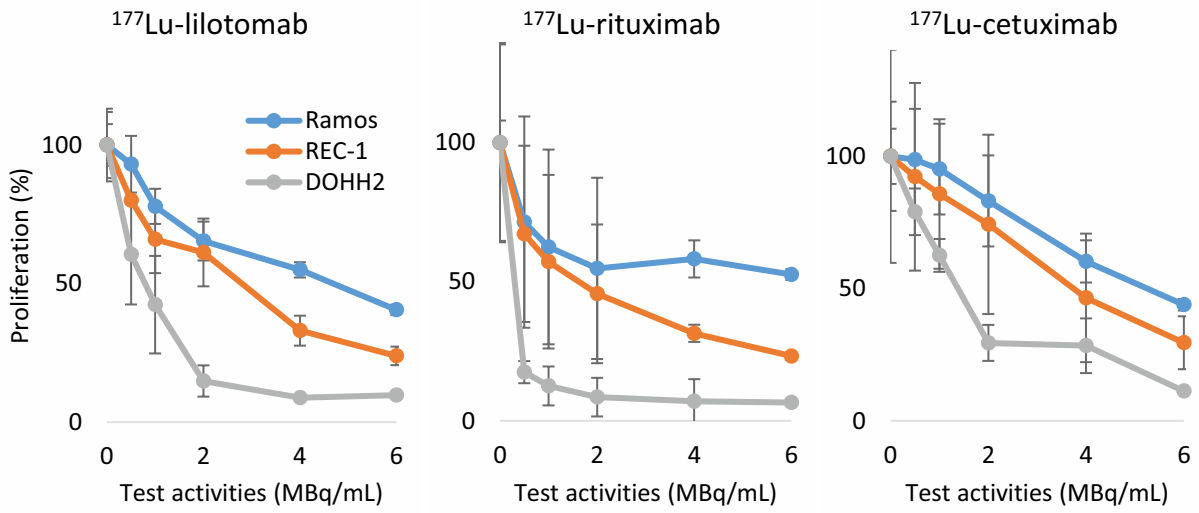

Figure 56: Proliferation of Ramos, DOHH2, and Rec-1 cells exposed for 18h to ^{177}Lu-lilotomab, ^{177}Lu-rituximab or ^{177}Lu-cetuximab

When the Rec-1 cell line was incubated for 18h with 6 MBq/mL ^{177}Lu-lilotomab, ^{177}Lu-rituximab and ^{177}Lu-cetuximab, the proliferation decrease was always between Ramos decrease and DOHH2 decrease.

Furthermore, Ramos cell line was always the cell line with the highest proliferation rate after treatments whereas DOHH2 was always the cell line with the lowest proliferation rate.

4. Key points

The therapeutic efficacy of mAbs and of ^{177}Lu-mAbs was assessed in Ramos, DOHH2 and Rec-1 cell lines.

- Response to lilotomab and rituximab was similar for Ramos and DOHH2 cells. Surviving fraction was then about 80% after treatment with lilotomab and 45% after treatment with rituximab.

- ^{177}Lu-cetuximab cytotoxicity was mediated by non-specific binding to cells but also by non-specific irradiation due to radioactivity present in culture medium. Its cytotoxicity was higher in DOHH2 cell line than in Ramos cell line, thus indicating DOHH2 were the most radiosensitive cells. This observation was confirmed using a proliferation assay and the radiosensibility of the Rec-1 cell line was shown as intermediary.

- In Ramos cell line, ^{177}Lu-rituximab was more efficient in cell killing than ^{177}Lu-lilotomab.

- In DOHH2 cell line, ^{177}Lu-lilotomab and ^{177}Lu-rituximab displayed the same therapeutic efficacy.

- Clonogenic survival results were confirmed with the proliferation results.

B. Cellular dosimetry for dose-effect relationship establishment

The paradigm of external beam radiotherapy (EBRT) is that radiobiological effects including DNA damage and cell death are proportional to cell absorbed dose. In this respect, nucleus has been for long defined as the main subcellular target and the mean nucleus absorbed dose as the reference parameter. This is part of the so called “target theory”, that considers that cells have to be hit by ionising particles to be killed. The probability for cells to die was then described using Poisson law that describes the number of hits per cell (dose), further improved by the Linear quadratic model (LQ) taking into account also cellular radiosensitivity parameters (a and b).

Therefore, a similar school of thought applied to RIT requires to determine first the mean nucleus absorbed using cellular MIRD formalism. Mean nucleus absorbed dose can then be used as a reference parameter responsible for cell death whatever the antibody, the cell, the isotope. Lack of dose-effect relationship was for example described during non-targeted effects as bystander effects. The existence of a dose-effect relationship indicates that by controlling the dose, it is possible to predict final cellular outcome of therapy.

Different numbers of receptors (CD20 and CD37) are expressed on the cell surface and these numbers are different for each cell line; the cell lines also show different kinetics of internalisation between both receptors. Moreover, the affinities of rituximab and lilotomab for their targets are different. All these parameters impact the conclusions of the clonogenic survival study. To rationally compare the clonogenic survival of cells upon treatment by the different ^{177}Lu-mAbs, it is thus necessary to calculate a common referential taking into account all these parameters: dosimetry. Without dosimetry, the comparisons between the cell lines or between

the mAbs are not possible (i.e., the number of CD20 on Ramos cell line can be ten times higher than the number of CD37 or the number of CD20 on the Ramos cell surface can be ten times higher than on the DOHH2 cell surface).

During radionuclide therapy, dosimetry is calculated according to the MIRD formalism that requires to determine two parameters: Ãrs, the total cumulative uptake of radioactivity by the cells, and *S*-factor.

The cellular MIRD formalism defines the dose (D) delivered to the target (t) by the radioactive source (s) using the following product:

$$D_{(t)} = \widetilde{Ar}_s \, S_{t \leftarrow s}$$

In my project, Ãrs was the total number of ^{177}Lu-mAbs decays (Bq.s) occurring in cell cytoplasm, at the cell surface or in extra-cellular medium. S-factor was a calculated value corresponding to the energy deposited in the nucleus at each decay. S (Gy/Bq.s) depended on variables such as cell and nucleus geometry, or nature and energy of particles emitted by ^{177}Lu.

1. Determination of Ãrs

Ãrs includes variables such as the number of receptors, the pharmacodynamic of antibody-receptor complexes, cells geometry, cells distribution within the flask culture, localisation of radioactivity and nature of the radiation. It was determined as described in Materials and Methods by measuring total radioactivity of cells exposed to ^{177}Lu-mAbs. Typically, cells were collected, centrifuged and washed to remove unbound radioactivity and radioactivity measured using a gamma counter divided by the number of cells contained in the pellets. The following results show both cells numbering and final determination of radioactivity uptake.

The uptake of radioactivity was determined over 144h in Ramos, DOHH2 or Rec-1 cells exposed for 18h to activities between 0 and 6 MBq/mL of either ^{177}Lu-lilotomab, ^{177}Lu-rituximab or irrelevant ^{177}Lu-cetuximab. At each time point the number of cells was determined and uptake of radioactivity per cell (Bq/cell) was calculated.

a. Ramos cell line

Figure 57A, 58A and 59A show that the number of untreated cells exponentially increased as a function of time.

Figure 57 shows that the number of Ramos cells exposed to the non-targeting ^{177}Lu-cetuximab was decreasing with time (2, 4 and 6 MBq/mL; $p < 0.001$). However, the uptake of radioactivity was below 0.02 Bq/cell for the highest test activity.

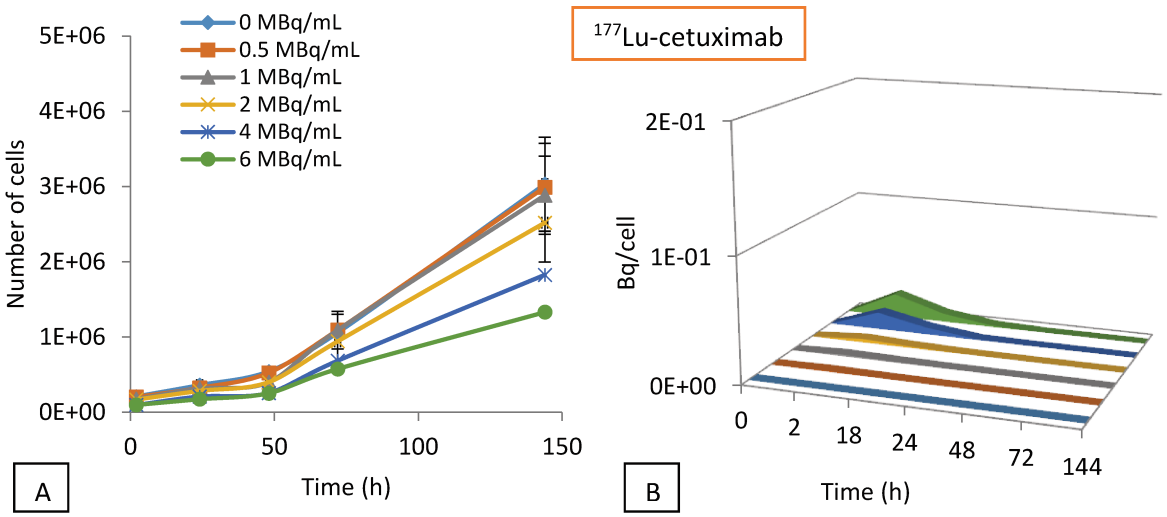

Figure 57: A) Number of cells per well after exposure for 18h of ^{177}Lu-cetuximab (0 to 6 MBq/mL). B) Uptake of radioactivity by Ramos cell exposed for 18h to ^{177}Lu-cetuximab

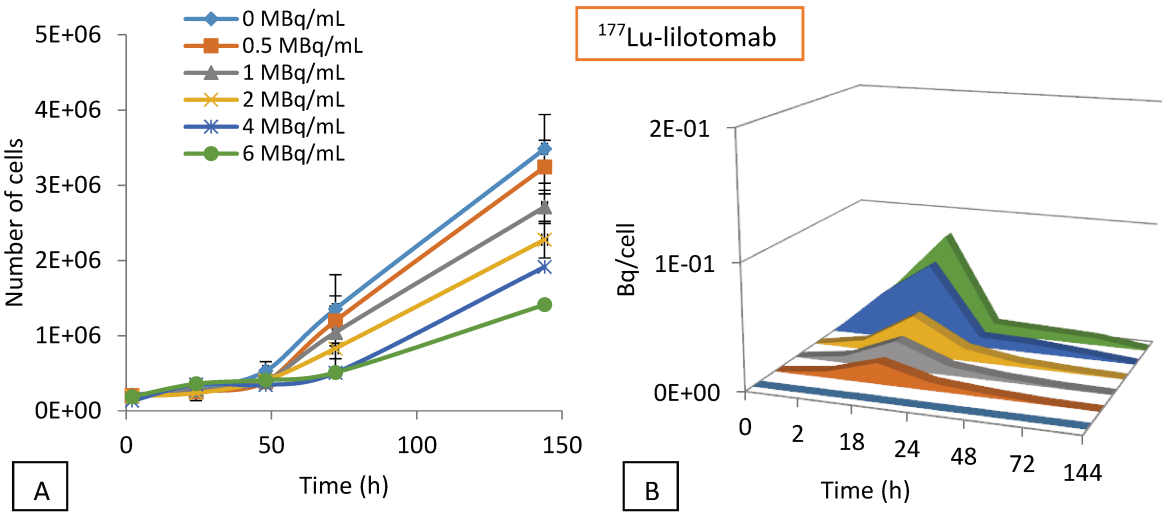

Figure 58: A) Number of cells per well after exposure for 18h of ^{177}Lu-lilotomab (0 to 6 MBq/mL). B) Uptake of radioactivity by Ramos cell exposed for 18h to ^{177}Lu-lilotomab

The same trend in proliferation assay was observed after exposure to ^{177}Lu-lilotomab (from 1 MBq/mL; $p < 0.001$) and ^{177}Lu-rituximab ($p < 0.001$) (Figures 58A and 59A).

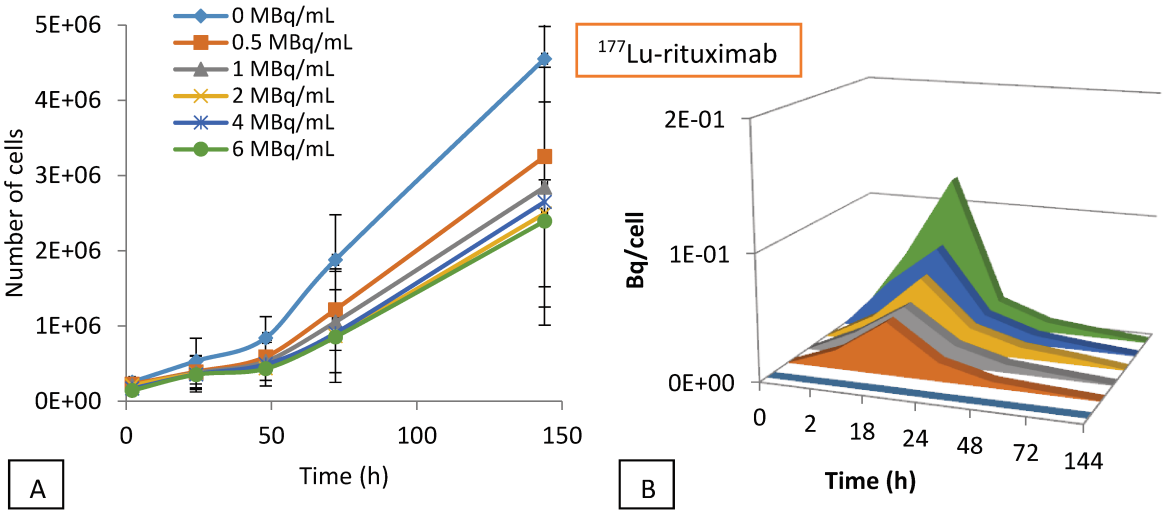

Figure 59: A) Number of cells per well after exposure for 18h of ^{177}Lu-rituximab (0 to 6 MBq/mL). B) Uptake of radioactivity by Ramos cell exposed for 18h to ^{177}Lu-rituximab

For ^{177}Lu-lilotomab and ^{177}Lu-rituximab, the highest uptake of radioactivity was observed 18h following onset of the treatment while nonspecific uptake of ^{177}Lu-cetuximab was maximal at 2h (Figures 57B, 58B and 59B). For the three ^{177}Lu-mAbs, the uptake of radioactivity was test activity-dependant. Maximal uptake of ^{177}Lu-lilotomab and ^{177}Lu-rituximab reached 0.08 and 0.12 Bq/cell, respectively.

By measuring the area under the curves of Figures 57B, 58B and 59B, the total cumulative decays occurring in cells (Ãrs) could be determined (Figure 60).

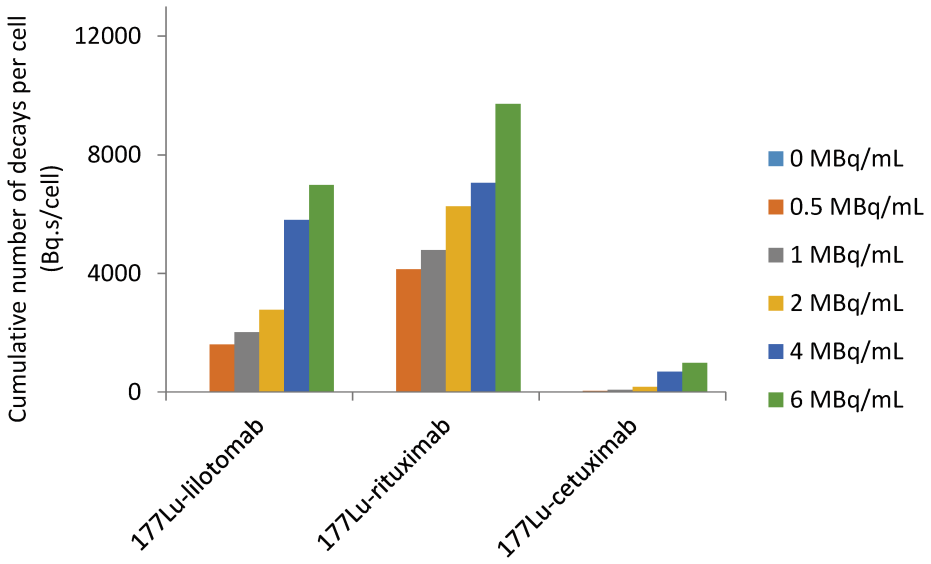

Figure 60: Cumulative number of decays per Ramos cell

The cumulated activity was test activity-dependant for the three ^{177}Lu-mAbs. The highest cumulated activity was measured after treatment with ^{177}Lu-rituximab (9712 Bq.s/cell at 6 MBq/mL); an intermediate value was obtained by exposure to ^{177}Lu-lilotomab (6980 Bq.s/cell at 6 MBq/mL) and the smallest was observed for the non-targeting ^{177}Lu-cetuximab (983 Bq.s/cell at 6 MBq/mL).

b. DOHH2 cell line

Figures 61, 62 and 63 shows the number of DOHH2 cells after exposure for 18h of ^{177}Lu-mAbs (0 to 6 MBq/mL) and the uptake of radioactivity per cell.

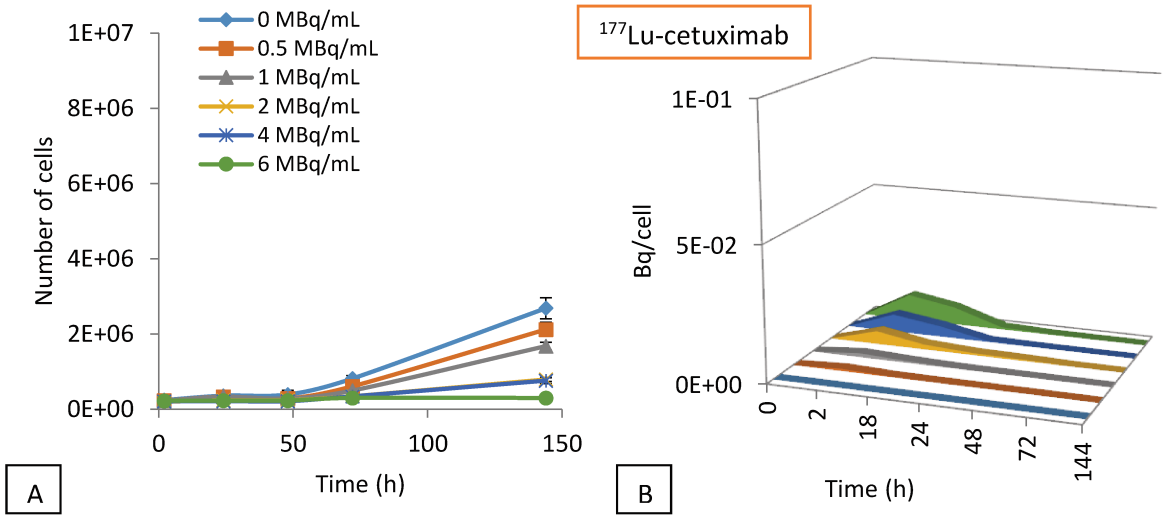

Figure 61: A) Number of cells per well after exposure for 18h of ^{177}Lu-cetuximab (0 to 6 MBq/mL). B) Uptake of radioactivity by DOHH2 cell exposed for 18h to ^{177}Lu-cetuximab

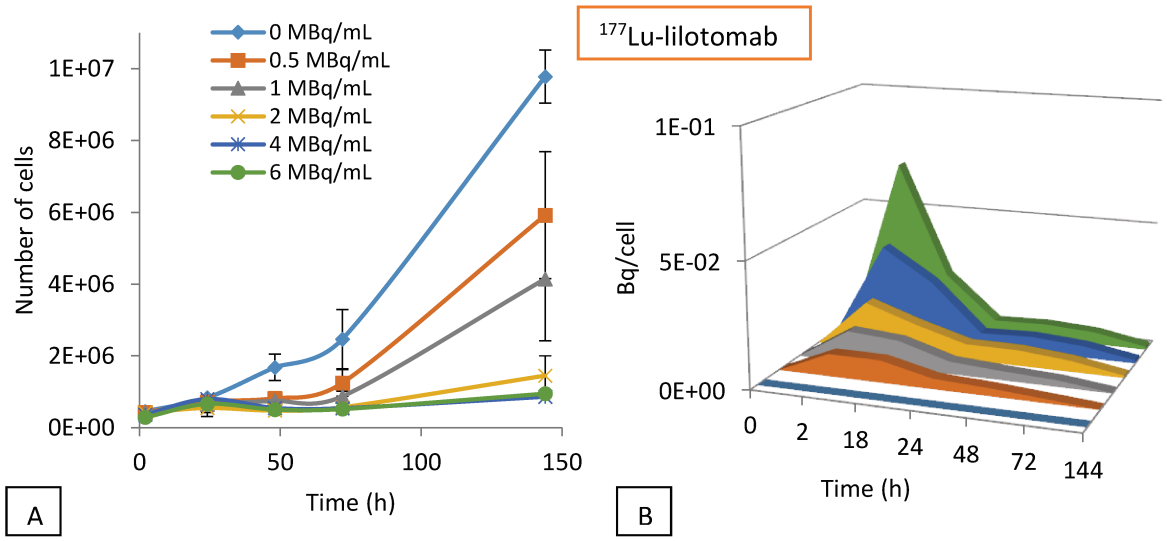

Figure 62: A) Number of cells per well after exposure for 18h of ^{177}Lu-lilotomab (0 to 6 MBq/mL). B) Uptake of radioactivity by DOHH2 cell exposed for 18h to ^{177}Lu-lilotomab

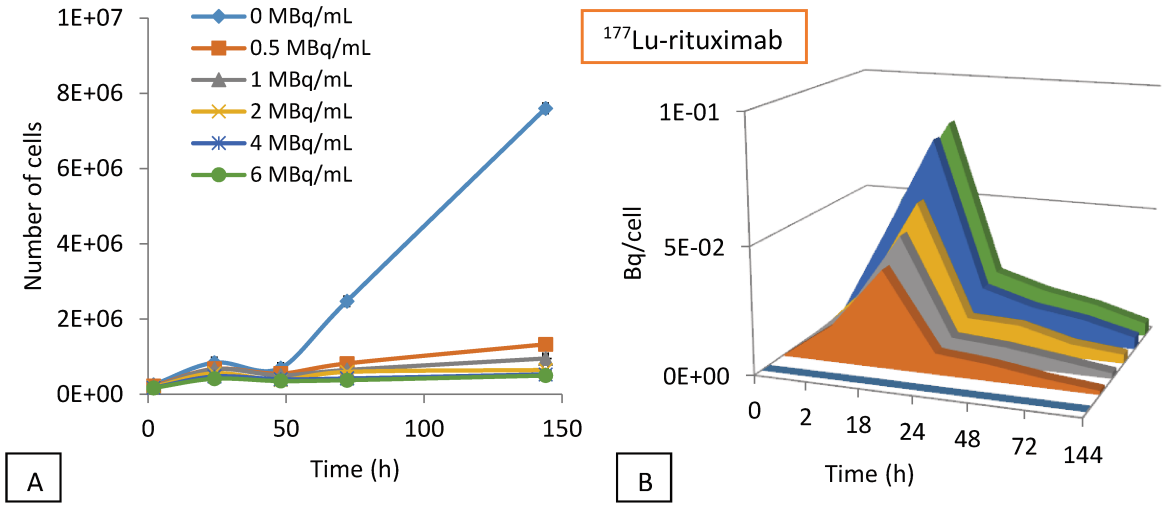

Figure 63: A) Number of cells per well after exposure for 18h of ^{177}Lu-rituximab (0 to 6 MBq/mL). B) Uptake of radioactivity by DOHH2 cell exposed for 18h to ^{177}Lu-rituximab

Figures 61A, 62A and 63A show that the number of untreated DOHH2 cells exponentially increases.

Figure 61 shows that after treatment with ^{177}Lu-cetuximab, cells showed a statistically significant decrease in the proliferation at 1, 2, 4 and 6 MBq/mL ($p < 0.001$). However, the uptake of radioactivity was below 0.01 Bq/cell for the highest test activity.

The same trend in proliferation was observed after exposure to ^{177}Lu-lilotomab (from 2 MBq/mL; $p < 0.001$) or to ^{177}Lu-rituximab ($p < 0.001$) (Figures 62A and 63A) (even if all the test activities were statistically significant ($p < 0.001$)).

For ^{177}Lu-lilotomab and ^{177}Lu-rituximab, the highest uptake of radioactivity was observed 2h and 18h following onset of the treatment respectively. For the three ^{177}Lu-mAbs, the uptake of radioactivity was test activity-dependant. Maximal uptake of ^{177}Lu-lilotomab and ^{177}Lu-rituximab reached 0.07 and 0.08 Bq/cell, respectively.

By measuring the area under the curves in Figures 61B, 62B and 63B, the total cumulative decays occurring in cells (Ãrs) could be determined (Figure 64).

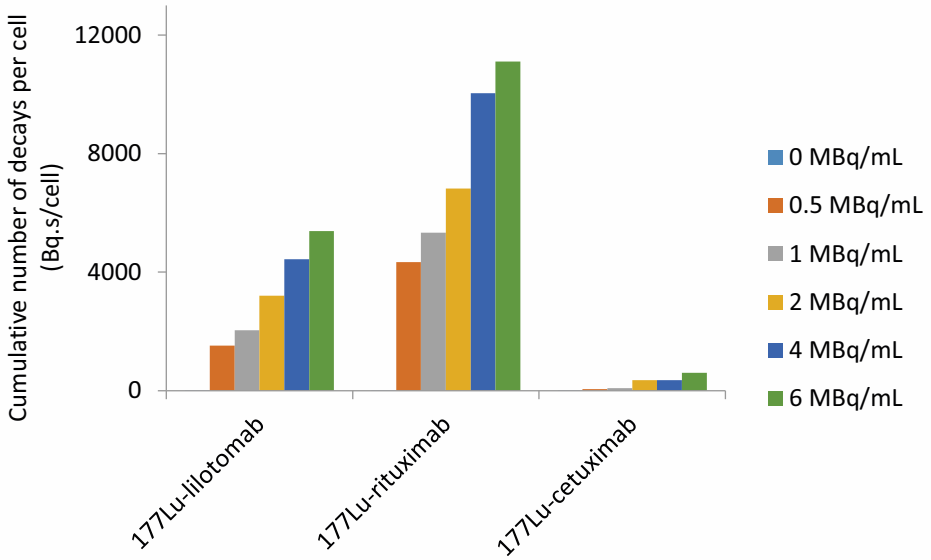

Figure 64: Cumulative number of decays per DOHH2 cell

Figure 64 shows the total number of decays per DOHH2 cell as a function of the test activity for each ^{177}Lu-mAb. The cumulated activity was test activity-dependant for the three ^{177}Lu-mAbs. The highest cumulated activity was obtained after treatment with ^{177}Lu-rituximab (11104 Bq.s/cell at 6 MBq/mL) and the smallest one after treatment with ^{177}Lu-cetuximab (601 Bq.s/cell at the highest activity).

c. Rec-1 cell line

Figure 65, 66 and 67 shows the number of Rec-1 cells after exposure for 18h to ^{177}Lu-mAbs (0 to 6 MBq/mL) and the uptake of radioactivity per cell.

Figure 65 shows that the number of Rec-1 cells exposed to the non-targeting ^{177}Lu-cetuximab was decreasing with time (at least $p < 0.01$). However, the uptake of radioactivity was below 0.01 Bq/cell for the highest test activity.

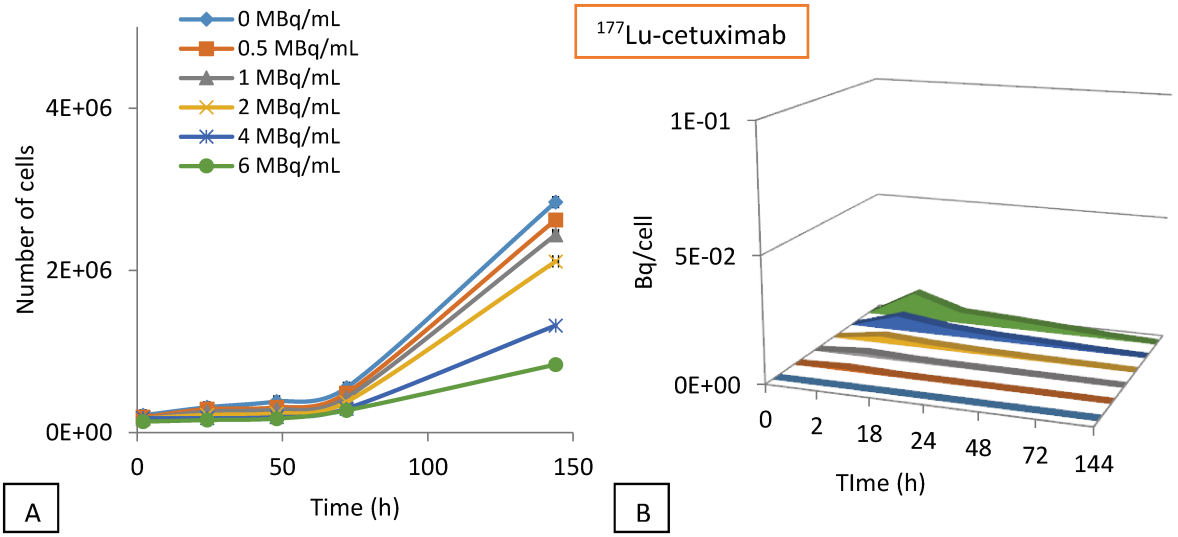

Figure 65: A) Number of cells per well after exposure for 18h of ^{177}Lu-cetuximab (0 to 6 MBq/mL). B) Uptake of radioactivity by Rec-1 cell exposed for 18h to ^{177}Lu-cetuximab

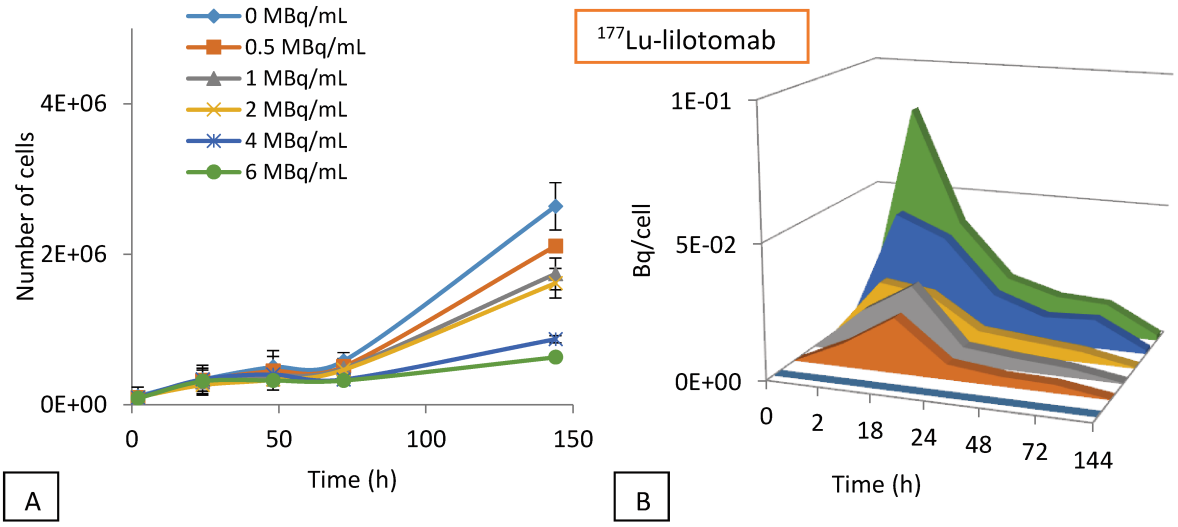

Figure 66: A) Number of cells per well after exposure for 18h of ^{177}Lu-lilotomab (0 to 6 MBq/mL). B) Uptake of radioactivity by Rec-1 cell exposed for 18h to ^{177}Lu-lilotomab

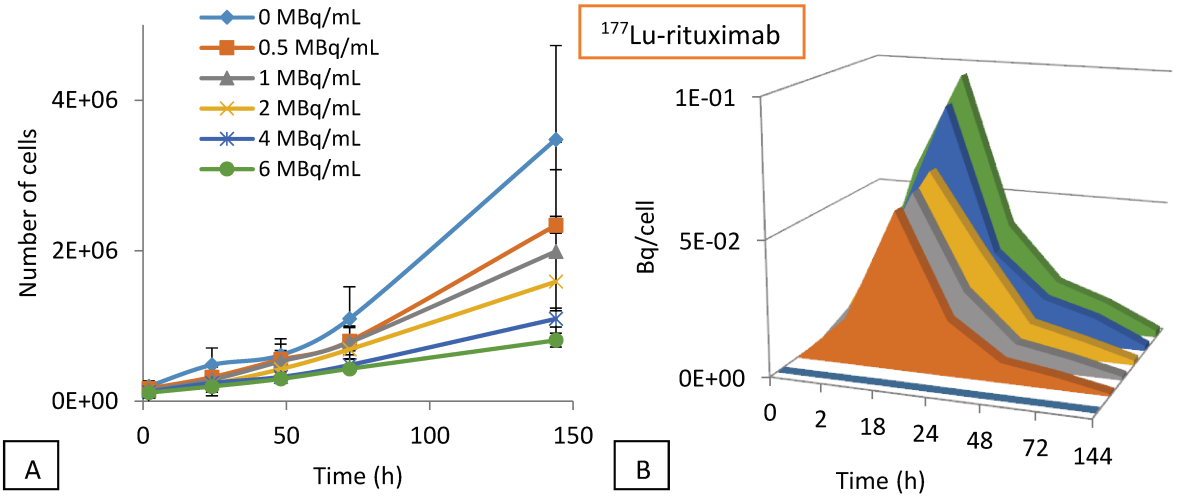

Figure 67: A) Number of cells per well after exposure for 18h of ^{177}Lu-rituximab (0 to 6 MBq/mL). B) Uptake of radioactivity by Rec-1 cell exposed for 18h to ^{177}Lu-rituximab

The same trend in proliferation was observed after exposure to ^{177}Lu-lilotomab ($p < 0.005$) and ^{177}Lu-rituximab ($p < 0.02$) (Figures 66 and 67).

For ^{177}Lu-lilotomab and ^{177}Lu-rituximab, the highest uptake of radioactivity was observed 2h and 18h respectively, following onset of the treatment. For the three ^{177}Lu-mAbs, the uptake of radioactivity was test activity-dependant. Maximal uptake of ^{177}Lu-lilotomab and ^{177}Lu-rituximab reached 0.08 and 0.10 Bq/cell, respectively.

By measuring the area under the curves of Figures 65B, 66B and 67B, the total cumulative decays occurring in cells (Ãrs) could be determined (Figure 68).

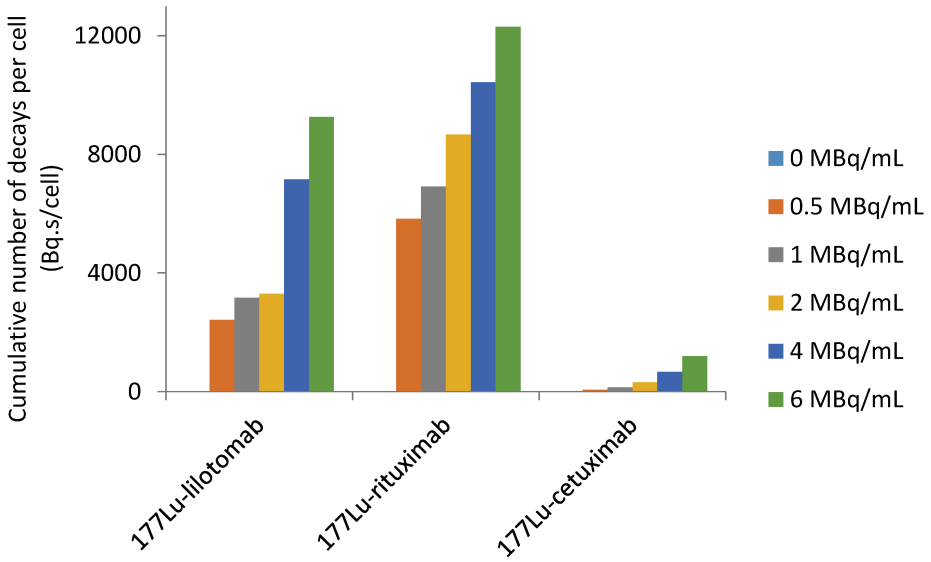

Figure 68: Cumulative number of decays per Rec-1 cell

Figure 68 shows the total number of decays per Rec-1 cell as a function of the test activity for each ^{177}Lu-mAb. The cumulated activity is test activity-dependant for the three ^{177}Lu-mAbs

The highest cumulated activity was observed after treatment with 6 MBq/mL ^{177}Lu-rituximab (12 307 Bq.s/cell) and the smallest one after treatment with ^{177}Lu-cetuximab (1 202 Bq.s/cell).

d. Key points

- In the three cell lines, the cumulated activity per cell was higher after treatment with ^{177}Lu-rituximab than after treatment with ^{177}Lu-lilotomab.

-The proliferation of DOHH2 cells upon treatment was always weaker than that of Ramos cells treated in the same conditions and Rec-1 proliferation was intermediate.

-Treatment with ^{177}Lu-cetuximab induced low cumulated activity thus confirming the non-specificity of this mAb for the NHL cell lines.

2. Determining the number of CD37 and CD20 on Ramos, Rec-1 and DOHH2 cells

Since uptake of radioactivity is tightly dependent on the number of receptors, I investigated whether the number of receptors per cell corroborated above results.

Scatchard method allowed to determine the dissociation constant (Kd) and the total number of antigen per cell (B_{max}) (see Figure 44 p101).

Table 9 shows Kd of lilotomab and rituximab for each cell line. Kd was around 1.5 nM for the lilotomab-CD37 targeting while it was around 4 nM for the rituximab-CD20 targeting.

Table 9: Kd of lilotomab and rituximab in Ramos and DOHH2 cells

	Lilotomab			Rituximab		
	Kd (x10^{-9} M)			Kd (x10^{-9} M)		
	Ramos	DOHH2	Rec-1	Ramos	DOHH2	Rec-1
Mean	1.6	1.0	1.4	4.7	4.6	1.5
Std dev	1.0	0.4		4.1	2.6	

In Figure 69 are reported the number of CD37 and CD20 receptors on the surface of either Ramos, DOHH2 or Rec-1 cells. The expression level of CD37 was about 120 ×10^3 receptors/cell for the three cell lines while the expression of CD20 was more variable: 305 ×10^3 CD20/Ramos cell, 466 ×10^3 CD20/DOHH2 cell and 563 ×10^3 CD20/Rec-1 cell. Thus, the number of CD20 receptor was 2.4 to 4.7 times higher than the number of CD37 receptors.

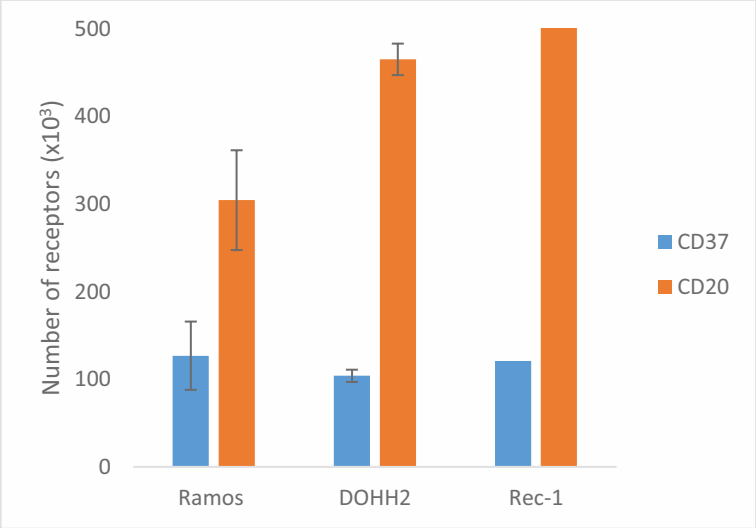

Figure 69: Number of CD37 and CD20 per cell line

3. Determination of *S*-factors

a. Cell geometry and cell distribution in culture flasks

This part of the work was performed in collaboration with Dr Sara Marcatili from INSERM Team 15 (Dr M. Bardiès) of CRCT (Centre de Recherche en Cancérologie de Toulouse).

The three cell lines showed the tendency to accumulate at the centre of the culture, and to form clusters of different sizes (Figure 70). Their spatial distribution was not isotropic in the 3D dimensions but organised in few layers. The average absorbed dose to the cell, strictly depends on the geometrical configuration of the cell culture. Since the density of cells (isolated), and clusters was very heterogeneous within the culture well, a preliminary determination of these parameters was performed on the basis of pictures acquired by optical microscopy.

During incubation time ($t < 18$ h), three concentric regions were identified in the cylindrical culture well of radius rw = 3.4 cm: centre (a cylindrical region of radius rc), halfway (a cylindrical shell with rc<r<rh) and edge (a cylindrical shell with rh<r<rw) (Figure 70). For each region and for both specific antibodies (^{177}Lu-lilotomab and ^{177}Lu-rituximab), two planar pictures were taken at ×50 and ×200 magnifications (Figure 71), in order to measure cell density in each area. In each region, the following parameters were extracted: the density of isolated cells (cell cm^{-2}); cluster density (clusters cm^{-2}); the average cluster radius in µm and its relative standard deviation. Culture thicknesses of one, two and three cell diameters were assumed for the edge, halfway-through and central regions respectively. The extracted parameters were used to estimate the total number of cells in each region. The size of the central region (rc) was determined by directly segmenting the cell macro-aggregate (visible to the naked eye) which lay approximately at the centre of the culture well. The outer radius of the halfway region (rh) was

tuned in order to obtain an overall number of cells in the culture of the order of the nominal value (4×10^6 cells).

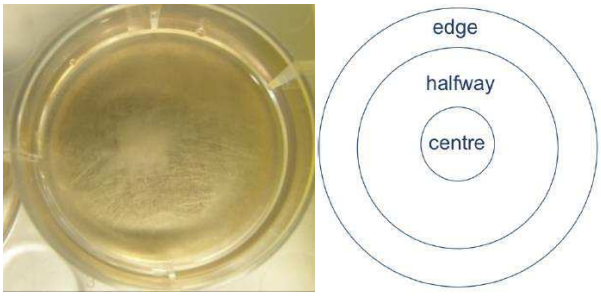

Figure 70: Picture of the culture well for Ramos cell treated with ^{177}Lu-lilotomab and the schematic representation of the three zones identified in the culture well.

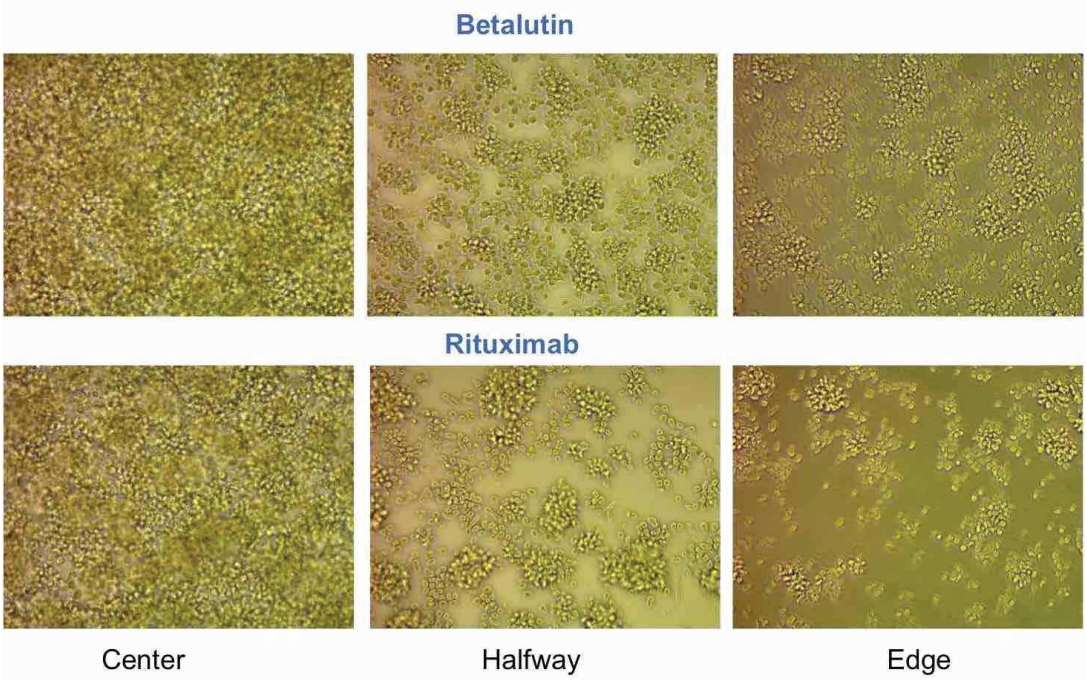

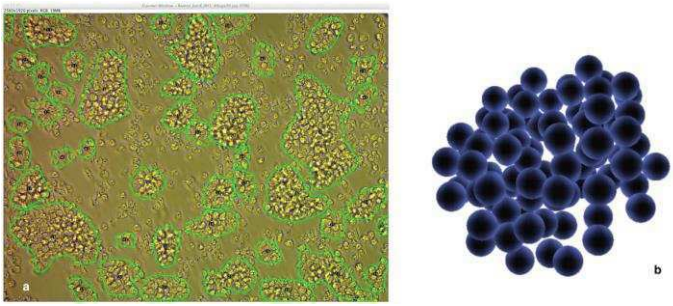

Figure 71: Example of Ramos cell culture acquired at ×200 magnification with an optical microscope at the edge of the culture well.

b. Cell and nucleus size

The cell and nucleus dimensions of Ramos cells were determined after propidium iodide staining and fluorescent microscopic analysis of 45 Ramos cells (Table 10).

Table 10: Cell and nucleus dimension of Ramos cell line

	Nucleus			Cells		
	Area (µm²)	Large diameter (µm)	Small diameter (µm)	Area (µm²)	Large diameter (µm)	Small diameter (µm)
Mean	52.0	8.8	7.2	81.8	11.2	9.3
Standard deviation	13.4	1.3	1.1	18.1	1.5	1.2
Min	26.6	6.7	4.8	48.8	8.6	6.7
Max	83.5	11.6	9.7	125.4	14.8	12.1
Mean	**52.0**	**8.0**		**81.8**	**10.2**	
Standard deviation	**13.4**	**1.4**		**18.1**	**1.6**	

For both cell and nucleus, the area and the size corresponding to the largest and smallest diameters were determined. Finally, areas of 52 and 81.8 µm² were determined for the nucleus and cell in Ramos cells, respectively. Mean diameter of Ramos cell and of nucleus were 10.2 and 8.0 µm, respectively.

For DOHH2 and Rec-1 cells, the cell dimensions were determined with Scepter™ 2.0 Cell Counter (Merck) and the nucleus dimensions were determined after Dapi staining and fluorescent microscopic analysis (Table 11).

Table 11: Cell and nucleus dimension of DOHH2 and Rec-1 cell lines

	DOHH2		Rec-1	
	Nucleus	Cells	Nucleus	Cells
	Diameter (µm)	Diameter (µm)	Diameter (µm)	Diameter (µm)
Min	5.0	10.0	5.9	9.9
Max	13.7	10.8	14.1	10.5
Mean	**9.3**	**10.5**	**9.5**	**10.1**
stdv	1.7	0.5	1.8	0.3

Mean cell diameter was 10.5 and 10.1 µm for DOHH2 and Rec-1 cells respectively. Mean nucleus diameter was 9.3 and 9.5 µm for DOHH2 and Rec-1 cells, respectively.

To conclude, cells diameters were 10.2, 10.5 and 10.1 µm for Ramos, DOHH2 and Rec-1 cells, respectively; and the nucleus diameters were 8.0, 9.3 and 9.5 µm for Ramos, DOHH2 and Rec-1 cells, respectively.

The cell model was implemented in Geant4.9.6 patch 04 in order to calculate the cell S-values for different hypotheses of antibody internalisation and different target regions. For this and all the Monte Carlo simulation performed for this work, the whole ^{177}Lu spectrum was considered as defined in the MIRD radionuclide data and decay schemes [216].

4. Determination of mean nucleus absorbed dose

This part was also performed in collaboration with Dr Marcatili.

As previously described, several physical parameters were considered in S-factor calculation:

- **The decay spectrum of ^{177}Lu**. Data are available in MIRD radionuclide data and decay schemes published by Eckerman and Endo (2008, Society for Nuclear Medicine) [216].

- **Cell and nucleus geometry**.

- **The spatial distribution of the cells** that may affect S-values for cross fire irradiation.

- **The subcellular localisation of ^{177}Lu-mAb**. This was determined and published in [154]. In this paper, the internalisation of lilotomab and rituximab were studied in Ramos cell line using immunofluorescence technique for 19h. Conclusions indicated that the complex lilotomab/CD37 was showing a quick internalisation into the cytoplasm whereas rituximab remained mostly at the cell surface. Similar results were observed by us for DOHH2 and Rec-1 cells (data not shown). From these data, it was reasonable to consider that in the case of ^{177}Lu-lilotomab, the source of the irradiation (source, rs) was about 50% at the cell surface and 50% into the cytoplasm while for the ^{177}Lu-rituximab and ^{177}Lu-cetuximab, rs was 100% at the cell surface.

Three target regions are considered: the cytoplasm, the nucleus and the whole cell. However, as mentioned above, the nucleus is considered as the main sensitive target of irradiation, although we know now that this is only partly true. Then, the mean nucleus absorbed dose was further used in my project as the reference dose to compare the three radiopharmaceuticals. Results obtained by Dr Marcatili are summarised in Table 12 (data not shown for Rec-1 cells)

Table 12: Total mean nucleus absorbed doses for Ramos and DOHH2 cells

Ramos cells	Test activities (MBq/mL)	Self dose (Gy)		Average crossfire dose		Non specific dose (Gy)		Total Dose (Gy)	
		Average dose (Gy)	St. Dev.	Average dose (Gy)	St. Dev.	Average dose (Gy)	St. Dev.	**Average dose (Gy)**	St. Dev.
^{177}Lu-lilotomab	0.5	0.31	0.17	0.75	0.16	0.00	0.36	**1.06**	0.43
	1	0.40	0.12	0.91	0.19	0.45	0.24	**1.77**	0.33
	2	0.56	0.25	1.32	0.28	1.43	0.54	**3.31**	0.66
	4	1.43	0.22	3.19	0.65	2.19	0.47	**6.81**	0.83
	6	1.65	0.34	3.70	0.75	4.33	0.71	**9.69**	1.09
^{177}Lu-rituximab	0.5	0.97	0.36	1.69	0.34	0.00	0.49	**2.66**	0.70
	1	1.06	0.38	1.86	0.38	0.11	0.53	**3.03**	0.75
	2	1.32	0.24	2.24	0.44	0.79	0.33	**4.35**	0.60
	4	1.92	0.26	3.25	0.64	2.57	0.37	**7.74**	0.78
	6	2.99	0.75	5.15	1.02	3.71	1.03	**11.85**	1.63
^{177}Lu-cetuximab	0.5	0.02	0.01	0.03	0.01	0.62	0.02	**0.67**	0.03
	1	0.04	0.03	0.06	0.01	1.24	0.05	**1.33**	0.06
	2	0.08	0.07	0.13	0.03	2.47	0.13	**2.67**	0.15
	4	0.36	0.03	0.48	0.10	4.58	0.06	**5.42**	0.12
	6	0.51	0.03	0.67	0.15	6.93	0.06	**8.11**	0.16

DOHH2 cells	Test activities (MBq/mL)	Self dose (Gy)		Average crossfire dose		Non specific dose (Gy)		Total Dose (Gy)	
		Average dose (Gy)	St. Dev.	Average dose (Gy)	St. Dev.	Average dose (Gy)	St. Dev.	**Average dose (Gy)**	St. Dev.
^{177}Lu-lilotomab	0.5	0.26	0.08	0.60	0.14	0.02	0.37	**0.87**	0.41
	1	0.34	0.15	0.82	0.20	0.15	0.74	**1.31**	0.78
	2	0.46	0.21	1.10	0.27	0.42	1.01	**1.98**	1.06
	4	0.90	0.32	2.12	0.51	0.83	1.54	**3.86**	1.66
	6	1.35	0.17	3.06	0.73	1.28	0.82	**5.69**	1.10
^{177}Lu-rituximab	0.5	0.84	0.27	1.71	0.32	0.05	0.88	**2.60**	0.98
	1	1.02	0.14	2.01	0.36	0.00	0.47	**3.03**	0.61
	2	1.21	0.04	2.35	0.42	0.31	0.12	**3.87**	0.44
	4	1.85	0.59	3.71	0.69	0.90	1.93	**6.46**	2.13
	6	2.07	0.35	4.08	0.74	1.04	1.13	**7.18**	1.40
^{177}Lu-cetuximab	0.5	0.02	0.00	0.04	0.01	0.56	0.01	**0.63**	0.02
	1	0.04	0.00	0.08	0.02	1.14	0.02	**1.26**	0.02
	2	0.13	0.05	0.28	0.07	2.05	0.23	**2.46**	0.25
	4	0.16	0.05	0.33	0.08	4.53	0.22	**5.02**	0.24
	6	0.24	0.01	0.49	0.12	6.78	0.05	**7.51**	0.13

5. Clonogenic survival as a function of the mean nucleus absorbed doses

Then, clonogenic survival was next expressed as a function of the mean nucleus absorbed doses (Figure 72 and 73).

a. Ramos cells

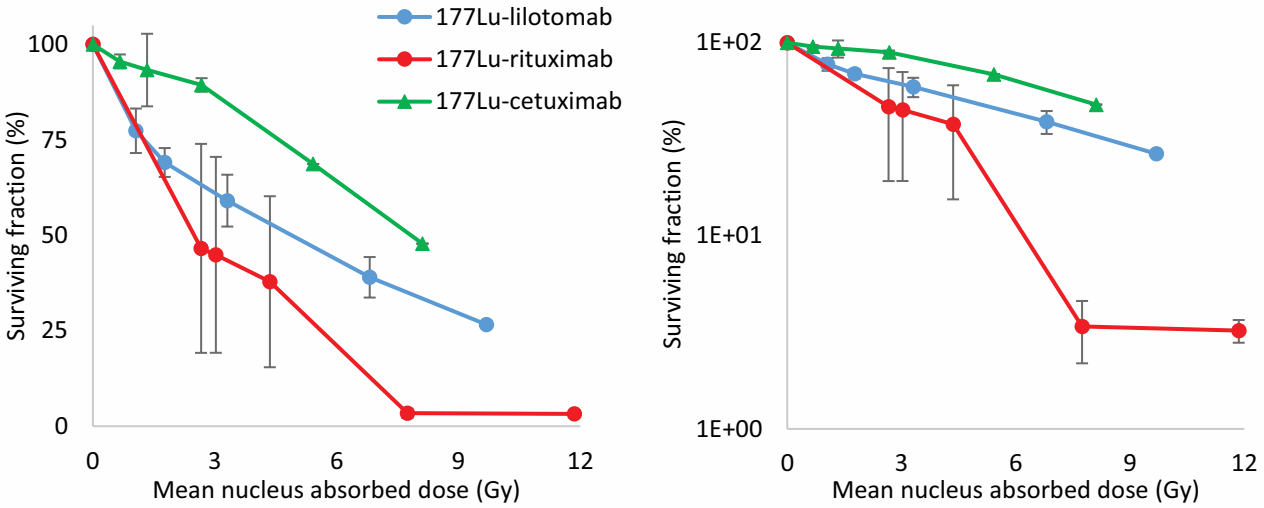

Figure 72: Clonogenic survival of Ramos cells as a function of mean nucleus absorbed dose (classical or semi-log scale)

Figure 72 confirmed that the treatment with the ^{177}Lu-cetuximab was less efficient in killing Ramos cells than specific ^{177}Lu-mAbs. Moreover, the ^{177}Lu-rituximab was more cytotoxic than ^{177}Lu-lilotomab.

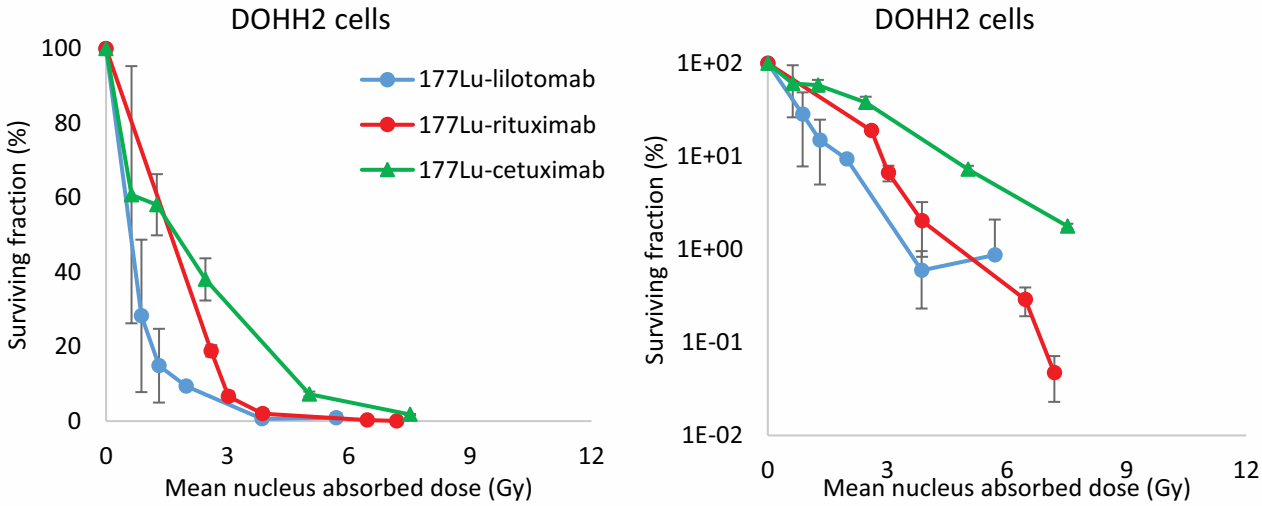

Figure 73: Clonogenic survival of DOHH2 cells as a function of mean nucleus absorbed dose (classical or semi-log scale)

Figure 73 confirmed that DOHH2 cells were more radiosensitive than Ramos cells. For example, at 7.5 Gy following ^{177}Lu-cetuximab exposure, only about 2% DOHH2 cells survived whereas 47% Ramos cells survived. Moreover, ^{177}Lu-lilotomab was shown to have a higher therapeutic efficacy than ^{177}Lu-rituximab.

6. Key points

In this part, a referential parameter, namely the mean nucleus absorbed dose, was determined to investigate therapeutic efficacy of the radiolabelled mAbs. We could demonstrate that:

- Ramos cell line was more radioresistant than DOHH2 cell line.

- In the most radioresistant cell line (Ramos), ^{177}Lu-rituximab was more efficient than ^{177}Lu-lilotomab.

- In the most radiosensitive cell line (DOHH2), ^{177}Lu-lilotomab and ^{177}Lu-rituximab had a similar therapeutic efficacy.

C. External beam radiation therapy

To confirm the radiosensitivity of the cell lines, the clonogenic survival of Ramos and DOHH2 cells was investigated after 2 and 4 Gy of EBRT (Figure 74).

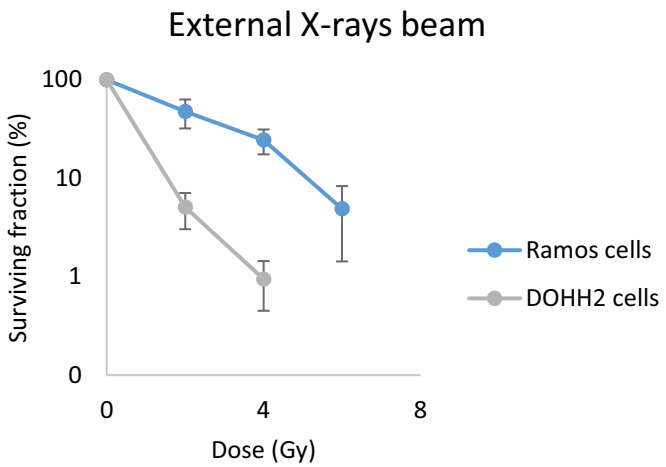

Figure 74: Clonogenic survival of Ramos and DOHH2 cells after irradiation with 225 kV X-ray

The clonogenic survival of Ramos cells was 48 ± 16 and 24 ± 7% after 2 and 4 Gy of EBRT respectively; for DOHH2 cell line, the survival was 5 ± 2% and 1 ± 0.5% after 2 and 4 Gy of EBRT respectively.

EBRT experiments confirmed the radiosensitivity of the cell lines, with Ramos cell line as the most radioresistant one, and DOHH2 cell line as the most radiosensitive.

D. Bliss independence model

Based on the data showing that ^{177}Lu-rituximab and ^{177}Lu-lilotomab could have the same therapeutic efficacy in one of both cell lines, whereas initially, rituximab had a higher efficiency than lilotomab, we were interested in evaluating separately the therapeutic efficacy of both naked mAbs and of the irradiation in a context of ^{177}Lu-lilotomab and of ^{177}Lu-rituximab treatment. For this purpose, a mathematical approach discriminating the radiobiological (due to ^{177}Lu) and immunological (due to mAb) effect of ^{177}Lu-lilotomab and ^{177}Lu-rituximab was developed. The Bliss independence model [217] was then used to investigate the additivity or synergy between radiobiological and immunological responses:

$$Theoretical\ efficacy_{177Lu\_mAb} = Efficacy_{mAb} + Efficacy_{177Lu} - (Efficacy_{mAb} \times Efficacy_{177Lu})$$

From the therapeutic efficacy of the unlabelled mAb and that of ^{177}Lu-cetuximab, the theoretical therapeutic efficacy of a ^{177}Lu-mAb was calculated. This theoretical efficacy was corresponding to a statistical addition of both radiobiological and immunological effects. By comparing the theoretical efficacy of a ^{177}Lu-mAb with its experimental therapeutic efficacy, the notion of additivity or synergy between the mAb and the ^{177}Lu could be highlighted. Briefly, the combination effects can be declared synergistic if the experimental effect is superior to the theoretical effect, meaning that when the two “drugs” (here, mAb and ^{177}Lu) are associated, they are more efficient than the simple “addition” of both effects (which is named additivity).

The therapeutic efficacy of the lilotomab or rituximab mAbs was determined by clonogenic survival. Considering the therapeutic efficacy of the ^{177}Lu, the clonogenic survival of cells after treatment with ^{177}Lu-cetuximab as a function of nucleus absorbed doses were used as the referential curves (one for Ramos and one for DOHH2 cells). After treatment with ^{177}Lu-lilotomab and ^{177}Lu-rituximab, each test activity corresponded to a nucleus absorbed dose. Thus, using this nucleus absorbed dose, the corresponding clonogenic survival was determined on the ^{177}Lu-cetuximab plot and the therapeutic efficacy only due to the ^{177}Lu used in the Bliss model. Finally, for each tumour absorbed dose, a theoretical therapeutic efficacy was calculated and a theoretical curve was obtained by plotting the points for each specific ^{177}Lu-mAb and for the two cell lines (Figure 75).

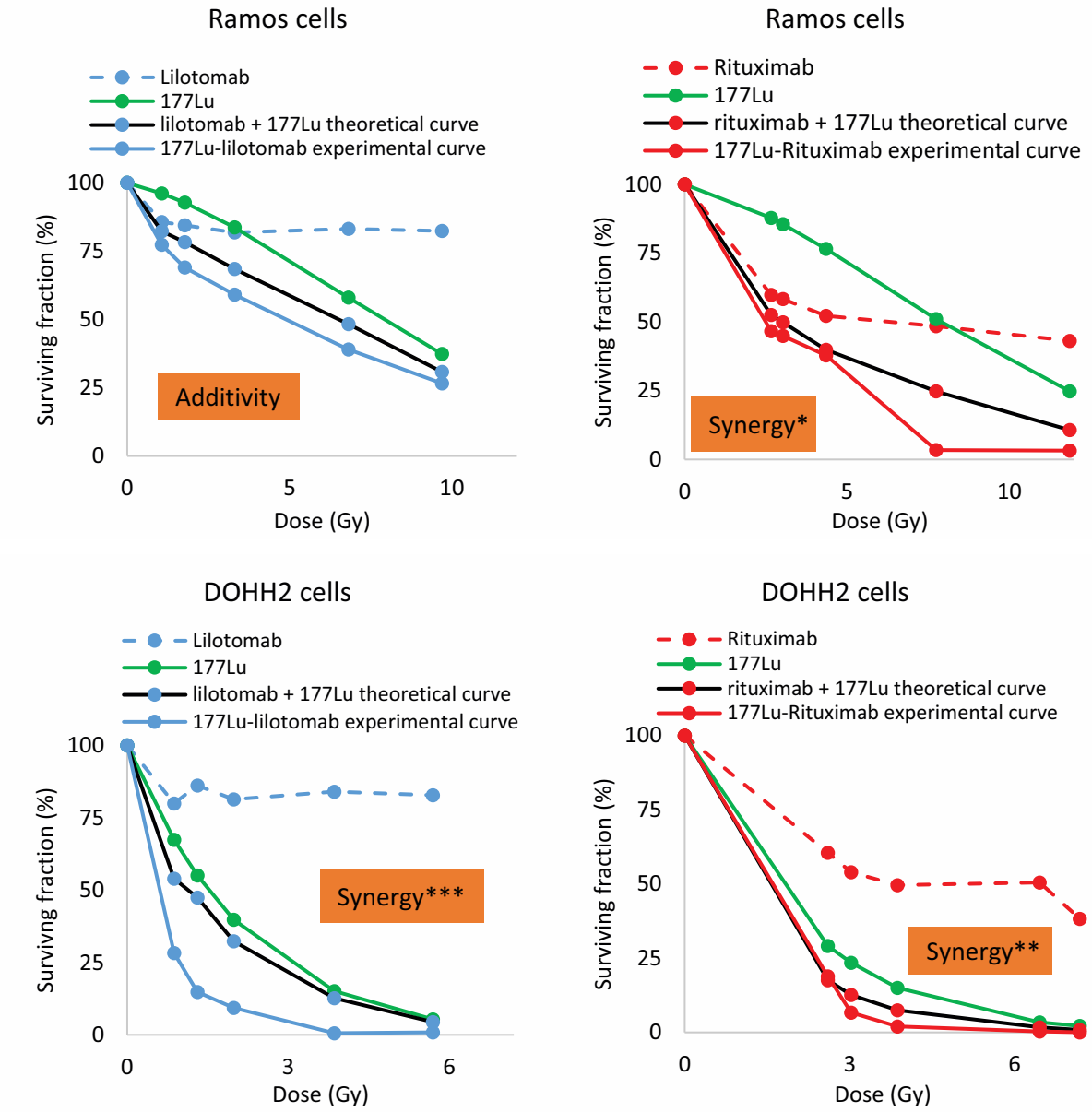

Figure 75: Comparison between experimental and theoretical surviving fractions as a function of mean nucleus absorbed doses for Ramos and DOHH2 cell lines

In the radioresistant cell line (Ramos), when cells were treated with ^{177}Lu-lilotomab, no statistically significant synergy was observed between lilotomab and ^{177}Lu (p= 0.093). After treatment with ^{177}Lu-rituximab, a slight synergy was shown between rituximab and ^{177}Lu (p= 0.029). On the contrary, in the radiosensitive cell line (DOHH2), synergy was observed after treatment with ^{177}Lu-rituximab and ^{177}Lu-lilotomab with a superiority for this latter (p= 0.003 and p= 0.001 respectively).

E. Discussion

As the beginning of my PhD project, I investigated in three different B-cell NHL cell lines, and using a standard radiobiological approach, the cytotoxicity of ^{177}Lu-lilotomab and compared it with the one of rituximab. For a better understanding of the mechanism involved in their biological effects I also included in this study a comparison with lilotomab and ^{177}Lu-rituximab. The ^{177}Lu-cetuximab was also used for investigating the radiation-induced biological effects of ^{177}Lu alone since cetuximab is in NHL cell lines a non-targeting antibody. Ramos (Burkitt lymphoma) and DOHH2 (transformed follicular lymphoma) cells have then been exposed for 18h to either ^{177}Lu-lilotomab, ^{177}Lu-rituximab, ^{177}Lu-cetuximab, rituximab or lilotomab and clonogenic survival was determined. Proliferation was also determined and extended to a third cell line, namely Rec-1 cells (mantle lymphoma) which do not form colonies. Cell uptake of radiolabelled mAbs was also determined for establishing cellular dosimetry according to MIRD formalism.

Lack of dose-effect relationship

Although bystander and abscopal effects have now slightly mitigated the paradigm, of radiobiology has considered for one century that cells only die if they have been traversed by ionising particles. According to this school of thought, biological effects, in particular clonogenic death is correlated with the energy (dose) deposited in cells. For low LET radiation like beta particles or gamma rays, clonogenic survival "S" is usually described by a linear quadratic (LQ) model of the dose according to the following equation:

$$S = \exp(-\alpha D - \beta D^2)$$

where α and β are parameters describing radiosensitivity.

The nature of this relationship is very informative since it can be affected by cell radiosensitivity, nature of radiation, dose rate, oxygenation, dose fractionation and of course absorbed dose.

As for conventional external beam radiotherapy, dose determination is a pre-requisite to understand how antibody radiolabelled conjugates (ARC) like ^{177}Lu-lilotomab work, and to perform a comparison with ^{177}Lu-rituximab and ^{177}Lu-cetuximab. For a given cell line, dose determination considers the decay spectrum of the radionuclide, the number of receptors, the pharmacodynamics, cell geometry and trafficking of receptor-^{177}Lu antibody complex. Finally a given mean nucleus absorbed dose should lead to the same cytotoxicity whatever the ARC. This is of main interest in our work where 3 ARCs were compared. In my work, cellular dosimetry was developed by Dr Sara Marcatili and results have been published in Marcatili, Pichard, *et al* Phys

med Biol 2016 [218] (see annexe). A multi-cellular dosimetry model was designated, taking into account the realistic distributions of cells in the petri dish, for the establishment of survival curves as a function of the mean nucleus absorbed dose. General purpose software tools were used for the generation of realistic, randomised 3D cell culture geometries based on experimentally determined parameters (cell size, cell density, cluster density, average cluster size and cell cumulated activity). A mixture of Monte Carlo and analytical approaches was implemented in order to achieve as accurate as possible results while reducing calculation time. Clonogenic survival experiments performed on Ramos and DOHH2 cells (Rec-1 cells do not form colony) was next expressed as a function of the mean nucleus absorbed dose as reported in Figures 71 and 72. Whereas survival curves should be fitted by a LQ model, the latter fitting was only satisfying for survival of cells exposed to ^{177}Lu-cetuximab but not for ^{177}Lu-rituximab nor ^{177}Lu-lilotomab. One possible explanation could be that in our models, ARCs efficacy can also be due to unlabelled antibody cytotoxicity. Therefore, I assessed in DOHH2 and Ramos cells and also in Rec-1 cells cytotoxic effects of unlabelled rituximab and lilotomab. Ramos and DOHH2 cell lines showed similar responses after treatment with unlabelled mAbs, with the highest efficiency observed for rituximab.

The same cytotoxicity between ^{177}Lu-lilotomab and ^{177}Lu-rituximab in the radiosensitive model is explained by the highest synergy between lilotomab and ^{177}Lu

I next decided to consider that cytotoxicity of radiolabelled mAbs can be discriminated in cytotoxicity of unlabelled mAbs combined with cytotoxicity of radiation, namely beta particles from ^{177}Lu. The latter effect could be assessed through the cytotoxic effect of ^{177}Lu-cetuximab, since as a non-specific mAb, it does not bind the cells and then only produces irradiation of the cells. Moreover, Marcatili showed that the final localisation (cell surface, cytoplasm or extracellular medium) of ^{177}Lu had little influence on energy deposited in cells such that ^{177}Lu-cetuximab could be used for mimicking irradiation produced by the three ARCs.

We observed that DOHH2 cells were more radiosensitive than Ramos cells during RIT using ARCs but also during EBRT experiments. In the “radioresistant” Ramos cell line, ^{177}Lu-rituximab was more effective to decrease survival than the ^{177}Lu-lilotomab; whereas in the radiosensitive cell line (DOHH2), the ^{177}Lu-lilotomab was as effective as ^{177}Lu-rituximab even though the unlabelled lilotomab is less efficient than the rituximab.

Using a Bliss mathematical independence model, it was next possible to investigate in each cell line, and for ^{177}Lu-lilotomab and ^{177}Lu-rituximab, the interaction between the cytotoxic effects of radiation and of unlabelled antibodies. The model indicates that synergy of different statistical

power was observed for the two ARCs in DOHH2 cells (with a superiority for the exposition of ^{177}Lu-lilotomab) while it was only observed in Ramos cells exposed to ^{177}Lu-rituximab. Synergy could explain that clonogenic survival cannot be fitted by LQ model even after having corrected of the cytotoxicity of unlabelled mAb.

To conclude, the lower efficacy of lilotomab, compared with rituximab, is counterbalanced in the radiosensitive DOHH2 cell line since ^{177}Lu-rituximab and ^{177}Lu-lilotomab show the same efficacy while rituximab is more cytotoxic than lilotomab. Synergy is observed between radiation (^{177}Lu) and both rituximab or lilotomab. Conversely, this phenomenon is not observed in the most radioresistant Ramos cells, since the relative lack of efficacy of the lilotomab, compared with rituximab, is not counterbalanced by ^{177}Lu when lilotomab is radiolabelled. In this respect only additive effect is observed between radiation and lilotomab. At this stage of my work, the reasons why ^{177}Lu irradiation was less effective in Ramos cells and to a lower extent in Rec-1 cells (see proliferation results: § I. A. 3. p116) was unclear.

II. *In vivo* studies

In vitro experiments showed that lilotomab was less efficient than rituximab. However, when radiolabelled, ^{177}Lu-lilotomab was as efficient as ^{177}Lu-rituximab in the radiosensitive DOHH2 cells. Indeed, synergy between radiation and lilotomab can counterbalance the lower efficacy of unlabelled lilotomab. I next investigated if these results could be confirmed in *in vivo* mice bearing tumour xenografts models.

A. Ramos tumour xenograft in athymic nude mice

Preliminary experiments consisted of determining maximum tolerated activity for the ^{177}Lu-lilotomab, ^{177}Lu-rituximab or ^{177}Lu-cetuximab.

1. Determination of the maximal tolerated activities

Maximal tolerated activity (MTA) is defined as the maximal injected activity without associated lethality. Healthy mice were injected with increasing activities of radiolabelled mAbs and weighed every three days to evaluate weight loss as a potential sign of toxicity induced by the treatment.

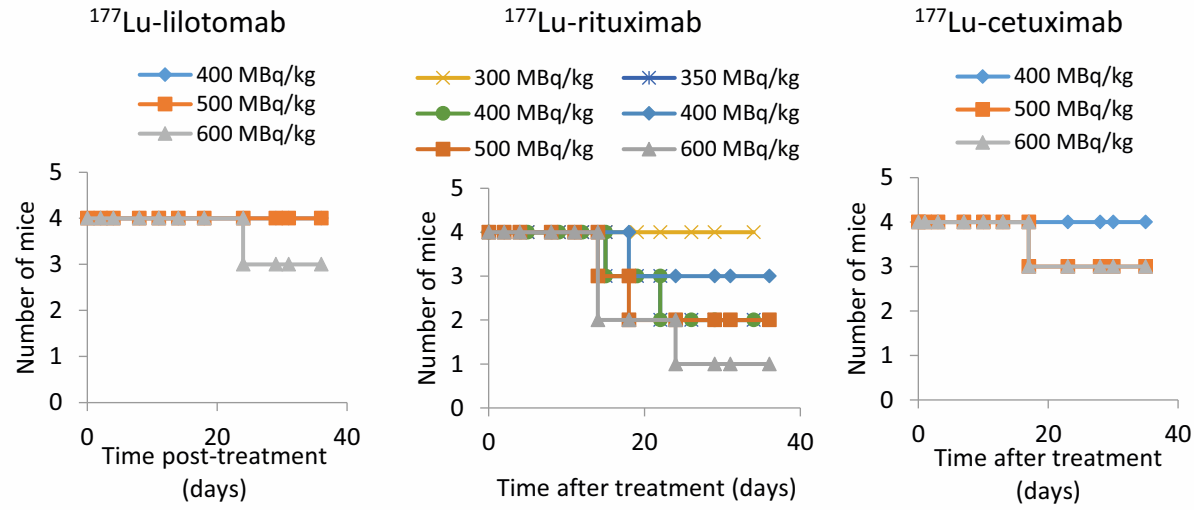

Figure 76: Survival of healthy Nude mice injected with ^{177}Lu-lilotomab, ^{177}Lu-rituximab and ^{177}Lu-cetuximab

Figure 76 shows survival of athymic nude mice injected with different activities of ^{177}Lu-lilotomab, ^{177}Lu-rituximab or ^{177}Lu-cetuximab. After treatment with ^{177}Lu-lilotomab, only the highest activity (600 MBq/kg) led to the death of one mouse (due to radiation toxicity), so the MTA was set at 500 MBq/kg. For ^{177}Lu-rituximab, the highest activities tested all led to death of mice except the activity of 300 MBq/kg. MTA for ^{177}Lu-cetuximab was set at 400 MBq/kg.

2. Biodistribution of radiolabelled mAbs in athymic nude mice bearing Ramos tumour xenografts

Mice bearing subcutaneous tumours were injected with the different ^{177}Lu-mAbs and were sacrificed at different time post-treatment. Radioactivity contained in tumours and organs was determined. For ^{177}Lu-rituximab and ^{177}Lu-cetuximab biodistribution experiments were performed by SPECT-CT imaging and quantification (example Figure 77).

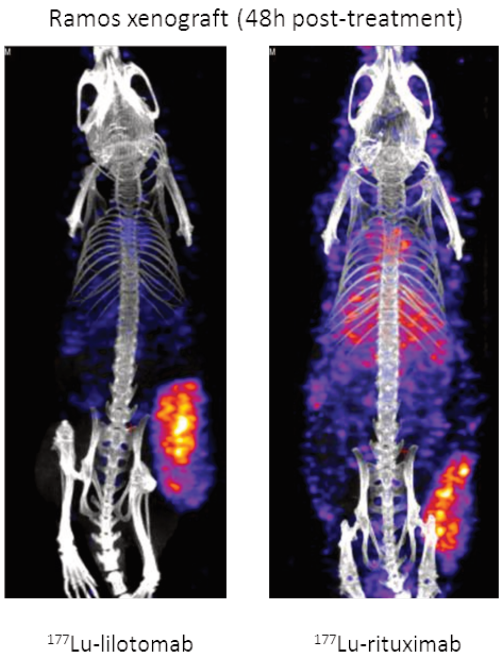

Figure 77: Example of SPECT-CT images of mice bearing Ramos tumour xenograft and injected with ^{177}Lu-lilotomab or ^{177}Lu-rituximab

Figure 78 shows the percentage of injected activity per gram of tissue after treatment with 500 MBq/kg of ^{177}Lu-lilotomab. Lungs, tumour and liver showed the highest uptakes, with maximum values for tumour measured at 48h post-injection (9% IA/g).

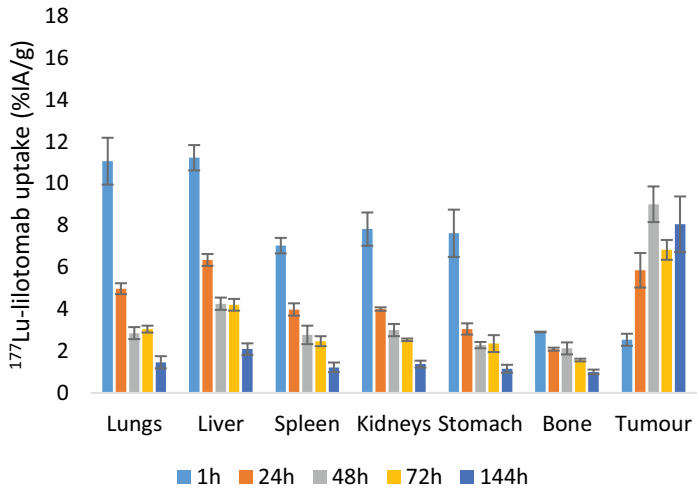

Figure 78: Percentage of injected activity (decay corrected) per gram of tissue as a function of time following treatment with 500 MBq/kg of ^{177}Lu-lilotomab in mice xenografted with Ramos cells

Figure 79 shows the percentage of injected activity per gram of tissue as a function of time after treatment with ^{177}Lu-rituximab. Lungs, liver, kidneys and tumour showed the highest uptakes. It must be noted that during SPECT-CT imaging, tissue uptake could be overestimated due to the presence of blood. This problem was further considered in dose assessment.

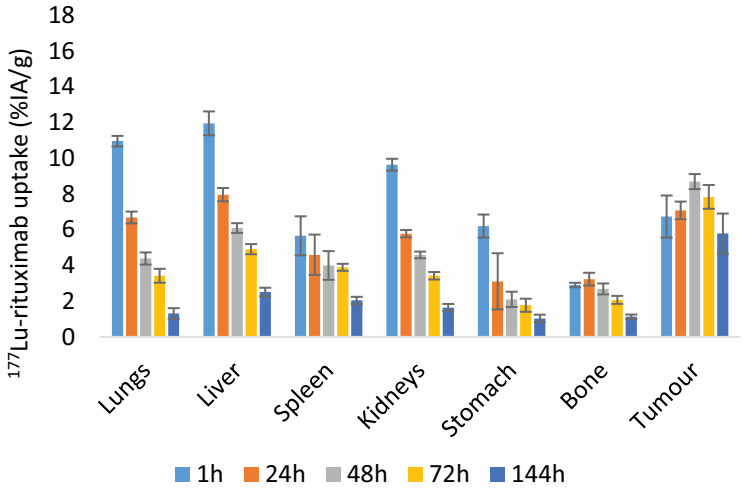

Figure 79: Percentage of injected activity (decay corrected) per gram of tissue as a function of time following treatment with 300 MBq/kg ^{177}Lu-rituximab in mice xenografted with Ramos cells

Figure 80 shows the percentage of injected activity per gram of tissue as a function of time after treatment with ^{177}Lu-cetuximab. Lungs, liver, kidneys and stomach showed the highest uptake.

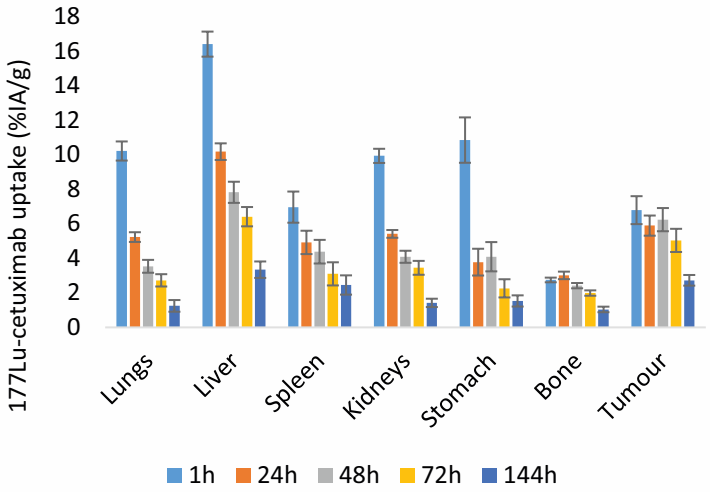

Figure 80: Percentage of injected activity (corrected decay) per gram of tissue as a function of time following treatment with 400 MBq/kg ^{177}Lu-cetuximab in mice xenografted with Ramos cells

Using these biodistribution data, it was possible to determine the total cumulative number of decays per organ (Ãrs). Next, using S-factors applied to mice anatomy and to ^{177}Lu decays, the tumour absorbed dose could be calculated. This work was done in collaboration with Alan Courteau (Cancer Research Centre of Toulouse, INSERM team 15). The tumour absorbed doses were summarised in the Table 13.

Table 13: Mean tumour absorbed doses during RIT of mice bearing Ramos tumours xenografts

	Mean tumour absorbed dose (Gy)	**Mean tumour absorbed dose/injected activity (Gy/MBq)**
^{177}Lu-lilotomab (500 MBq/kg)	9.7	1.0
^{177}Lu-rituximab (300 MBq/kg)	4.4	0.7
^{177}Lu-cetuximab (400 MBq/kg)	3.6	0.4

The mean tumour absorbed dose was higher in mice treated with ^{177}Lu-lilotomab than in those treated with ^{177}Lu-rituximab (9.7 *vs* 4.4 Gy). Moreover, for each injected activity (MBq), ^{177}Lu-lilotomab was shown to be more efficient than ^{177}Lu-rituximab in delivering dose to the tumour.

3. Therapeutic efficacy of unlabelled and radiolabelled mAbs in Ramos tumour xenograft model

Therapeutic efficacy of ^{177}Lu-mAbs (injected at the MTA) was determined. Since Table 14 shows that tumour absorbed dose following injections at MTA was about two times higher for ^{177}Lu-lilotomab than for ^{177}Lu-rituximab, ^{177}Lu-lilotomab was also injected at the MTA/2 (namely

250 MBq/Kg). Unlabelled mAbs were injected at concentrations corresponding to those used during RIT on the basis of 200 MBq/mg specific activity and at 10 mg/kg (Table 14).

Table 14: Injected activities or concentrations for therapeutic experiments in athymic nude mice

Treatment	Injected activity/concentration	Mean tumour absorbed dose (Gy)
NaCl		
Lilotomab	2.5 mg/kg and 10 mg/kg	
Rituximab	1.5 mg/kg and 10 mg/kg	
^{177}Lu-lilotomab	500 MBq/kg and 250 MBq/kg	9.7 and 4.8
^{177}Lu-rituximab	300 MBq/kg	4.4
^{177}Lu-cetuximab	400 MBq/kg	3.6

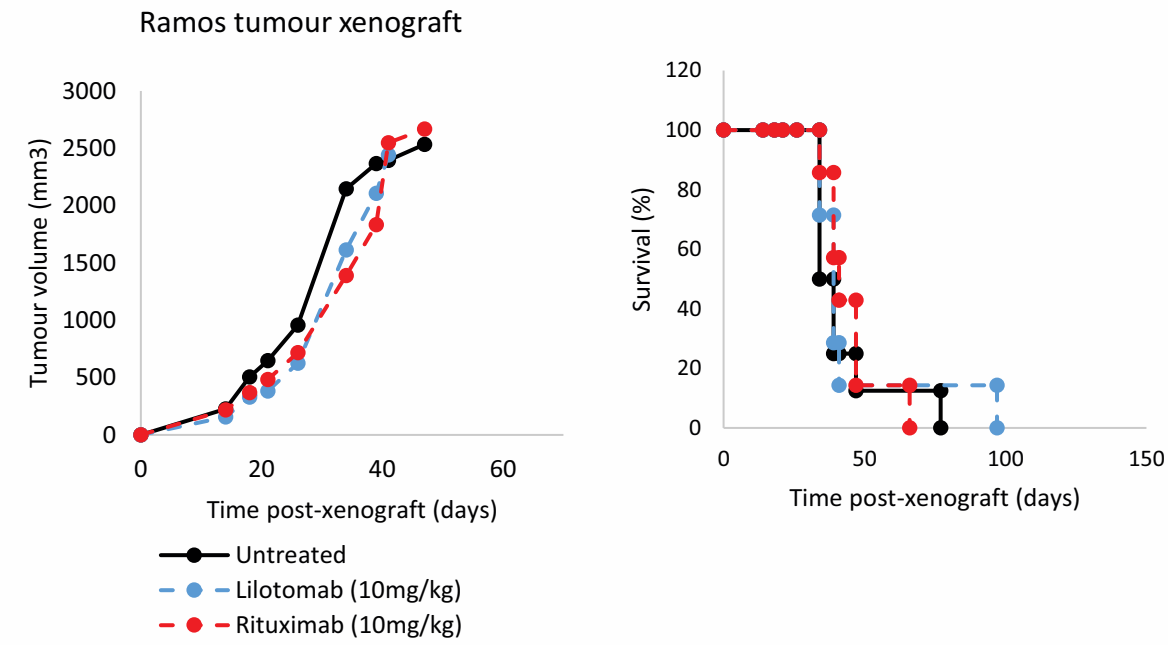

Figure 81: Mean tumour volumes and survival of mice bearing Ramos tumour xenograft treated with NaCl, 10 mg/kg lilotomab or rituximab

Figure 81 shows growth curves of Ramos tumour xenograft and survival of mice as a function of the time after treatment with 10 mg/kg of lilotomab or 10 mg/kg of rituximab. No statistical difference in tumour growth was observed between mice treated with lilotomab (p= 0.131) or rituximab (p= 0.089) *versus* NaCl-treated mice. Again, mice treated with lilotomab or rituximab did not show significant difference in survival compared with mice injected with NaCl (p= 0.3484 and p= 0.0955 respectively).

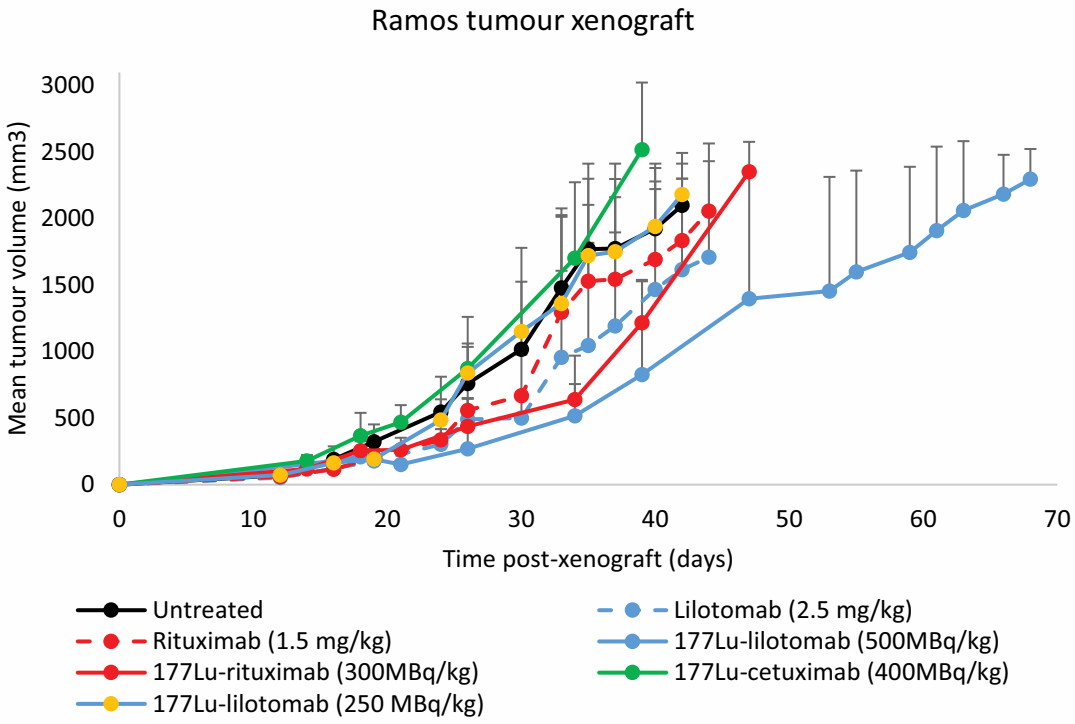

Figure 82: Mean tumour volumes of mice treated with NaCl, unlabelled mAbs or radiolabelled mAbs

Figure 82 shows growth curves of Ramos tumour xenograft as a function of the time for each treatment. Mice treated with ^{177}Lu-cetuximab, ^{177}Lu-lilotomab (250 MBq/kg), rituximab and lilotomab did not show significant difference in tumour growth compared with mice injected with NaCl ($p= 0.936$, 0.063, 0.684 and 0.507, respectively). Conversely, tumours of mice treated with ^{177}Lu-rituximab and ^{177}Lu-lilotomab used at the MTA (namely 300 and 500 MBq/kg, respectively) showed a significant difference compared with NaCl-treated group ($p= 0.035$ and $p< 0.001$). Moreover, under these conditions ^{177}Lu-lilotomab (500 MBq/kg) was more efficient than ^{177}Lu-rituximab (300MBq/kg).

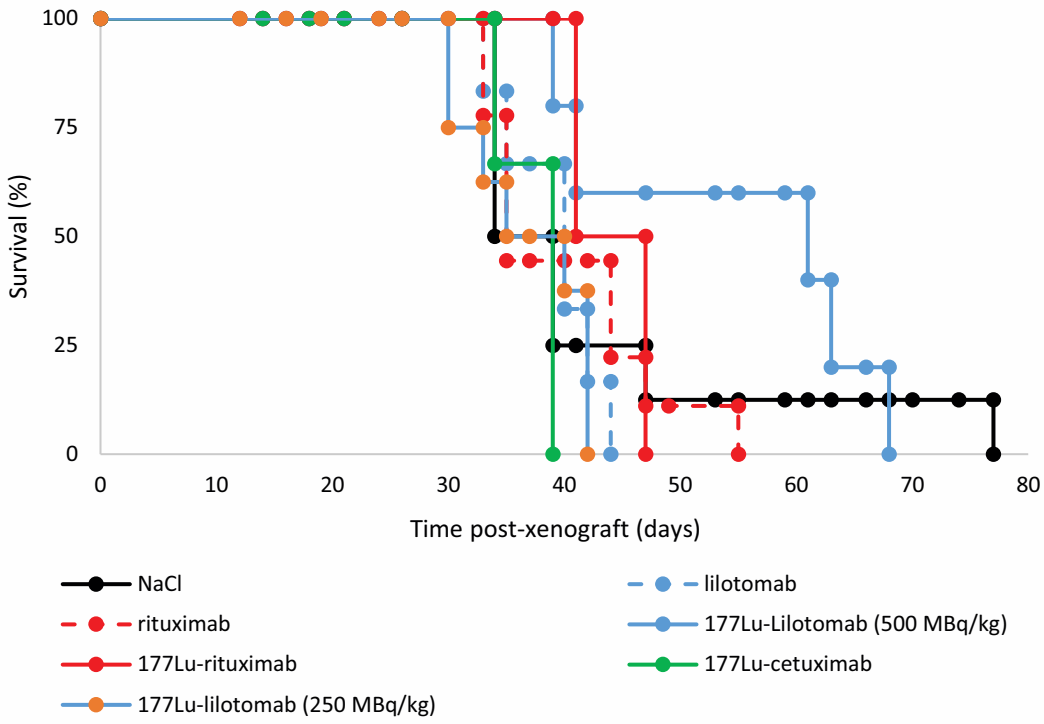

Figure 83: Survival of mice treated with NaCl, unlabelled or radiolabelled mAbs (end point: tumour volume ≥ 2000 mm³)

Figure 83 shows the survival of mice treated with NaCl, unlabelled or radiolabelled mAbs. Median survivals (MS) are summarised in Table 15.

Table 15: Median survivals of mice bearing Ramos tumour xenograft (end point: tumour volume ≥ 2000 mm³)

Treatment	Median survival
NaCl	34
Lilotomab	40
Rituximab	35
^{177}Lu-lilotomab (250 MBq/kg)	35
^{177}Lu-rituximab (300 MBq/kg)	41
^{177}Lu-cetuximab (400 MBq/kg)	39
^{177}Lu-lilotomab (500 MBq/kg)	61

Compared to NaCl, only the treatment with the ^{177}Lu-lilotomab (500 MBq/kg) demonstrated a statistical difference (p= 0.009); MS of mice treated with ^{177}Lu-rituximab was rather significant (p= 0.0536).

4. Haematological toxicity

Haematological toxicity was assessed in mice bearing Ramos tumour xenograft at different time (d-5; d+1; d+5; d+8; d+13; d+21; d+26; d+34) post-treatment with NaCl, unlabelled mAbs, or ^{177}Lu-mAbs.

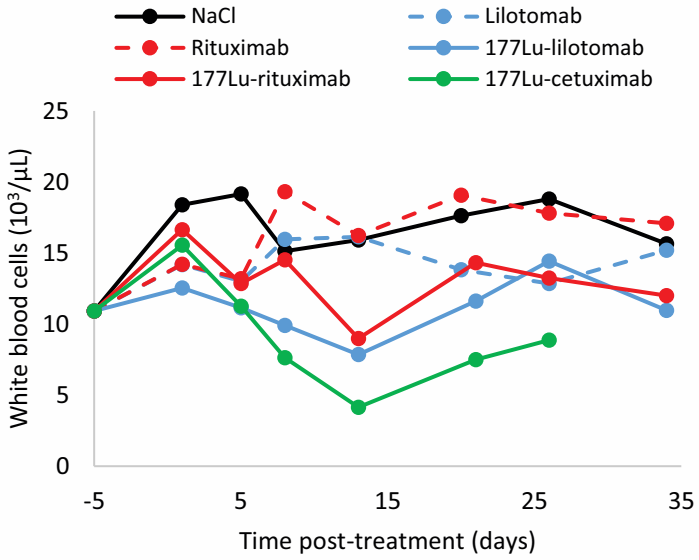

Figure 84: White blood cells express as a function of time for mice treated with NaCl, mAbs or ^{177}Lu-mAbs

No difference was observed between the levels of white blood cells of mice treated with NaCl or with unlabelled mAbs with a mean value around 15 ×10³ ± 5 ×10³ white blood cells/µL (Figure 84). Compared with the NaCl-treated group, a decrease in white blood cells number was observed for all the mice treated with ^{177}Lu-mAbs at day 13 post-injection. However, this decrease was transient.

5. Key points

Treatment of athymic nude mice bearing Ramos tumour xenograft showed that:

- Unlabelled lilotomab and rituximab had no effect on tumour growth, even injected at 10 mg/kg; tumour growth curves were similar to the NaCl-treated group.

- ^{177}Lu-lilotomab was more efficient in delaying tumour growth than ^{177}Lu-rituximab when activity was increased from 250 to 500 MBq/kg.

- When both RIT were injected at activities leading to similar tumour absorbed doses (around 4.5 Gy), ^{177}Lu-rituximab showed statistical difference with NaCl ($p = 0.035$) whereas ^{177}Lu-lilotomab did not show difference with NaCl ($p = 0.063$).

B. DOHH2 tumour xenograft in Scid mice

1. Determination of the maximal tolerated activities

As in athymic nude mice, healthy Scid mice were injected with increasing activities of radiolabelled mAbs. The mice were weighed every three days to evaluate the potential toxicity of the treatment.

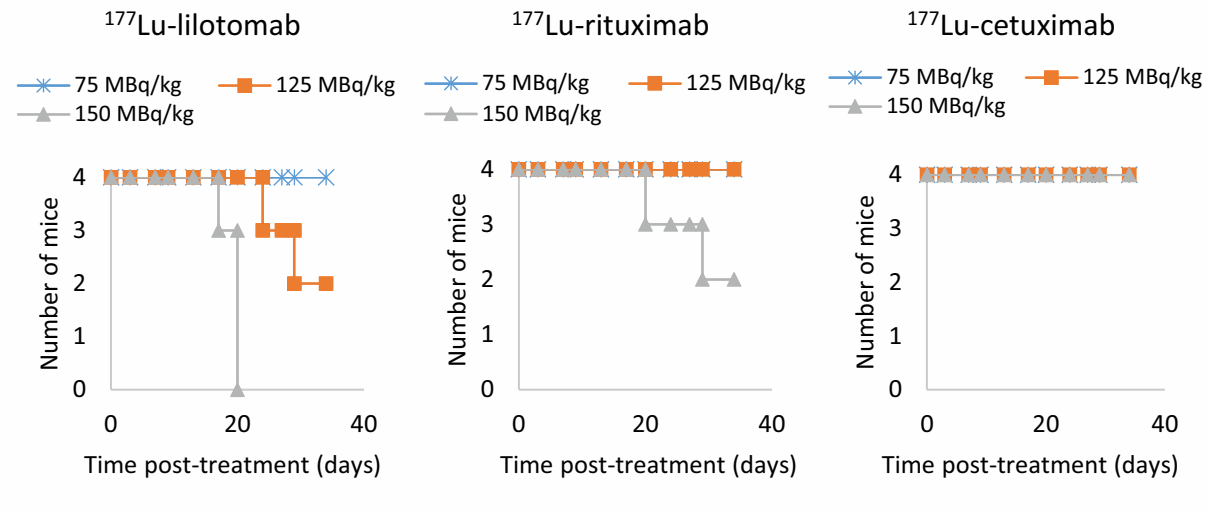

Figure 85: Survival of healthy Scid mice injected with ^{177}Lu-lilotomab, ^{177}Lu-rituximab and ^{177}Lu-cetuximab

Figure 85 shows the survival of mice injected with different activities of ^{177}Lu-lilotomab, ^{177}Lu-rituximab and ^{177}Lu-cetuximab. After treatment with ^{177}Lu-rituximab, only the highest activity (150 MBq/kg) led to death, so MTA was set at 125 MBq/kg. For ^{177}Lu-lilotomab, all the tested activities led to mice death except the lowest activity, 75 MBq/kg. MTA for ^{177}Lu-cetuximab was set at 150 MBq/kg. Next by lack of time, an arbitrary intermediary activity of 100MBq/kg ^{177}Lu-lilotomab was chosen for the following therapeutic experiments. The lack of toxicity associated with this activity was next confirmed. However, we cannot exclude that MTA was in reality slightly higher (between 100 and 125MBq/kg).

2. Biodistribution of radiolabelled mAbs in Scid mice bearing DOHH2 tumour xenografts

Mice injected with the different radiolabelled mAbs were sacrificed at different time post-treatment, organs and tumours were collected and radioactivity measured.

Figure 86 shows the percentage of injected activity per gram of tissue as a function of time after treatment with 100 MBq/kg of ^{177}Lu-lilotomab. Spleen and tumour displayed the highest uptake, with maximum values measured at 48h for spleen and measured at 72h post-injection for tumour (48 ± 19% IA/g).

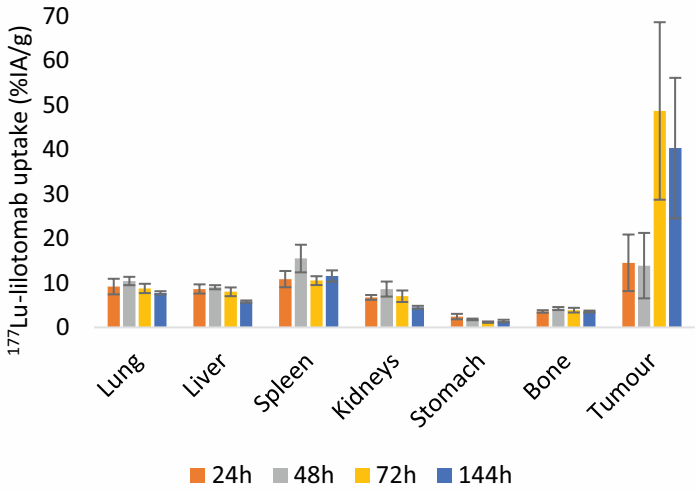

Figure 86: Percentage of injected activity (corrected decay) per gram of tissue as a function of time following treatment with 100 MBq/kg of ^{177}Lu-lilotomab in mice bearing DOHH2 tumour xenograft

Figure 87 shows the percentage of injected activity per gram of tissue as a function of time after treatment with 125 MBq/kg ^{177}Lu-rituximab. Lungs, spleen and tumour (34 ± 12% at 72h) showed the highest uptake.

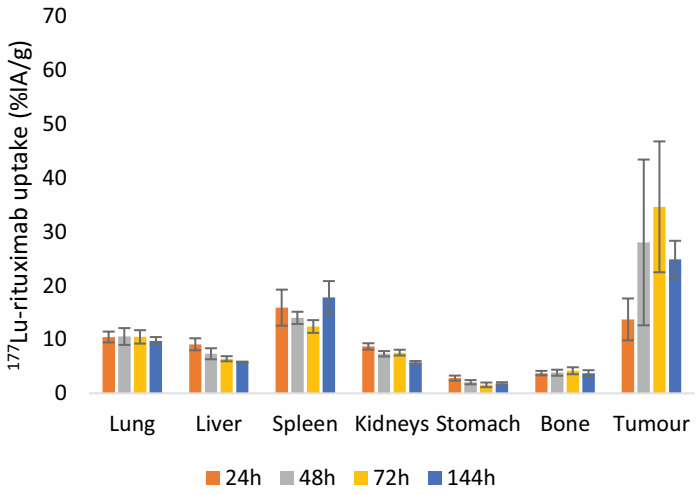

Figure 87: Percentage of injected activity (corrected decay) per gram of tissue as a function of time following treatment with 125 MBq/kg ^{177}Lu-rituximab in mice bearing DOHH2 tumour xenograft

Figure 88 shows the percentage of injected activity per gram of tissue as a function of time after treatment with 125 MBq/kg ^{177}Lu-cetuximab. Lungs, liver and spleen showed the highest uptake.

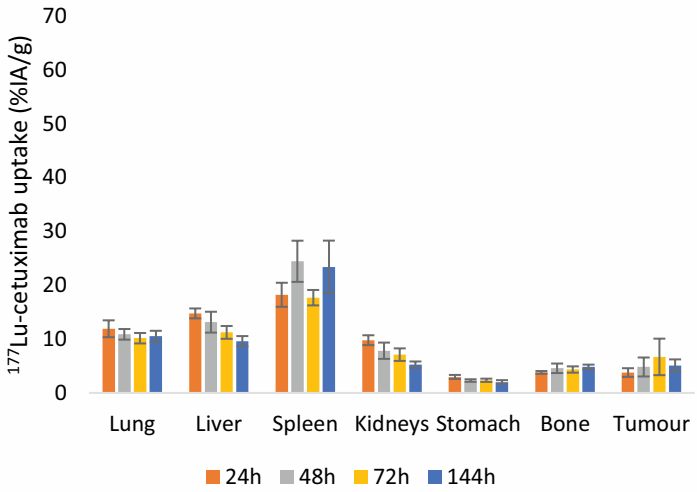

Figure 88: Percentage of injected activity (corrected decay) per gram of tissue as a function of time following treatment with 125 MBq/kg ^{177}Lu-cetuximab in mice bearing DOHH2 tumour xenograft

As for Ramos tumour xenograft model, the total cumulative number of decays (Ãrs) per organ was determined and was next used for mean tumour dose calculation according to MIRD formalism. Mean tumour absorbed doses are reported in Table 16.

Table 16: Mean DOHH2 tumour absorbed doses

	Mean tumour absorbed dose (Gy)	**Mean tumour absorbed dose/injected activity (Gy/MBq)**
^{177}Lu-lilotomab (100 MBq/kg)	8.9	4.5
^{177}Lu-rituximab (125 MBq/kg)	12.4	5.0
^{177}Lu-cetuximab (125 MBq/kg)	2.1	0.8

Therapy with ^{177}Lu-rituximab was accompanied with a higher tumour absorbed dose than with ^{177}Lu-lilotomab. Moreover, per injected activity (MBq), ^{177}Lu-rituximab and ^{177}Lu-lilotomab delivered roughly similar tumour absorbed doses.

3. Therapeutic efficacy of unlabelled and radiolabelled mAbs in DOHH2 tumour xenograft model

Therapeutic efficacy of unlabelled and radiolabelled mAbs was further determined. ^{177}Lu-mAbs were injected at the MTA. ^{177}Lu-rituximab was also injected at 100 MBq/kg leading to a tumour absorbed dose similar to that of ^{177}Lu-lilotomab. Unlabelled mAbs were injected at 10 mg/kg and at concentrations corresponding to those used during RIT on the basis of 200 MBq/mg specific activity (Table 17).

Table 17: Injected activities or concentrations used for therapeutic experiments in Scid mice

Treatment	Injected activity/concentration	Mean tumour absorbed dose (Gy)
NaCl		
Lilotomab	0.5 mg/kg and 10 mg/kg	
Rituximab	0.62 mg/kg and 10 mg/kg	
^{177}Lu-lilotomab	100 MBq/kg	8.9
^{177}Lu-rituximab	125 and 100 MBq/kg	12.4 and 9.9
^{177}Lu-cetuximab	125 MBq/kg	2.1

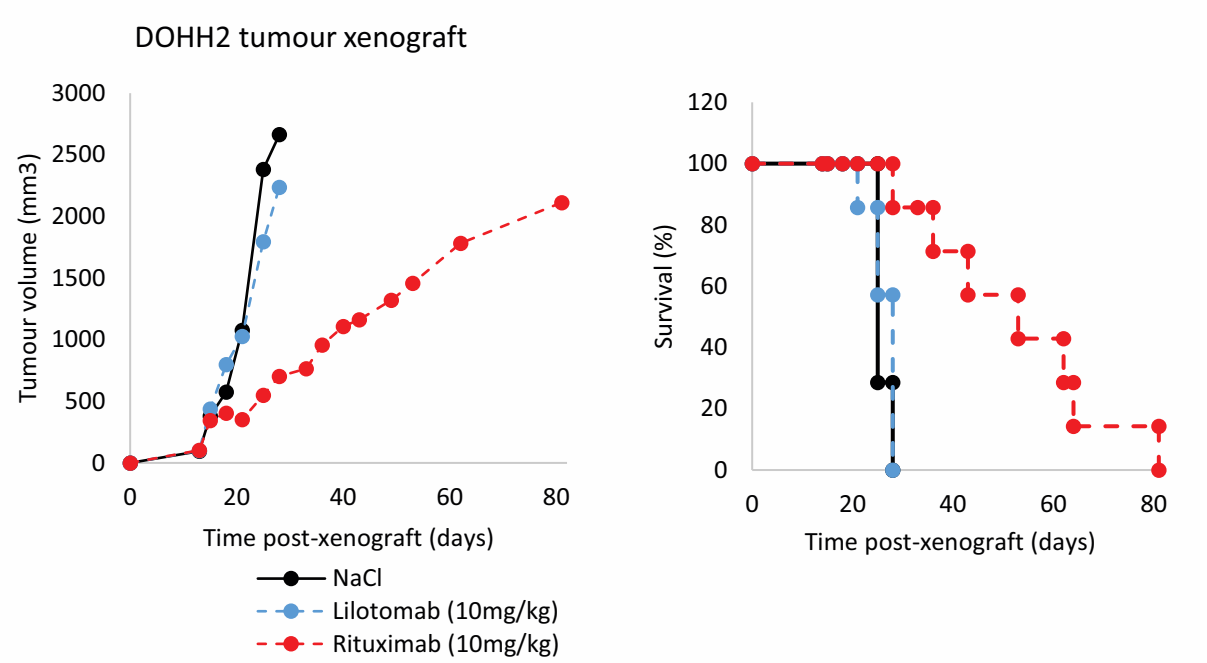

Figure 89: Mean tumour volumes and survival of mice bearing DOHH2 tumour xenograft treated with NaCl, 10 mg/kg lilotomab or rituximab

Figure 89 shows growth curves of DOHH2 tumour xenograft and survival of mice as a function of the time after treatment with 10 mg/kg of lilotomab or 10 mg/kg of rituximab. No statistical difference in tumour growth was observed between mice treated with lilotomab ($p= 0.951$) *versus* NaCl-treated mice while a strong difference was observed after treatment with rituximab ($p< 0.001$). Moreover, mice treated with lilotomab did not show significant difference in survival compared with mice injected with NaCl ($p= 0.677$). Conversely, after treatment with 10 mg/kg rituximab, survival of mice was statistically increased compared with NaCl-treated group ($p< 0.0001$).

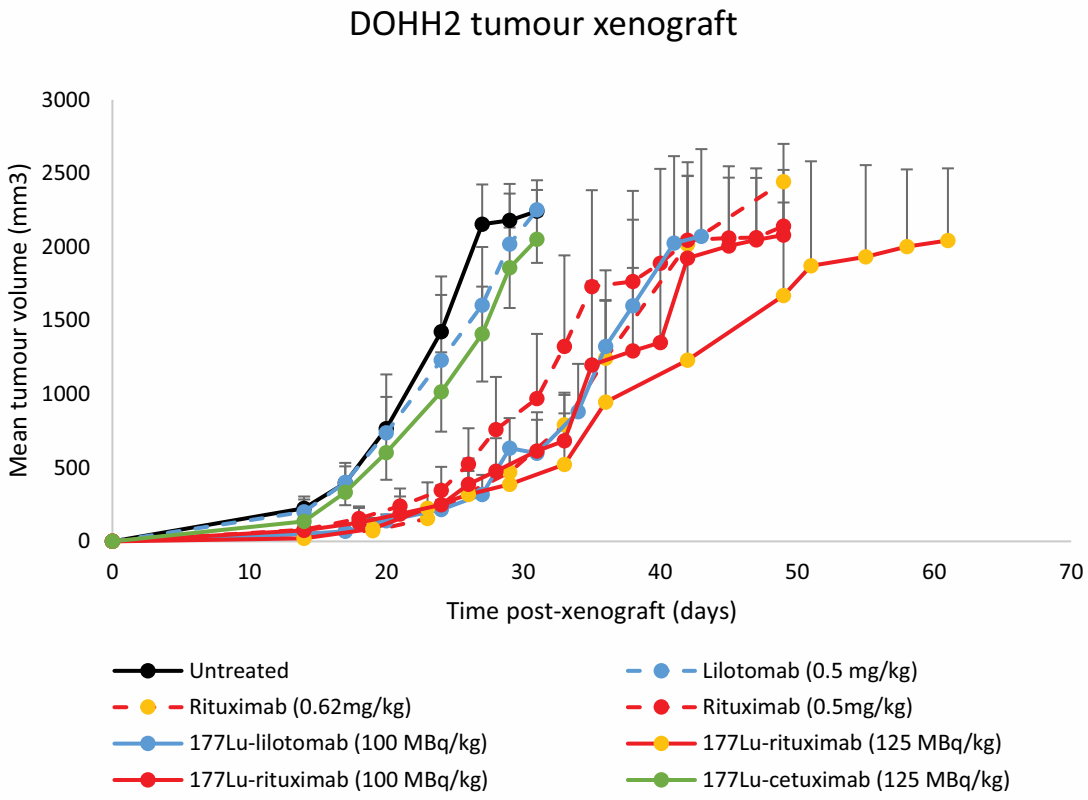

Figure 90: Mean tumour volumes of mice treated with NaCl unlabelled mAbs or radiolabelled mAbs

Figure 90 shows the growth of DOHH2 tumour xenograft as a function of the time for each treatment. Tumours treated with NaCl, ^{177}Lu-cetuximab and lilotomab showed similar growth curves compared to NaCl ($p= 0.08$ and 0.068 respectively). Tumours of mice treated with rituximab, ^{177}Lu-lilotomab or ^{177}Lu-rituximab showed statistical difference in tumour growth compared to NaCl ($p< 0.001$) and ^{177}Lu-rituximab (125 MBq/kg) showing the highest therapeutic efficacy.

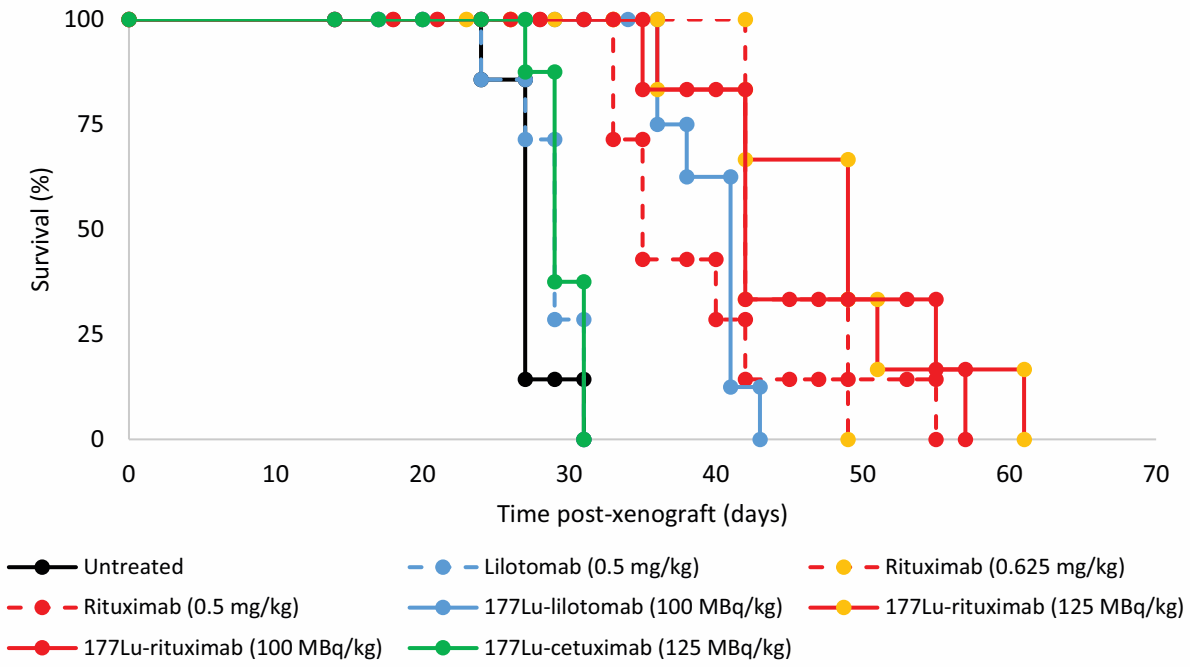

Figure 91: Survival of mice treated with NaCl, unlabelled or radiolabelled mAbs (end point: tumour volume ≥ 2000 mm^3)

Figure 91 shows the survival of mice treated with NaCl, unlabelled or radiolabelled mAbs. MS are summarised in Table 18.

Table 18: Median survivals of mice bearing DOHH2 tumour xenograft (end point: tumour volume ≥ 2000 mm^3)

Treatment	Median survival
NaCl	27
Lilotomab	29
Rituximab (0.5 mg/kg)	35
Rituximab (0.62 mg/kg)	42
^{177}Lu-lilotomab (100 MBq/kg)	41
^{177}Lu-rituximab (100 MBq/kg)	42
^{177}Lu-rituximab (125 MBq/kg)	49
^{177}Lu-cetuximab (125 MBq/kg)	29

MS was not statistically different between NaCl-, lilotomab- and ^{177}Lu-cetuximab-treated groups (p= 0.2252 and 0.3363 respectively). All the other treatments were accompanied by a statistically significant improvement of MS compared with the NaCl- treated group (p< 0.001). MS of unlabelled rituximab was 35 (0.5 mg/kg) and 42 (0.62 mg/kg) days *vs* 27 days for NaCl, while MS of ^{177}Lu-rituximab and of ^{177}Lu-lilotomab were 42 and 49 days, respectively. It is important to highlight, that when ^{177}Lu-rituximab and ^{177}Lu-lilotomab were injected at the same activity

(leading to similar tumour absorbed dose), they were accompanied with the same MS (42 *vs* 41 days). Conversely, lilotomab had no therapeutic effect on tumour growth while rituximab was very efficient. Finally, the difference of therapeutic efficacy between rituximab and ^{177}Lu-rituximab was not statistically significant (p= 0.102 and p= 0.2153 at 0.5 mg/kg and 0.62 mg/kg, respectively).

4. Haematological toxicity

Blood samples were collected at different time following treatment to assess haematological toxicity.

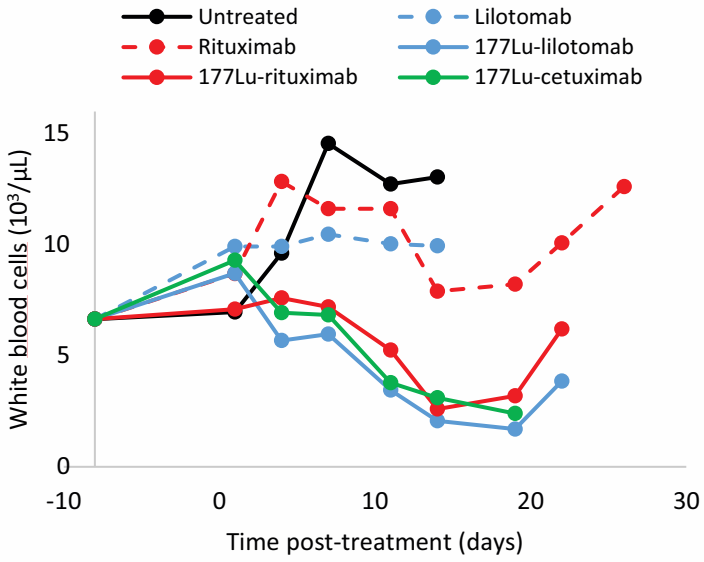

Figure 92: White blood cells express as a function of time for mice treated with NaCl, mAbs or ^{177}Lu-mAbs

Figure 92 shows the level in white blood cells of mice treated with NaCl, unlabelled mAbs or ^{177}Lu-mAbs as a function of time. No difference was observed between mice treated with NaCl or unlabelled mAbs, with a mean value around 12 000 ± 3000 white blood cells/µL. A decrease in white blood cells was observed for all mice treated with ^{177}Lu-mAbs with a maximal decrease between days 12 to 19 post-treatment.

5. Key points

Treatment of Scid mice bearing DOHH2 tumour xenograft showed that:

- Lilotomab had no effect on tumour growth, even injected at 10 mg/kg, whereas rituximab had a very high therapeutic efficacy.

- For the same tumour absorbed dose, ^{177}Lu-lilotomab and ^{177}Lu-rituximab had the same therapeutic efficacy on DOHH2 tumour growth.

- The radiolabelling of the rituximab did not allow any increase of the therapeutic efficacy on DOHH2 tumour growth.

C. Discussion

Ramos and DOHH2 cell lines were subcutaneously xenografted in athymic nude mice and Scid mice respectively. After intravenous injection with the different mAbs or ^{177}Lu-mAbs, tumour growth and haematological toxicity were monitored, mouse survival was determined considering tumour size threshold above 2000 mm^3. Biodistribution of ^{177}Lu-rituximab and of ^{177}Lu-lilotomab was also determined and organ dosimetry performed using MIRD formalism.

In Ramos tumor xenograft models, ^{177}Lu-lilotomab is more efficient than rituximab and than ^{177}Lu-rituximab when ^{177}Lu-mAbs are used at the MTA

No delay on tumour growth was observed when unlabelled antibodies were administered to mice bearing Ramos tumours even at 10 mg/kg. This is in disagreement with results obtained *in vitro* showing the highest efficacy of rituximab. When ^{177}Lu-lilotomab and ^{177}Lu-rituximab were injected at an activity leading to similar tumour absorbed dose (4.8 Gy for 250 MBq/kg and 4.4 Gy for 300 MBq/kg, respectively), ^{177}Lu-rituximab was accompanied by a significant delay in tumour growth compared with NaCl-treatment. Conversely, no difference with control group was observed for ^{177}Lu-lilotomab. The discrepancy in efficacy between the two radiolabelled mAbs, although delivering the same tumor dose, could be explained by the synergy described between rituximab and ^{177}Lu in the Ramos model while only additivity was observed between lilotomab and ^{177}Lu.

However, in athymic nude mice, the MTA of ^{177}Lu-lilotomab was 500 MBq/kg (delivering a tumour dose of 9.7 Gy) *versus* a MTA of 300MBq/kg for ^{177}Lu-rituximab. Then, when used at the MTA, ^{177}Lu-lilotomab was found to be more efficient than ^{177}Lu -rituximab in delaying tumour growth and improving MS ($p=0.017$) .

^{177}Lu-lilotomab is more efficient than rituximab in DOHH2 tumour cells and as efficient as ^{177}Lu-rituximab when ^{177}Lu-mAbs are used at the MTA

In DOHH2 tumour xenograft model, rituximab (10 mg/kg) showed a very high therapeutic efficacy whereas lilotomab did not show any efficacy at the same concentration. These results are

in accordance with those obtained *in vitro*. When rituximab and lilotomab were radiolabelled, for a similar tumour absorbed dose (8.9 Gy and 9.9 Gy, respectively), no difference in tumour growth was observed between ^{177}Lu-lilotomab and ^{177}Lu-rituximab. Thus, the relative lack of efficacy of lilotomab compared with rituximab was counterbalanced by the radiolabelling with ^{177}Lu. This could be explained by the higher synergy between lilotomab and radiation from ^{177}Lu shown in PART I. Synergy was less marked between rituximab and ^{177}Lu. In Scid mice, by injecting ^{177}Lu-rituximab at a higher activity (125 MBq/kg) a higher therapeutic efficacy was finally observed. However, the differences between rituximab and ^{177}Lu-rituximab efficacies were not statistically significant ($p= 0.269$), showing that the radiolabelling of rituximab did not increase the therapeutic efficacy of this mAb in the radiosensitive DOHH2 tumour cell line which is in agreement with the lower synergy mentioned above between rituximab and ^{177}Lu.

Then finally, we showed that ^{177}Lu-lilotomab was more efficient than rituximab in DOHH2 cells but also in Ramos tumour xenograft models when activity was increased up to 500 MBq/kg. It must be kept in mind that only rituximab is used in clinic in NHL treatment, ^{177}Lu-rituximab was only assessed for a better understanding of mechanisms involved in therapeutic efficacy of rituximab and ^{177}Lu-lilotomab.

In clinic, Betalutin® (^{177}Lu-lilotomab) is proposed to patients with relapsed or refractory B-cell NHL after following several injections of rituximab. These patients have become refractory to anti-CD20 mAb therapy. In this context, ^{177}Lu-lilotomab, targeting the CD37 provides a therapeutic option when cells do not express or express low levels of CD20 receptors at cell surface. In DOHH2 tumour xenograft model, rituximab used at 10 mg/kg was shown to be strongly efficient and more that ^{177}Lu-lilotomab during RIT experiments. This is partly explained by the limitation of the Scid mice models which are radiosensitive and that did not allow to inject more radiolabelled mAbs.

It would have also been interesting to:

- Compare the therapeutic efficacy of Betalutin® and Zevalin® as it is the only radiopharmaceutical approved in Europe for NHL. However, since Zevalin® emits very energetic beta particles, the relevance of preclinical models is questionable.

- Use rituximab-resistant cell lines as a models. However, the providing of such tumour cell models is not easy and to our knowledge only some labs developed these models such as follicular resistant model [219] or Burkitt resistant model [90], [91].

The third part of my work was focused on investigating the molecular mechanisms involved in the therapeutic efficacy of ^{177}Lu-lilotomab.

III. Biological mechanisms

This part of my work aimed at investigating *in vitro* the molecular mechanisms involved in the cytotoxic effects of ^{177}Lu-lilotomab and ^{177}Lu-rituximab in Ramos, DOHH2 and Rec-1 cells.

Cycle progression, apoptosis induction, expression of cell signalling proteins, and stem cells marker expression have been investigated in cells exposed to ^{177}Lu-mAbs. ^{177}Lu-cetuximab was used as a non-specific antibody, i.e. a control of nonspecific irradiation.

A. Apoptosis induction

Since the role of apoptosis has extensively been highlighted in radiation-induced cell death of haematological cells and during cell response to rituximab, we measured apoptosis in Ramos, DOHH2 and Rec-1 cells following incubation with unlabelled or radiolabelled mAbs. Incubation of DOHH2 with rituximab was accompanied by a strong apoptosis induction with a plateau at 18h (52 ± 1%) lasting until day 2. Apoptosis level was lower in Ramos cells (22 ± 3 % at peak time of 24h), and intermediate for Rec-1 cells (42 ± 12 % at peak time of 24h). No apoptosis was induced following treatment with lilotomab (Figure 93).

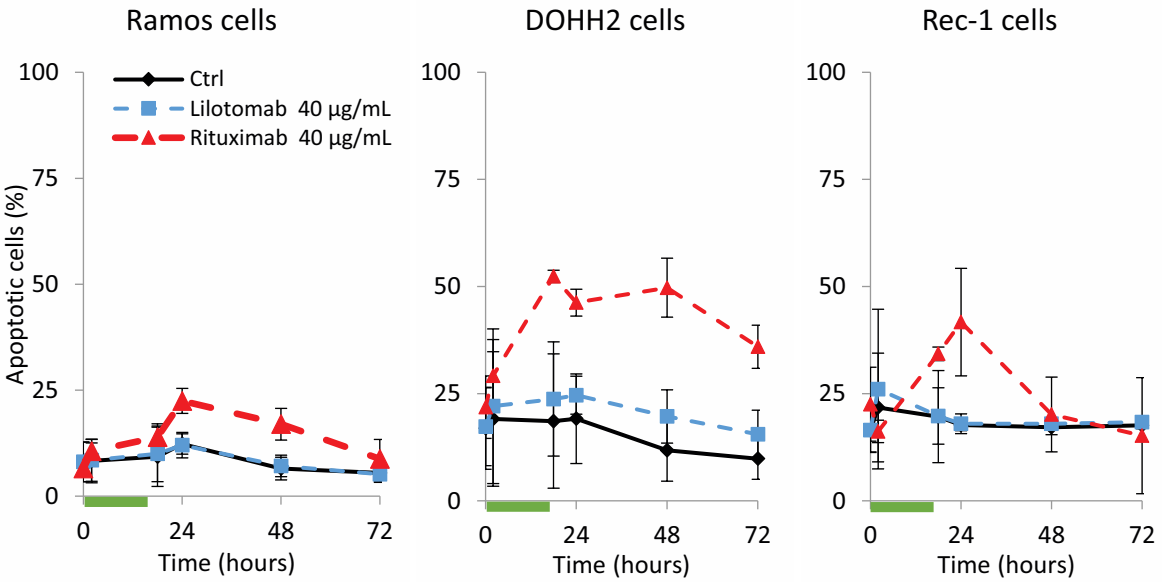

Figure 93: Apoptosis measurement in Ramos, DOHH2 and Rec-1 cells, after exposure for 18h to unlabelled mAbs (treatment period: green bars)

Apoptosis was induced in the three cell lines (Figure 94) treated with radiolabelled mAbs. After exposure to ^{177}Lu-rituximab, the highest level of apoptosis was measured in DOHH2 cells (97 ± 3% at peak time of 72h) while the lowest was observed in Ramos cells (56 ± 12%, at peak

time of 72h), and an intermediate one in Rec-1 cells (79 ± 16%, at peak time of 72h). In DOHH2 cells, a similar trend was observed for the three ^{177}Lu-mAbs. In Ramos cells, apoptosis reached a maximal level at 72h with similar levels after exposure to ^{177}Lu-lilotomab and ^{177}Lu-cetuximab (33 ± 8% and 27 ± 10%, respectively). In Rec-1 cells, a peak of apoptosis was measured at 72h with values of 79 ± 16%, 67 ± 18% and 60 ± 19% following exposure to ^{177}Lu-rituximab, ^{177}Lu-lilotomab and ^{177}Lu-cetuximab, respectively.

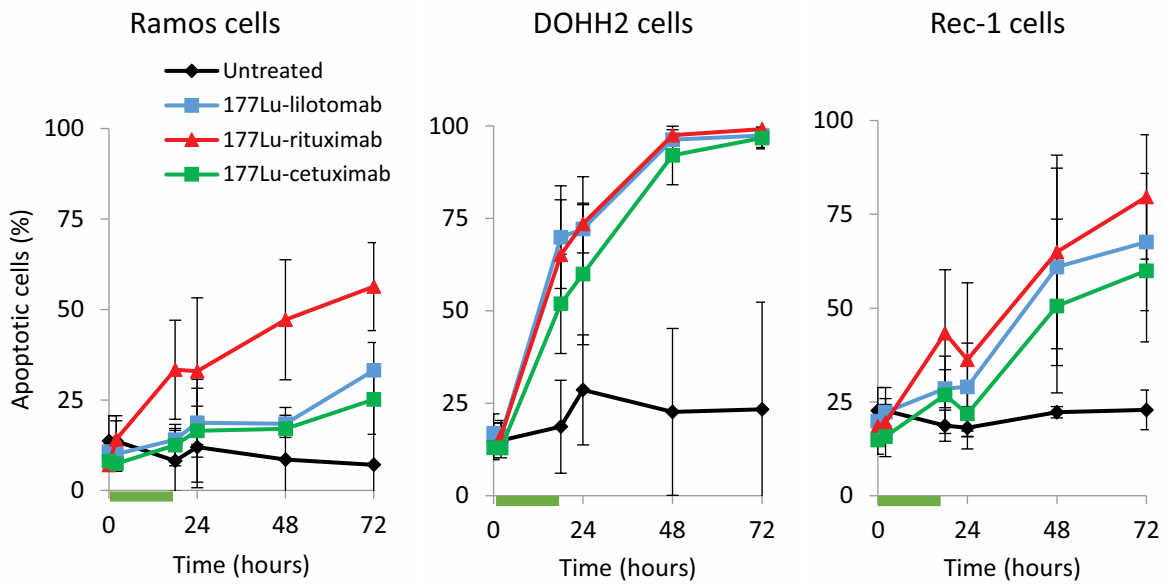

Figure 94: Apoptosis measurement in Ramos, DOHH2 and Rec-1 cells, after exposure to 6 MBq/mL of radiolabelled mAbs for 18h (treatment period: green bars)

B. Cell cycle effect in Ramos, DOHH2 and Rec-1 cell lines

The distribution of Ramos, DOHH2 and Rec-1 cells through cell cycle following exposure to 0, 2 (data not shown) and 6 MBq/mL of ^{177}Lu-mAbs was investigated.

1. Following exposure to radiolabelled mAbs

Figure 95 shows that for non-exposed Ramos, DOHH2 and Rec-1 cells, the distribution in cell cycle phases was: 39-48% in G0/G1, 25-35% in S, and 23-40% in G2/M. When cells were exposed to 6 MBq/mL of ^{177}Lu-lilotomab, the proportion of cells showing a G2/M cell cycle arrest at 24h was 64 ± 16%, 45 ± 11% and 44 ± 11% for Ramos, DOHH2 and Rec-1 cells, respectively. Corresponding values in untreated cells were 30%, 30% and 25%, respectively. Moreover, when cells were exposed to 6 MBq/mL of ^{177}Lu-rituximab, the proportion of cells showing a G2/M cell cycle arrest at 24h was 56 ± 13%, 38 ± 2% and 40 ± 11% for Ramos, DOHH2 and Rec-1 cells, respectively.

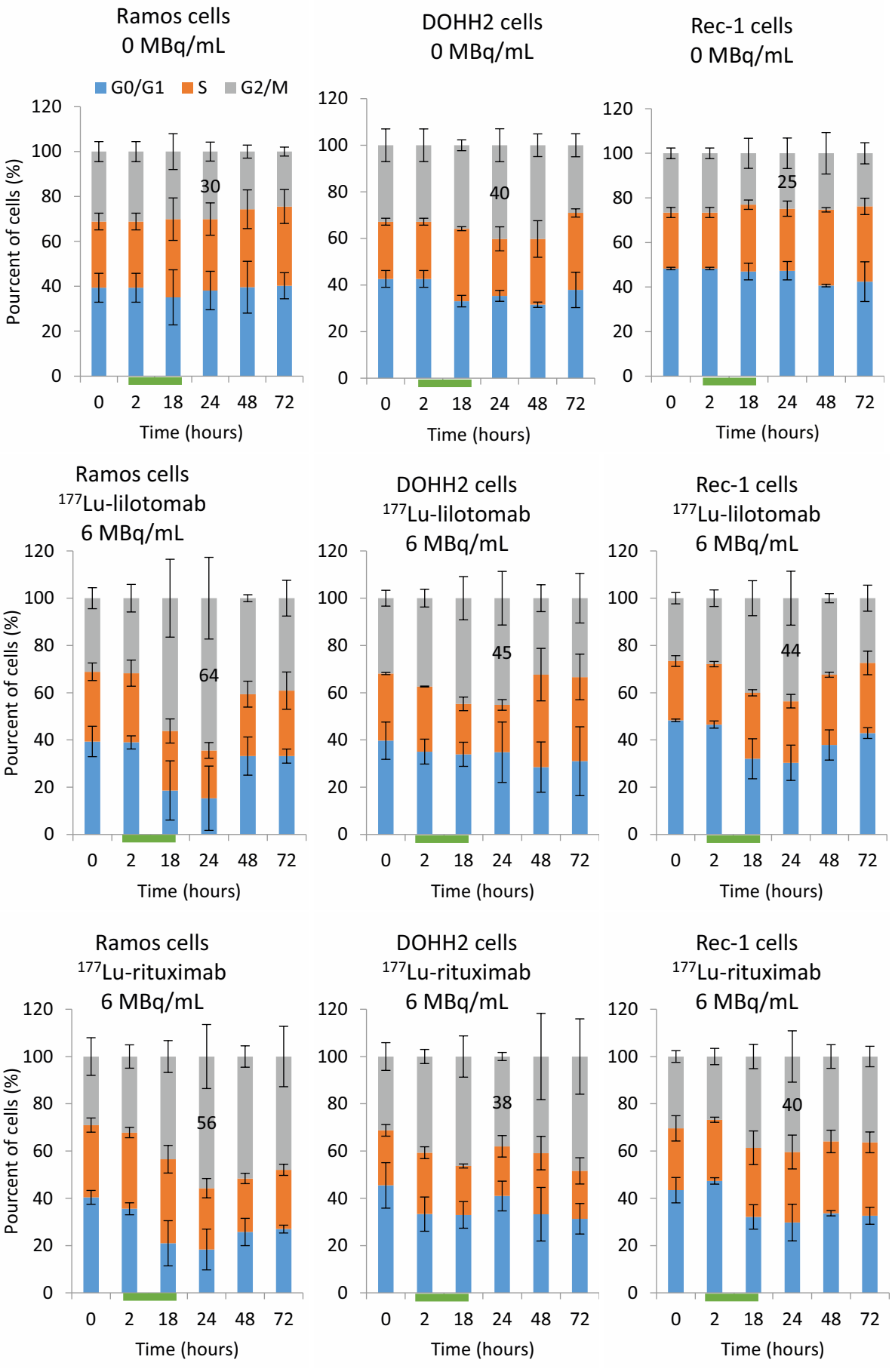
Ramos cells
0 MBq/mL
DOHH2 cells
0 MBq/mL
Rec-1 cells
0 MBq/mL
G0/G1
S
G2/M
Pourcent of cells (%)
Time (hours)
30
40
25
Ramos cells
177Lu-lilotomab
6 MBq/mL
DOHH2 cells
177Lu-lilotomab
6 MBq/mL
Rec-1 cells
177Lu-lilotomab
6 MBq/mL
64
45
44
Ramos cells
177Lu-rituximab
6 MBq/mL
DOHH2 cells
177Lu-rituximab
6 MBq/mL
Rec-1 cells
177Lu-rituximab
6 MBq/mL
56
38
40

Figure 95: Distribution of Ramos, DOHH2 and Rec-1 cells in cell cycle phases, after exposure for 18h to 0 or 6 MBq/mL of ^{177}Lu-lilotomab or ^{177}Lu-rituximab (treatment period: green bars)

2. Following exposure to unlabelled mAbs

When the three cell lines were exposed to 40 µg/mL lilotomab (Figure 96), the distribution of cells in the cycle phases was similar to the one of untreated cells. Moreover, when cells were exposed to 40 µg/mL rituximab, the proportion of cells showing a G1/G0 cell cycle arrest at 18h was 51 ± 9%, 52 ± 9% and 43 ± 7% for Ramos, DOHH2 and Rec-1 cells, respectively. Corresponding values for untreated cells were 31 ± 2%, 35 ± 6% and 42 ± 3%, respectively.

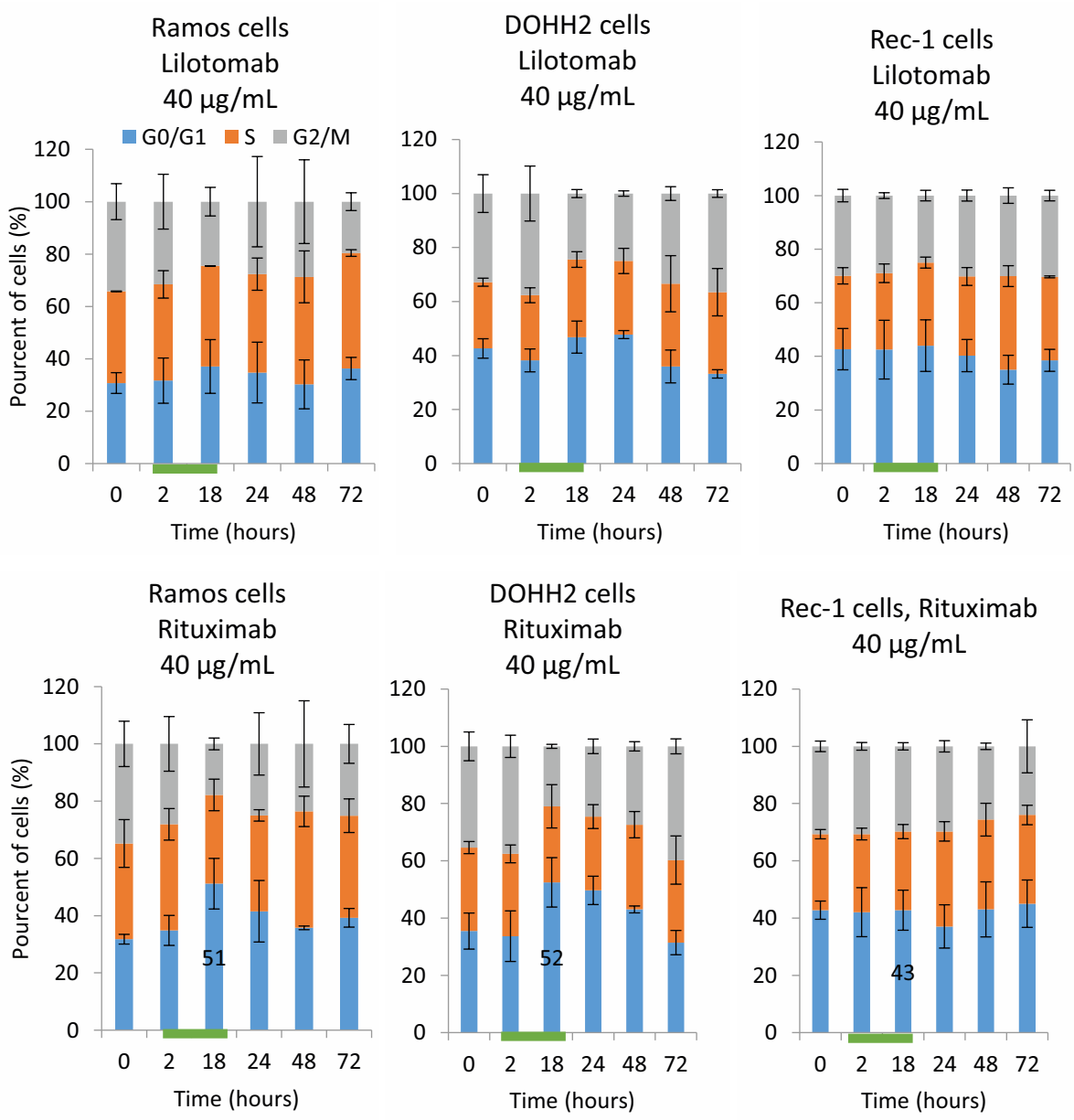

Figure 96: Distribution of Ramos, DOHH2 and Rec-1 cells in cell cycle phases, after exposure for 18h to 0 or 40 µg/mL of lilotomab or rituximab (treatment period: green bars)

3. Key points

The radiobiological response of cells to mAbs or ^{177}Lu-mAbs treatment was assessed:

- Apoptosis was induced after treatment with rituximab but not after lilotomab treatment in the three cell lines.

- ^{177}Lu-mAbs induced apoptosis in the three cell lines with a higher level in the radiosensitive DOHH2 cell line and a lower level in the radioresistant Ramos cell line.

- ^{177}Lu-lilotomab induced as much apoptosis as ^{177}Lu-rituximab in the radiosensitive DOHH2 cell line whereas in the two other cell lines, the induction was lower.

- ^{177}Lu-mAbs led to an increase of the number of Ramos cells in G2/M compared to untreated cells (x2), whereas this increase did not occur in the radiosensitive DOHH2 cell line (x1.1) (Rec-1 was between both; x1.7).

- A cell cycle arrest in G1 phase was observed after treatment with rituximab in Ramos (x1.6) and DOHH2 (x1.5) but not in Rec-1 cell line.

Apoptosis induction was inversely proportional to G2/M cell cycle arrest. Indeed, Ramos cell line being the most radioresistant model, showed a weak induction of apoptosis after treatment with ^{177}Lu-mAbs but displayed the highest accumulation of cells in G2/M. Conversely, DOHH2 cell line which was the most radiosensitive model, showed the highest level of induction of apoptosis after treatment with ^{177}Lu-mAbs but also demonstrated the lowest arrest in G2/M. We hypothesised that the G2/M cell cycle arrest was a major component of the cell radiosensitivity. The proteins involved in this arrest were investigated.

C. Proteins involved in G2/M cell accumulation

The CDK1 kinase is a major protein involved in the control of the G2/M transition. This kinase is tightly regulated by the inhibitory phosphorylations on its Thr14 and Tyr15 residues respectively by the Myt-1 and Wee-1 kinases and by the activating phosphorylation on Thr161 by the CDK-activating kinase.

The expression of CDK1 kinase and its phosphorylations were investigated (Figure 97).

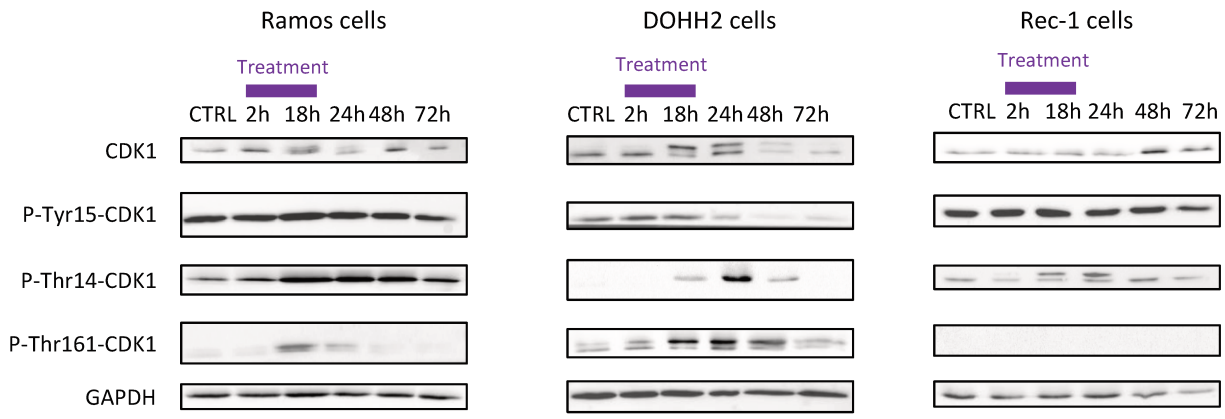

Figure 97: Expression of CDK1 and its phosphorylations in Ramos, DOHH2 and Rec-1 cells at different time after exposure to 6 MBq/mL of ^{177}Lu-lilotomab for 18h

CDK1 level was quite stable in Ramos and Rec-1 cells, whereas it decreased in DOHH2 at 48h and 72h after ^{177}Lu-lilotomab addition. In Ramos cells high persistent levels of the inhibitory pTyr15 and pThr14 CDK1 phosphorylations were present whereas transient low levels of the activating pThr161 phosphorylation were observed at 18-24h after exposure to ^{177}Lu-lilotomab. Similar results were shown with the Rec-1 cells, however, pThr161-CDK1 was undetectable. Conversely, the opposite was observed in DOHH2 cells. Phosphorylation levels of Tyr15 and Thr14 dropped respectively at 24h and 48h after ^{177}Lu-lilotomab exposure. This decrease in levels of inhibitory phosphorylations was associated with a persistent increase in the expression of the activating pThr161 phosphorylation.

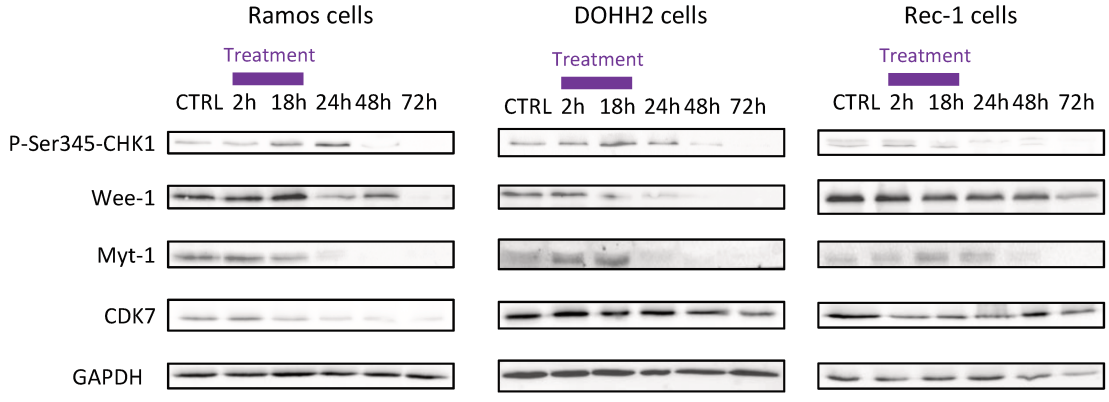

Figure 98: Expression of p345-Chk1, Wee-1, Myt-1 and CDK7 in Ramos, DOHH2 and Rec-1 cells at different time after exposure to 6 MBq/mL of ^{177}Lu-lilotomab for 18h

The levels of CDK7, which is part of the complex involved in the phosphorylation of CDK1 on its Thr161 residue, was stable or increased in DOHH2 and Rec-1 compared with Ramos cells (Figure 98). Also, expression of Wee-1, which mediates CDK1 phosphorylation at Tyr15 leading to G2/M arrest, was comparable in control and treated Ramos and Rec-1 cells between 18 and 48h. Conversely, in DOHH2 cells, baseline was low and became undetectable at 24h post-

treatment. These observations supported our previous results on the accumulation of Ramos, but not DOHH2 cells, in G2/M cell cycle phase following exposure to ^{177}Lu-lilotomab. The level of phosphorylated CHK1 (Ser345), which is involved in Wee-1 and Myt-1 activation after cell irradiation, was increased in Ramos and DOHH2 cells at 18-24h, but not in Rec-1 cells where it remained stable until 18h before progressively decreasing. Expression of Myt-1, the kinase involved in Thr14-CDK1 phosphorylation that also contributes to a G2/M arrest, decreased in all three cell lines 18h after treatment.

D. Wee-1 and Myt-1 inhibitors

Since Wee-1 and Myt-1 kinases seemed to be involved in the G2/M cell cycle phase accumulation in Ramos cells exposed to ^{177}Lu-lilotomab, cells were treated with the MK-1775 and PD-166285 pharmacological inhibitors of theses kinases in combination with ^{177}Lu-lilotomab. MK-1775 inhibits the Wee-1 catalytic activity and subsequently the pTyr15-CDK1 phosphorylation. PD-166285 inhibits both Wee-1 and Myt-1 and subsequently the phosphorylations of CDK1 on both Tyr15 and Thr14.

1. Proliferation study

Figure 99 shows the ratio between the number of cells exposed for 18h to ^{177}Lu-lilotomab or to the inhibitor alone or to the combination and the number of untreated cells, 6 days after start of treatment. The activity used for the treatment with ^{177}Lu-lilotomab was chosen to decrease the proliferation to about 50% for the three cell lines compared with non-treated cells.

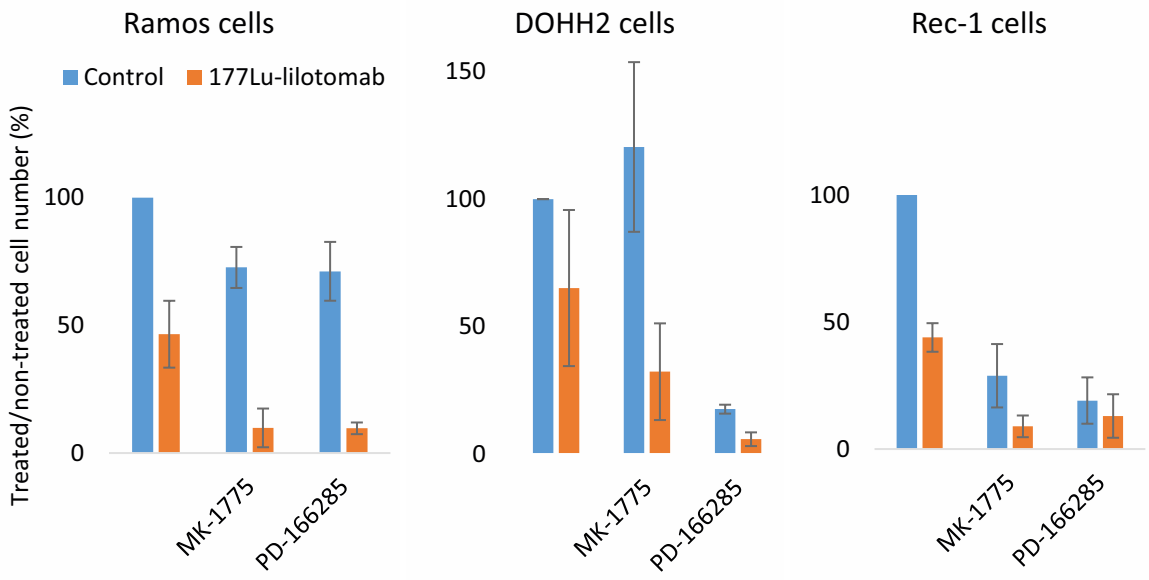

Figure 99: Effect of inhibitors of G2/M arrest on cell proliferation

In Ramos cells, both inhibitors induced a decrease of the proliferation to 70% and the combinations of RIT with MK-1775 or RIT with PD-166285 induced a similar decrease close to 10%. Those decreases in proliferation were statistically different from treatments using ^{177}Lu-lilotomab or the inhibitors alone (p= 0.0495) but no difference was observed between the two combinations (p= 0.5127)

For DOHH2 cells, only the PD-166285 was shown to modify proliferation with a strong decrease (18%). Although the anti-proliferative effect of ^{177}Lu-lilotomab was more pronounced in the presence of the two inhibitors, no statistical difference was shown compared with the inhibitors alone (p= 0.1213) or with ^{177}Lu-lilotomab alone (p= 0.1213).

A significant reduction in proliferation was also observed for Rec-1 cells exposed to inhibitors (p= 0.0495). However, only the combination of ^{177}Lu-lilotomab and MK-1775 statistically reduced the proliferation compared with the inhibitor alone (p= 0.0495) or to the ^{177}Lu-lilotomab alone (p= 0.0495).

2. Phosphorylation of CDK1

The therapeutic efficacy of both combinations (RIT + MK1775 or RIT + PD166285) corroborated the phosphorylation of the CDK1 in the three cell lines.

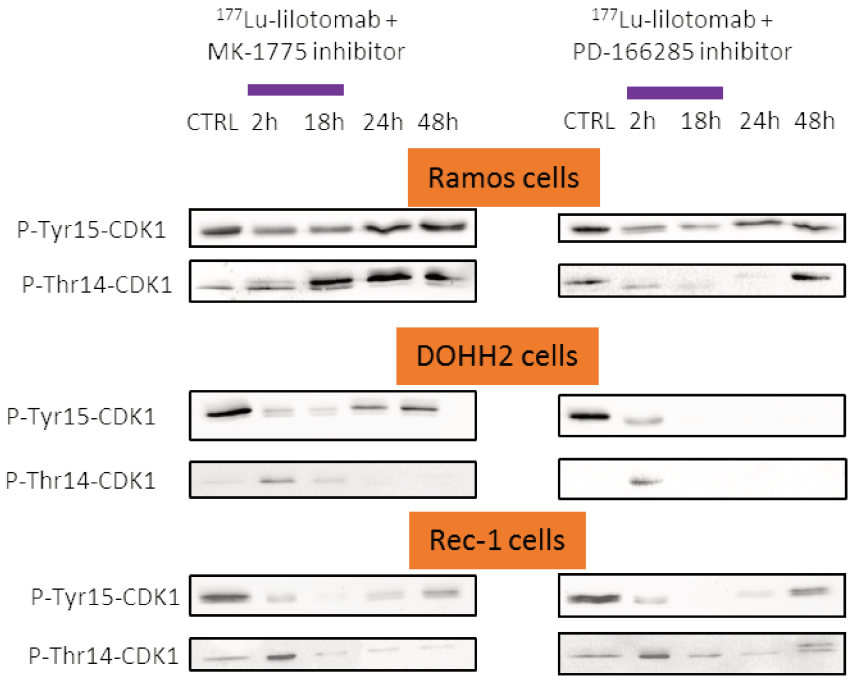

Figure 100: Expression of p14-CDK1 and p15-CDK1 in Ramos, DOHH2 and Rec-1 cells after treatment for 18h with ^{177}Lu-lilotomab + MK-1775 or ^{177}Lu-lilotomab + PD-166285

The relatively high persistent levels of pTyr15-CDK1 and pThr14-CDK1 in Ramos cells exposed to ^{177}Lu-lilotomab were then decreased in the presence of the corresponding inhibitors

at 2 and 18h before re-increasing (Figure 100). In DOHH2 cells, this re-increase after 18h was less pronounced or even not observable for pTyr15-CDK1; for pThr14-CDK1, the basal level was too low to be modulated and detected. For Rec-1 cells, since basal level of pThr14-CDK1 was low, inhibitors did not show any effect on phosphorylation expression whereas expression of pTyr15-CDK1 was decreased during treatment and increased at 48h.

3. Inhibition of G2/M cell cycle arrest

Figure 101 shows the variations between the number of cells in G2/M after treatment with ^{177}Lu-lilotomab alone or combined with MK-1775 or PD-166285, and the untreated cells. As previously shown, the proportion of Ramos and Rec-1 cell in G2/M phase was increased following treatment with ^{177}Lu-lilotomab. When the inhibitors were combined with ^{177}Lu-lilotomab, the proportion of cell in G2/M decreased. In Ramos cells, after treatment with both combinations, the proportion of G2/M cells became similar to the one of untreated cells. For Rec-1 cells, both combinations decreased by half the proportion of cells in G2/M. In DOHH2 cells, the decrease in the proportion of G2/M cells induced by the combination ^{177}Lu-lilotomab and PD-166285 is higher than that induced by the combination with the MK-1775.

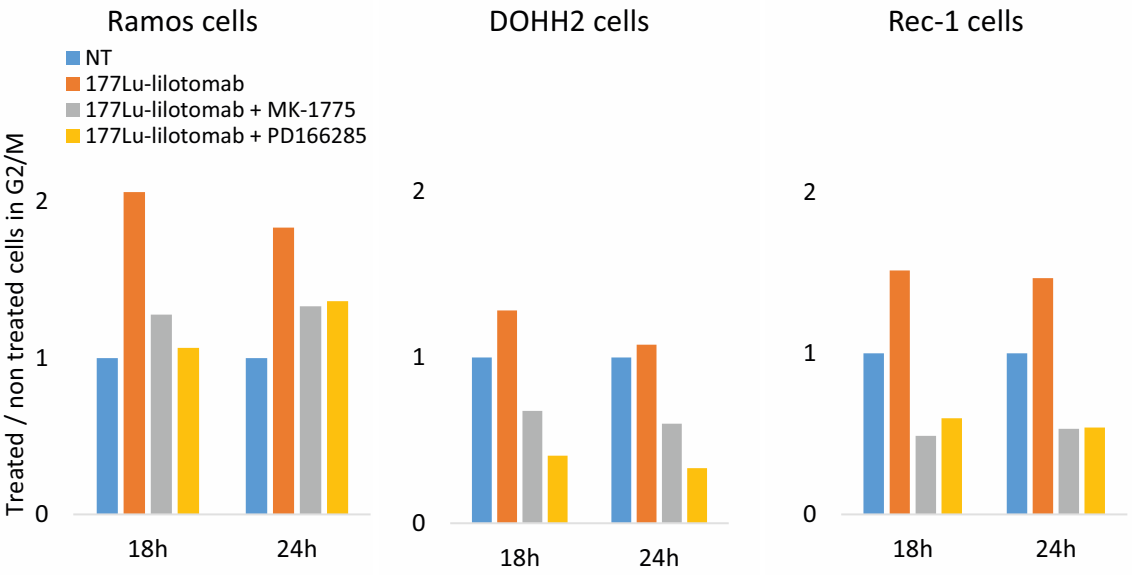

Figure 101: Ratio between the number of treated cells in G2/M and the number of untreated cells in G2/M. Treatments were ^{177}Lu-lilotomab alone or combined with MK-1775 or PD-166285.

4. Key points

- Both combinations showed a strong decrease in Ramos cells proliferation associated with a reduction of CDK1 phosphorylations leading to a decrease in G2/M cells proportion. No difference in proliferation of cells treated with the combinations ^{177}Lu-lilotomab and MK-1775 or

^{177}Lu-lilotomab and PD-166285 was observed, showing that the principal phosphorylation playing a role in the G2/M cell cycle arrest was the pTyr15-CDK1 in the Ramos cell line.

In DOHH2 cells, the basal level of the two inhibitory phosphorylations (p14 and p15) was weak. When the inhibitors were used, cell proliferation was decreased (particularly for the PD-166285) but this was not statistically significant and was in lower extent than in Ramos cell line.

For Rec-1 cell line, the major inhibitory phosphorylation was the P-Tyr15-CDK1. When the inhibitors were associated with ^{177}Lu-lilotomab, the MK-1775 was as efficient as the PD-166285 in reducing cell proliferation corroborating the importance of the P-Tyr15-CDK1 in Rec-1 cell response.

E. Discussion

In this part of my work, I investigated the biological mechanisms that could explain why ^{177}Lu lilotomab is more efficient in DOHH2 cells than in Ramos cells, Rec-1 cells showing intermediary response. Moreover, we showed in part I that synergy between radiation and rituximab was observed, although at different extent, in both Ramos and DOHH2 cells while synergy was only observed in DOHH2 cells for ^{177}Lu-lilotomab. The latter results were supported by *in vivo* data where ^{177}Lu-lilotomab was as efficient as ^{177}Lu-rituximab in DOHH2 tumour xenograft model, although unlabelled rituximab was more efficient than lilotomab.

Apoptosis induction is higher in radiosensitive DOHH2 model after treatment with ^{177}Lu-mAbs

Since haematological disease is known to respond to irradiation through apoptosis, apoptosis induction was measured in Ramos, DOHH2 and Rec-1 cells after treatment with unlabelled or radiolabelled mAbs. In agreement with previous studies [61], [62], rituximab was shown to induce strong apoptosis induction in the three cell lines whereas lilotomab not. However, when mAbs were radiolabelled, apoptosis level was increased in the three cell lines but mostly for DOHH2 cells in a similar way for both ^{177}Lu-lilotomab and ^{177}Lu-rituximab. Apoptosis level was lower in Ramos cells and in between for Rec-1 cells. These results are in agreement with *in vitro* and *in vivo* results indicating that the therapeutic efficacy of ^{177}Lu-lilotomab and ^{177}Lu-rituximab is higher in DOHH2 models and can be correlated with observed cell radiosensitivity.

Radioresistant Ramos model is characterised by an increase number of cells in G2/M after treatment with ^{177}Lu-mAbs

Since apoptosis is tightly under the control of cell cycle checkpoints, the distribution of treated cells through cell cycle phases (G0/G1, S and G2/M) was analysed. In response to ^{177}Lu-

mAb treatments, the number of cells in G2/M was strongly increased compared to untreated cells in the radioresistant cell line while it was not in the most radiosensitive cell line. During G2 phase, CDK1 is activated by binding to cyclins A2 and B [220]. When entering M phase, cyclin A2 is degraded and the CDK1-cyclin B complex remains that will be further degraded during late mitosis. Besides the association of CDK1 with cyclins, G2/M cell cycle progression is promoted when CDK1 is phosphorylated on Thr161. Conversely, a phosphorylation on Tyr 15 by Wee-1 and/or on Thr14 by Myt-1 blocks the cells in G2/M [221], [222]. In the radiosensitive DOHH2 cells, after treatment with ^{177}Lu-lilotomab, pTyr15-CDK1 and pThr14-CDK1 levels are decreased, whereas pThr161-CDK1 ones are increased. Conversely in Ramos and Rec-1 cells, the expression of pTyr15-CDK1 and pThr14-CDK1 is high whereas the expression of pThr161-CDK1 is low. These proteins phosphorylation are in agreement with cell cycle analysis. Then, G2/M arrest would be the major checkpoint affecting the radiosensitivity of the cell lines. G2/M arrest provides cells time to repair DNA damage in response to ^{177}Lu-mAb treatment, before progressing through cell cycle. In DOHH2 cells, lack of G2/M arrest is accompanied by strong apoptosis induction. In order to confirm the role of G2/M arrest, inhibitors of the phosphorylation of the CDK1 on Thr14 and Tyr15 were used. The MK-1775, a specific inhibitor of Wee-1 and PD-166285 inhibiting both Wee-1 and Myt-1 were used. These inhibitors were used in combination with ^{177}Lu-lilotomab. First, inhibition of the Wee-1 and Myt-1 kinase activity was confirmed by Western Blotting since a decrease in CDK1 phosphorylations was observed in the three treated cell lines. Subsequently, the percentage of cells in G2/M was shown to decrease in cells treated with the combinations compared to the cells only treated with ^{177}Lu-lilotomab in all the cell lines. Next, the anti-proliferative effects of these inhibitors on cells exposed to ^{177}Lu-liotomab was shown with a more marked effect in the radioresistant Ramos cell line. The results confirm the implication of the CDK1 phosphorylations in cell response after treatment with radiolabelled mAbs.

Inhibition of G2/M cell cycle arrest radiosensitises radioresistant Ramos model

The Bliss independence mathematical model was next used to investigate the role of MK-1775 or PD-166285 on the response to ^{177}Lu-lilotomab. A theoretical therapeutic efficacy was calculated for the two combinations (MK-1775 or PD-166285) in the three cell lines. And the comparison between the experimental and the theoretical curves was done.

$$Theoretical\ efficacy_{RIT+inhib} = Efficacy_{RIT} + Efficacy_{inhib} - (Efficacy_{RIT} \times Efficacy_{Inhib})$$

A synergy (p= 0.0495) between inhibitors and ^{177}Lu-lilotomab was shown in Ramos cells. In DOHH2 and Rec-1 cells, the combination was shown to be additive only. This can be probably

explained by the fact that G2/M cell cycle arrest is less marked in Rec-1 cells and absent in DOHH2 cells.

Finally, the following mechanism of action of ^{177}Lu-lilotomab (Figure 102) was proposed.

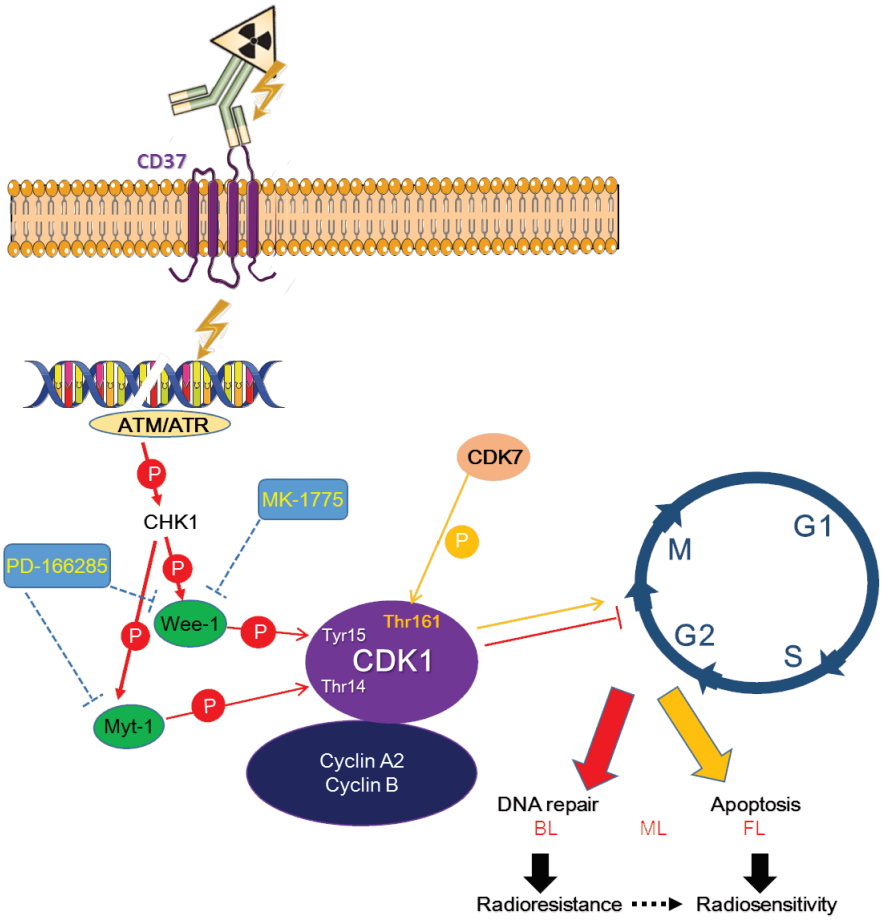

Figure 102: Proposed mechanism of action of ^{177}Lu-lilotomab

CONCLUSION & PERSPECTIVES

My PhD project consisted of investigating in three NHL models the therapeutic efficacy of ^{177}Lu-lilotomab and to compare it with that of rituximab and ^{177}Lu-rituximab using clonogenic assay and dosimetry approaches (for radiolabelled mAbs). In a second time, my work aimed at investigating the molecular mechanisms underlying tumour cell response.

^{177}Lu-lilotomab was more efficient than rituximab in transformed follicular lymphoma preclinical models. ^{177}Lu-lilotomab was also efficient in Burkitt's lymphoma cells, but much higher doses were required. Moreover, reduced CDK1-mediated G2/M cell cycle arrest was shown to predict ^{177}Lu-lilotomab efficacy. Release of Ramos and Rec-1 cells from G2/M cell cycle arrest using a Wee-1 pharmacological inhibitor (MK-1775) sensitised these cells to ^{177}Lu-lilotomab. These results support the clinical studies showing that ^{177}Lu-lilotomab was particularly active in relapsed indolent lymphoma. Finally, it must be noted that in our experimental approach, immunological response was reduced because we used immunodeficient mice, although some ADCC effects could be expected because NK cells are active in both mouse strains. In a clinical setting, the immunological response could be enhanced by using the chimeric version of lilotomab that can activate ADCC.

Correlation between ^{177}Lu-lilotomab cytotoxicity and CDK1 phosphorylation on biopsies

To validate results, we will perform experiments on biopsies from patient which are suffering from follicular lymphoma, diffuse large B-cell lymphoma and chronic lymphoid leukemia. Indeed, 9 biopsies (3 of each type) will be treated with ^{177}Lu-lilotomab and the CDK1 phosphorylations will be analysed.

Presence of stem cell markers on radiosensitive DOHH2 cells after treatment

A preliminary study to determine how cells can survive after treatment was performed. Cancer stem cells are described by the American Association of Cancer Research, as cells that "constitute a reservoir of self-sustaining cells with the exclusive ability to self-renew and maintain the tumour" [223]. To better understand why the radiolabelled mAb treatment did not eradicate the tumour cells in the petri dish even in the radiosensitive cell line, the expression of the cancer stem cell markers at the surface of the treated cells was analysed from the beginning of the treatment to 9 days post-treatment.

A variety of cancer stem cells have been identified in an increasing number of epithelial tumours, including breast, prostate, pancreatic, and head and neck carcinomas, the majority of them express the cell-surface glycoprotein CD44. Another cell surface marker, the CD133

glycoprotein, defined the tumour-initiating cells of brain and colon carcinomas [223]. In lymphoma, a first study [224] could indicate the existence of the $CD45^{+}/CD19^{-}$ subpopulation in Mantle lymphoma which are highly tumorigenic and display self-renewal capacity *in vivo*.

For a preliminary study, investigation of the expression of CD133 and CD44 at the surface of cells treated for 18h with 6 MBq/mL ^{177}Lu-lilotomab and ^{177}Lu-rituximab was done. Figure 103 shows the ratio between the number of receptors at the treated cell surface and the number of receptors at the untreated cell surface.

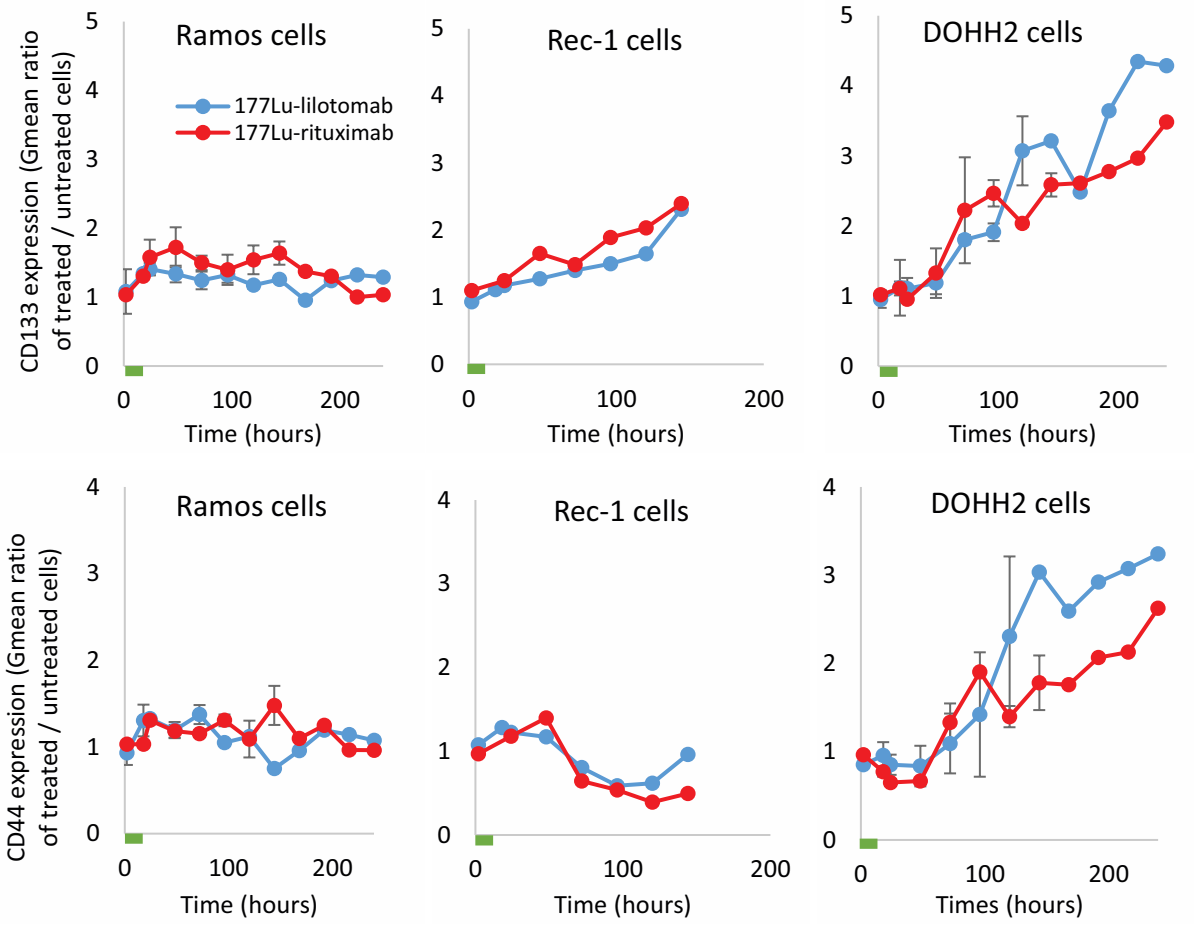

Figure 103: Quantification of CD133 and CD44 at the Ramos, DOHH2 and Rec-1 cell surface after RIT (green bar: treatment period)

The proportion of cells expressing CD44 and CD133 strongly increased up to 9 days post-RIT in the radiosensitive DOHH2 cell line exposed to ^{177}Lu-lilotomab or ^{177}Lu-rituximab and also in Rec-1 cells to a lower extent, but not in Ramos cells. These results suggest that after RIT in the radiosensitive cell line, the population of surviving cells is modified. The hypothesis is that this population is resistant to the treatment and allows forming afresh the tumour; in the radioresistant cell line, the treatment did not select enough stem cell population to show a modification of the cell population.

In order to go further, it would be interesting to determine if this new population ($CD133^+/CD44^+$) is more radioresistant than the primary population and to determine the differences of characteristics between this new population and the primary one (time of culture growth, xenograft growth, response to treatment, …). Finally, another question is to know if the population becomes CD133+/CD44+, or if the treatment selects the cells CD133+/CD44+ already present.

Combination RIT and Wee-1 inhibitor in clinic

Anyway, it would be interesting to consider the combination (RIT + cell cycle arrest inhibitor) in clinic treatment. Indeed, I show that in all the cell lines the combination is always more efficient on cell proliferation than the RIT alone. In clinic, we could think that the results will be similar. Even, without data on the tumour radiosensibility:

-if the tumour is radioresistant, the combination of ^{177}Lu-lilotomab and the cell cycle arrest inhibitor potentiates the effect of ^{177}Lu-lilotomab and radiosensitises the tumour;

-if the tumour is radiosensitive, the combination is also more effective than the RIT alone, at least due to the additivity of the effects, but in a lower extent than in the previous case.

Furthermore, this association is especially interesting, as inhibitors of proteins required for cell cycle progression, such as CD4/CDK6, pan-CDK and Wee-1 inhibitors, have gained interest for cancer therapy of haematological tumours and are assessed in clinical trials [225], [226]. Particularly, MK-1775 enhances the efficacy of SRC inhibitors in Burkitt's lymphoma [227] and the combination of CHK1 and Wee-1 inhibitors is synergistic in mantle cell lymphoma [228].

Moreover, clinical trials are assessing CHK1 pharmacological inhibitors to sensitize tumour cells to DNA damage [229], [230], because CHK1 is involved in Wee-1 and Myt-1 phosphorylations [185].However, it must be noted that in our experimental model, P-CHK1 expression were not modified by exposure to^{177}Lu-mAbs.

Implication of the protein 14-3-3 in cell radiosensitivity?

Other proteins could be targeted to potentiate the effect of ^{177}Lu-lilotomab. For example, the protein 14-3-3 can also be a great candidate of targeting during a RIT. A critical role of 14-3-3 proteins in cancer has been studied particularly in breast, lung and head and neck cancers [231]. In support of a predominant role of 14-3-3, high expression of 14-3-3 is associated with poor prognosis of breast cancer patients [232].

This protein is implicated in the cytoplasmic sequestration of CDC25C and prevents mitotic entry [179] through the non dephosphorylation of CDK1 in position 14 and 15 by the CDC25C. Moreover, 14-3-3 binds also to the phosphorylated protein Bad in order to inhibit its

pro-apoptotic function because Bad promotes the release of the cytochrome C through its inactivation of Bcl-xL or Bcl-2, leading to apoptosis induction. To conclude, the inhibition of 14-3-3 during RIT treatment could decrease the cell cycle arrest and increase the apoptosis induction driving cells even more sensitive to the radiation damages.

To support this reflexion, in the study of [233], the therapeutic efficacy of the difopein (a 14-3-3 antagonist) on human glioma cells was studied. The authors showed that this 14-3-3 antagonist had strong effects to induce glioma cell apoptosis through down-regulating Bcl-2, up-regulating Bax and activating caspase-9 and caspase-3. Moreover, the treated cells showed a reduce percentage of cells in G2/M and this inhibitor decreased the tumour xenograft growth compared to control.

BIBLIOGRAPHY

[1] S. H. Swerdlow *et al.*, 'The 2016 revision of the World Health Organization classification of lymphoid neoplasms', *Blood*, vol. 127, no. 20, pp. 2375–2390, May 2016.
[2] J. Ferlay *et al.*, 'Cancer incidence and mortality worldwide: Sources, methods and major patterns in GLOBOCAN 2012', *Int. J. Cancer*, vol. 136, no. 5, pp. E359–E386, Mar. 2015.
[3] J. L. Ziegler *et al.*, 'Non-Hodgkin's lymphoma in 90 homosexual men. Relation to generalized lymphadenopathy and the acquired immunodeficiency syndrome', *N. Engl. J. Med.*, vol. 311, no. 9, pp. 565–570, Aug. 1984.
[4] P. Andreone *et al.*, 'Posttransplantation Lymphoproliferative Disorders', *Arch. Intern. Med.*, vol. 163, no. 17, pp. 1997–2004, Sep. 2003.
[5] J. J. Castillo, R. R. Ingham, J. L. Reagan, M. Furman, S. Dalia, and J. Mitri, 'Obesity Is Associated With Increased Relative Risk of Diffuse Large B-Cell Lymphoma: A Meta-Analysis of Observational Studies', *Clin. Lymphoma Myeloma Leuk.*, vol. 14, no. 2, pp. 122–130, Apr. 2014.
[6] J. Cuttner, H. Spiera, K. Troy, and S. Wallenstein, 'Autoimmune disease is a risk factor for the development of non-Hodgkin's lymphoma', *J. Rheumatol.*, vol. 32, no. 10, pp. 1884–1887, Oct. 2005.
[7] I. W. G. on the E. of C. R. to Humans, *Epstein-Barr Virus and Kaposi's Sarcoma Herpesvirus/Human Herpesvirus 8*. International Agency for Research on Cancer, 1997.
[8] R. Wilks *et al.*, 'Patterns of HTLV-I infection among family members of patients with adult T-cell leukemia/lymphoma and HTLV-I associated myelopathy/tropical spastic paraparesis', *Int. J. Cancer*, vol. 65, no. 2, pp. 272–273, Jan. 1996.
[9] G. Pozzato *et al.*, 'Low-grade malignant lymphoma, hepatitis C virus infection, and mixed cryoglobulinemia', *Blood*, vol. 84, no. 9, pp. 3047–3053, Nov. 1994.
[10] A. C. Wotherspoon, C. Ortiz-Hidalgo, M. R. Falzon, and P. G. Isaacson, 'Helicobacter pylori-associated gastritis and primary B-cell gastric lymphoma', *Lancet Lond. Engl.*, vol. 338, no. 8776, pp. 1175–1176, Nov. 1991.
[11] S. Jelić and I. Filipović-Ljesković, 'Positive serology for Lyme disease borrelias in primary cutaneous B-cell lymphoma: a study in 22 patients; is it a fortuitous finding?', *Hematol. Oncol.*, vol. 17, no. 3, pp. 107–116, Sep. 1999.
[12] D. B. Richardson *et al.*, 'Positive Associations Between Ionizing Radiation and Lymphoma Mortality Among Men', *Am. J. Epidemiol.*, vol. 169, no. 8, pp. 969–976, Apr. 2009.
[13] N. Puebla-Osorio *et al.*, 'Induction of B-cell lymphoma by UVB Radiation in p53 Haploinsufficient Mice', *BMC Cancer*, vol. 11, p. 36, 2011.
[14] D. Luo, T. Zhou, Y. Tao, Y. Feng, X. Shen, and S. Mei, 'Exposure to organochlorine pesticides and non-Hodgkin lymphoma: a meta-analysis of observational studies', *Sci. Rep.*, vol. 6, p. srep25768, May 2016.
[15] Y. Zhang *et al.*, 'Personal use of hair dye and the risk of certain subtypes of non-Hodgkin lymphoma', *Am. J. Epidemiol.*, vol. 167, no. 11, pp. 1321–1331, Jun. 2008.
[16] B. W. Steward and C. . Wild, *World Cancer Report 2014 - WHO - OMS* -. IARC Press, 2014.
[17] S.-H. Lee, T. Miyagi, and C. A. Biron, 'Keeping NK cells in highly regulated antiviral warfare', *Trends Immunol.*, vol. 28, no. 6, pp. 252–259, Jun. 2007.
[18] M. J. Smyth, Y. Hayakawa, K. Takeda, and H. Yagita, 'New aspects of natural-killer-cell surveillance and therapy of cancer', *Nat. Rev. Cancer*, vol. 2, no. 11, pp. 850–861, Nov. 2002.
[19] T. Walzer, M. Dalod, S. H. Robbins, L. Zitvogel, and E. Vivier, 'Natural-killer cells and dendritic cells: "l9union fait la force"', *Blood*, vol. 106, no. 7, pp. 2252–2258, Oct. 2005.
[20] N. Zhang and M. J. Bevan, 'CD8+ T Cells: Foot Soldiers of the Immune System', *Immunity*, vol. 35, no. 2, pp. 161–168, Aug. 2011.
[21] R. V. Luckheeram, R. Zhou, A. D. Verma, and B. Xia, 'CD4+T Cells: Differentiation and Functions', *Clin. Dev. Immunol.*, vol. 2012, 2012.
[22] D. A. A. Vignali, L. W. Collison, and C. J. Workman, 'How regulatory T cells work', *Nat. Rev. Immunol.*, vol. 8, no. 7, pp. 523–532, Jul. 2008.

[23] F. E. Lund, 'Cytokine-producing B lymphocytes – key regulators of immunity', *Curr. Opin. Immunol.*, vol. 20, no. 3, pp. 332–338, Jun. 2008.
[24] R. Berry, Z. Chen, J. McCluskey, and J. Rossjohn, 'Insight into the basis of autonomous immunoreceptor activation', *Trends Immunol.*, vol. 32, no. 4, pp. 165–170, Apr. 2011.
[25] R. Küppers, 'Mechanisms of B-cell lymphoma pathogenesis', *Nat. Rev. Cancer*, vol. 5, no. 4, pp. 251–262, Apr. 2005.
[26] J. Charles A Janeway, P. Travers, M. Walport, and M. J. Shlomchik, 'T-cell receptor gene rearrangement', 2001.
[27] 'Lymph Nodes Immune System', *Human Anatomy Chart*, 24-Jul-2015. [Online]. Available: http://humananatomychart.us/lymph-nodes-immune-system/. [Accessed: 22-Sep-2017].
[28] 'VAT: The Lymphatic System'. [Online]. Available: https://www-s.acm.illinois.edu/sigbio/project/updated-lymphatic/lymph6.html. [Accessed: 24-Sep-2017].
[29] P. M. Kluin, 'Origin and migration of follicular lymphoma cells', *Haematologica*, vol. 98, no. 9, pp. 1331–1333, Sep. 2013.
[30] C. S. Osborne *et al.*, 'Myc dynamically and preferentially relocates to a transcription factory occupied by Igh', *PLoS Biol.*, vol. 5, no. 8, p. e192, Aug. 2007.
[31] J. Zheng, 'Oncogenic chromosomal translocations and human cancer (Review)', *Oncol. Rep.*, vol. 30, no. 5, pp. 2011–2019, Nov. 2013.
[32] F. Schüler *et al.*, 'Prevalence and frequency of circulating t(14;18)-MBR translocation carrying cells in healthy individuals', *Int. J. Cancer J. Int. Cancer*, vol. 124, no. 4, p. 958, Feb. 2009.
[33] J. O. Armitage, R. D. Gascoyne, M. A. Lunning, and F. Cavalli, 'Non-Hodgkin lymphoma', *The Lancet*, vol. 0, no. 0, Jan. 2017.
[34] M. M. Le Beau *et al.*, 'The t(2;5)(p23;q35): a recurring chromosomal abnormality in Ki-1-positive anaplastic large cell lymphoma', *Leukemia*, vol. 3, no. 12, pp. 866–870, Dec. 1989.
[35] B. Streubel, U. Vinatzer, M. Willheim, M. Raderer, and A. Chott, 'Novel t(5;9)(q33;q22) fuses ITK to SYK in unspecified peripheral T-cell lymphoma', *Leukemia*, vol. 20, no. 2, pp. 313–318, Dec. 2005.
[36] A. J. M. Ferreri, S. Govi, S. A. Pileri, and K. J. Savage, 'Anaplastic large cell lymphoma, ALK-positive', *Crit. Rev. Oncol. Hematol.*, vol. 83, no. 2, pp. 293–302, Aug. 2012.
[37] P. P. Carbone, H. S. Kaplan, K. Musshoff, D. W. Smithers, and M. Tubiana, 'Report of the Committee on Hodgkin9s Disease Staging Classification', *Cancer Res.*, vol. 31, no. 11, pp. 1860–1861, Nov. 1971.
[38] T. A. Lister *et al.*, 'Report of a committee convened to discuss the evaluation and staging of patients with Hodgkin's disease: Cotswolds meeting', *J. Clin. Oncol. Off. J. Am. Soc. Clin. Oncol.*, vol. 7, no. 11, pp. 1630–1636, Nov. 1989.
[39] 'Hodgkin Lymphoma Staging', 26-Feb-2015. [Online]. Available: https://www.lls.org/lymphoma/hodgkin-lymphoma/diagnosis/hodgkin-lymphoma-staging. [Accessed: 30-Jun-2017].
[40] T. I. N.-H. L. P. F. Project, 'A Predictive Model for Aggressive Non-Hodgkin's Lymphoma', *N. Engl. J. Med.*, vol. 329, no. 14, pp. 987–994, Sep. 1993.
[41] M. M. Oken *et al.*, 'Toxicity and response criteria of the Eastern Cooperative Oncology Group', *Am. J. Clin. Oncol.*, vol. 5, no. 6, pp. 649–655, Dec. 1982.
[42] D. M. Noll, T. M. Mason, and P. S. Miller, 'Formation and Repair of Interstrand Cross-Links in DNA', *Chem. Rev.*, vol. 106, no. 2, pp. 277–301, Feb. 2006.
[43] U. F. O. Themes, 'Alkylating agents and platinum antitumor compounds', *Oncohema Key*, 12-Apr-2017. .
[44] K.-T. Lin and L.-H. Wang, 'New dimension of glucocorticoids in cancer treatment', *Steroids*, vol. 111, no. Supplement C, pp. 84–88, Jul. 2016.

[45] J. Sigmond and G. J. Peters, 'Pyrimidine and purine analogues, effects on cell cycle regulation and the role of cell cycle inhibitors to enhance their cytotoxicity', *Nucleosides Nucleotides Nucleic Acids*, vol. 24, no. 10–12, pp. 1997–2022, 2005.
[46] J. T. Bau, Z. Kang, C. A. Austin, and E. U. Kurz, 'Salicylate, a Catalytic Inhibitor of Topoisomerase II, Inhibits DNA Cleavage and Is Selective for the α Isoform', *Mol. Pharmacol.*, vol. 85, no. 2, pp. 198–207, Feb. 2014.
[47] PDQ Adult Treatment Editorial Board, 'Adult Non-Hodgkin Lymphoma Treatment (PDQ®): Health Professional Version', in *PDQ Cancer Information Summaries*, Bethesda (MD): National Cancer Institute (US), 2002.
[48] 'Oncomip - Référentiel de traitement des LYMPHOMES de l'ADULTE (2016)', Apr-2016. [Online]. Available: http://www.oncomip.org/fr/espace-professionnel/referentiels/traitement-des-lymphomes-de-l-adulte2016-68/. [Accessed: 04-Jul-2017].
[49] J. Harry W Schroeder, 'Structure and Function of Immunoglobulins', *J. Allergy Clin. Immunol.*, vol. 125, no. 2 0 2, p. S41, Feb. 2010.
[50] P. Carter, 'Improving the efficacy of antibody-based cancer therapies', *Nat. Rev. Cancer*, vol. 1, no. 2, pp. 118–129, Nov. 2001.
[51] J. R. Dunkelberger and W.-C. Song, 'Complement and its role in innate and adaptive immune responses', *Cell Res.*, vol. 20, no. 1, pp. 34–50, Dec. 2009.
[52] 'The complement system'. [Online]. Available: http://www.virology.ws/2009/09/28/the-complement-system/. [Accessed: 14-Jul-2017].
[53] D. Metes, L. K. Ernst, W. H. Chambers, A. Sulica, R. B. Herberman, and P. A. Morel, 'Expression of Functional CD32 Molecules on Human NK Cells Is Determined by an Allelic Polymorphism of the FcγRIIC Gene', *Blood*, vol. 91, no. 7, pp. 2369–2380, Apr. 1998.
[54] W. Wang, A. K. Erbe, J. A. Hank, Z. S. Morris, and P. M. Sondel, 'NK Cell-Mediated Antibody-Dependent Cellular Cytotoxicity in Cancer Immunotherapy', *Front. Immunol.*, vol. 6, Jul. 2015.
[55] N. Gül *et al.*, 'Macrophages eliminate circulating tumor cells after monoclonal antibody therapy', *J. Clin. Invest.*, vol. 124, no. 2, pp. 812–823, Feb. 2014.
[56] G. Köhler and C. Milstein, 'Continuous cultures of fused cells secreting antibody of predefined specificity', *Nature*, vol. 256, no. 5517, pp. 495–497, Aug. 1975.
[57] M. E. Reff *et al.*, 'Depletion of B cells in vivo by a chimeric mouse human monoclonal antibody to CD20', *Blood*, vol. 83, no. 2, pp. 435–445, Jan. 1994.
[58] J. A. Ernst, H. Li, H. S. Kim, G. R. Nakamura, D. G. Yansura, and R. L. Vandlen, 'Isolation and Characterization of the B-Cell Marker CD20', *Biochemistry (Mosc.)*, vol. 44, no. 46, pp. 15150–15158, Nov. 2005.
[59] P. Stashenko, L. M. Nadler, R. Hardy, and S. F. Schlossman, 'Characterization of a human B lymphocyte-specific antigen.', *J. Immunol.*, vol. 125, no. 4, pp. 1678–1685, Jan. 1980.
[60] K. C. Anderson, M. P. Bates, B. L. Slaughenhoupt, G. S. Pinkus, S. F. Schlossman, and L. M. Nadler, 'Expression of human B cell-associated antigens on leukemias and lymphomas: a model of human B cell differentiation', *Blood*, vol. 63, no. 6, pp. 1424–1433, Jun. 1984.
[61] J. K. Bubien, L. J. Zhou, P. D. Bell, R. A. Frizzell, and T. F. Tedder, 'Transfection of the CD20 cell surface molecule into ectopic cell types generates a Ca2+ conductance found constitutively in B lymphocytes.', *J. Cell Biol.*, vol. 121, no. 5, pp. 1121–1132, Jun. 1993.
[62] C. A. Walshe *et al.*, 'Induction of Cytosolic Calcium Flux by CD20 Is Dependent upon B Cell Antigen Receptor Signaling', *J. Biol. Chem.*, vol. 283, no. 25, pp. 16971–16984, Jun. 2008.
[63] 'Rituximab - Product Approval Information - Licensing Action'. [Online]. Available: https://www.accessdata.fda.gov/drugsatfda_docs/appletter/1997/ritugen112697L.htm. [Accessed: 17-Sep-2017].
[64] J. P. Deans, S. M. Robbins, M. J. Polyak, and J. A. Savage, 'Rapid redistribution of CD20 to a low density detergent-insoluble membrane compartment', *J. Biol. Chem.*, vol. 273, no. 1, pp. 344–348, Jan. 1998.

[65] M. Binder, F. Otto, R. Mertelsmann, H. Veelken, and M. Trepel, 'The epitope recognized by rituximab', *Blood*, vol. 108, no. 6, pp. 1975–1978, Sep. 2006.
[66] S. H. Lim *et al.*, 'Fc gamma receptor IIb on target B cells promotes rituximab internalization and reduces clinical efficacy', *Blood*, vol. 118, no. 9, pp. 2530–2540, Sep. 2011.
[67] H. T. C. Chan *et al.*, 'CD20-induced Lymphoma Cell Death Is Independent of Both Caspases and Its Redistribution into Triton X-100 Insoluble Membrane Rafts', *Cancer Res.*, vol. 63, no. 17, pp. 5480–5489, Sep. 2003.
[68] A. M. Mattila and S. Meri, 'Responses to rituximab vary among follicular lymphoma B cells of different maturation stages', *Scand. J. Immunol.*, vol. 68, no. 2, pp. 159–168, Aug. 2008.
[69] E. E. Idusogie *et al.*, 'Mapping of the C1q binding site on rituxan, a chimeric antibody with a human IgG1 Fc', *J. Immunol. Baltim. Md 1950*, vol. 164, no. 8, pp. 4178–4184, Apr. 2000.
[70] A. Harjunpää, S. Junnikkala, and S. Meri, 'Rituximab (anti-CD20) therapy of B-cell lymphomas: direct complement killing is superior to cellular effector mechanisms', *Scand. J. Immunol.*, vol. 51, no. 6, pp. 634–641, Jun. 2000.
[71] G. Cartron *et al.*, 'Therapeutic activity of humanized anti-CD20 monoclonal antibody and polymorphism in IgG Fc receptor FcγRIIIa gene', *Blood*, vol. 99, no. 3, pp. 754–758, Feb. 2002.
[72] D. Shan, J. A. Ledbetter, and O. W. Press, 'Signaling events involved in anti-CD20-induced apoptosis of malignant human B cells', *Cancer Immunol. Immunother. CII*, vol. 48, no. 12, pp. 673–683, Mar. 2000.
[73] J. K. Hofmeister, D. Cooney, and K. M. Coggeshall, 'Clustered CD20 Induced Apoptosis: Src-Family Kinase, the Proximal Regulator of Tyrosine Phosphorylation, Calcium Influx, and Caspase 3-Dependent Apoptosis', *Blood Cells. Mol. Dis.*, vol. 26, no. 2, pp. 133–143, Apr. 2000.
[74] P. M. Kasi, H. A. Tawbi, C. V. Oddis, and H. S. Kulkarni, 'Clinical review: Serious adverse events associated with the use of rituximab - a critical care perspective', *Crit. Care*, vol. 16, no. 4, p. 231, 2012.
[75] J. Eeva *et al.*, 'The involvement of mitochondria and the caspase-9 activation pathway in rituximab-induced apoptosis in FL cells', *Apoptosis*, vol. 14, no. 5, pp. 687–698, May 2009.
[76] S. Alas, C. Emmanouilides, and B. Bonavida, 'Inhibition of Interleukin 10 by Rituximab Results in Down-Regulation of Bcl-2 and Sensitization of B-cell Non-Hodgkin's Lymphoma to Apoptosis', *Clin. Cancer Res.*, vol. 7, no. 3, pp. 709–723, Mar. 2001.
[77] S. Alas and B. Bonavida, 'Rituximab Inactivates Signal Transducer and Activation of Transcription 3 (STAT3) Activity in B-Non-Hodgkin's Lymphoma through Inhibition of the Interleukin 10 Autocrine/Paracrine Loop and Results in Down-Regulation of Bcl-2 and Sensitization to Cytotoxic Drugs', *Cancer Res.*, vol. 61, no. 13, pp. 5137–5144, Jul. 2001.
[78] A. R. Jazirehi, M. I. Vega, D. Chatterjee, L. Goodglick, and B. Bonavida, 'Inhibition of the Raf–MEK1/2–ERK1/2 Signaling Pathway, Bcl-$_{xL}$ Down-Regulation, and Chemosensitization of Non-Hodgkin's Lymphoma B Cells by Rituximab', *Cancer Res.*, vol. 64, no. 19, pp. 7117–7126, Oct. 2004.
[79] K. C. Yeung *et al.*, 'Raf kinase inhibitor protein interacts with NF-kappaB-inducing kinase and TAK1 and inhibits NF-kappaB activation', *Mol. Cell. Biol.*, vol. 21, no. 21, pp. 7207–7217, Nov. 2001.
[80] E. Suzuki, K. Umezawa, and B. Bonavida, 'Rituximab inhibits the constitutively activated PI3K-Akt pathway in B-NHL cell lines: involvement in chemosensitization to drug-induced apoptosis', *Oncogene*, vol. 26, no. 42, pp. 6184–6193, Apr. 2007.
[81] X. Deng, T. Ito, B. Carr, M. Mumby, and W. S. May, 'Reversible phosphorylation of Bcl2 following interleukin 3 or bryostatin 1 is mediated by direct interaction with protein phosphatase 2A', *J. Biol. Chem.*, vol. 273, no. 51, pp. 34157–34163, Dec. 1998.
[82] S. Sato, N. Fujita, and T. Tsuruo, 'Modulation of Akt kinase activity by binding to Hsp90', *Proc. Natl. Acad. Sci. U. S. A.*, vol. 97, no. 20, pp. 10832–10837, Sep. 2000.

[83] J. Golay *et al.*, 'Biologic response of B lymphoma cells to anti-CD20 monoclonal antibody rituximab in vitro: CD55 and CD59 regulate complement-mediated cell lysis', *Blood*, vol. 95, no. 12, pp. 3900–3908, Jun. 2000.
[84] N. Di Gaetano *et al.*, 'Complement activation determines the therapeutic activity of rituximab in vivo', *J. Immunol. Baltim. Md 1950*, vol. 171, no. 3, pp. 1581–1587, Aug. 2003.
[85] J. Golay *et al.*, 'The role of complement in the therapeutic activity of rituximab in a murine B lymphoma model homing in lymph nodes', *Haematologica*, vol. 91, no. 2, pp. 176–183, Jan. 2006.
[86] S.-Y. Wang, E. Racila, R. P. Taylor, and G. J. Weiner, 'NK-cell activation and antibody-dependent cellular cytotoxicity induced by rituximab-coated target cells is inhibited by the C3b component of complement', *Blood*, vol. 111, no. 3, pp. 1456–1463, Feb. 2008.
[87] R. A. Clynes, T. L. Towers, L. G. Presta, and J. V. Ravetch, 'Inhibitory Fc receptors modulate in vivo cytotoxicity against tumor targets', *Nat. Med.*, vol. 6, no. 4, pp. 443–446, Apr. 2000.
[88] W.-K. Weng and R. Levy, 'Two immunoglobulin G fragment C receptor polymorphisms independently predict response to rituximab in patients with follicular lymphoma', *J. Clin. Oncol. Off. J. Am. Soc. Clin. Oncol.*, vol. 21, no. 21, pp. 3940–3947, Nov. 2003.
[89] T. A. Davis *et al.*, 'Rituximab Anti-CD20 Monoclonal Antibody Therapy in Non-Hodgkin's Lymphoma: Safety and Efficacy of Re-Treatment', *J. Clin. Oncol.*, vol. 18, no. 17, pp. 3135–3143, Sep. 2000.
[90] K. Takei, T. Yamazaki, U. Sawada, H. Ishizuka, and S. Aizawa, 'Analysis of changes in CD20, CD55, and CD59 expression on established rituximab-resistant B-lymphoma cell lines', *Leuk. Res.*, vol. 30, no. 5, pp. 625–631, May 2006.
[91] A. R. Jazirehi, M. I. Vega, and B. Bonavida, 'Development of Rituximab-Resistant Lymphoma Clones with Altered Cell Signaling and Cross-Resistance to Chemotherapy', *Cancer Res.*, vol. 67, no. 3, pp. 1270–1281, Feb. 2007.
[92] S. H. Olejniczak, F. J. Hernandez-Ilizaliturri, J. L. Clements, and M. S. Czuczman, 'Acquired Resistance to Rituximab Is Associated with Chemotherapy Resistance Resulting from Decreased Bax and Bak Expression', *Clin. Cancer Res.*, vol. 14, no. 5, pp. 1550–1560, Mar. 2008.
[93] A. Molina, 'A Decade of Rituximab: Improving Survival Outcomes in Non-Hodgkin's Lymphoma', *Annu. Rev. Med.*, vol. 59, no. 1, pp. 237–250, 2008.
[94] T. A. Davis *et al.*, 'Single-Agent Monoclonal Antibody Efficacy in Bulky Non-Hodgkin's Lymphoma: Results of a Phase II Trial of Rituximab', *J. Clin. Oncol.*, vol. 17, no. 6, pp. 1851–1851, Jun. 1999.
[95] J. M. Foran *et al.*, 'A UK multicentre phase II study of rituximab (chimaeric anti-CD20 monoclonal antibody) in patients with follicular lymphoma, with PCR monitoring of molecular response', *Br. J. Haematol.*, vol. 109, no. 1, pp. 81–88, Apr. 2000.
[96] M. S. Czuczman, R. Weaver, B. Alkuzweny, J. Berlfein, and A. J. Grillo-López, 'Prolonged Clinical and Molecular Remission in Patients With Low-Grade or Follicular Non-Hodgkin's Lymphoma Treated With Rituximab Plus CHOP Chemotherapy: 9-Year Follow-Up', *J. Clin. Oncol.*, vol. 22, no. 23, pp. 4711–4716, Dec. 2004.
[97] P. Feugier *et al.*, 'Long-term results of the R-CHOP study in the treatment of elderly patients with diffuse large B-cell lymphoma: a study by the Groupe d'Etude des Lymphomes de l'Adulte', *J. Clin. Oncol. Off. J. Am. Soc. Clin. Oncol.*, vol. 23, no. 18, pp. 4117–4126, Jun. 2005.
[98] V. Singh, D. Gupta, and A. Almasan, 'Development of Novel Anti-Cd20 Monoclonal Antibodies and Modulation in Cd20 Levels on Cell Surface: Looking to Improve Immunotherapy Response', *J. Cancer Sci. Ther.*, vol. 7, no. 11, pp. 347–358, Nov. 2015.
[99] A. W. Pawluczkowycz *et al.*, 'Binding of submaximal C1q promotes complement-dependent cytotoxicity (CDC) of B cells opsonized with anti-CD20 mAbs ofatumumab (OFA) or rituximab (RTX): considerably higher levels of CDC are induced by OFA than by RTX', *J. Immunol. Baltim. Md 1950*, vol. 183, no. 1, pp. 749–758, Jul. 2009.

[100] S. A. Bhat and M. S. Czuczman, 'Novel antibodies in the treatment of non-Hodgkin's lymphoma', *Neth. J. Med.*, vol. 67, no. 8, pp. 311–321, Sep. 2009.
[101] G. Hale, M.-Q. Xia, H. P. Tighe, M. J. S. Dyer, and H. Waldmann, 'The CAMPATH-1 antigen (CDw52)', *Tissue Antigens*, vol. 35, no. 3, pp. 118–127, Mar. 1990.
[102] T. Watanabe *et al.*, 'CD52 is a novel costimulatory molecule for induction of CD4+ regulatory T cells', *Clin. Immunol. Orlando Fla*, vol. 120, no. 3, pp. 247–259, Sep. 2006.
[103] M. E. Keir, M. J. Butte, G. J. Freeman, and A. H. Sharpe, 'PD-1 and Its Ligands in Tolerance and Immunity', *Annu. Rev. Immunol.*, vol. 26, no. 1, pp. 677–704, 2008.
[104] A. M. Lesokhin *et al.*, 'Nivolumab in Patients With Relapsed or Refractory Hematologic Malignancy: Preliminary Results of a Phase Ib Study', *J. Clin. Oncol.*, vol. 34, no. 23, pp. 2698–2704, Aug. 2016.
[105] M. Yunta and P. A. Lazo, 'Tetraspanin proteins as organisers of membrane microdomains and signalling complexes', *Cell. Signal.*, vol. 15, no. 6, pp. 559–564, Jun. 2003.
[106] S. Barrena *et al.*, 'Aberrant expression of tetraspanin molecules in B-cell chronic lymphoproliferative disorders and its correlation with normal B-cell maturation', *Leukemia*, vol. 19, no. 8, pp. 1376–1383, Jun. 2005.
[107] R. Schwartz-Albiez, B. Dörken, W. Hofmann, and G. Moldenhauer, 'The B cell-associated CD37 antigen (gp40-52). Structure and subcellular expression of an extensively glycosylated glycoprotein', *J. Immunol. Baltim. Md 1950*, vol. 140, no. 3, pp. 905–914, Feb. 1988.
[108] X. Zhao *et al.*, 'CD37 Is a Potential Therapeutic Target for B-Cell Non-Hodgkin Lymphoma', *Blood*, vol. 116, no. 21, pp. 3098–3098, Nov. 2010.
[109] D. S. Pereira *et al.*, 'AGS67E, an Anti-CD37 Monomethyl Auristatin E Antibody–Drug Conjugate as a Potential Therapeutic for B/T-Cell Malignancies and AML: A New Role for CD37 in AML', *Mol. Cancer Ther.*, vol. 14, no. 7, pp. 1650–1660, Jul. 2015.
[110] K.-P. Knobeloch *et al.*, 'Targeted Inactivation of the Tetraspanin CD37 Impairs T-Cell-Dependent B-Cell Response under Suboptimal Costimulatory Conditions', *Mol. Cell. Biol.*, vol. 20, no. 15, pp. 5363–5369, Jan. 2000.
[111] A. B. van Spriel *et al.*, 'The Tetraspanin CD37 Orchestrates the $\alpha_4\beta_1$ Integrin–Akt Signaling Axis and Supports Long-Lived Plasma Cell Survival', *Sci Signal*, vol. 5, no. 250, pp. ra82-ra82, Nov. 2012.
[112] R. Lapalombella *et al.*, 'Tetraspanin CD37 Directly Mediates Transduction of Survival and Apoptotic Signals', *Cancer Cell*, vol. 21, no. 5, pp. 694–708, May 2012.
[113] R. Burger, 'Impact of interleukin-6 in hematological malignancies', *Transfus. Med. Hemotherapy Off. Organ Dtsch. Ges. Transfusionsmedizin Immunhamatologie*, vol. 40, no. 5, pp. 336–343, Oct. 2013.
[114] C. M. de Winde *et al.*, 'Tetraspanin CD37 protects against the development of B cell lymphoma', *J. Clin. Invest.*, vol. 126, no. 2, pp. 653–666, 2016.
[115] F. Meyer-Wentrup *et al.*, 'Dectin-1 Interaction with Tetraspanin CD37 Inhibits IL-6 Production', *J. Immunol.*, vol. 178, no. 1, pp. 154–162, Jan. 2007.
[116] J. M. Pagel *et al.*, 'Otlertuzumab (TRU-016), an anti-CD37 monospecific ADAPTIR(™) therapeutic protein, for relapsed or refractory NHL patients', *Br. J. Haematol.*, vol. 168, no. 1, pp. 38–45, Jan. 2015.
[117] J. C. Byrd *et al.*, 'A phase 1 study evaluating the safety and tolerability of otlertuzumab, an anti-CD37 mono-specific ADAPTIR therapeutic protein in chronic lymphocytic leukemia', *Blood*, vol. 123, no. 9, pp. 1302–1308, Feb. 2014.
[118] A. K. Gopal *et al.*, 'Phase 1b study of otlertuzumab (TRU-016), an anti-CD37 monospecific ADAPTIR™ therapeutic protein, in combination with rituximab and bendamustine in relapsed indolent lymphoma patients', *Invest. New Drugs*, vol. 32, no. 6, pp. 1213–1225, Dec. 2014.

[119] T. Robak *et al.*, 'Randomized phase 2 study of otlertuzumab and bendamustine versus bendamustine in patients with relapsed chronic lymphocytic leukaemia', *Br. J. Haematol.*, vol. 176, no. 4, pp. 618–628, Feb. 2017.
[120] A. Stathis *et al.*, 'A Phase I Study of IMGN529, an Antibody-Drug Conjugate (ADC) Targeting CD37, in Adult Patients with Relapsed or Refractory B-Cell Non-Hodgkin's Lymphoma (NHL)', *Blood*, vol. 124, no. 21, pp. 1760–1760, Dec. 2014.
[121] C. Peters and S. Brown, 'Antibody–drug conjugates as novel anti-cancer chemotherapeutics', *Biosci. Rep.*, vol. 35, no. 4, Jul. 2015.
[122] K. J. Hamblett *et al.*, 'Effects of drug loading on the antitumor activity of a monoclonal antibody drug conjugate', *Clin. Cancer Res. Off. J. Am. Assoc. Cancer Res.*, vol. 10, no. 20, pp. 7063–7070, Oct. 2004.
[123] H. Bouchard, C. Viskov, and C. Garcia-Echeverria, 'Antibody–drug conjugates—A new wave of cancer drugs', *Bioorg. Med. Chem. Lett.*, vol. 24, no. 23, pp. 5357–5363, Dec. 2014.
[124] J. A. Francisco *et al.*, 'cAC10-vcMMAE, an anti-CD30–monomethyl auristatin E conjugate with potent and selective antitumor activity', *Blood*, vol. 102, no. 4, pp. 1458–1465, Aug. 2003.
[125] C. Vaklavas and A. Forero-Torres, 'Safety and efficacy of brentuximab vedotin in patients with Hodgkin lymphoma or systemic anaplastic large cell lymphoma', *Ther. Adv. Hematol.*, vol. 3, no. 4, pp. 209–225, Aug. 2012.
[126] H. M. Kantarjian *et al.*, 'Inotuzumab Ozogamicin versus Standard Therapy for Acute Lymphoblastic Leukemia', *N. Engl. J. Med.*, vol. 375, no. 8, pp. 740–753, Aug. 2016.
[127] M. C. A. Palanca-Wessels *et al.*, 'Safety and activity of the anti-CD79B antibody-drug conjugate polatuzumab vedotin in relapsed or refractory B-cell non-Hodgkin lymphoma and chronic lymphocytic leukaemia: a phase 1 study', *Lancet Oncol.*, vol. 16, no. 6, pp. 704–715, Jun. 2015.
[128] R. H. Advani *et al.*, 'Phase I Study of the Anti-CD22 Antibody-Drug Conjugate Pinatuzumab Vedotin with/without Rituximab in Patients with Relapsed/Refractory B-cell Non-Hodgkin Lymphoma', *Clin. Cancer Res. Off. J. Am. Assoc. Cancer Res.*, vol. 23, no. 5, pp. 1167–1176, Mar. 2017.
[129] W. A. Volkert, W. F. Goeckeler, G. J. Ehrhardt, and A. R. Ketring, 'Therapeutic Radionuclides: Production and Decay Property Considerations', *J. Nucl. Med.*, vol. 32, no. 1, pp. 174–185, Jan. 1991.
[130] S. C. Srivastava, 'Criteria for the selection of radionuclides for targeting nuclear antigens for cancer radioimmunotherapy', *Cancer Biother. Radiopharm.*, vol. 11, no. 1, pp. 43–50, Feb. 1996.
[131] J. G. Jurcic *et al.*, 'Phase I Trial of Targeted Alpha-Particle Therapy Using Actinium-225 (225Ac)-Lintuzumab (Anti-CD33) in Combination with Low-Dose Cytarabine (LDAC) for Older Patients with Untreated Acute Myeloid Leukemia (AML)', *Blood*, vol. 124, no. 21, pp. 5293–5293, Dec. 2014.
[132] J.-P. Pouget and S. J. Mather, 'General aspects of the cellular response to low- and high-LET radiation', *Eur. J. Nucl. Med.*, vol. 28, no. 4, pp. 541–561, Apr. 2001.
[133] B. Shapiro, 'Optimization of radioiodine therapy of thyrotoxicosis: what have we learned after 50 years?', *J. Nucl. Med. Off. Publ. Soc. Nucl. Med.*, vol. 34, no. 10, pp. 1638–1641, Oct. 1993.
[134] R. P. Baum, *Therapeutic Nuclear Medicine*. Springer, 2014.
[135] S. Gupta, S. Batra, and M. Jain, 'Antibody Labeling with Radioiodine and Radiometals', *Methods Mol. Biol. Clifton NJ*, vol. 1141, pp. 147–157, 2014.
[136] M. B. Chadwick *et al.*, 'ENDF/B-VII.1 Nuclear Data for Science and Technology: Cross Sections, Covariances, Fission Product Yields and Decay Data', *Nucl. Data Sheets*, vol. 112, no. 12, pp. 2887–2996, Dec. 2011.
[137] A. Dash, M. R. A. Pillai, and F. F. Knapp, 'Production of 177Lu for Targeted Radionuclide Therapy: Available Options', *Nucl. Med. Mol. Imaging*, vol. 49, no. 2, pp. 85–107, Jun. 2015.

[138] M. S. Kaminski *et al.*, 'Radioimmunotherapy of B-Cell Lymphoma with [131I]Anti-B1 (Anti-CD20) Antibody', *N. Engl. J. Med.*, vol. 329, no. 7, pp. 459–465, Aug. 1993.
[139] A. J. Davies *et al.*, 'Tositumomab and iodine I 131 tositumomab for recurrent indolent and transformed B-cell non-Hodgkin's lymphoma', *J. Clin. Oncol. Off. J. Am. Soc. Clin. Oncol.*, vol. 22, no. 8, pp. 1469–1479, Apr. 2004.
[140] M. S. Kaminski *et al.*, '131I-tositumomab therapy as initial treatment for follicular lymphoma', *N. Engl. J. Med.*, vol. 352, no. 5, pp. 441–449, Feb. 2005.
[141] M. S. Kaminski *et al.*, 'Radioimmunotherapy with iodine (131)I tositumomab for relapsed or refractory B-cell non-Hodgkin lymphoma: updated results and long-term follow-up of the University of Michigan experience', *Blood*, vol. 96, no. 4, pp. 1259–1266, Aug. 2000.
[142] M. S. Kaminski *et al.*, 'Pivotal study of iodine I 131 tositumomab for chemotherapy-refractory low-grade or transformed low-grade B-cell non-Hodgkin's lymphomas', *J. Clin. Oncol. Off. J. Am. Soc. Clin. Oncol.*, vol. 19, no. 19, pp. 3918–3928, Oct. 2001.
[143] J. M. Vose *et al.*, 'Multicenter phase II study of iodine-131 tositumomab for chemotherapy-relapsed/refractory low-grade and transformed low-grade B-cell non-Hodgkin's lymphomas', *J. Clin. Oncol. Off. J. Am. Soc. Clin. Oncol.*, vol. 18, no. 6, pp. 1316–1323, Mar. 2000.
[144] J. P. Leonard *et al.*, 'Abbreviated chemotherapy with fludarabine followed by tositumomab and iodine I 131 tositumomab for untreated follicular lymphoma', *J. Clin. Oncol. Off. J. Am. Soc. Clin. Oncol.*, vol. 23, no. 24, pp. 5696–5704, Aug. 2005.
[145] O. W. Press *et al.*, 'Phase II trial of CHOP chemotherapy followed by tositumomab/iodine I-131 tositumomab for previously untreated follicular non-Hodgkin's lymphoma: five-year follow-up of Southwest Oncology Group Protocol S9911', *J. Clin. Oncol. Off. J. Am. Soc. Clin. Oncol.*, vol. 24, no. 25, pp. 4143–4149, Sep. 2006.
[146] T. E. Witzig *et al.*, 'Phase I/II Trial of IDEC-Y2B8 Radioimmunotherapy for Treatment of Relapsed or Refractory CD20+ B-Cell Non-Hodgkin's Lymphoma', *J. Clin. Oncol.*, vol. 17, no. 12, pp. 3793–3803, Dec. 1999.
[147] J. W. Kylstra, T. E. Witzig, M. Huang, C. E. Emmanouilides, A. Hagenbeek, and G. F. Tidmarsh, 'Discriminatory power of the 111-indium scan (111-In) in the prediction of altered biodistribution of radio-immunoconjugate in the 90-yttrium ibritumomab tiuxetan therapeutic regimen: Meta-analysis of five clinical trials and 9 years of post-approval safety data.', *J. Clin. Oncol. Off. J. Am. Soc. Clin. Oncol.*, vol. 29, no. 15_suppl, p. 8048, May 2011.
[148] D. Rizzieri, 'Zevalin® (ibritumomab tiuxetan): After more than a decade of treatment experience, what have we learned?', *Crit. Rev. Oncol. Hematol.*, vol. 105, pp. 5–17, Sep. 2016.
[149] G. A. Wiseman *et al.*, 'Radiation dosimetry results from a Phase II trial of ibritumomab tiuxetan (Zevalin) radioimmunotherapy for patients with non-Hodgkin's lymphoma and mild thrombocytopenia', *Cancer Biother. Radiopharm.*, vol. 18, no. 2, pp. 165–178, Apr. 2003.
[150] T. E. Witzig *et al.*, 'Randomized controlled trial of yttrium-90-labeled ibritumomab tiuxetan radioimmunotherapy versus rituximab immunotherapy for patients with relapsed or refractory low-grade, follicular, or transformed B-cell non-Hodgkin's lymphoma', *J. Clin. Oncol. Off. J. Am. Soc. Clin. Oncol.*, vol. 20, no. 10, pp. 2453–2463, May 2002.
[151] S. M. Ansell, K. M. Ristow, T. M. Habermann, G. A. Wiseman, and T. E. Witzig, 'Subsequent chemotherapy regimens are well tolerated after radioimmunotherapy with yttrium-90 ibritumomab tiuxetan for non-Hodgkin's lymphoma', *J. Clin. Oncol. Off. J. Am. Soc. Clin. Oncol.*, vol. 20, no. 18, pp. 3885–3890, Sep. 2002.
[152] K. Hohloch *et al.*, 'Radioimmunotherapy Confers Long-Term Survival to Lymphoma Patients with Acceptable Toxicity: Registry Analysis by the International Radioimmunotherapy Network', *J. Nucl. Med.*, vol. 52, no. 9, pp. 1354–1360, Sep. 2011.
[153] J. Dahle *et al.*, 'Evaluating Antigen Targeting and Anti-tumor Activity of a New Anti-CD37 Radioimmunoconjugate Against Non-Hodgkin's Lymphoma', *Anticancer Res.*, vol. 33, no. 1, pp. 85–95, Jan. 2013.

[154] A. H. V. Repetto-Llamazares *et al.*, 'Targeted Cancer Therapy with a Novel Anti-CD37 Beta-Particle Emitting Radioimmunoconjugate for Treatment of Non-Hodgkin Lymphoma', *PloS One*, vol. 10, no. 6, p. e0128816, 2015.

[155] A. Repetto-Llamazares, N. Abbas, Ø. S. Bruland, J. Dahle, and R. H. Larsen, 'Advantage of Lutetium-177 versus Radioiodine Immunoconjugate in Targeted Radionuclide Therapy of B-cell Tumors', *Anticancer Res.*, vol. 34, no. 7, pp. 3263–3269, Jan. 2014.

[156] A. H. V. Repetto-Llamazares, R. H. Larsen, C. Mollatt, M. Lassmann, and J. Dahle, 'Biodistribution and Dosimetry of 177Lu-tetulomab, a New Radioimmunoconjugate for Treatment of Non-Hodgkin Lymphoma', *Curr. Radiopharm.*, vol. 6, no. 1, pp. 20–27, Mar. 2013.

[157] A. H. V. Repetto-Llamazares *et al.*, '177Lu-DOTA-HH1, a novel anti-CD37 radio-immunoconjugate: a study of toxicity in nude mice', *PloS One*, vol. 9, no. 7, p. e103070, 2014.

[158] J. Blakkisrud *et al.*, 'Tumor-Absorbed Dose for Non-Hodgkin Lymphoma Patients Treated with the Anti-CD37 Antibody Radionuclide Conjugate 177Lu-Lilotomab Satetraxetan', *J. Nucl. Med.*, vol. 58, no. 1, pp. 48–54, Jan. 2017.

[159] J. Blakkisrud *et al.*, 'Red Marrow-Absorbed Dose for Non-Hodgkin Lymphoma Patients Treated with 177Lu-Lilotomab Satetraxetan, a Novel Anti-CD37 Antibody-Radionuclide Conjugate', *J. Nucl. Med. Off. Publ. Soc. Nucl. Med.*, vol. 58, no. 1, pp. 55–61, Jan. 2017.

[160] K. Garber, 'Users Fear that Lymphoma Drugs Will Disappear', *JNCI J. Natl. Cancer Inst.*, vol. 99, no. 7, pp. 498–501, Apr. 2007.

[161] C. Emmanouilides *et al.*, 'Safety and efficacy of yttrium-90 ibritumomab tiuxetan in older patients with non-Hodgkin's lymphoma', *Cancer Biother. Radiopharm.*, vol. 22, no. 5, pp. 684–691, Oct. 2007.

[162] Q. Chen, T. Ayer, A. C. Rose, L. J. Nastoupil, and C. R. Flowers, 'Comparing the cost-effectiveness of rituximab maintenance and radio-immunotherapy consolidation versus observation following first-line therapy in follicular lymphoma patients', *Value Health J. Int. Soc. Pharmacoeconomics Outcomes Res.*, vol. 18, no. 2, pp. 189–197, Mar. 2015.

[163] R. C. Lee, D. Zou, D. J. Demetrick, L. M. Difrancesco, K. Fassbender, and D. Stewart, 'Costs associated with diffuse large B-cell lymphoma patient treatment in a Canadian integrated cancer care center', *Value Health J. Int. Soc. Pharmacoeconomics Outcomes Res.*, vol. 11, no. 2, pp. 221–230, Apr. 2008.

[164] N. G. Schaefer, J. Ma, P. Huang, J. Buchanan, and R. L. Wahl, 'Radioimmunotherapy in Non-Hodgkin Lymphoma: Opinions of U.S. Medical Oncologists and Hematologists', *J. Nucl. Med.*, vol. 51, no. 6, pp. 987–994, Jan. 2010.

[165] N. G. Schaefer, P. Huang, J. W. Buchanan, and R. L. Wahl, 'Radioimmunotherapy in Non-Hodgkin Lymphoma: Opinions of Nuclear Medicine Physicians and Radiation Oncologists', *J. Nucl. Med. Off. Publ. Soc. Nucl. Med.*, vol. 52, no. 5, pp. 830–838, May 2011.

[166] P. F. Ferrucci *et al.*, 'High activity 90Y-ibritumomab tiuxetan (Zevalin) with peripheral blood progenitor cells support in patients with refractory/resistant B-cell non-Hodgkin lymphomas', *Br. J. Haematol.*, vol. 139, no. 4, pp. 590–599, Nov. 2007.

[167] A. K. Gopal *et al.*, 'High-dose chemo-radioimmunotherapy with autologous stem cell support for relapsed mantle cell lymphoma', *Blood*, vol. 99, no. 9, pp. 3158–3162, May 2002.

[168] O. W. Press *et al.*, 'Phase II trial of 131I-B1 (anti-CD20) antibody therapy with autologous stem cell transplantation for relapsed B cell lymphomas', *Lancet Lond. Engl.*, vol. 346, no. 8971, pp. 336–340, Aug. 1995.

[169] J. W. T. Spinks and R. J. Woods, *An introduction to radiation chemistry*. Wiley, 1990.

[170] L. H. Gray, A. D. Conger, M. Ebert, S. Hornsey, and O. C. A. Scott, 'The Concentration of Oxygen Dissolved in Tissues at the Time of Irradiation as a Factor in Radiotherapy', *Br. J. Radiol.*, vol. 26, no. 312, pp. 638–648, Dec. 1953.

[171] W. F. Morgan and M. B. Sowa, 'Effects of ionizing radiation in nonirradiated cells', *Proc. Natl. Acad. Sci. U. S. A.*, vol. 102, no. 40, p. 14127, Oct. 2005.

[172] R. L. Warters, K. G. Hofer, C. R. Harris, and J. M. Smith, 'Radionuclide toxicity in cultured mammalian cells: elucidation of the primary site of radiation damage', *Curr. Top. Radiat. Res. Q.*, vol. 12, no. 1–4, pp. 389–407, Jan. 1978.
[173] J. F. Ward, 'DNA damage produced by ionizing radiation in mammalian cells: identities, mechanisms of formation, and reparability', *Prog. Nucleic Acid Res. Mol. Biol.*, vol. 35, pp. 95–125, 1988.
[174] J. Cadet, M. Berger, T. Douki, and J. L. Ravanat, 'Oxidative damage to DNA: formation, measurement, and biological significance', *Rev. Physiol. Biochem. Pharmacol.*, vol. 131, pp. 1–87, 1997.
[175] Z. Nackerdien, G. Rao, M. A. Cacciuttolo, E. Gajewski, and M. Dizdaroglu, 'Chemical nature of DNA-protein cross-links produced in mammalian chromatin by hydrogen peroxide in the presence of iron or copper ions', *Biochemistry (Mosc.)*, vol. 30, no. 20, pp. 4873–4879, May 1991.
[176] R. K. Sachs, L. R. Hlatky, and B. J. Trask, 'Radiation-produced chromosome aberrations: colourful clues', *Trends Genet.*, vol. 16, no. 4, pp. 143–146, Apr. 2000.
[177] R. Ladjohounlou, *Contribution des effets ciblés et non ciblés en radioimmunothérapie alpha et Auger de carcinoses péritonéales*. Montpellier, 2016.
[178] K. A. Wilson and D. F. Stern, 'NFBD1/MDC1, 53BP1 and BRCA1 have both redundant and unique roles in the ATM pathway', *Cell Cycle Georget. Tex*, vol. 7, no. 22, pp. 3584–3594, Nov. 2008.
[179] T. T. Su, 'Cellular Responses to DNA Damage: One Signal, Multiple Choices', *Annu. Rev. Genet.*, vol. 40, no. 1, pp. 187–208, 2006.
[180] 'BD Biosciences Research - Apoptosis, Cell Cycle, and Cell Proliferation - Analysis - Cell Cycle'. [Online]. Available: http://www.bdbiosciences.com/br/research/apoptosis/analysis/index.jsp. [Accessed: 05-Aug-2017].
[181] S. Matsuoka, M. Huang, and S. J. Elledge, 'Linkage of ATM to Cell Cycle Regulation by the Chk2 Protein Kinase', *Science*, vol. 282, no. 5395, pp. 1893–1897, Dec. 1998.
[182] Q. Liu *et al.*, 'Chk1 is an essential kinase that is regulated by Atr and required for the G2/M DNA damage checkpoint', *Genes Dev.*, vol. 14, no. 12, pp. 1448–1459, Jun. 2000.
[183] J. B. Millar, C. H. McGowan, G. Lenaers, R. Jones, and P. Russell, 'p80cdc25 mitotic inducer is the tyrosine phosphatase that activates p34cdc2 kinase in fission yeast.', *EMBO J.*, vol. 10, no. 13, pp. 4301–4309, Dec. 1991.
[184] A. L. Hein, M. M. Ouellette, and Y. Yan, 'Radiation-induced signaling pathways that promote cancer cell survival (review)', *Int. J. Oncol.*, vol. 45, no. 5, pp. 1813–1819, Nov. 2014.
[185] T. Otto and P. Sicinski, 'Cell cycle proteins as promising targets in cancer therapy', *Nat. Rev. Cancer*, vol. 17, no. 2, pp. 93–115, Feb. 2017.
[186] R. Hakem, 'DNA-damage repair; the good, the bad, and the ugly', *EMBO J.*, vol. 27, no. 4, pp. 589–605, Feb. 2008.
[187] I. R. Radford, T. K. Murphy, J. M. Radley, and S. L. Ellis, 'Radiation response of mouse lymphoid and myeloid cell lines. Part II. Apoptotic death is shown by all lines examined', *Int. J. Radiat. Biol.*, vol. 65, no. 2, pp. 217–227, Feb. 1994.
[188] L. P. Billen, C. L. Kokoski, J. F. Lovell, B. Leber, and D. W. Andrews, 'Bcl-XL inhibits membrane permeabilization by competing with Bax', *PLoS Biol.*, vol. 6, no. 6, p. e147, Jun. 2008.
[189] F. Edlich *et al.*, 'Bcl-x(L) retrotranslocates Bax from the mitochondria into the cytosol', *Cell*, vol. 145, no. 1, pp. 104–116, Apr. 2011.
[190] E. Oda *et al.*, 'Noxa, a BH3-only member of the Bcl-2 family and candidate mediator of p53-induced apoptosis', *Science*, vol. 288, no. 5468, pp. 1053–1058, May 2000.
[191] K. Nakano and K. H. Vousden, 'PUMA, a novel proapoptotic gene, is induced by p53', *Mol. Cell*, vol. 7, no. 3, pp. 683–694, Mar. 2001.

[192] X. Saelens, N. Festjens, L. Vande Walle, M. van Gurp, G. van Loo, and P. Vandenabeele, 'Toxic proteins released from mitochondria in cell death', *Oncogene*, vol. 23, no. 16, pp. 2861–2874, Apr. 2004.
[193] H. Nagasawa and J. B. Little, 'Induction of sister chromatid exchanges by extremely low doses of alpha-particles', *Cancer Res.*, vol. 52, no. 22, pp. 6394–6396, Nov. 1992.
[194] S. Demaria *et al.*, 'Ionizing radiation inhibition of distant untreated tumors (abscopal effect) is immune mediated', *Int. J. Radiat. Oncol. Biol. Phys.*, vol. 58, no. 3, pp. 862–870, Mar. 2004.
[195] J.-P. Pouget, C. Lozza, E. Deshayes, V. Boudousq, and I. Navarro-Teulon, 'Introduction to Radiobiology of Targeted Radionuclide Therapy', *Front. Med.*, vol. 2, Mar. 2015.
[196] B. Piron *et al.*, 'DNA damage-centered signaling pathways are effectively activated during low dose-rate Auger radioimmunotherapy', *Nucl. Med. Biol.*, vol. 41 Suppl, pp. e75-83, May 2014.
[197] S. Paillas *et al.*, 'Localized Irradiation of Cell Membrane by Auger Electrons Is Cytotoxic Through Oxidative Stress-Mediated Nontargeted Effects', *Antioxid. Redox Signal.*, vol. 25, no. 8, pp. 467–484, Sep. 2016.
[198] C. Shao, Y. Furusawa, M. Aoki, H. Matsumoto, and K. Ando, 'Nitric oxide-mediated bystander effect induced by heavy-ions in human salivary gland tumour cells', *Int. J. Radiat. Biol.*, vol. 78, no. 9, pp. 837–844, Sep. 2002.
[199] K. M. Prise and J. M. O'Sullivan, 'Radiation-induced bystander signalling in cancer therapy', *Nat. Rev. Cancer*, vol. 9, no. 5, pp. 351–360, May 2009.
[200] R. M. Macklis, P. M. Mauch, S. J. Burakoff, and B. R. Smith, 'Lymphoid irradiation results in long-term increases in natural killer cells in patients treated for Hodgkin's disease', *Cancer*, vol. 69, no. 3, pp. 778–783, Feb. 1992.
[201] S. Kusmartsev and D. I. Gabrilovich, 'Immature myeloid cells and cancer-associated immune suppression', *Cancer Immunol. Immunother. CII*, vol. 51, no. 6, pp. 293–298, Aug. 2002.
[202] R. Loevinger, T. F. Budinger, and E. E. Watson, *MIRD Primer for Absorbed Dose Calculations*. Society of Nuclear Medicine, 1988.
[203] R. Loevinger and M. Berman, 'A formalism for calculation of absorbed dose from radionuclides', *Phys. Med. Biol.*, vol. 13, no. 2, pp. 205–217, Apr. 1968.
[204] W. H. Ellett, A. B. Callahan, and G. L. Brownell, 'GAMMA-RAY DOSIMETRY OF INTERNAL EMITTERS. MONTE CARLO CALCULATIONS OF ABSORBED DOSE FROM POINT SOURCES', *Br. J. Radiol.*, vol. 37, pp. 45–52, Jan. 1964.
[205] Y. L. Kasamon, R. J. Jones, and R. L. Wahl, 'Integrating PET and PET/CT into the Risk-Adapted Therapy of Lymphoma', *J. Nucl. Med.*, vol. 48, no. 1 suppl, p. 19S–27S, Jan. 2007.
[206] W. S. Snyder, H. L. Fisher, M. R. Ford, and G. G. Warner, 'Estimates of absorbed fractions for monoenergetic photon sources uniformly distributed in various organs of a heterogeneous phantom', *J. Nucl. Med. Off. Publ. Soc. Nucl. Med.*, p. Suppl 3:7-52, Aug. 1969.
[207] S. M. Goddu, R. W. Howell, and D. V. Rao, 'Cellular dosimetry: absorbed fractions for monoenergetic electron and alpha particle sources and S-values for radionuclides uniformly distributed in different cell compartments', *J. Nucl. Med. Off. Publ. Soc. Nucl. Med.*, vol. 35, no. 2, pp. 303–316, Feb. 1994.
[208] J. P. Archambault and E. Mainegra-Hing, 'Comparison between EGSnrc, Geant4, MCNP5 and Penelope for mono-energetic electron beams', *Phys. Med. Biol.*, vol. 60, no. 13, pp. 4951–4962, Jul. 2015.
[209] L. Ferrer, *Dosimétrie clinique en radiothérapie moléculaire : optimisation de protocoles et implémentation clinique*. Nantes, 2011.
[210] A. Bitar, *Dosimétrie en radiothérapie vectorisée : conception d'un modèle dosimétrique par simulation Monte-Carlo*. Nantes, 2007.
[211] D. Benjamin, I. T. Magrath, R. Maguire, C. Janus, H. D. Todd, and R. G. Parsons, 'Immunoglobulin secretion by cell lines derived from African and American undifferentiated

lymphomas of Burkitt's and non-Burkitt's type', *J. Immunol. Baltim. Md 1950*, vol. 129, no. 3, pp. 1336–1342, Sep. 1982.
[212] H. C. Kluin-Nelemans *et al.*, 'A new non-Hodgkin's B-cell line (DoHH2) with a chromosomal translocation t(14;18)(q32;q21)', *Leukemia*, vol. 5, no. 3, pp. 221–224, Mar. 1991.
[213] M. J. Dyer *et al.*, 'Concurrent activation of MYC and BCL2 in B cell non-Hodgkin lymphoma cell lines by translocation of both oncogenes to the same immunoglobulin heavy chain locus', *Leukemia*, vol. 10, no. 7, pp. 1198–1208, Jul. 1996.
[214] R. Rimokh *et al.*, 'Detection of the chromosomal translocation t(11;14) by polymerase chain reaction in mantle cell lymphomas', *Blood*, vol. 83, no. 7, pp. 1871–1875, Apr. 1994.
[215] T. Mauxion, J. Barbet, J. Suhard, J.-P. Pouget, M. Poirot, and M. Bardiès, 'Improved realism of hybrid mouse models may not be sufficient to generate reference dosimetric data', *Med. Phys.*, vol. 40, no. 5, p. n/a-n/a, May 2013.
[216] K. F. Eckerman and A. Endo, *MIRD: radionuclide data and decay schemes*, 2nd ed. Reston, VA: Society of Nuclear Medicine, 2008.
[217] C. I. Bliss, 'The Toxicity of Poisons Applied Jointly1', *Ann. Appl. Biol.*, vol. 26, no. 3, pp. 585–615, Aug. 1939.
[218] S. Marcatili *et al.*, 'Realistic multi-cellular dosimetry for (177)Lu-labelled antibodies: model and application', *Phys. Med. Biol.*, vol. 61, no. 19, pp. 6935–6952, Oct. 2016.
[219] S. Dalle, S. Dupire, S. Brunet-Manquat, L. Reslan, A. Plesa, and C. Dumontet, 'In vivo Model of Follicular Lymphoma Resistant to Rituximab', *Clin. Cancer Res.*, vol. 15, no. 3, pp. 851–857, Feb. 2009.
[220] D. Santamaría *et al.*, 'Cdk1 is sufficient to drive the mammalian cell cycle', *Nature*, vol. 448, no. 7155, pp. 811–815, Aug. 2007.
[221] P. R. Mueller, T. R. Coleman, A. Kumagai, and W. G. Dunphy, 'Myt1: a membrane-associated inhibitory kinase that phosphorylates Cdc2 on both threonine-14 and tyrosine-15', *Science*, vol. 270, no. 5233, pp. 86–90, Oct. 1995.
[222] L. L. Parker and H. Piwnica-Worms, 'Inactivation of the p34cdc2-cyclin B complex by the human WEE1 tyrosine kinase', *Science*, vol. 257, no. 5078, pp. 1955–1957, Sep. 1992.
[223] M. F. Clarke *et al.*, 'Cancer Stem Cells—Perspectives on Current Status and Future Directions: AACR Workshop on Cancer Stem Cells', *Cancer Res.*, vol. 66, no. 19, pp. 9339–9344, Oct. 2006.
[224] H. J. Jung, Z. Chen, and N. McCarty, 'Stem-like tumor cells confer drug resistant properties to mantle cell lymphoma', *Leuk. Lymphoma*, vol. 52, no. 6, pp. 1066–1079, Jun. 2011.
[225] P. T. Ferrao, E. P. Bukczynska, R. W. Johnstone, and G. A. McArthur, 'Efficacy of CHK inhibitors as single agents in MYC-driven lymphoma cells', *Oncogene*, vol. 31, no. 13, pp. 1661–1672, Mar. 2012.
[226] E. Aleem and R. J. Arceci, 'Targeting cell cycle regulators in hematologic malignancies', *Front. Cell Dev. Biol.*, vol. 3, p. 16, 2015.
[227] M. Cozzi *et al.*, 'Antitumor activity of new pyrazolo[3,4-d]pyrimidine SRC kinase inhibitors in Burkitt lymphoma cell lines and its enhancement by WEE1 inhibition', *Cell Cycle Georget. Tex*, vol. 11, no. 5, pp. 1029–1039, Mar. 2012.
[228] R. Chilà *et al.*, 'Combined inhibition of Chk1 and Wee1 as a new therapeutic strategy for mantle cell lymphoma', *Oncotarget*, vol. 6, no. 5, pp. 3394–3408, Oct. 2014.
[229] A. I. Daud *et al.*, 'Phase I dose-escalation trial of checkpoint kinase 1 inhibitor MK-8776 as monotherapy and in combination with gemcitabine in patients with advanced solid tumors', *J. Clin. Oncol. Off. J. Am. Soc. Clin. Oncol.*, vol. 33, no. 9, pp. 1060–1066, Mar. 2015.
[230] G. Scagliotti *et al.*, 'Phase II evaluation of LY2603618, a first-generation CHK1 inhibitor, in combination with pemetrexed in patients with advanced or metastatic non-small cell lung cancer', *Invest. New Drugs*, vol. 34, no. 5, pp. 625–635, Oct. 2016.
[231] J. Zhao, C. L. Meyerkord, Y. Du, F. R. Khuri, and H. Fu, '14-3-3 proteins as potential therapeutic targets', *Semin. Cell Dev. Biol.*, vol. 22, no. 7, pp. 705–712, Sep. 2011.

[232] C. L. Neal *et al.*, '14-3-3zeta overexpression defines high risk for breast cancer recurrence and promotes cancer cell survival', *Cancer Res.*, vol. 69, no. 8, pp. 3425–3432, Apr. 2009.
[233] W. Cao *et al.*, 'Targeting 14-3-3 protein, difopein induces apoptosis of human glioma cells and suppresses tumor growth in mice', *Apoptosis*, vol. 15, no. 2, pp. 230–241, Feb. 2010.

ANNEXES

Articles

E Deshayes, R Ladjohounlou, P Le Fur, **A Pichard**, C Lozza, V Boudousq, S Sevestre, M Jarlier, R Kashani, J Koch, J Sosaboski, J Foster, N Chouin, F Bruchertseifer, A Morgenstern, PO Kotzki, I Navarro-Teulon, and JP Pouget. Anti-MISRII radiolabeled antibodies: new tools for a theranostic approach in ovarian cancer. JNM 2018. Submitted

A Pichard, S Marcatili, A Courteau, M Jarlier, P Coopman, G Cartron, I Navarro-Teulon, AH Repetto-Llamazares, H Heyerdahl, J Dahle, M Bardiès and JP Pouget: The advantage of ^{177}Lu-lilotomab over rituximab in B-cell NHL involves modulation of radiation-mediated G2/M cell cycle arrest. Blood 2017. **Submitted**

A Maisonial-Besset, T Witkowski, I Navarro-Teulon, O Berthier-Vergnes, G Fois, Y Zhu, S Besse, O Bawa, A Briat, M Quintana, **A Pichard**, M Bonnet, E Rubinstein, JP Pouget, P Opolon, L Maigne, E Miot-Noirault, JM Chezal, C Boucheix, F Degoul. Tetraspanin 8 (TSPAN 8) as a potential target for radioimmunotherapy of colorectal cancer. Oncotarget. 2017 Mar.

P Estupina, A Fontayne, JM Barret, N Kersual, O Dubreuil, M Le Blay, **A Pichard**, M Jarlier, M Pugnière, M Chauvin, T Chardès, JP Pouget, E Deshayes, A Rossignol, T Abache, C de Romeuf, A Terrier, L Verhaeghe, C Gaucher, JF Prost, A Pèlegrin, I Navarro-Teulon. The anti-tumor efficacy of 3C23K, a glyco-engineered humanized anti-MISRII antibody, in an ovarian cancer model is mainly mediated by engagement of immune effector cells. Oncotarget. 2017.

A Pichard, S Marcatili, A Courteau, R Ladjohounlou, I Navarro-Teulon, A Repetto-Llamazares, H Heyerdahl, J Dahle, M Bardiès and JP Pouget. Realistic multi-cellular dosimetry for ^{177}Lu labelled antibodies: model and application. Phys. Med. Biol. 2016 September.

S Paillas, R Ladjohounlou, C Lozza, **A Pichard**, E Deshayes, M Jarlier, S Sevestre, M Le Blay, V Boudousq, J Sosabowski, T Chardes, I Teulon, R Mairs, JP Pouget. Localized irradiation of cell membrane by Auger electrons is cytotoxic through oxidative stress-mediated non-targeted effects. Antioxid Redox Signal. 2016 May

AH Repetto-Llamazares, RH Larsen, S Patzke, KG Fleten, D Didierlaurent, **A Pichard**, JP Pouget, J Dahle. Targeted cancer therapy with a novel anti-CD37 beta-particle emitting radioimmunoconjugate for treatment of non-Hodgkin lymphoma. PLoS One. 2015

Oral presentations

Labex MabImprove 2017: ^{177}Lu-lilotomab is as efficient as ^{177}Lu-rituximab in the therapy of non-Hodgkin B lymphoma cells showing reduced phosphorylation of CDK1.

EANM'16 - Annual Congress of the European Association of Nuclear Medicine: Targeted radionuclide therapy of non-Hodgkin B-cell lymphoma using ^{177}Lu-lilotomab or ^{177}Lu-rituximab: a radiobiological approach.

Labex MabImprove 2016: Targeted radiotherapy of Non Hodgkin B cell Lymphoma with anti-CD37 antibody radiolabelled with ^{177}Lutetium: Comparison with ^{177}Lu-Rituximab.

EANM'15 - Annual Congress of the European Association of Nuclear Medicine: Compared therapeutic efficacy of ^{177}Lu-HH1 and ^{177}Lu-rituximab in non-Hodgkin B-cell lymphoma.

11ème Colloque International de Radiobiologie Fondamentale et Appliquée: Autoradiographie digitale et immunohistochimie pendant une radioimmunothérapie alpha au ^{212}Pb

The future of radiation oncology workshop: Digital autoradiography and immmunohistochemistry during targeted alpha therapy using ^{212}Pb-labelled mAbs.

Poster

3rd Nuclear Technologies for Health Symposium - NTHS 2015 : Compared therapeutic efficacy of ^{177}Lu-HH1 and ^{177}Lu-Rituximab in non-Hodgkin B lymphoma. A Pichard, R Ladjohounlou, S Marcatili, D Didierlaurent, I Navarro-Teulon, G Cartron, A Repetto-Llamazares, H Heyerdahl, M Bardiès, J Dahle and J-P Pouget.

Résumé en français

Introduction :

L'essor de l'immunothérapie, particulièrement avec le développement du rituximab, a significativement augmenté l'efficacité des traitements du lymphome non-hodgkinien (LNH). Le rituximab est un anticorps monoclonal chimérique dirigé contre le récepteur CD20 surexprimé à la surface des cellules de LNH. La corrélation entre la mise sur le marché du rituximab aux Etats-Unis et la diminution de la courbe de mortalité des patients met en évidence la grande efficacité de ce traitement. En clinique, cet anticorps thérapeutique est actuellement utilisé en combinaison avec la chimiothérapie pour potentialiser leurs effets. Après une première ligne thérapeutique (rituximab + chimiothérapie), le rituximab est à nouveau injecté au patient en consolidation de la réponse au traitement. Cependant, après ces nombreuses injections, les patients peuvent devenir réfractaires au rituximab et le ciblage du CD20 devient moins efficace.

Une autre possibilité thérapeutique des patients atteints de LNH est la radioimmunothérapie (RIT). Elle est basée sur le couplage d'un anticorps monoclonal avec un radionucléide. En effet, les cellules tumorales ciblées par l'anticorps subissent ensuite les effets de l'anticorps par lui-même et les effets des rayonnements ionisants émis par le radionucléide. Actuellement en clinique, deux RIT sont approuvées par l'agence américaine des produits médicamenteux (FDA) le Bexxar® et le Zevalin® (uniquement le Zevalin® en Europe). Comme le rituximab, ces deux spécialités ciblent également le CD20 mais avec deux radionucléides différents. Ces deux RIT ont montré une grande efficacité dans le traitement du LNH mais actuellement elles ne sont que très peu utilisées et ne sont indiquées qu'en fin de parcours de traitement du malade. Or ces deux RIT ciblant également le CD20, elles sont moins efficaces puisque les patients sont déjà réfractaires au ciblage de ce récepteur.

Dans ce contexte, une nouvelle RIT a été développé par la société Nordic Nanovector ASA pour surpasser cette résistance en ciblant un récepteur différent, le CD37 (récepteur surexprimé à la surface de cellules de LNH). Le Betalutin® est une nouvelle RIT composée d'un anticorps monoclonal (lilotomab) dirigé contre le récepteur CD37 et radiomarqué avec le Luthétium-177 (^{177}Lu). Cet anticorps radiomarqué (^{177}Lu-lilotomab) a fait l'objet de plusieurs études pré-cliniques prometteuses.

Le but de ma thèse a donc été de comparer *in vitro* et *in vivo* (sur modèle murin) l'efficacité thérapeutique du ^{177}Lu-lilotomab dans plusieurs modèles cellulaires de LNH et d'étudier les mécanismes de réponse cellulaire mis en jeu.

Plus précisément, ce nouveau radiopharmaceutique a été étudié *in vitro* dans les cellules Ramos, DOHH2 et Rec-1, modèles du lymphome de Burkitt, du lymphome folliculaire et du lymphome du manteau respectivement. *In vivo*, il a été testé sur des tumeurs de cellules Ramos et DOHH2 préalablement xénogreffées en sous-cutanée chez la souris. En plus de comparer les résultats du ^{177}Lu-lilotomab avec l'anticorps thérapeutique standard utilisé en clinique dans le traitement du LNH, le rituximab, l'efficacité thérapeutique du lilotomab non radiomarqué mais également du rituximab radiomarqué au ^{177}Lu ont été étudiées.

Dans un premier temps, les efficacités thérapeutiques des différents traitements (lilotomab, ^{177}Lu-lilotomab, rituximab et ^{177}Lu-rituximab) ont été étudiées *in vitro* et un nouveau référentiel dosimétrique a été mis au point. En effet, le paradigme de la radiobiologie actuelle est la corrélation entre la dose absorbée par les cellules et les effets observés lors d'un traitement par RIT. Cependant, ce paradigme est basé sur des connaissances déterminées par radiothérapie externe transposées au contexte de RIT. Pour aller plus loin et permettre la comparaison rationnelle des efficacités thérapeutiques des différents traitements (déterminées par survie clonogénique), nous avons développé une méthodologie mathématique prenant en compte les paramètres physique, biologique et spatial du système pour calculer la dose absorbée par les cellules. En effet, les dimensions des cellules et des noyaux des différentes lignées cellulaires ont été déterminées ; les densités cellulaires des flasques de culture lors des traitements ont été analysées pour chaque traitement et pour chaque lignée cellulaire ainsi que la formation d'amas cellulaire, leurs densités et leurs tailles. Simultanément, les activités cumulées par cellule ont été déterminées pour chaque anticorps radiomarqué pour permettre le calcul de la dose moyenne absorbée au noyau pour tous les traitements (qui est la valeur de référence en radiobiologie).

Dans un second temps, l'efficacité thérapeutique des différents traitements a été étudiée *in vivo*, sur des souris porteuses de xénogreffes sous-cutanées ; et à nouveau dans le but de comparer rationnellement les traitements, des études dosimétriques ont été faites à travers des biodistributions conventionnelles ou des analyses des souris au SPECT-CT.

Dans un dernier temps, une fois le support dosimétrique créé et les efficacités thérapeutiques étudiées, les mécanismes d'actions mis en jeu en réponse au ^{177}Lu-lilotomab ont été analysés. En effet, chaque lignée cellulaire a montré des sensibilités différentes aux traitements. Pour expliquer ces différences, plusieurs mécanismes ont été étudiés comme l'induction d'apoptose, le cycle cellulaire, l'expression et l'activation de protéines.

Résultats-discussion :

Nous avons montré qu'*in vitro,* l'efficacité thérapeutique du rituximab était plus importante que celle du lilotomab dans les trois modèles cellulaires (environ 50% de diminution de survie cellulaire *vs* 15% pour le lilotomab). La version radiomarqué des anticorps était toujours plus efficace que la version non radiomarqué dans l'élimination des cellules. En comparant le ^{177}Lu-lilotomab et le ^{177}Lu-rituximab, deux cas de figure étaient présents ; soit la lignée cellulaire était dite radiorésistante comme la lignée Ramos, et le ^{177}Lu-rituximab était plus efficace que le ^{177}Lu-lilotomab ; soit la lignée cellulaire était dite radiosensible, comme la lignée DOHH2, et le ^{177}Lu-lilotomab et le ^{177}Lu-rituximab avait la même efficacité thérapeutique (Rec-1 montrant une radiosensibilité intermédiaire). Cela signifie que dans les lignées radiosensibles le manque d'efficacité du lilotomab comparé au rituximab était compensé quand il était radiomarqué. Pour expliquer cette compensation, nous avons utilisé le modèle mathématique d'indépendance de Bliss permettant de mettre en évidence si deux « drogues » utilisées simultanément en thérapie (ici l'anticorps et les rayonnements ionisants), agissent de manière antagoniste (moins efficace que mise indépendamment), additive (addition des deux effets indépendants) ou de manière synergique (potentialisation des deux effets). Nous avons montré que dans le cas de la lignée radiorésistante, les effets du lilotomab et du ^{177}Lu étaient simplement additifs alors que dans le cas du traitement de la lignée radiosensible, les effets étaient synergiques. Des effets synergiques ont également été observés entre le rituximab et le ^{177}Lu mais dans une moindre mesure expliquant que le ^{177}Lu-rituximab et le ^{177}Lu-lilotomab avaient au final la même efficacité thérapeutique dans cette lignée cellulaire radiosensible. Nous avons également étudié la relation dose-effet des différents traitements mais nous n'avons pas mis en évidence de corrélation entre la dose absorbée au noyau et les effets induits par les différentes RIT.

In vivo, les souris ont été xénogreffées en sous-cutanée avec les lignées cellulaires Ramos et DOHH2 pour déterminer l'efficacité thérapeutique du lilotomab, ^{177}Lu-lilotomab, rituximab et ^{177}Lu-rituximab. Nous avons pu observer que dans le modèle tumorale radiorésistant (Ramos), les anticorps non radiomarqué n'avaient pas statistiquement d'effet sur la croissance tumorale. Dans ce modèle, le ^{177}Lu-lilotomab étant moins toxique pour les souris, il a donc pu être injecté à une activité supérieure que le ^{177}Lu-rituximab. Ce qui a entrainé une efficacité thérapeutique supérieure avec une dose absorbée à la tumeur plus importante que celle du ^{177}Lu-rituximab. A dose équivalente, dans ce modèle radiorésistant, le ^{177}Lu-rituximab était statistiquement efficace sur le ralentissement de la croissance tumorale alors que le ^{177}Lu-lilotomab ne l'était pas, validant les résultats *in vitro*. Dans le modèle tumoral radiosensible (DOHH2), le rituximab avait une efficacité très importante sur la croissance tumorale alors que le lilotomab n'avait aucun effet.

Dans ce modèle, le ^{177}Lu-rituximab présentait une toxicité pour la souris légèrement plus faible, il a donc pu être injecté à une activité légèrement plus forte. Ce qui a entrainé une dose absorbée moyenne à la tumeur plus élevée et finalement il montrait une efficacité thérapeutique plus importante que le ^{177}Lu-lilotomab. Cependant à dose équivalente, les deux radiopharmaceutiques présentaient la même efficacité thérapeutique.

In vitro et *in vivo*, nous avons donc déterminé l'efficacité thérapeutique du ^{177}Lu-lilotomab et nous l'avons comparé au rituximab et au ^{177}Lu-rituximab. Nous avons pu observer que le rituximab avait toujours une efficacité thérapeutique plus importante que le lilotomab et que le ^{177}Lu-lilotomab était toujours plus efficace que le rituximab non radiomarqué. En comparant le ^{177}Lu-lilotomab au ^{177}Lu-rituximab, deux cas de figures se sont présentés : dans le modèle cellulaire et tumoral radiorésistant (Ramos), le manque d'efficacité du lilotomab n'était pas contrebalancé et ainsi le ^{177}Lu-rituximab était plus efficace que le ^{177}Lu-lilotomab. Inversement, dans le modèle cellulaire et tumoral radiosensible (DOHH2), le manque d'efficacité thérapeutique du lilotomab était contrebalancé et le ^{177}Lu-lilotomab et le ^{177}Lu-rituximab avait la même efficacité thérapeutique.

Pour expliquer ces différences d'efficacité thérapeutique, différents mécanismes comme l'apoptose et le cycle cellulaire ont été analysés. Nous avons pu observer que le rituximab induisait beaucoup d'apoptose alors que le lilotomab n'en induisait pas. De plus, cette induction était plus importante dans la lignée radiosensible DOHH2 que dans la lignée radiorésistante Ramos (Rec-1 étant entre les deux). Lors des traitements avec les formes radiomarquées des anticorps, l'induction d'apoptose était présente pour tous les anticorps radiomarqués et plus marquées dans la lignée radiosensible.

Lors de l'analyse du cycle cellulaire, un arrêt de cycle cellulaire en G2/M a été mis en évidence dans la lignée cellulaire radiorésistante après traitement avec les anticorps radiomarqués, alors que cet arrêt n'était pas observé dans la lignée radiosensible. De plus, cet arrêt n'a pas été observé dans les cellules traitées avec les anticorps non radiomarqués. L'arrêt de cycle cellulaire en G2/M est dirigé par la protéine CDK1 associée avec la cycline B. CDK1 possède trois sites de phosphorylation :

-Thr161, permettant le passage G2 à M et phosphorylé par un complexe trimérique formé de CDK7, cyclin H et MAT1.

-Thr14, inhibant le passage G2 à M et phosphorylé par la protéine Myt-1

-Tyr15, inhibant le passage G2 à M et phosphorylé par la protéine Wee-1

L'état de phosphorylation de la protéine CDK1 a été étudié après traitement des cellules avec le ^{177}Lu-lilotomab pour confirmer les mécanismes mis en jeu lors de l'arrêt du cycle cellulaire. En effet la protéine CDK1 présentait un état de phosphorylation « inhibiteur » dans la lignée radiorésistante (Thr14 et Tyr15 phosphorylés) et « activateur » dans la lignée radiosensible (déphosphorylé sur les sites inhibiteurs et Thr161 phosphorylé) (Rec-1 étant entre les deux).

L'hypothèse émise a donc été que l'arrêt de cycle cellulaire en G2/M permettait aux cellules de détecter et réparer les dommages induits par les rayonnements ionisants et diminuait donc l'efficacité thérapeutique des radiopharmaceutiques. Pour mettre en évidence ce phénomène, des inhibiteurs des Wee-1 et du duo Wee-1/Myt-1 ont été utilisés dans la lignée radiorésistante. Après avoir validé leurs effets sur l'état de phosphorylation de CDK1 après traitement avec la combinaison inhibiteur + ^{177}Lu-lilotomab et sur l'inhibition de l'arrêt de cycle, une radiosensibilisation de la lignée radiorésistante a été montrée (la prolifération passant d'environ 50% avec le radiopharmaceutique seul, à moins de 10% avec la combinaison thérapeutique).

Pour conclure, nous avons montré que l'efficacité thérapeutique du ^{177}Lu-lilotomab était plus importante que celle du rituximab dans les trois modèles cellulaires testés. La comparaison avec le ^{177}Lu-rituximab était dépendante de la radiosensibilité de la lignée cellulaire due à l'arrêt ou non des cellules en phase G2/M du cycle cellulaire après traitement avec les radiopharmaceutiques. En inhibant l'arrêt du cycle, les cellules présentaient une radiosensibilité accrue au radiopharmaceutique montrant l'importance de ce contrôle cellulaire sur la réponse des cellules à ce traitement.

IOP Publishing | Institute of Physics and Engineering in Medicine Physics in Medicine & Biology

Phys. Med. Biol. **61** (2016) 6935–6952 doi:10.1088/0031-9155/61/19/6935

Realistic multi-cellular dosimetry for ^{177}Lu-labelled antibodies: model and application

S Marcatili[1,2,8], A Pichard[3,4,5,6,8], A Courteau[1,2], R Ladjohounlou[3,4,5,6], I Navarro-Teulon[3,4,5,6], A Repetto-Llamazares[7], H Heyerdahl[7], J Dahle[7], J P Pouget[3,4,5,6,9] and M Bardiès[1,2,9]

[1] INSERM, UMR1037 CRCT, F-31000 Toulouse, France
[2] Université Toulouse III-Paul Sabatier, UMR1037 CRCT, F-31000 Toulouse, France
[3] IRCM, Institut de Recherche en Cancérologie de Montpellier, Montpellier, F-34298, France
[4] INSERM, U1194, Montpellier, F-34298, France
[5] Université de Montpellier, Montpellier, F-34090, France
[6] Institut régional du Cancer de Montpellier, Montpellier, F-34298, France
[7] Nordic Nanovector ASA, Kjelsåsveien 168, 0884, Oslo, Norway

E-mail: sara.marcatili@inserm.fr and manuel.bardies@inserm.fr

Received 9 February 2016, revised 29 June 2016
Accepted for publication 15 July 2016
Published 12 September 2016

Abstract

Current preclinical dosimetric models often fail to take account of the complex nature of absorbed dose distribution typical of *in vitro* clonogenic experiments in targeted radionuclide therapy. For this reason, clonogenic survival is often expressed as a function of added activity rather than the absorbed dose delivered to cells/cell nuclei. We designed a multi-cellular dosimetry model that takes into account the realistic distributions of cells in the Petri dish, for the establishment of survival curves as a function of the absorbed dose. General-purpose software tools were used for the generation of realistic, randomised 3D cell culture geometries based on experimentally determined parameters (cell size, cell density, cluster density, average cluster size, cell cumulated activity). A mixture of Monte Carlo and analytical approaches was implemented in order to achieve as accurate as possible results while reducing calculation time. The model was here applied to clonogenic survival experiments carried out to compare the efficacy of Betalutin®, a novel ^{177}Lu-labelled antibody radionuclide conjugate for the treatment of non-Hodgkin lymphoma, to that

[8] These authors contributed equally to this work
[9] Co-last authors

of ^{177}Lu-labelled CD20-specific (rituximab) and non-specific antibodies (Erbitux) on lymphocyte B cells. The 3D cellular model developed allowed a better understanding of the radiative and non-radiative processes associated with cellular death. Our approach is generic and can also be applied to other radiopharmaceuticals and cell distributions.

Keywords: targeted radionuclide therapy, cellular dosimetry, radiobiology, Betalutin, rituximab

(Some figures may appear in colour only in the online journal)

1. Introduction

The absorbed dose–effect correlation has been largely verified in external beam radiotherapy (EBRT) with the development and application of the linear-quadratic model. Conversely, in targeted radionuclide therapy (TRT), the establishment of a dose–effect relation is not straightforward. The main reason for that lies in the intrinsic complexity of TRT irradiation. Compared with EBRT, in TRT, cells are irradiated at lower absorbed dose rates ($<$1 Gy h^{-1}) and therefore they have more time to repair; irradiation can be highly heterogeneous even at the cellular level and protracted (hours to days); both high- and low-LET particles can be involved in the same treatment; and finally, the contribution of vector cytotoxicity should be considered to identify specific radiation effects. Moreover, the *in vitro* absorbed dose of a given cell depends on the radiopharmaceutical spatial distribution in the target cell itself (self-absorbed dose) and the surrounding cells (cross-absorbed dose), and on the amount of radiopharmaceuticals in the culture medium (non-specific absorbed dose). The need for taking into account all these variables can make it difficult to assess the response of cell populations to a given radiopharmaceutical. Nevertheless, previous works demonstrated that heterogeneity of cell culture parameters produces significant effects on the shape of survival curves (Kvinnsland *et al* 2001, Uusijärvi *et al* 2008, Howell *et al* 2012). At the same time, the works of Dale (1985) and Fowler (1990) showed the consequences of low-dose rate irradiation to the biological effective dose (BED), taking into account the rate of repair or radiation damage.

Over the last few decades, many teams have developed digital models for the calculation of cellular absorbed dose for *in vitro* experiments using both Monte Carlo (MC) and analytical methods. Many of these works focus on the study of α and Auger emitters and therefore consider cell culture geometries of limited sizes: typically, cell clusters in close-packing geometry are generated for the calculation of the cell cross-absorbed dose (Faraggi *et al* 1998, Dahle *et al* 2009, Chouin *et al* 2009, Cai *et al* 2010). Goddu *et al* (1994) calculated the self-dose-to-cross-dose ratios to the cell nucleus for different cluster sizes (up to 400 μm) considering α, Auger and β-emitters: for β-emitters they demonstrated that the cross-absorbed dose is important irrespective of cluster size and sub-cellular source distribution, and increases as the cluster size increases. Other authors performed cellular dosimetry for more realistic geometries in the case of β-emitters (Freudenberg *et al* 2011) and mono-energetic electrons up to 1 MeV (Rajon *et al* 2011). In most of these works, however, the contribution of non-specific irradiation is usually disregarded since they focus on *in vivo* applications.

Despite the great research interest in cellular dosimetry, the availability of pre-calculated cellular *S* values is limited to the self-absorption contribution (Goddu *et al* 1997). The only exception is represented by the MIRDcell software (Vaziri *et al* 2014) which is freely available online and allows the user to predict cell survival curves for many radionuclides and mono-energetic radiations of different types. Unfortunately, only few specific geometrical

configurations (single clusters of cells and cell monolayers in close-packing geometry) are implemented in MIRDcell: as a consequence, the complexity of certain *in vitro* experiments cannot be appropriately modelled.

This work reports the development of an *in silico* model for the determination of the average cell absorbed dose in 3D colonies. On the basis of experimentally determined parameters (cell size, cell density, cluster density, average cluster size, cell cumulated activity), the model generates realistic, randomised culture geometries taking into account the cell's tendency to aggregate into clusters of different sizes. Within the same virtual colony, cells may have different radii, different levels of radiopharmaceutical internalisation and different intracellular activity distributions. The physical size of the modelled experiment is not limited in order to cover the range in water of β-emitters. A mixture of MC and analytical approaches was applied to achieve as accurate as possible results while reducing calculation time. This general-purpose cellular model is here illustrated through a practical example involving the *in vitro* dosimetry of lymphocyte B cells (Ramos cells) treated with ^{177}Lu-labelled monoclonal antibodies (mAbs). The aim of this experiment was to investigate the therapeutic efficacy of a novel radiopharmaceutical, ^{177}Lu-HH1, also called Betalutin®(Dahle *et al* 2013), in human lymphoma cells and to compare it with that of ^{177}Lu-rituximab and of the non-specific ^{177}Lu-IgG, namely ^{177}Lu-Erbitux, which targets epidermal growth factor receptors. In the next sections, the application of the dosimetric model developed to these experiments is discussed in detail.

2. Materials and methods

2.1. Experiments

Ramos human B-cell lymphoma cells, expressing both CD20 and CD37 cell surface receptors, were targeted with rituximab, HH1 or cetuximab. Rituximab is a chimeric antibody established from the murine mAb, namely ibritumomab, targeting CD20 receptors expressed by B-cells and B-cell lymphomas. HH1 is a murine mAb targeting CD37 receptors also expressed by B-cells. Cetuximab (or Erbitux®, its commercial name) is a chimeric antibody directed against the type I human epidermal receptor which is not expressed by lymphoma cells. It was used as a non-specific isotype mAb for control purposes. Rituximab, HH1 and cetuximab are full-size antibodies having a molecular weight of approximately 150 kDa. All mAbs were conjugated with p-SCN-benzyl-DOTA (Repetto-Llamazares *et al* 2015) and radiolabelled with ^{177}Lu at a concentration of 10 mg ml^{-1} and a specific activity of 200 MBq mg^{-1}. One million cells ml^{-1} of a culture medium was incubated in micro-well plates for 18 h with increasing activity (0, 0.5, 1, 2, 4 and 6 MBq ml^{-1}) of the three ^{177}Lu-labelled mAbs and varying mAb concentrations (0, 5, 10, 15, 25, and 40 μg ml^{-1}) of the unlabelled mAbs. Then, the cells were washed twice and separated into two groups; radioactivity remaining in the medium was below 0.1% the initial amount, and was thus neglected.

The first group was used to assess the average cell uptake of the radiopharmaceutical. Cells exposed to the radiolabelled mAbs were seeded in 12 micro-well plates containing 1 ml of the culture medium at a concentration of 2×10^5 cells ml^{-1}. At different times after the start of incubation (2 h and 18 h before re-seeding, 24 h, 48 h, 72 h and 144 h after re-seeding), an aliquot (8 μl) was used for cell numbering using a cell counter (Muse, Merck Millipore, Billerica, MA), while activity was determined using a gamma counter (Hewlett Packard, Palo Alto, CA). Activity per cell (Bq/cell) was next obtained at each time point. For each mAb, experiments were done in triplicate, allowing for the extrapolation of a statistical error on the average cellular cumulated activity. The average cell cumulated activity was obtained for

each mAb from the integration of the time activity curves (TACs) using the trapezoidal rule (Whittaker and Robinson 1967).

The second group was used to assess the therapeutic efficacy of radiolabelled and unlabelled mAbs using clonogenic assay. Cells were suspended in 5 ml of an RPMI (Roswell Park Memorial Institute) medium and counted. One thousand five hundred cells were mixed with 4.5 ml of a MethoCult® (Stem Cell Technologies) medium and seeded at increasing concentrations for increasing test activity (500–10 000 cells/Petri dish containing 1.5 ml medium). Petri dishes were next kept for 12 to 16 d for determining the number of colonies. Colonies containing 50 or more cells were scored and the surviving fraction was calculated. All the experiments were done at least three times.

The survival curves issued from experiments with radiolabelled mAbs were corrected for antibody toxicity in order to identify purely radiative effects. The activity concentration in the medium (MBq ml^{-1}) used in the experiments with the radiolabelled mAbs was expressed in terms of antibody concentration (μg ml^{-1}). Then, the cell survival fraction (expressed as a % of surviving cells), supposedly including only radiative effects (SF_{rad}), was obtained by subtracting the survival fractions obtained with radiolabelled mAbs (SF_l), from the survival fractions obtained with unlabelled mAbs (SF_u). Equation (1) is valid under the assumption that radiative and non-radiative cell death mechanisms are independent phenomena.

$$SF_{rad} = 100 - (SF_u - SF_l) \tag{1}$$

2.2. Determination of culture cell geometry

Since the average absorbed dose of the cell strictly depends on the geometrical configuration of the cell culture, a preliminary determination of the relevant geometrical parameters was performed on the basis of pictures acquired by optical microscopy.

During incubation time ($t < 18$ h), three concentric regions were identified in the cylindrical culture well of radius $r_w = 3.4$ cm: centre (a cylindrical region of radius r_c), halfway (a cylindrical shell with $r_c < r < r_h$) and edge (a cylindrical shell with $r_h < r < r_w$). For each region and for both specific antibodies (^{177}Lu-HH1 and ^{177}Lu-rituximab), two planar pictures were taken at $\times 5$ and $\times 20$ magnifications (see figure 1(a) as an example), in order to measure cell density in each area. In each region, the following parameters were extracted: the density of isolated cells (cell cm^{-2}); cluster density (clusters cm^{-2}); the average cluster radius in μm and its relative standard deviation. Culture thicknesses of one, two and three cell diameters were assumed for the edge, halfway-through and central regions respectively. The extracted parameters were used to estimate the total number of cells in each region. The size of the central region (r_c) was determined by directly segmenting the cell macro-aggregate (visible to the naked eye) which lay approximately at the centre of the culture well. The outer radius of the halfway region (r_h) was tuned in order to obtain an overall number of cells in the culture of the order of the nominal value (4×10^6 cells). Microscope observation of culture suspensions in flasks did not reveal any significant difference in geometrical arrangement according to whether cells were exposed to ^{177}Lu-Erbitux, ^{177}Lu-HH1 or ^{177}Lu-rituximab. Hence, for further modelling of cell suspension analysis, the parameters obtained with ^{177}Lu-HH1 were arbitrarily used for ^{177}Lu-Erbitux.

After incubation ($18\text{ h} < t < 144$ h) the cells seeded in Petri dishes exhibited an approximately uniform and isotropic spatial distribution. A maximum density of 6667 cells cm^{-3} was found for the cells treated with ^{177}Lu-rituximab at a concentration of 10 000 cells/Petri dish).

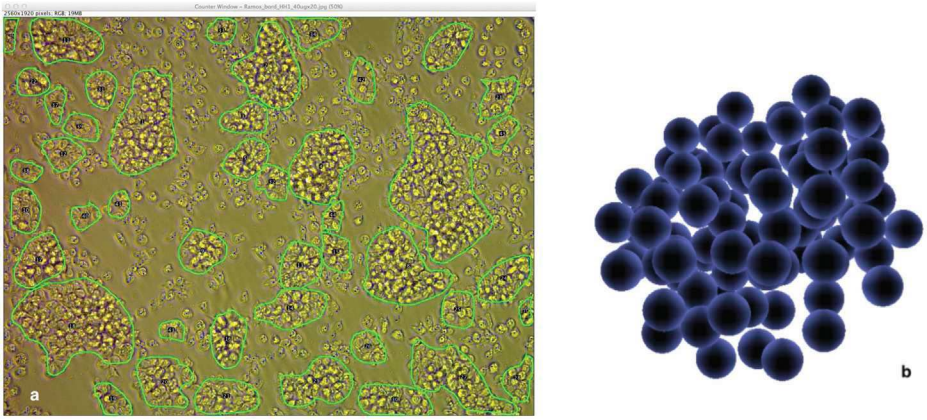

Figure 1. Figure (a): example of Ramos cell culture acquired at $\times 20$ magnification with an optical microscope at the edge of the culture well. In order to extract the geometrical characteristics of the culture, cell clusters were segmented while isolated cells were tagged and counted. Figure (b): example of one cluster generated *in silico* for the calculation of the cross-irradiation absorbed dose.

3. Dosimetric model

The absorbed dose of a target cell (D_{t}) can be obtained by summing up the contribution of activity in the target cell (D_{self}) itself, in cells other than the target (D_{cross}), and in the culture medium (D_{m}). According to the standard MIRD schema (Loevinger *et al* 1991), each of these components can be calculated as the product of the S value corresponding to the appropriate source/target combination and the cumulated activity in the source:

$$D_{\mathrm{t}} = D_{\mathrm{self}} + D_{\mathrm{cross}} + D_{\mathrm{m}} = \tilde{A}_{\mathrm{t}}\, S_{\mathrm{t}\leftarrow\mathrm{t}} + \sum_{s}^{N-1} \tilde{A}_s\, S_{\mathrm{t}\leftarrow\mathrm{s}}(d_s) + \tilde{A}_{\mathrm{m}}\, S_{\mathrm{t}\leftarrow\mathrm{m}} \tag{2}$$

where the sum is, in principle, extended to the N cells constituting the colony. In equation (2), $\tilde{A}_{\mathrm{t}}$, $\tilde{A}_s$ and $\tilde{A}_{\mathrm{m}}$ respectively indicate the cumulated activity in the target cell (both internalised and at the surface), in the sth source cell and in the culture medium, while $S_{\mathrm{t}\leftarrow\mathrm{t}}$, $S_{\mathrm{t}\leftarrow\mathrm{s}}$ and $S_{\mathrm{t}\leftarrow\mathrm{m}}$ are the S values for the coupled target cell/target cell, target cell/source cell and target cell/medium. The variable d_s indicates the distance of the sth source from the target cell.

In the next paragraphs, the techniques implemented for the calculation of self-absorption, cross-irradiation and non-specific irradiation absorbed doses are described.

3.1. Self-irradiation absorbed dose

Cell geometry was modelled with two concentric homogeneous unit density spheres representing the cell and the nucleus. Each cell was hence composed of three compartments: the cell nucleus (N), cell cytoplasm (Cy) and cell surface (CS). Cell sizes were defined according to experimentally determined cell ($R_{\mathrm{C}} = 5.1 \pm 0.7\ \mu$m) and nucleus ($R_{\mathrm{N}} = 4.0 \pm 0.6\ \mu$m) radii. The sub-cellular localisation of radiopharmaceuticals was experimentally determined from immunofluorescence imaging. On this basis, a 50% CS + 50% Cy distribution was assumed for ^{177}Lu-HH1, and a 100% CS distribution for ^{177}Lu-rituximab. For the non-specific ^{177}Lu-Erbitux a 100% CS radiopharmaceutical distribution was also assumed to take into account the measurable cell uptake. The cell model was implemented in Geant4.9.6 patch 04

(Agostinelli *et al* 2003). The arbitrary choice of using Geant4 was made for convenience, since the group had already developed a Geant4-based application for the calculation of cellular *S* values. For this and all MC simulation performed for this work, the whole ^{177}Lu spectrum was considered as defined in the MIRD book (Eckerman and Endo 2008). The Livermore physics list (Geant4 Collaboration 2015) was selected as it allows tracking particles down to an energy of 250 eV: this corresponds to a cut in range of 10 nm, which is adequate for energy deposition in cells of few microns. A total of 10^6 primary particles were generated for the simulation of each self-irradiation *S* value, in order to obtain a statistical uncertainty below 1%.

Since in cellular dosimetry it is generally recognised that radiosensitive sites are associated with DNA (Humm *et al* 1994), only the absorbed dose in the nucleus is reported in this paper.

The cell average cumulated activity obtained from the integration of TACs between 0 and 144 h (corresponding to the latest measured time point) was multiplied by the relevant *S* value in order to obtain the average self-irradiation absorbed dose for the three mAbs. We arbitrarily chose to neglect the cumulated activity after the last measured time point in order to avoid possible inaccuracies related to the use of an extrapolated time activity curve. The associated error was obtained by propagating the standard deviations of cell cumulated activity according to conventional error propagation rules.

3.2. Cross-irradiation absorbed dose

Beta particles emitted by ^{177}Lu have a maximum value in tissue of 1.76 mm (Berger *et al* 2009); hence, for the calculation of the absorbed dose of a cell in the culture, the contribution of all source cells placed at distances between two cell radii and of at least 1.76 mm should be taken into account. This requires knowledge of the cross-irradiation *S* values up to a cell-to-cell distance of at least 1.76 mm.

3.2.1. Generation of cross-irradiation S values. In this work, three different approaches for the calculation of cross-irradiation *S* values were implemented: (a) direct MC simulation at short cell-to-cell distances, (b) the use of MIRDcell software, and (c) the generation of *S* values from dose point kernels (DPKs).

(a) The same simulation set-up implemented for the generation of self-irradiation *S* values was used for the generation of cross-irradiation *S* values for different distributions of radiopharmaceuticals within the source cell (100% CS, 100% Cy, 50% CS + 50% Cy). In this case, however, the absorbed dose was scored in the nucleus of a target cell placed at a variable surface-to-surface distance from the source cell (0.0, 5.1, 10.2, 15.3, 20.4 and 51.75 μm). The simulation did not easily converge for larger cell-to-cell distances because of the reduced solid angle between the source and target cells.

(b) The 'cell source/target tab' of the MIRDcell applet (Vaziri *et al* 2014) was used for the calculation of cross-irradiation *S* values for two cells placed at a variable centre-to-centre distance ranging from 10 (adjacent cells) to 1578 μm. The upper limit roughly corresponded to the continuous slowing down approximation (CSDA) range of ^{177}Lu β-particles in water and was set by the software. Cells with a 5 μm radius that had 4 μm radius nuclei were considered; as in MIRDcell, cell radii can only be defined as integers. In MIRDcell, the ^{177}Lu beta spectrum is defined according to MIRD radionuclide data and decay schemes as in the MC simulations implemented for this study. The absorbed dose was calculated analytically in the CSDA.

(c) ^{177}Lu DPKs were simulated using MCNPX (Briesmeister *et al* 2000): the energy deposited by a punctual ^{177}Lu source between 17.6 and 2552 μm was scored in concentric spherical

shells of 17.6 μm thickness, simulating 8×10^8 primary particles. Eight hundred million additional particles were also generated for the simulation of DPKs between 17.6 and 228.8 μm on a shell thickness of 8.8 μm, in order to increase DPK sampling accuracy in the steepest region of the curve at short distances from the source. MCNPX is the natural choice for the generation of DPKs as it easily allows scoring of the deposited energy in concentric spherical shells through macro scripting. In contrast, implementation of the same geometry in Geant4 would require the development of user-defined C++ classes. In addition, an MCNPX-based application for the generation of DPKs was already available in our group. The DPKs obtained were subsequently used to calculate the absorbed dose per disintegration (S values) in a sphere (representing the target cell nucleus) placed at a variable distance from the source. For this calculation, the point source and the target were considered, so the DPKs and the S values basically coincided except for a change in units (MeV cm^{-3} Bq^{-1} s versus Gy Bq^{-1} s). This approximation is easily verified for cell-to-cell distances much greater than the cell size. At shorter distances, a validation of S values obtained from the DPKs is required.

3.2.2. Generation of multi-cellular geometries. Following equation (2), in order to calculate D_{cross}, knowledge of the 3D spatial distribution of cells in the culture is required for the determination of d_s and hence $S_{t \leftarrow s}(d_s)$. According to the cell spatial distribution (see for example figure 1(a)) observed during the incubation experiments ($0 < t < 18$ h), calculation of the cross-irradiation absorbed dose was performed in three separate steps to account for the contribution of radioactivity (i) in isolated cells (D_{IC}, the dose from isolated cells); (ii) in cells from the cluster the target cell belongs to (D_{TC}, the dose from the target cluster); and (iii) in cells from surrounding clusters (D_{SC}, the dose from surrounding clusters). Since the experiments indicated that Ramos cells tend to aggregate, the target cell was arbitrarily assumed to belong to a cluster. Three separate models for the description of cell culture geometry were developed in order to allow the calculation of D_{IC}, D_{TC} and D_{SC}. With a maximum value in water of 1.76 mm for ^{177}Lu β-particles, the contribution of cells located at larger distances was neglected. Moreover, considering that the cells were arranged in few layers along the vertical axis (Z) of the culture well, the geometrical models were restricted to cylindrical volumes (hereafter called model volume) having a radius of 2550 μm (=500 Ramos cell radii) and a height corresponding to the number of observed cell layers (N_{Layers}) times the cell diameter ($2R_{\text{C}}$) expressed in microns. The *model volume* is arbitrarily determined so that its radius in the XY plane is larger than the maximum beta range in water, to also include the bremsstrahlung contribution; this volume is small enough to fit into all well regions defined in this study, so that we could safely neglect the cross-irradiation from adjacent well regions.

In this volume, 50 independent random distributions of non-overlapping isolated cells and clusters were generated for each mAb and each well region with a series of C++ classes implemented in ROOT[10] (Brun and Rademakers 1997). The absorbed doses obtained for each region were then summed up using the total number of cells in the region (estimated from experiments) as weights. Then, the average cross-irradiation absorbed dose was calculated by summing up the contributions of isolated cells, the target cluster and surrounding clusters. At each stage, the standard deviation for the absorbed dose was obtained according to standard error propagation rules. The generation of multiple configurations allowed the establishment of an average absorbed dose that does not depend on the specific geometrical configuration modelled.

[10] https://root.cern.ch

For the calculation of the cross-irradiation absorbed dose after 18 h (uniform cell distribution), only isolated cells' contributions were modelled. In this case, the *model volume* was a cylinder with a radius of 2550 μm and a height of 1.6 mm, corresponding to the full height of the culture medium in the Petri dishes.

3D model of isolated cells. Fifty randomly distributed, non-overlapping, isolated cells were modelled. The minimum allowed distance between two cells was equal to two cell radii. The software takes as input the cell density (cell cm^{-2}) and computes the number of cells to be placed in the model volume. Then, it generates random X, Y, and Z coordinates (cell centres) within the established limits: if the current cell does not overlap with any previously created cell, its coordinates are stored. The output of this piece of software is a list (in a text format) of distances (d_s) between source cells and the target cell arbitrarily placed at the barycentre of the model volume.

3D model of target cell cluster. By analogy with the 3D isolated cell model, 50 cell clusters of different sizes were modelled. The clusters' radii (on the XY plane) were randomly sampled according to a Gaussian distribution having the mean and the standard deviation equal to experimentally determined values. The maximum cluster thickness was set to $N_{\text{Layers}} \times 2R_{\text{C}}$. Assuming a packing factor of 0.74 (typical of hexagonal close-packing lattices), randomly distributed, non-overlapping cells were generated to cover the cluster volume. Figure 1(b) shows one of the clusters generated, as an example.

Subsequently, within each cluster generated, the relative distances between each cell and the others were computed and stored in a text file. This approach allowed obtaining a cell absorbed dose averaged over the possibility of each cell being the target. This was necessary as, at short cell-to-cell distances, the difference between the absorbed doses of cells placed at the centre and at the edge of the cluster may be significant.

3D model of surrounding cell clusters. Fifty configurations of the many clusters present in the *model volume* were modelled as non-overlapping cylinders with a thickness of $N_{\text{Layers}} \times 2R_{\text{C}}$, and a randomly selected radius obtained from the sampling of a Gaussian distribution having a mean and a standard deviation equal to experimentally measured values. The number of clusters to be generated was determined according to the experimental cluster density (cluster cm^{-2}). The number of cells (N_{cells}) that constituted each cluster was calculated as the ratio between the given cluster volume (V_{cluster}) and the cell volume (V_{cell}), assuming a packing factor of 0.74. The target cell was placed at the barycentre of the volume model and included in a cluster of random size. For each cluster, its distance to the target cell (calculated from the cluster barycentre to the *model volume* barycentre), its radius and the number of cells included are stored for the subsequent calculation of the cell absorbed dose.

3.2.3. Cell cumulated activity. The cumulated activity $\tilde{A}_s$ for the sth source cell (see the second term of equation (2)) was randomly assigned by sampling a lognormal distribution (L) of the form:

$$L(\tilde{A}_s) = \frac{1}{\sqrt{2\pi}\ \ln k}\frac{1}{\tilde{A}_s}\exp\left(-\frac{(\ln(\tilde{A}_s/\mu))^2}{2(\ln k)^2}\right) \tag{3}$$

with $k = (\sigma/m) + 1$ and $\mu = m$ (Cousins 2010), where m and σ are, respectively, the experimentally determined average cell cumulated activity (in the time frame of interest) and standard deviation. In the case of clusters, the lognormal distribution was directly used to generate a random value for the total cumulated activity ($\tilde{A}_{\text{cluster}} = \sum_s \tilde{A}_s$).

3.2.4. Calculation of cross-irradiation absorbed dose between 0 and 18 h. The cross-irradiation absorbed dose was calculated according to the second term of equation (2). The cell cumulated activity ($\tilde{A}_s$) between 0 and 18 h was randomly sampled according to equation (3). The cross-irradiation S value ($S_{t\leftarrow s}(d_s)$) was evaluated for each source-to-target distance d_s, linearly interpolating merged S value data obtained with approaches (a) and (b) in section 3.2.1.

For the calculation of the absorbed dose from surrounding clusters (D_{SC}), the $S_{t\leftarrow s}(d_s)$ term was assumed to slowly vary within a given cluster. In fact, for each source cell in the cluster, its distance from the target cell can be written as $\mathbf{d}_s = \mathbf{d}_{cluster} + \mathbf{\Delta}_s$, where $\mathbf{d}_{cluster}$ is the vector describing the centre of the cluster with respect to the target cell position, and $\mathbf{\Delta}_s \ll \mathbf{d}_{cluster}$ is the relative distance between the cluster centre and the source cell. Under this approximation, in the neighbourhood of $d_{cluster}$, the cross-irradiation S value ($S_{t\leftarrow s}(d_s)$) can be approximated by its Taylor series of order 0 ($S_{t\leftarrow cluster}(d_{cluster})$), and the absorbed dose of the target cell (D_{cross}) can be written as:

$$D_{cross} = \sum_{s}^{N-1} \tilde{A}_s \; S_{t\leftarrow s}(d_s) \approx S_{t\leftarrow cluster}(d_{cluster}) \sum_{i}^{N_c-1} \tilde{A}_{cluster} \tag{4}$$

where $\tilde{A}_{cluster} = \sum_j^n \tilde{A}_s$ is the total cumulated activity in the cluster between 0 and 18 h, and n is the number of cells in each cluster. Here, $\tilde{A}_{cluster}$ was directly generated by randomly sampling the lognormal distribution in equation (3). In the first part of equation (4) the sum is extended to all cells (N) from all clusters, while in the second part, it is extended to the number of clusters generated (N_c).

3.2.5. Calculation of cross-irradiation absorbed dose between 18 h and 14 d. The cells seeded in Petri dishes after 18 h were uniformly distributed throughout the dish volume. Ten different geometrical configurations of isolated cells were generated to model the conditions of maximum cell density (6667 cells cm^{-3}), for which the highest cross-absorbed dose was expected. For the calculation of the cross-absorbed dose according to the second term of equation (2), a lognormal cumulated activity distribution was also assumed: the average cumulated activity and standard deviation were obtained from the integration of cell TACs between the time of cell rinsing (18 h) and the last time point available (144 h). Since the cross-irradiation absorbed dose found for the maximum cell density conditions was very low ($4.30 \times 10^{-5} \pm 5.16 \times 10^{-6}$ Gy), the cross-absorbed dose after 18 h was neglected for all mAbs considered.

3.3. Non-specific irradiation absorbed dose

3.3.1. Generation of non-specific S values. The non-specific irradiation S value was simulated with Geant4, modelling a homogeneous spherical water medium of a 2.55 mm radius uniformly filled with ^{177}Lu and surrounding the target cell. The sphere's radius was arbitrarily selected to be larger than 1.76 mm in order to account for bremsstrahlung radiation. The presence of cells other than the target was not modelled since the volume they occupied was negligible with respect to the total culture volume (10^6 Ramos cells per ml corresponds to 0.007% of the culture volume occupied by cells). The same source and physics parameters used for the generation of cellular S values were adopted for this simulation. The simulation of 3.7×10^9 events guaranteed a statistical uncertainty below 5%. The simulation time was about three weeks on a single CPU (3.1 GHz Intel Core i5). A nucleus non-specific S value of 3.01×10^{-10} Gy Bq^{-1} s was found.

3.3.2. Calculation of non-specific absorbed dose. For each region, the cumulated activity in the culture medium was obtained from the integration of the initial activity concentrations

Table 1. Summary table of the dosimetric models adopted for the calculation of the self-irradiation, cross-radiation and non-specific irradiation cross-absorbed doses.

Abs. dose contribution	Incubation time $0 < t < 18$ h	Clonogenic experiments $0 < t < 144$ h	Dosimetric model
Self	[a]	[a]	Symmetric sphere
Cross	[a]		IC, TC, SC (3 regions)
		Negligible[a]	IC
Non-specific	[a]		Uniform sphere (3 regions)

[a]The integration time considered for the assessment of each contribution.
Note: IC = isolated cell model; TC = target cluster model; SC = surrounding clusters model.

(0.5, 1, 2, 4, and 6 MBq ml^{-1}) over the incubation time (18 h), considering the actual volume occupied by the cells and subtracting the fraction of cumulated activity uptaken by the cells. Subsequently, for each combination of antibody and well region, the corresponding cumulated activity was multiplied by the non-specific irradiation S value to obtain the non-specific nucleus absorbed dose. The different contributions were summed up using the total number of cells in each region as weights. Standard error propagation was applied throughout the calculation.

3.4. Total absorbed dose and clonogenic survival

For each mAb considered, the average absorbed dose of a target cell placed at the centre of the *model volume* was calculated as the sum of three contributions: (i) the self-absorbed dose, (ii) the non-specific absorbed dose and (iii) the cross-irradiation absorbed dose. The squared error on the total absorbed dose was computed as the sum of the squared errors of the single components. The dosimetric results obtained for the Ramos cells treated with ^{177}Lu-HH1, ^{177}Lu-rituximab and ^{177}Lu-Erbitux were applied to clonogenic survival curves in order to express cell survival in terms of the average nucleus absorbed dose. Table 1 provides a summary of the models used and the integration times considered for the determination of each contribution.

4. Results

4.1. Experiments

4.1.1. Clonogenic survival experiments. In figure 2, the survival curves obtained with the radiolabelled and the unlabelled version of HH1 and rituximab are expressed in terms of mAb concentration (μg ml^{-1}) in the medium for direct comparison. The high cytotoxicity of rituximab is evidenced in figure 2(b), where approximately half of the cell population is killed by the treatment. In contrast, HH1 (figure 2(a)) showed a lower (although not negligible) cytotoxicity with only 10% of cells killed.

4.2. Dosimetry

4.2.1. Self-irradiation S values. A self-irradiation S value of 3.75×10^{-4} Gy Bq^{-1} s was found for cells treated with ^{177}Lu-rituximab and ^{177}Lu-Erbitux, and an S value of 4.68×10^{-4} Gy Bq^{-1} s for cells treated with ^{177}Lu-HH1.

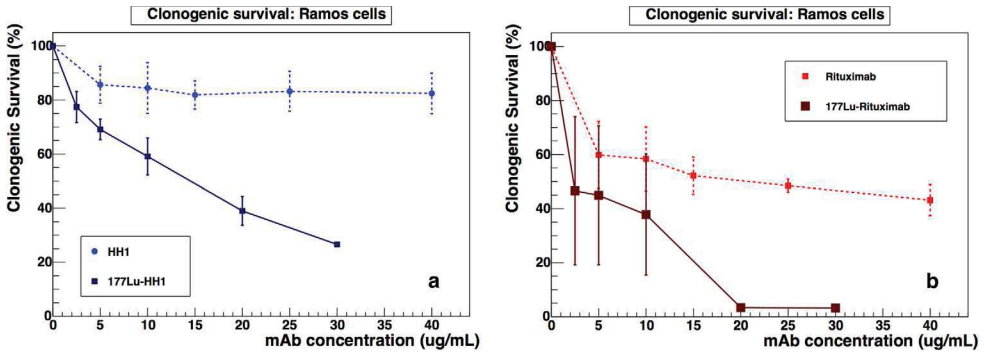

Figure 2. Ramos cells' clonogenic survival as a function of the initial mAb concentration (μg ml^{-1}) in the medium. Cell survivals in figure (a) are obtained with the radiolabelled and unlabelled versions of HH1, and those in figure (b) with the radiolabelled and unlabelled versions of rituximab.

4.2.2. Cross-irradiation S values. The results of the direct MC simulation (approach a, cf section 3.2.1) showed that source localisation within the cell has no significant impact on the absorbed dose of the target cell: the largest discrepancy ($\sim$1.8%) is found between 100% CS and 100% Cy source distributions in the case of contiguous cells. This result justifies the use, at larger cell-to-cell distances, of cross-irradiation S values not taking into consideration the heterogeneity of radiopharmaceutical distribution within the cell. The simulated S values for a 50% CS + 50% Cy source distribution are shown, as an example, in figure 3(a) (green triangular points).

In figure 3(a), the DPK S values (blue dashed line) are compared to those calculated with MIRDcell (continuous red line) and to ^{177}Lu cross-irradiation S values obtained via direct MC simulation (green triangular points). In the range 22.0–61.95 μm, where three of the simulated S values superpose the DPK S values, the percentage difference between the two datasets is below 5% (see figure 3, triangular points). Their agreement at short cell-to-cell distances validates the assumption of a punctual target and source made for the generation of DPK S values. At the same time, at rather short cell-to-cell distances, the MIRDcell and DPK data visually show the same behaviour. However, the MIRDcell S values display an artificial periodicity that increases with cell-to-cell distance, and that most probably depends on a malfunctioning of the MIRDcell applet. Even in the range 22.0–120 μm, where the MIRDcell periodic response is less obvious, the percentage differences between the DPK and the MIRDcell datasets (DPK–MIRDcell) $\times$ 100/MIRDcell) are quite high: a maximum and an average percentage difference of 28.8% and 20.0% are observed respectively (see figure 3, red circular points).

4.2.3. Cross-irradiation absorbed dose. The separate contributions of D_{IC}, D_{TC} and D_{SC} are shown in figure 4 for cells treated with the two specific antibodies (^{177}Lu-HH1 (a) and ^{177}Lu-rituximab (b)). In all experiments, the highest absorbed dose comes from radioactivity in the cluster the target cell belongs to; D_{TC} is about two times the D_{SC}. On the other hand, the impact of radioactivity in isolated cells is low but generally not negligible ($\sim$0.5 Gy for Ramos cells treated with ^{177}Lu-rituximab). The higher absorbed dose obtained for cells treated with ^{177}Lu-rituximab is mostly due to the correspondingly higher cumulated activity per cell. The cross-irradiation absorbed doses for cells treated with the non-specific antibody (^{177}Lu-Erbitux, data not shown) were considerably lower than the ^{177}Lu-HH1 (5.5 times at 6 MBq ml^{-1}) and ^{177}Lu-rituximab (7.7 times at 6 MBq ml^{-1}) absorbed doses.

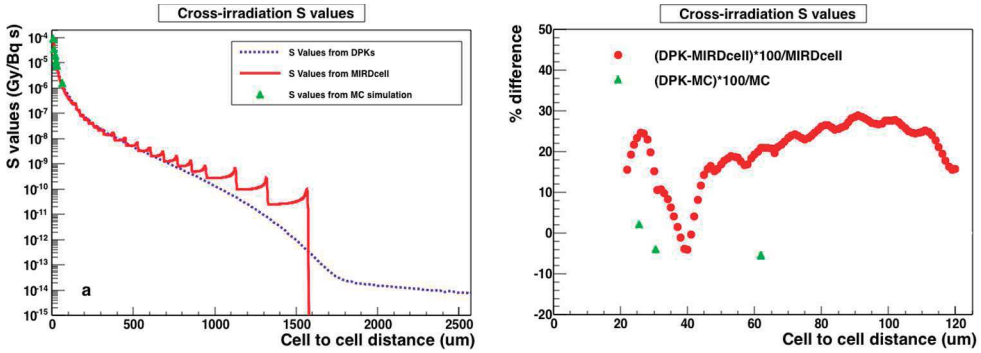

Figure 3. Figure (a): cross-irradiation S values obtained from MIRDcell (red), from DPKs (blue), and via direct MC simulation (green). Figure (b): percentage differences between MIRDcell and MC data with respect to S values derived from DPKs.

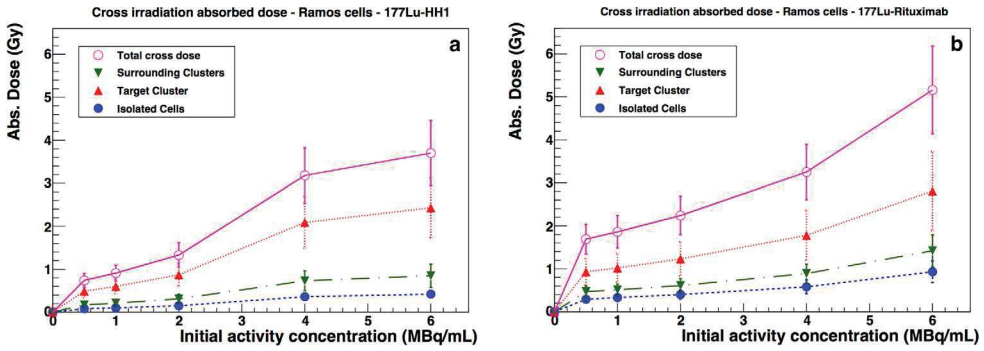

Figure 4. Different contributions of D_{IC}, D_{SC} and D_{TC} are shown for the two specific mAbs: ^{177}Lu-HH1 (a) and ^{177}Lu-rituximab (b). IC = isolated cell model; TC = target cluster model; SC = surrounding cluster model.

For all mAbs considered, the relative standard deviation on the total cross-irradiation absorbed dose was on average 24%. This value directly depends on the randomisation of the cellular uptake of radiopharmaceuticals and geometrical configurations implemented in the dosimetric model; it in turn provides a measure of the high heterogeneity of parameters characterising a cellular system both *in vitro* and *in vivo*.

4.2.4. Total absorbed dose. In figure 5, the self-irradiation, cross-irradiation and non-specific irradiation absorbed doses of the nucleus are reported as a function of the initial activity concentration in the medium, for cells treated with ^{177}Lu-HH1, ^{177}Lu-rituximab and ^{177}Lu-Erbitux. For the two specific mAbs, the absorbed dose is mostly due to cross-irradiation, while for the non-specific mAb non-specific irradiation is dominant and linearly increases with increasing activity concentration in the medium. A less linear behaviour is observed for the non-specific absorbed dose of cells treated with the two specific mAbs. Indeed, if more radiolabelled mAb is internalised in the cells, activity in the medium and hence the corresponding absorbed dose are reduced accordingly. Furthermore, at low activity concentrations, for which cellular receptors are not saturated, cross- and self-irradiation absorbed doses are higher than non-specific absorbed doses, for cells treated with ^{177}Lu-rituximab. Conversely,

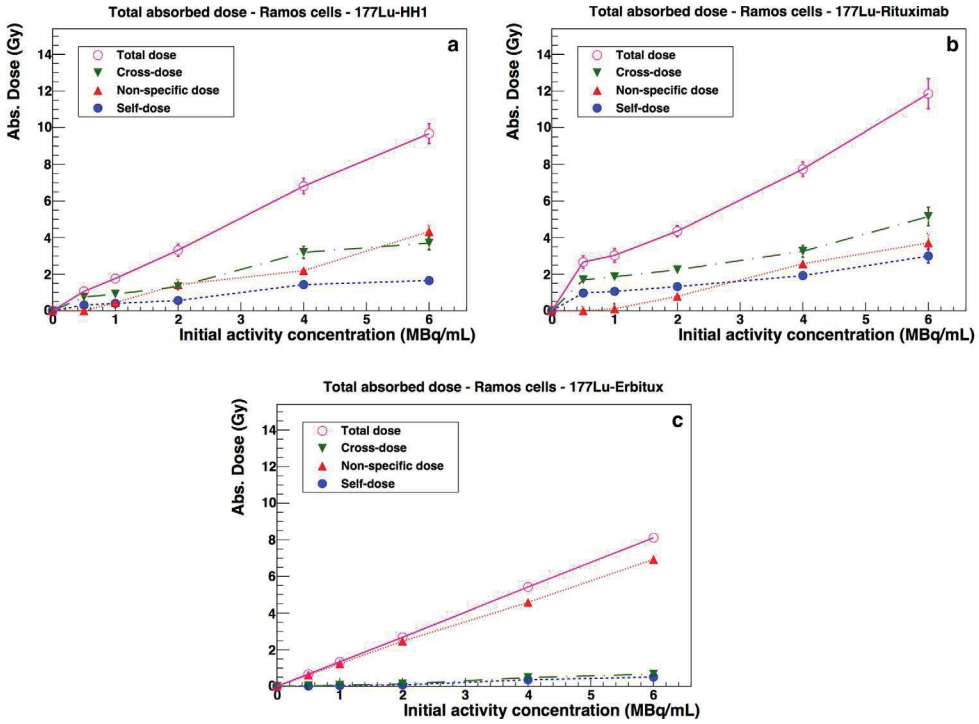

Figure 5. Different contributions of self-irradiation, cross-irradiation and non-specific irradiation absorbed doses are shown for the three mAbs considered: mAbs ^{177}Lu-HH1 (a), ^{177}Lu-rituximab (b), and ^{177}Lu-Erbitux (c).

for cells treated with ^{177}Lu-HH1, the cross-irradiation absorbed dose becomes dominant at quite low initial activity (>1 MBq ml^{-1}).

Despite the self-absorbed dose being calculated over a larger temporal frame with respect to the cross-absorbed dose (144 h versus 18 h), its contribution is, on average, the smallest. The results here presented correspond to specific internalisation hypotheses for the three antibodies. Other possibilities have been explored, reaching close absorbed dose values: indeed, in the dosimetric model implemented, cell internalisation properties only contribute to the self-irradiation absorbed dose.

4.3. Clonogenic survival

In figure 6, Ramos cell survival curves are presented as a function of the nucleus absorbed dose for the three ^{177}Lu-mAbs considered, before (a) and after (b) correction for mAb toxicity. A linear quadratic (LQ) model (Dale 1985) was considered for the fit of all datasets. Errors on both axes were considered, using a generalised version of the χ^2 method (the effective variance method) as implemented in ROOT. The fit results are displayed in figure 6 (b): the parameters p0 and p1 correspond to the α and β parameters of the LQ model.

For cells treated with ^{177}Lu-HH1 and ^{177}Lu-rituximab, data not corrected for unlabelled mAb toxicity showed a linear behaviour ($\beta = 0$), while for ^{177}Lu-Erbitux β was significantly different from zero. According to these results, the combination of radiation damage and biological toxicity was more effective for ^{177}Lu-rituximab than for the non-specific ^{177}Lu-mAb

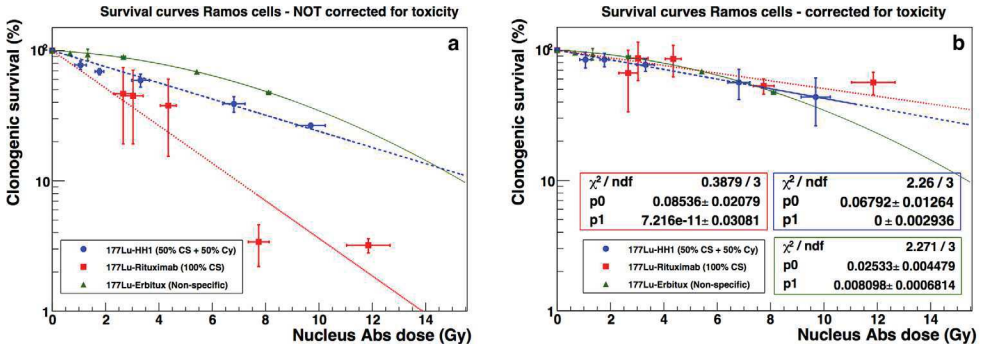

Figure 6. Ramos cells' clonogenic survival as a function of the nucleus absorbed dose. The survival curves in figure (a) include both radiative and mAb-induced cytotoxic effects, while those in figure (b) are corrected for antibody toxicity.

(^{177}Lu-Erbitux), with ^{177}Lu-HH1 in between. After correction for antibody toxicity, ^{177}Lu-HH1 and ^{177}Lu-rituximab still displayed a linear behaviour, with β compatible with zero. The effect of the correction was a significant increase in the D_{37} value (the absorbed dose required to achieve 37% survival) for both specific mAbs, without direct impact on the shape of the curve: from 6.5 Gy to 11.6 Gy for ^{177}Lu-HH1, and from 3.7 Gy to 16.2 Gy for ^{177}Lu-rituximab. For the non-specific antibody, which was supposed to be non-cytotoxic, survival curves followed the LQ model with $D_{37} = 9.7$ Gy and $\alpha/\beta = 3.9$ Gy.

An interesting effect of the toxicity correction is that the survival curves of the three mAbs get closer: in particular at low absorbed doses, where the experimental errors are relatively low, the three curves almost perfectly superpose. If the hypothesis that cell deaths by radiation and by mAb-induced cytotoxicity are additive phenomena is correct, the curves in figure 6(b) only account for radiative effects. Indeed, under these conditions (the same radioisotope and the same cell line), a similar absorbed dose–response relationship is expected for the three radiopharmaceuticals. In order to determine if the treatment has a significant effect on the curve shape, the three corrected survivals have been compared with an F-test (Motulsky and Christopoulos 2005), which is appropriate for nested data. For each couple of datasets, the null hypothesis is that the same curve fits both data points and the difference is purely due to random factors. The high p-values found for all couples of survival curves demonstrated that, given the errors introduced by the experiments and the absorbed dose model, it is not possible to reject the null hypothesis if considering a 5% significance.

5. Discussion

One of the paradigms of radiobiology is that radiation-induced biological effects are proportional to the delivered absorbed dose (Pouget *et al* 2015). Therefore in conventional EBRT linear or LQ response is generally established for the survival of cells exposed to radiation. However, such an assumption is not straightforward in TRT because cell irradiation between EBRT and TRT differs in many ways. In TRT, irradiation is highly heterogeneous and protracted for hours or days, and the cytotoxicity of the biological vector should be extracted to separate purely radiative effects and thus verify an absorbed dose–effect relationship. The pioneering works of Dale (1985) and Fowler (1990) have established how to include the effects of low-dose rate irradiation in the calculation of the BED. However, a comprehensive dosimetric approach that takes into account the full complexity of TRT is not yet established.

Clonogenic assay is one of the reference techniques for investigating the biological effects of radiation on cells: the relationship between clonogenic survival and the nucleus absorbed dose allows the comparison of differences in efficacy of various treatments. Calculating the nucleus absorbed dose in TRT is much more complex than in EBRT. Many variables can affect the absorbed dose of a given cell in a colony *in vitro*: sub-cellular and intra-cellular radiopharmaceutical distribution, cell spatial distribution, cell size, etc. Taking into account this level of variability can make dosimetry a challenge, especially for what concerns the calculation of the cross-absorbed dose. In particular, when considering beta-emitting radiopharmaceuticals with a range in water of a few millimetres, the average cell cross-absorbed dose depends on the heterogeneous characteristics of a large number of cells.

5.1. Dosimetric model

The dosimetric model developed allows the calculation of the average cell absorbed dose for *in vitro* experiments taking into consideration realistic culture characteristics (cell size, isolated cell/cluster density, cluster size, average cell cumulated activity). The intracellular variability of these parameters is further taken into account by randomising the geometrical properties of the modelled colony, and calculating a standard deviation for the resulting cell absorbed dose. The approach used is generic and can be applied to any type of radiation, provided that the relevant self-absorbed dose S values and DPKs are known. The former are easily found in the literature for most common radionuclides (Goddu *et al* 1997), while the latter are available for some β-emitters (Prestwich *et al* 1989, Papadimitroulas *et al* 2012) and mono-energetic electrons (Cross *et al* 1982). Here, we arbitrarily chose to generate them using Geant4 and MCNPX since dedicated applications were already available in our group.

In this work, the model was applied to the dosimetry of Ramos cells treated with three mAbs radiolabelled with a β-emitter (^{177}Lu). For this particular scenario, the greatest contribution to the cell absorbed dose was in general due to cross-irradiation and non-specific irradiation. Clearly, this outcome is specific to *in vitro* experiments where cells and cell clusters are well spaced and most of the culture volume is occupied by the incubation medium. *In vivo*, cells are closer and non-specific activity is expected to contribute less, while cross-irradiation is expected to contribute even more than it does *in vitro*. The cross-absorbed dose contribution from the cluster the target cell belonged to was about two times the cross-absorbed dose due to other clusters. At the same time, the cross-absorbed dose contribution from isolated cells was the lowest but, in some cases, not negligible (e.g. $\sim$0.7 Gy for cells treated with ^{177}Lu-rituximab, at 6 MBq ml^{-1} of medium activity). The contributions of both surrounding cell clusters and isolated cells are large enough to produce a measurable modification of survival curves if neglected, which proves the necessity of modelling the whole culture geometry when β-emitters are involved. On average, the cross-irradiation absorbed doses were two times as high as those found for self-irradiation.

The results obtained also showed that the total absorbed dose only weakly depended on the sub-cellular radiopharmaceutical distribution in the case of ^{177}Lu. In fact, this variable is only included in the calculation of the self-absorbed dose, which only minimally contributes to the total cell absorbed dose. At the same time, ^{177}Lu cross-irradiation S values have been demonstrated to be independent of sub-cellular uptake for cell-to-cell distances larger than 20.4 μm (four cell radii). Moreover, the cross-irradiation S values calculated in the punctual approximation were able to well reproduce (within 5%) the S values obtained via direct MC simulation and take into account the actual cell size. The aim of this work was to generate a multi-cellular model that is as realistic as possible. Still, some approximations had to be made in order to keep it reasonably simple. The main assumption was to consider constant the number of cells

in the colony during the 18 h-incubation time with radioactivity, while proliferation may occur with a direct impact on cell/cluster density and cluster size. Also, a non-conventional approach was used to take into account cell labelling heterogeneity. While in many works (Rajon *et al* 2011, Vaziri *et al* 2014) only a fixed fraction of cells are assumed to be radiolabelled, and hence considered in the dosimetric calculation, here all modelled cells were included in the dosimetry. In this work, in fact, experimental determination of cell cumulated activity (and its standard deviation) was performed on samples of about 8000 cells; in principle, within these cells, different levels of radiopharmaceutical uptake are achieved, with some cells remaining unlabelled. Therefore, randomly sampling cell cumulated activity on the basis of these variables indirectly guarantees the adequate modelling of cell labelling heterogeneity.

5.2. Interpretation of survival curves

Despite the experimental errors involved and the approximation introduced by the dosimetric model, we have been able to establish curves expressing clonogenic survival as a function of the nucleus absorbed dose. We observed that correcting clonogenic survival response for unlabelled mAb toxicity modified the shape of the absorbed dose–effect relationship, with the curves getting closer: this effect suggested a certain degree of absorbed dose–effect correlation. Under this hypothesis, the rather similar cell survival curves obtained for the specific (^{177}Lu-rituximab and ^{177}Lu-HH1) and the non-specific (^{177}Lu-Erbitux) antibodies may be interpreted as an indirect validation of the dosimetric model. This is particularly true for the simplest of the three models, which consisted of cells exposed to ^{177}Lu-Erbitux. In this case, the nucleus absorbed dose almost exclusively depends on the radioactivity accumulated in the culture medium. The dosimetric model is therefore extremely simple and hence more reliable (the model depends on fewer *a priori* assumptions). At the same time, adding the complexity of the cross-absorbed dose calculation (see ^{177}Lu-rituximab and ^{177}Lu-HH1) produces survival curves close to those of ^{177}Lu-Erbitux, which is the expected effect in the case of the absorbed dose–effect correlation. Besides, in the case of ^{177}Lu-Erbitux, the cell killing mechanism is by definition purely radiative since Erbitux does not bind to cells (or at least not significantly). Therefore, the fact that ^{177}Lu-rituximab and ^{177}Lu-HH1 survival curves get close to ^{177}Lu-Erbitux survival after correction for mAb-induced cytotoxicity supports the hypothesis that radiation and mAb toxicity are the main mechanisms of action of these radiopharmaceuticals.

In order to quantitatively demonstrate the presence of an absorbed dose–effect correlation in Ramos cell experiments, the survival curves were fitted with an LQ model as is generally done in EBRT for low-LET radiation. The idea was to compare the LQ curves and determine if the three mAb survivals could be described by a single absorbed dose–effect relationship. It was found that the differences between the three curves were not significant (5% confidence level) after correction for cytotoxicity of the naked mAb. This indicates that the differences between the D_{37} values found for the ^{177}Lu-rituximab and ^{177}Lu-HH1 curves may also not be significative. Nonetheless, it is hard to say whether this result depends on the large experimental errors, on the few experimental points or on whether we are observing a perfect absorbed-dose correlation. Obviously, interpretation of the survival curves should take into account the possible limitations of our model which still neglects some aspects like the effects of cell proliferation and cell reparation. However, since in principle both these parameters only depend on the cell line considered, the relative comparison of different radiopharmaceuticals should not bias the result.

A possible weakness of our work may lie in the hypothesis that radiative and cytotoxic effects are the only mechanisms involved in cell death, and that they are independent. This assumption neglects, on one side, the possible presence of a bystander effect and, on the other, a possible synergy in the action of the radionuclide and the biological vector. Even if this was

considered the safest approach in the absence of specific experimental evidence, it should be mentioned that the presence of both effects would increase the corrected cell survival for the two specific radiopharmaceuticals (with reference to figure 6(b)).

6. Conclusions

In the context of clonogenic survival experiments for the evaluation of novel radiopharmaceuticals, accurate assessment of the cell absorbed dose is crucial to better understand cell death mechanisms, and to evaluate therapeutic efficacy *in vitro*. The calculation of the absorbed dose in TRT is intrinsically more complex than in EBRT since it depends on many variables. Especially when β-emitters are involved, particular attention should be paid to the calculation of the cross-irradiation absorbed dose.

A realistic multi-cellular dosimetric model was developed for the calculation of the average cell absorbed dose on the basis of experimentally determined parameters (cell size, isolated cell/cluster density, cluster size, average cell cumulated activity). The model was here applied to the study of novel ^{177}Lu-labelled radiopharmaceuticals targeting CD37 receptors expressed by B cells. Its use allowed the demonstration of a dose–effect correlation for the three radiopharmaceuticals considered in the study, thus providing an indirect validation of the model itself. This approach is generic and can be useful for the determination of the average cell absorbed dose in clonogenic survival experiments involving any type of radiation.

Acknowledgments

This work was supported by Action Nu1.1 of Plan Cancer 2009–2013 (ASC 13038FSA), by the French National Research Agency under the program Investissements d'avenir (Grant Agreement LabEx MAbImprove: ANR-10-LABX-53), by Grant INCa-DGOS-Inserm 6045 and Nordic Nanovector ASA.

References

Agostinelli S *et al* 2003 Geant4: a simulation toolkit *Nucl. Instrum. Methods* **506** 250–303

Berger M J, Coursey J S, Zucker M A and Chang J 2009 *Stopping-Power and Range Tables for Electrons, Protons, and Helium Ions* (NIST) (http://www.nist.gov/pml/data/star/)

Briesmeister J F 2000 MCNPTMa general Monte Carlo *N*-particle transport code, version 4C *Report* LA13709M, Los Alamos National Laboratory, Los Alamos, NM MCNP^{TM} - A general Monte Carlo *N*-particle transport code, version 4C Report LA13709M, Los Alamos National Laboratory, Los Alamos, NM, USA

Brun R and Rademakers F 1997 ROOT—an object oriented data analysis framework *Nucl. Instrum. Methods Phys. Res.* A **389** 81–6

Cai Z, Pignol J P, Chan C and Reilly R M 2010 Cellular dosimetry of ^{111}In using Monte Carlo *N*-particle computer code: comparison with analytic methods and correlation with *in vitro* cytotoxicity *J. Nucl. Med.* **51** 462–70

Chouin N, Bernardeau K, Bardiès M, Faivre-Chauvet A, Bourgeois M, Apostolidis C, Morgenstern A, Lisbona A, Chérel M and Davodeau F 2009 Evidence of extra-nuclear cell sensitivity to alpha irradiation using a new microdosimetric model II. Application of the new microdosimetric model to experimental results *Radiat. Res.* **171** 664–73

Cousins B 2010 Probability density functions for positive nuisance parameters, internal note of the CMS statistic committee (http://www.physics.ucla.edu/~cousins/stats/cousins_lognormal_prior.pdf)

Cross W G, Ing H, Freedman N O and Mainville J 1982 Tables of beta ray dose distributions in water, air and other media *Report* AECL-7617, Atomic Energy of Canada Ltd, Chalk River Nuclear Laboratories, Ontario, Canada (https://inis.iaea.org/search/search.aspx?orig_q=RN:15004875)

Dahle J, Krogh C, Melhus K B, Borrebaek J, Larsen R H and Kvinnsland Y 2009 *In vitro* cytotoxicity of low-dose-rate radioimmunotherapy by the alpha-emitting radioimmunoconjugate thorium-227-DOTA-rituximab *Int. J. Radiat. Oncol. Biol. Phys.* **75** 886–95

Dahle J, Repetto-Llamazares A, Mollatt C S, Melhus K B, Bruland O S, Kolstad A and Larsen R H 2013 Evaluating antigen targeting and anti-tumor activity of a new anti-CD37 radioimmunoconjugate against non-Hodgkin's lymphoma *Anticancer Res.* **33** 85–95

Dale R G 1985 The application of the linear-quadratic dose-effect equation to fractionated and protracted radiotherapy *Br. J. Radiol.* **58** 515–28

Eckerman K F and Endo A 2008 *MIRD Radionuclide Data and Decay Schemes* 2nd edn (Reston, VA: The Society of Nuclear Medicine)

Faraggi M, Gardin I, Stievenart J L, Bok B D and Le Guludec D 1998 Comparison of cellular and conventional dosimetry in assessing self-dose and cross-dose delivered to cell nucleus by electron emissions of ^{99m}Tc, ^{123}I, ^{11}In, ^{67}Ga and ^{201}Tl *Eur. J. Nucl. Med.* **25** 205–14

Fowler J F 1990 Radiobiological aspects of low dose rates in radioimmunotherapy *Int. J. Radiat. Oncol. Biol. Phys.* **18** 1261–9

Freudenberg R, Wendisch M and Kotzerke J 2011 Geant4-simulations for cellular dosimetry in nuclear medicine *Z. Med. Phys.* **21** 281–9

Geant4 Collaboration 2015 Geant4 physics reference manual (http://geant4.web.cern.ch/geant4/UserDocumentation/UsersGuides/PhysicsReferenceManual/fo/PhysicsReferenceManual.pdf)

Goddu S M, Rao D V and Howell R W 1994 Multicellular dosimetry for micrometastases: dependence of self-dose versus cross-dose to cell nuclei on type and energy of radiation and subcellular distribution of radionuclides *J. Nucl. Med.* **35** 521–30

Goddu S M, Howell R W, Bouchet L G, Bolch W E and Rao D V 1997 *MIRD Cellular S Values* (Reston, VA: The Society of Nuclear Medicine)

Howell R W, Rajon D and Bolch W E 2012 Monte Carlo simulation of irradiation and killing in three dimensional cell populations with lognormal cellular uptake of radioactivity *Int. J. Radiat. Biol.* **88** 115–22

Humm J L, Howell R W and Rao D V 1994 Dosimetry of Auger-electron-emitting radionuclides: report no. 3 of AAPM nuclear medicine task group no. 6 *Med. Phys.* **21** 1901–15

Kvinnsland Y, Stokke T and Aurlien E 2001 Radioimmunotherapy with alpha-particle emitters: microdosimetry of cells with a heterogeneous antigen expression and with various diameters of cells and nuclei *Radiat. Res.* **155** 288–96

Loevinger R, Budinger T F and Watson E E 1991 *MIRD Primer for Absorbed Dose Calculations* revised edn (New York: The Society of Nuclear Medicine)

Motulsky H J and Christopoulos A 2005 *Fitting Models to Biological Data Using Linear and Nonlinear Regression. A Practical Guide to Curve Fitting* (San Diego, CA: GraphPad Software)

Papadimitroulas P, Loudos G, Nikiforidis G C and Kagadis G C 2012 A dose point kernel database using GATE Monte Carlo simulation toolkit for nuclear medicine applications: comparison with other Monte Carlo codes *Med. Phys.* **39** 5238–47

Pouget J P, Lozza C, Deshayes E, Boudousq V and Navarro-Teulon I 2015 Introduction to radiobiology of targeted radionuclide therapy *Frontiers Med.* **2** 1–11

Prestwich W V, Nunes J and Kwok C S 1989 Beta dose point kernels for radionuclides of potential use in radioimmunotherapy *J. Nucl. Med.* **30** 1036–46 (PMID: 2738686)

Rajon D, Bolch W E and Howell R W 2011 Lognormal distribution of cellular uptake of radioactivity-Monte Carlo simulation of irradiation and cell killing in 3-dimensional populations in carbon scaffolds *J. Nucl. Med.* **52** 926–33

Repetto-Llamazares A, Larsen R H, Patzke S, Fleten K G, Didierlaurent D, Pichard A, Pouget J P and Dahle J 2015 Targeted cancer therapy with a novel anti-CD37 beta-particle emitting radioimmunoconjugate for treatment of non-hodgkin lymphoma *PLOS ONE* **10** e0128816

Uusijärvi H, Bernhardt P and Forssell-Aronsson E 2008 Tumor control probability (TCP) for non-uniform activity distribution in radionuclide therapy *Phys. Med. Biol.* **53** 4369–81

Vaziri B, Wu H, Dhawan A P, Du P and Howell R W 2014 MIRD pamphlet no. 25: MIRDcell V2.0 software tool for dosimetric analysis of biologic response of multicellular populations *J. Nucl. Med.* **55** 1557–64

Whittaker E T and Robinson G 1967 *The Trapezoidal and Parabolic Rules. The Calculus of Observations: a Treatise on Numerical Mathematics* 4th edn (New York: Dover) pp 156–8

Abstract

B-cell Non-Hodgkin Lymphoma (NHL) treatment relies on the anti-CD20 antibody rituximab and chemotherapy. However, some patients become refractory to this therapy. Here, the efficacy of the novel anti-CD37 antibody-radionuclide conjugate ^{177}Lu-lilotomab (Betalutin®) was investigated in three NHL preclinical models and compared to both rituximab and ^{177}Lu-rituximab. The ^{177}Lu-cetuximab was also used as a non-targeting antibody for investigating the biological effects of ^{177}Lu alone.

In vitro, clonogenic survival and proliferation assays showed that rituximab and ^{177}Lu-rituximab were more cytotoxic than lilotomab and ^{177}Lu-lilotomab in the radioresistant Ramos cell line. Conversely, in the radiosensitive follicular lymphoma DOHH2 cell line, ^{177}Lu-rituximab and ^{177}Lu-lilotomab showed similar efficacy. Mantle cell lymphoma (Rec-1 cells) showed intermediate radiosensitivity leading to intermediate response to ^{177}Lu-lilotomab. A radiobiological approach discriminating the cytotoxic effects of unlabelled antibodies and of radiation showed that synergy was observed between the cytotoxic effects of ^{177}Lu and of rituximab involved in ^{177}Lu-rituximab efficacy. Conversely, for ^{177}Lu-lilotomab, synergy between ^{177}Lu and lilotomab was only observed in DOHH2 cells.

The high response of DOHH2 cells to ^{177}Lu-lilotomab was confirmed in vivo. Mice bearing subcutaneous DOHH2 or Ramos xenografts mouse models were intravenously injected with either ^{177}Lu-labelled- or unlabelled lilotomab and rituximab. ^{177}Lu-lilotomab and ^{177}Lu-rituximab showed the same therapeutic efficacy on DOHH2 tumours, although unlabelled lilotomab was less efficient than rituximab. Conversely, in Ramos tumour xenografts, the lower efficacy of ^{177}Lu-lilotomab compared with ^{177}Lu-rituximab could only be compensated by increasing ^{177}Lu-lilotomab tumour absorbed dose.

At the molecular level, tumour cells radiation-response was shown to be dependent on their ability to undergo apoptosis. This was associated with a reduction of G2/M cell cycle arrest, itself under the control of Wee-1 and Myt-1-mediated phosphorylation of cyclin-dependent kinase-1 (CDK1) at tyrosine 15 and threonine 14.

In conclusion, these results indicate that ^{177}Lu-lilotomab is an efficient therapeutic tool for NHL, particularly for tumours showing reduced CDK1 phosphorylation levels, such as in transformed follicular lymphoma (DOHH2 cells), and associated with synergistic cytotoxic effects between ^{177}Lu irradiation and lilotomab.

Résumé

Le traitement du lymphome B non hodgkinien (NHL) est généralement basé sur la combinaison d'un anticorps monoclonal anti-CD20, le rituximab, avec la chimiothérapie. Cependant, de nombreux patients deviennent réfractaires au ciblage du récepteur CD20 et ne répondent plus aux traitements. Dans cette thèse, l'efficacité d'un nouvel anticorps monoclonal anti-CD37 conjugué au Luthétium-177 (^{177}Lu-lilotomab, Betalutin®) a été étudié dans trois modèles précliniques de NHL et comparé au rituximab et à sa forme radiomarquée au luthétium-177 (^{177}Lu-rituximab). Le ^{177}Lu-cetuximab a également été utilisé comme anticorps non-spécifique pour étudier les effets biologiques du ^{177}Lu seul.

In vitro, des tests de survie clonogénique et de prolifération ont montré que le rituximab et le ^{177}Lu-rituximab étaient plus cytotoxiques que le lilotomab et le ^{177}Lu-lilotomab dans la lignée cellulaire radiorésistante Ramos (modèle du lymphome de Burkitt). Inversement, dans la lignée cellulaire radiosensible DOHH2 (modèle de lymphome folliculaire transformé), le ^{177}Lu-lilotomab et le ^{177}Lu-rituximab ont montré la même cytotoxicité. La lignée cellulaire Rec-1 (modèle du lymphome du manteau) présentait une radiosensibilité intermédiaire entrainant une réponse intermédiaire au ^{177}Lu-lilotomab. Une approche radiobiologique discriminant les effets cytotoxiques de l'anticorps seul et des radiations a montré de la synergie entre les effets cytotoxiques du ^{177}Lu et du rituximab dans l'efficacité globale du ^{177}Lu-rituximab. Inversement, pour le ^{177}Lu-lilotomab, de la synergie n'était observée que dans le modèle radiosensible DOHH2.

L'importante efficacité du ^{177}Lu-lilotomab dans le modèle DOHH2 a été confirmée in vivo. Des souris porteuses de xénogreffes sous-cutanées de cellules Ramos ou DOHH2 ont été traitées par intraveineuse avec le lilotomab, le rituximab et leur version radiomarquée. Le ^{177}Lu-lilotomab et le ^{177}Lu-rituximab ont montré la même efficacité thérapeutique sur les tumeurs radiosensibles DOHH2, alors que le lilotomab non radiomarqué était moins efficace que le rituximab. Inversement, sur les tumeurs radiorésistantes Ramos, la plus faible efficacité du ^{177}Lu-lilotomab comparé au ^{177}Lu-rituximab pouvait seulement être compensée par une augmentation de dose absorbée à la tumeur par le ^{177}Lu-lilotomab. A l'échelle moléculaire, la réponse des cellules tumorales aux radiations a été montrée comme dépendante de leur capacité à induire l'apoptose. Cela a été associé avec une réduction de l'arrêt en G2/M du cycle cellulaire lui-même sous le contrôle des phosphorylations médiées par Wee-1 et Myt-1 de la kinase dépendante des cyclines-1 (CDK1) sur la tyrosine 15 et thréonine 14.

En conclusion, ces résultats indiquent que le ^{177}Lu-lilotomab est un outil thérapeutique efficace dans le traitement des NHL et particulièrement dans les tumeurs montrant une réduction des niveaux de phosphorylations de CDK1, comme dans le modèle de lymphome folliculaire transformé (cellules DOHH2), et associé avec des effets cytotoxiques synergiques entre le ^{177}Lu et le lilotomab.